Molecular Dynamics Simulations of ZnO:

A step by step approach towards a detailed understanding of the complex solid/liquid/bio interface

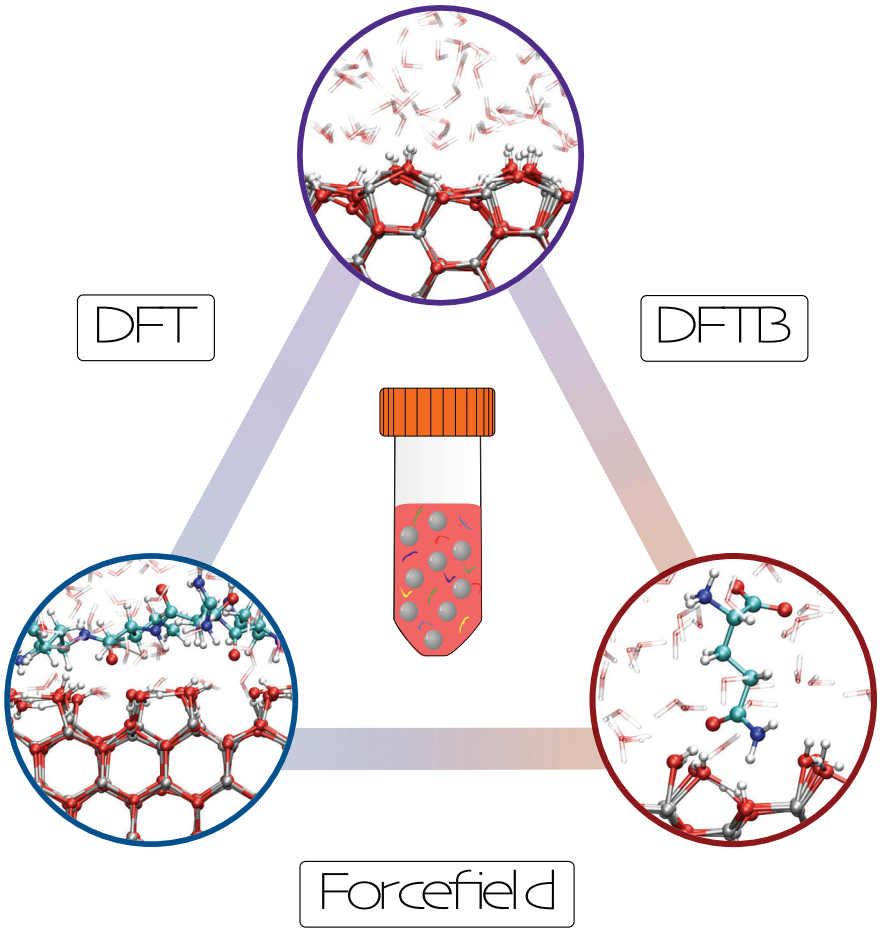

Svea große Holthaus

Bremen Center for BCCMS Computational Materials Science

Universität Bremen

Molecular Dynamics Simulations of ZnO:

A step by step approach towards a detailed understanding of the complex solid/liquid/bio interface

Vom Fachbereich für Physik und Elektrotechnik

der Universität Bremen

zur Erlangung des akademischen Grades eines

Doktors der Naturwissenschaften (Dr. rer. nat.)

genehmigte Dissertation

von

Dipl. Phys. Svea große Holthaus

aus Bremen

Mai 2014

Referent: Prof. Dr. rer. nat. T. Frauenheim

Korreferent: Prof. Dr.-Ing. Lucio Colombi Ciacchi

Eingereicht am: 07. Mai 2014

Tag des Promotionskolloquiums: 20. Juni 2014

Contents

Abstract

Several experimental studies so far have linked the toxicity of ZnO directly to solvated zinc ions. Therefore this study examines interactions occurring at the ZnO/water/bio interface by means of molecular dynamics simulations. In order to describe this interface theoretically, a step-by-step approach is used that splits the solid-liquid/bio interface into various sub-systems, so that each one of these systems isolates and addresses one specific problem.

Starting point is an analysis of the adsorption behavior of water over the zinc oxide $(1\bar{2}10)$ surface starting from single molecules up to bulk liquid. In doing this, results obtained with density-functional theory, density-functional tight binding and a recently developed reactive force field are compared. The methods perform comparably up to the level of a single monolayer of adsorbed water, predicting only small differences in adsorption energies and, as a consequence, adsorption geometries. However, the discrepancies among the methods have a dramatic effect on the dissociation equilibria and the structuring of liquid water layers in contact with the surface. In a next step a simple model describing two surface defects on zinc oxide $(10\bar{1}0)$ in contact with liquid water is used in to analyze the water structuring over different starting points of the dissolution process. Results for both surface kinks considered suggest that surface reconstruction of the defect site is to be expected under the influence of bulk water.

Taking the strongly adsorbed first water layer into account, the adsorption behavior of four different amino acids (glutamine, glutamate, serine, cysteine) on the zinc oxide $(10\bar{1}0)$ surface, comparing the geometry and energy associated with a number of different adsorption configurations are investigated in a bulk water environment . In doing this, the benefits and limits of using density-functional tight-binding (DFTB) with respect to standard density functional theory (DFT) are highlighted. The DFTB method is found to reliably reproduce the DFT adsorption geometries, however energetic comparisons between DFTB and DFT are made difficult by the long time necessary to achieve convergence of potential energy values in MD simulations and the necessity to include higher-order corrections to DFTB to obtain a good description of the hydrogen bond energetics. Analysis of the adsorption configurations emphasizes the fundamental role of the first hydration layer in mediating the interactions between the amino acids and the surface. Direct surface-molecule bonds are found to form predominantly via the carboxylate groups of the studied amino acids. This affinity of the carboxylate group towards surface zinc atoms was also observed for other models systems considered, like the adsorption of glutamate on a surface defect or the adsorption of a specific binder motif on ZnO.

1 Chapter 1. Introduction

1.1. Motivation, Aim and Structure of this Work

In ancient times zinc oxide (ZnO) was called "philosopher's wool" due to the cloudy appearance it adopts when produced by burning Zn in air. It was mainly used by alchemists in incantation rituals [WOO14]. Since then numerous other interesting properties of ZnO have been discovered. Nowadays world-wide use of 1.2 million tons of ZnO per year proves that it has advanced to an important material in various kinds of modern applications. Although ZnO is already a part of the every-day-life by being a component of solar cells, paints or cosmetic products, the scientific interest is still large due to the alleged potential of this material. The range of research fields includes e.g. the manipulation of electronic properties or growth of nano structures. A common factor in all these studies is the trend towards ever smaller and more efficient components for technical applications.

With the increasing importance of nano materials in today's research and development, it appears essential to weight the potential benefits against possible negative implications like unforeseen environmental or health issues. Hence parallel to the application-oriented research on nano materials, the field of nano toxicology has become increasingly important. The effects of ZnO nano structures (mostly nano particles) on human health and the environment has been addressed in several studies. The results suggest that ZnO nano structures are cytotoxic regarding bacteria (E.Coli) [HCWH09] or mammalian cells [XKL+08], but are also harmful to larger organisms like crustaceans [HIB+08] or zebrafish embryos [BZT+10]. The reactions responsible for this toxic effect of ZnO are discussed controversially and the mechanisms behind it are not yet unambiguously proven. However one indisputable key aspect in the toxicity of nano particles is the release of toxic ions as their solubility strongly influences their cytotoxicity [HIB+08]. Several studies suggest that for ZnO the toxicity is not size-related, since the rate of dissolution and the saturation solubility are similar for bulk and nano ZnO [FRA+07, HIB+08]. Heinlaan and co-workers [HIB+08] thereby stress that nano particles do not need to infiltrate

the cell to cause damage. Rather the contact between cell and particle might lead to a change in the microenvironment that could change the solubility of metal oxides. The argumentation that the solubility might be affected by biological compounds is substantiated by findings of Xia et al. [XKL+08]. They report a distinctively different saturation solubility of Zn ions in two different cell-culture media (CDMEM and BEGM)[1] compared to pure water. Furthermore this study demonstrates once more that the toxicity towards two kinds of cells (RAW 264.7, BEAS-SB)[2] of ZnO is directly related to particle dissolution and the release of toxic Zn ions into solution. In addition also the uptake of particle remnants into the cells is observed. The dissolution of ZnO is thereby linked to the production of high level reactive oxygen species (ROS) either at the particles surface or from biological compounds [XKL+08]. However a detailed description of the underlying reaction paths that occur in such a complex system have not yet been investigated. The interactions occurring at such a nano-bio interface are diverse and elaborately discussed in a review article by Nel and co-workers [NMV+09]. The correlations between reactions and system-determining parameters like particle shape or surface hydrations are quite complex, since also the effect of the surrounding solvent is crucial for the description of this interface. Therefore, starting from the nano particle, the description of the solid-liquid interface [3] can be seen as a key step in the description of more complicated systems.

Nevertheless the interaction between bio molecules and ZnO surface is also capitalized in some research fields. One of particular interest, namely molecular biomimetics, focuses on the unique interactions between engineered proteins and inorganic material, regarding the assembly of nano materials as well as the inherent problem of nano toxicity. That means polypeptides engineered to bind to a specific surface are used to control, for example, growth processes [DCT+05] or for detection purposes [KSK01]. These polypeptides are therefore called "Genetically Engineered Proteins for Inorganics" or short GEPI. Sarikaya[4], one of the leading scientists in the field of biomimetics, describes two different experimental set-ups to identify proteins that display a specific binding affinity towards a given material [STB+03], namely via phage display or cell-surface display. Thereby DNA fragments consisting of randomly generated peptides are either incorporated into the coat protein of a phage or surface proteins of a cell. These phages and cells, all displaying a different peptide sequence, are then brought into contact with the inorganic surface. Through specific washing cycles those phages (cells) displaying a strong binding affinity towards the surface are eliminated. In a last step the corresponding incorporated peptides are sequenced in order to identify the amino acid sequences responsible for the strong binding

[1] CDMEM is a cell-culture medium which consists of Dulbecco's Modidfied Eagle's Medium with added 10 % fetal bovine serum. BEGM is the short form of bronchial epithelial cell growth medium

[2] RAW 264.7 is a representative of a phagocytic cell line while BEAS-SB represents transformed human bronchial epithelial cells [XKL+08].

[3] That means the interface between particle surface and solvent.

[4] Mehmet Sarikaya professor at the University of Washington heading the Professor of Materials Science & Engineering group.

affinity[5].

Several experimental studies so far have focused on the identification of GEPI for ZnO and possible applications (e.g. [BXAM09, LDPP11, KSK01]). However the identified sequences differ significantly among the various studies. This is due to the pronounced surface selectivity of the evaluated protein sequences. In particular a good binder for a ZnO powder sample does not need to display a similar property when brought into contact with single crystal surfaces or nano particles. At this point the analysis of the binding behavior of identified specific binders on the corresponding surfaces by means of computer simulations can lead to a deep understanding of the binding characteristics. The acquired knowledge might then be transferred to various ZnO surface topologies and pave the way to new possible capabilities in the use of GEPI. But until now, studies that consequently combine sophisticated experimental and theoretical approaches are still missing.

In order to regulate and control reactions occurring at these underlying direct boundary surfaces between ZnO and the surrounding environment as in the case of the environment-dependent solubility or in the analysis of GEPI, one has to fully understand the configurations and mechanisms behind them. Hence this work sets out for an accurate theoretical description of solid-liquid/bio interfaces as the one exemplarily depicted in figure 1.1. The complexity, even of this already reduced system, requires a step by step approach. Therefore this work splits the solid-liquid/bio interface into various sub-systems, so that each one of these systems isolates and describes one specific problem. I depict this process as numerous puzzle pieces which, put together in the right way, give rise to a theoretical description of the discussed interface (see figure 1.1). Accordingly after a broad survey of the main research fields of ZnO in the remaining part of this chapter and a short introduction to the underlying theory of this work in chapter 2, the first sections in chapter 3 center on an appropriate validation of the computational set-up. This is followed by a comprehensive analysis of the water adsorption on the non-polar $(1\bar{2}10)$ ZnO surface (chapter 3.3 and red puzzle piece in Fig. 1.1). Moreover this model system is used to verify the performance of two approximate methods, namely density functional theory based tight binding (DFTB) and a reactive force field ReaxFF, against results from ab-initio density functional theory (DFT). These approximate methods will be of use for simulations that require system sizes and simulation time that are computationally unfeasible by full DFT molecular dynamics. Chapter 3 closes with the presentation of results of a first and simple model of two surface defects in contact with liquid water (see yellow puzzle piece in Fig. 1.1). Taking the strongly adsorbed first water layer into account, the interactions between the ZnO $(10\bar{1}0)$ surface and single amino acids are investigated in a bulk water environment (chapter 4) using DFT and DFTB (green puzzle piece). This model system is also used to further optimize the DFTB set-up. Moreover the interface of composite systems comprising ZnO, water and biological compounds is analyzed for more complex surfaces like a ZnO nanowire and the ZnO $(10\bar{1}0)$

[5] A more detailed description of the utilized processing parameters can be found in [STB+03]

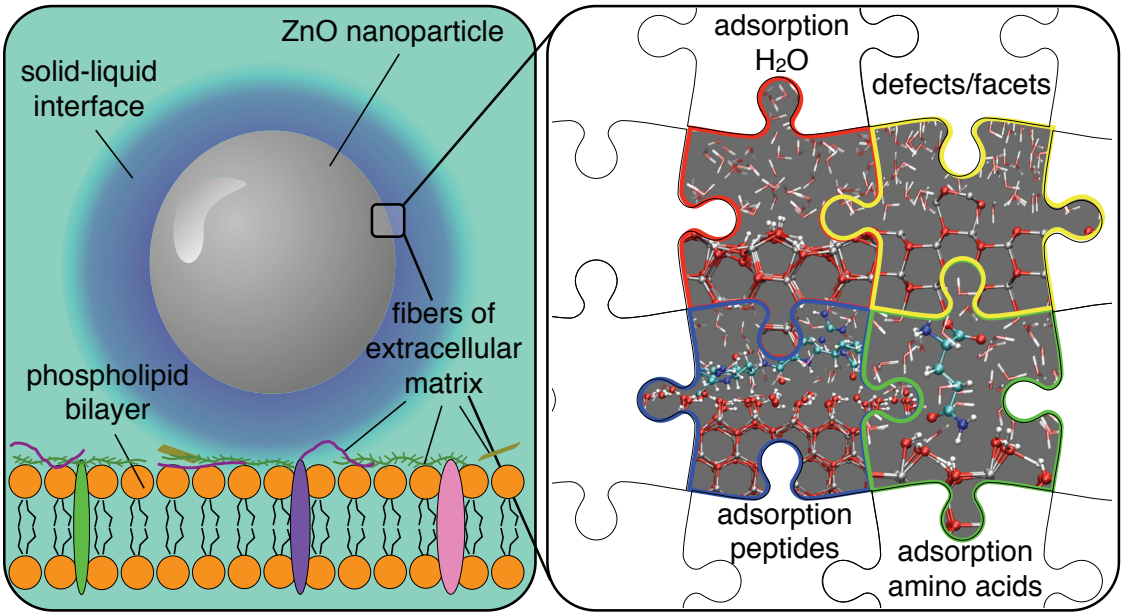

Figure 1.1.: Depiction of the nano-bio interface (left) inspired by the figures of Nel and co-workers [NMV+09]. Pictured as an enlargement of the solid-liquid interface are the single simulation set-ups (right) analyzed in this work, that are used to understand reactions at the interface and that contribute to a correct description of the latter.(Both schemes are not to scale)

surface featuring an oxygen kink defect. The step towards a description of even larger systems comprising ten thousands of atoms is made in chapter 5 through the introduction of parameters for a classical forcefield describing the ZnO/water/bio interface. One preliminary application of the latter focusing on genetically engineered proteins in contact with a ZnO surface under three different hydration states constitutes the final part of this work (This part is represented by the blue puzzle piece in Fig. 1.1).

The common reference point in all simulations of the different sub-systems is the evaluation of the influence of an aqueous environment. The inclusion of this factor constitutes a unique feature of this thesis, since it has only been the focus of very few theoretical studies on ZnO [RDG+11, RDBH08]. However, given the fact that hardly any application comprising ZnO is manufactured to work in an ultra-high vacuum environment, the impact of a water-containing environment constitutes an issue that cannot be neglected in modern computational surface science. Certainly the results shown in this work will not be enough to claim that a complete description of this interface and therefore of possible dissolution processes can be derived from them. Nevertheless the knowledge acquired in this work will lead a fair bit of the way to a clearer picture of the mechanisms at this solid-liquid interface and therefore on the way to understanding the toxicity of ZnO and its nano structures.

1.2. Survey of the Research Fields

1.2.1. Important Facts about Zinc oxide

Zinc oxide (ZnO) is a II-VI compound semiconductor. The crystal structures observed for ZnO are wurtzite, zinc blende and rocksalt, depending on the applied pressure. Under ambient conditions the most stable phase is the wurtzite phase belonging to the space group $P6_3mc$. In this case each anion is tetrahedrally surrounded by four cations and vice versa. This arrangement of zinc and oxygen atoms effectuates a polar symmetry along the hexagonal axis, which is the origin of the piezoelectricity of ZnO. A depiction of the structure and directions of ZnO in the wurtzite phase is shown in figure 1.2. The wurtzite crystal is based on the hexagonal crystal

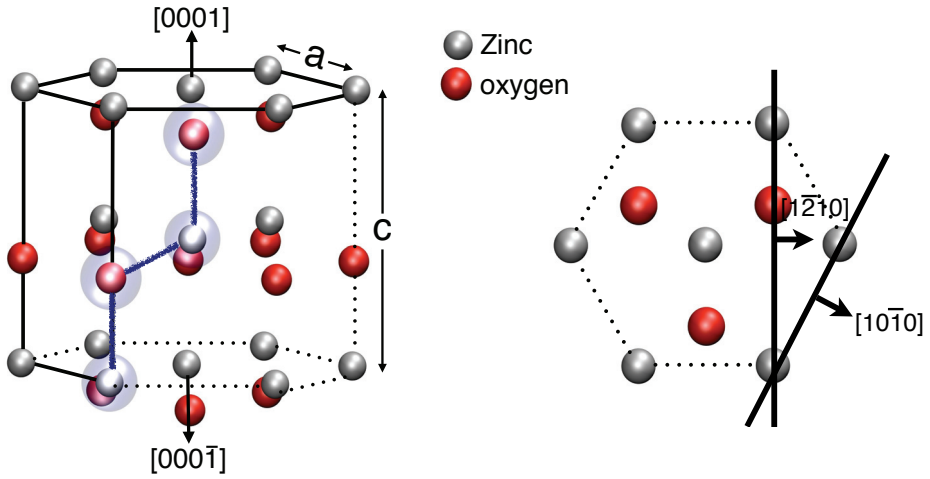

Figure 1.2.: Illustration of the wurtzite phase of bulk ZnO. The right depiction is a top view of the left crystal structure. The blue marked atoms belong to the hexagonal unit cell. The squared brackets denote the characteristic directions of the crystal.

system and therefore a hexagonal unit cell is necessary to built the ZnO crystal. The four atoms of the unit cell are marked by blue spheres in figure 1.2. The size of the unit cell is defined by the cell parameters a and c. X-ray diffraction measurements at 298K assigned values of a= 3.250 Å and c=5.207 Å [AB69] to the ZnO unit cell.
A tetrahedral coordination is usually found in materials with an sp^3 covalent bonding nature. However the rather large direct band gap of ZnO with a value of 3.437 eV [LCR$^+$11] (near-UV) at 2 K is an evidence for the pronounced ionic character of ZnO. The bonding in ZnO can therefore be described as coordinative bonding, that means as a mixture of covalent and ionic bonding.

Four surfaces are prevalent in the ZnO crystal, namely the Zn-terminated (0001) surface, the O-terminated (000$\bar{1}$) surface and the mixed-terminated and therefore non polar surfaces (10$\bar{1}$0) and (1$\bar{2}$10). The directions associated with these surfaces are depicted in figure 1.2.

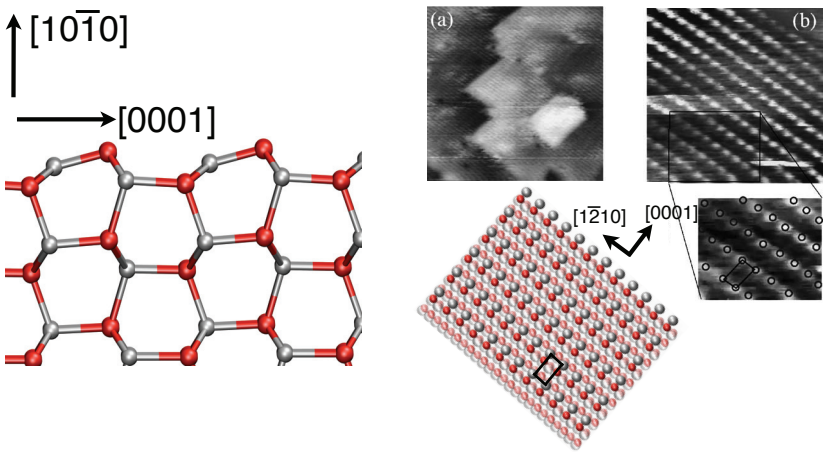

Figure 1.3.: Depiction of the relaxed surface structures of the ZnO(10$\bar{1}$0) surface from DFT calculations [this work] and STM imaging by Diebold and co-workers [DKD04]. In the left part the surface is shown in a sideward view whereas on the right side the theoretical model and STM images show a top view of the surface.

DFT calculations of the corresponding cleavage energies, using an LDA and a GGA approach respectively, yield the (10$\bar{1}$0) surface as the most stable surface with the (1$\bar{2}$10) surface being only slightly higher in energy [MMD$^+$04]. The polar surfaces are often used in growth experiments as the direction of growth. Neverthess as this work focuses on the two non-polar surfaces of ZnO only the latter will be discussed in detail. The (10$\bar{1}$0) surface has been the subject of many experimental as well as theoretical studies. Like the (1$\bar{2}$10) surface it is composed an equal number of Zn and O atoms. Using low-energy-electron-diffraction (LEED) [LDC$^+$76] the (10$\bar{1}$0) surface was found to exhibit the same periodicity as expected from bulk. This means that no reconstruction on the (10$\bar{1}$0) surface is observed. The comparison of intensities obtained in an elastic LEED experiment with calculated intensities from model systems complied with a rearrangement of the upper most ZnO surface dimers [DLC$^+$77]. DFT studies performed by Meyer and coworkers confirmed this kind of surface relaxation [MRM06, MM03, MMD$^+$04]. A depiction of the relaxed (10$\bar{1}$0) surface structure is displayed in figure 1.3. The ZnO dimers of the surface layer are tilted towards the surface, while the zinc oxygen bond length decreases. While a distinct tilt of the dimer is expected for covalently bonded material a decrease in bond length is presumed for ionic systems. Thus the relaxation characteristics account once more for the two-faced nature of ZnO bonding, namely ionic and covalent. Images of the (10$\bar{1}$0) surface using scanning tunneling microscopy (STM) taken by Diebold and co-workers [DKD04] (right part of figure 1.3) show a well-defined terrace-step structure. STM images with atomic resolution furthermore confirm the configuration of the zinc oxygen dimer rows. The positions of the upper-most zinc atoms of the surface layer, displayed as bright spots in the STM image, match the corresponding positions found in DFT calculations[DKD04]. Roughness measurements in

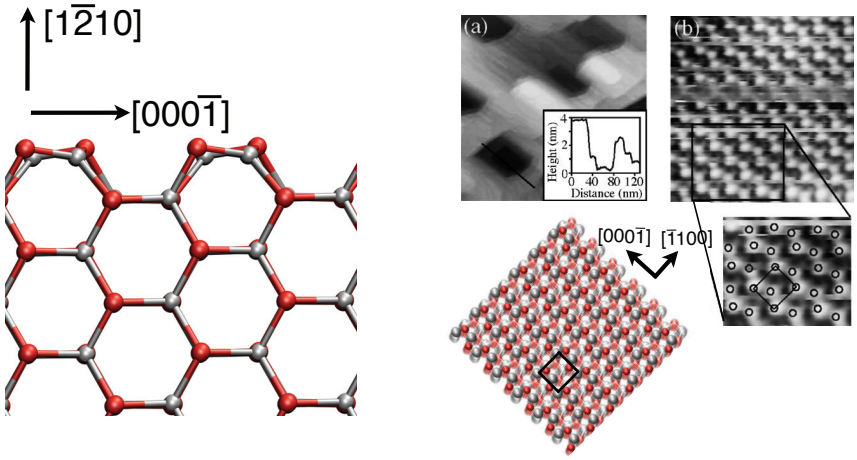

Figure 1.4.: Depiction of the relaxed surface structures of the ZnO(10$\bar{1}$0) surface from DFT calculations [this work] and STM imaging by Diebold and co-workers [DKD04]. In the left part the surface is shown in a sideward view whereas on the right side the theoretical model and STM images show a top view of the surface. The inset graph depicts the rms roughness measure of the surface.

the same work yielded a small roughness (height variations < 2 nm) even at higher temperatures.

The second non-polar surface (1$\bar{2}$10) either does not display signs of surface reconstruction. Like for the (10$\bar{1}$0) surface, the first layer ZnO dimers are tilted compared to the bulk structure (see figure 1.4). Meyer et al. [MM03] calculated tilt angles and bond reduction similar to those found for the (10$\bar{1}$0) surface. For the (1$\bar{2}$10) surface Diebold et al. [DKD04] have measured a more distinct surface roughness as seen from the root-mean-square roughness graph in figure 1.4. They rationalized the high roughness by the higher cleavage energy and a correspondingly less stable surface, which could not be confirmed by theoretical calculations[MM03]. The bright spots in the STM images with atomic resolution in figure 1.4 again depict the zinc atoms of the upper most ZnO dimers. Their positions are consistent with DFT calculations depicted in the same figure. The higher surface roughness of the (1$\bar{2}$10) surface compared to the (10$\bar{1}$0) surface and the corresponding higher effort to generate well defined surface samples presumably have effected that this non-polar surface has only been the focus of very few studies.

The reason why ZnO became an increasing field of research around the 1930s, was its large exciton binding energy of 60 meV which made it an interesting material especially for applications in optoelectronics. ZnO is a direct semiconductor. The minimum of the lowest conduction band and the maximum of the uppermost valence band are located at the Γ-Point. The lowest conduction band (LUMO) is formed by the unoccupied 4s orbitals of Zn^{2+}. The highest valence band (HOMO) is defined by the 2p orbitals of O^{2-}. Including spin and the effect of the hexagonal crystal field, the valance band is split into three twofold-degenerate sub valence bands

[Kli07]. Excitons assemble from an electron in the conduction band and a hole from one of the three sub-valence bands. Regardless of the sub-valence band the binding energy is approximately 60 meV at room temperature. The large exciton binding energy [6] could be used for example in lasing (blue/UV) devices that work well above room temperature.

In order to realize ZnO devices for optoelectronic applications, such as light emitting diodes (LED), it is necessary to dope ZnO. For that matter a lot of studies focused on doping of ZnO. The native doping of ZnO is n-type. The reason for this was thoroughly discussed in various publications. Earlier works identified either interstitial Zn (Zn_I) zinc vacancies (V_Zn) or oxygen vacancies (V_O) as dominant donors [LHS99, Har54, UH75, Hag76]. Nevertheless their high formation energies evaluated in later studies contradicted this assumption. A recent study applying experimental and theoretical methods concludes that a nitrogen substitute for oxygen that forms a complex with a Zn_I is a very promising candidate to explain properties found in n-type ZnO [LFR$^+$05]. However compared to the starting days of ZnO research, the interest in ZnO significantly decreased in the 1980s partly due to the missing ability to dope ZnO ambipolar that means in both n and p type manner. The p-type doping difficulty in ZnO is among others due to low solubility of p-type dopants or compensation by low-energy native defects [PZW02]. Apart from the problem of stable p-type doping, the inability to grow structures with reduced dimensionality constituted a drawback in the first period of ZnO research

The interest in ZnO started growing again in the late 1990s when it became apparent that it is possible to grow ZnO in various kinds of structures with reduced dimensionality like nano rods, quantum dots or nano particles [ZKA$^+$97, DCZ97, PDW01]. Furthermore, lately the results of several studies have shown promising results regarding the p-type doping of ZnO by building p-conducting nanowires and pn-junctions [YZJ$^+$08, PLP$^+$11, HCK$^+$13]. The variety of possible applications fields of ZnO has been growing ever since.

1.2.2. ZnO Applications Fields: Nanostructures and Development Potentials

The world-wide use of 1.2 million tons of ZnO per year emphasizes that it has long been a significant material in a broad range of processes in many industries (see figure 1.5). As such, it improves, for example the absorption of frictional heat in tires or guarantees bright colors in the production of tiles. Among others, it plays an important role as an ingredient in animal feed, a mild antiseptic and its property to absorb UV-light is used in sunscreens. In the field of technological devices, the properties of ZnO are utilized for sensing, optical, acoustic and electronic devices. In particular ZnO is an interesting material in the field of transparent electronics due to it high optical transmittivity and conductivity. In 2003, Nomura and co-workers demonstrated that an invisible thin film transistor comprising ZnO shows a distinctly higher field-effect mobility than SnO_2 devices [NOU$^+$03]. Regarding optical devices, ZnO is

[6] GaN has a exciton energy of 25 meV.

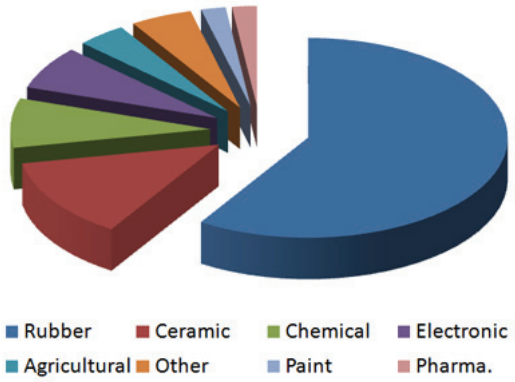

Figure 1.5.: World-wide ZnO Applications in the year 2012 taken from a study by Dr. Stefan Schlag [IHS14]

perceived as the alternative for GaN to build optoelectronic devices in the blue/UV range. The current technological importance and the prevailing ambition to miniaturize devices have initiated the development of a new research area focusing on growth, characterization and applicability of ZnO nano structures. Presently it is possible to synthesize ZnO nano particles, belts, wires or flowers under various conditions and in various sizes as depicted in figure 1.6. Recently Zheng and co-workers [ZLP+13] even succeeded in selectively growing specific patterns (see figure 1.6 d)). Besides showing the synthesis of nano rods without a seed layer by using a galvanic-cell structure, they also found a significantly enhanced photoelectric response.

The fast growth directions of ZnO are given by the low index directions $[10\bar{1}0]$,$[1\bar{2}10]$ and $[000\bar{1}(1)]$ of its wurtzite crystal structure. The final morphology of the nanostructure is therefore determined by the relative activities of the corresponding surfaces. The activities are determined by their kinetic parameters which highly depend on the chosen growth conditions. Since the two non-polar surfaces exhibit the lowest surface energy, nano structures assemble by maximizing the area of the corresponding facets. Therefore for most nano structures, like nano rods, the typical growth direction is in the direction of the polar axis.

There are various production processes known in the synthesis of ZnO nano structures such as chemical vapor disposition (CVD), vapor-liquid-solid depositions, pulse laser deposition, flame spray pyrolisis or wet chemistry growth methods [ZLP+13]. ZnO nano rods grown by a vapor-phase epitaxy were shown to exhibit a uniform thickness and length distribution [PKJY02]. Since no catalyst was used in the processing, the risk to incorporate defects in the nanostructure that might change its electronic properties is minimized compared to e.g. vapor-liquid-solid deposition methods that use gold as a catalyst [HWF+01]. However the vapor-phase epitaxy grows the nano structures on single-crystal substrates which do not meet the requirement for low fabrication costs - an absolute prerequisite for industrial application. Solution based methods fulfill this requirement and can also be used in scaled-up productions. Vayssieres [Vay03] showed that

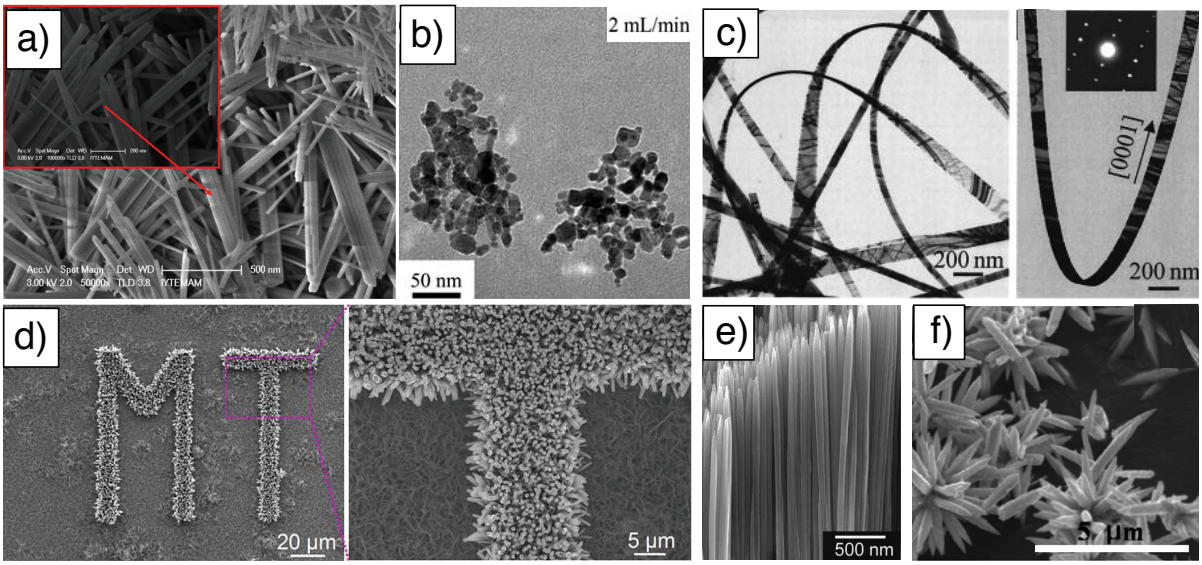

Figure 1.6.: Depiction of nano rods (a) [CEE12], nano particles (b) [TMP02], nano belts l' [PDW01], selectively grown (d) [ZLP+13] and aligned (e) nanorods [PKJY02] and nano flowers [WAK+07] made of ZnO

ZnO nano wires and arrayed nano rods can be grown from aqueous solutions. Nanoflowers and microspindles were grown on indium-doped tin oxide by Peng and co-workers using a chemical bath deposition process [PQCW06]. Nevertheless solution based methods either require a seed layer of ZnO as nucleations site or special substrates (e.g. single crystalline sapphire) that involve an extensive preparations or are rather expensive. Altogether a low cost, but at the same time large scale and tunable fabrication of ZnO nano structures with excellent optoelectronic properties is an ongoing field of research.

The high surface-to-volume ratio of ZnO nano wires is of particular utility for sensing applications. ZnO nano wires exposed to a reductive gas like ethanol show a response in conductivity [WLC+04], yielding a high sensitivity and a fast response and recovery time. Still the selectivity of such sensors needs to be improved through synthesis of composite nano structures [Wan04]. Dye-sensitized solar cells (DSSC), which couple the photo absorption of a dye with a semiconductor, utilize the wide band gap and the various processable nano structures of ZnO. In such a device the ZnO nanostructure is covered by a thin layer of dye. Incoming photons are absorbed by the dye, subsequently the excited electrons are injected into the conduction band of ZnO. Although energy conversion efficiency could be improved using nano forest structures of ZnO, the fill factor [7] values for ZnO are lower than for otherwise used TiO_2 nano particles [KLK+11]. Moreover ZnO nano wires are found to be a promising material for in situ biosensing [ZXW06], while ZnO nano particles are used to functionalize cotton fabrics [YPK+06]. These are just a

[7] Important parameter in solar cells that determines the power conversion efficiency

few examples of devices where nano ZnO is used. Needlessly to say that there are still a lot of issues, electronic as well as structural properties, to investigate in order to integrate these into commercial products.

Chapter 2.
2 Principles of Computational Materials Science

This chapter focuses on a short description of the theoretical background and approximations this work is based on. Starting from an introduction to molecular dynamics, two different approaches of the latter, namely Born-Oppenheimer molecular dynamics and Car-Parinello molecular dynamics, are discussed regarding their constitutive equations and approximations. Subsequently the junction between experiment and theory, the field of statistical mechanics, is used to introduce the different statistical ensembles employed in this work. The remaining sections of the chapter are addressed to the different approaches to solve the electronic problem, going from full ab-initio methods like Hartree-Fock or density functional theory over to more approximate methods like density functional-based tight binding to classical force field methods. Lastly the pros and cons of the methods used in this work are shortly summarized and discussed for possible applications.

The structuring of this chapter is closely related to chapters in the textbooks "Ab Initio Molecular Dynamics" [MH09], "A Chemist's Guide to Density Functional Theory" [KH01], "Statistical Mechanics" [PB11], "Understanding Molecular Simulation" [FS01] and "Solid State Theory" [Czy07].

2.1. Molecular Dynamics

Probably the best description of molecular dynamics (MD) is to understand it as a virtual laboratory approach. Molecular dynamics thereby works with atomistic resolution, that means MD in general depicts the time dependent behavior of atoms. The possible application area ranges from surfaces over hybrid interfaces to the description of complex systems like DNA. By using this ansatz in computational materials research it is possible not only to gain insight into reactions occurring at the atomistic scale but also to understand why they happen. In an ideal case, results obtained from molecular dynamics runs are able to predict material properties or help to design new materials without the need to conduct a real experiment. Furthermore the ability to

design new materials or material properties on a computer opens the way to different approaches possible, compared to the probe preparation known from experimental research. The greatest challenge of computational simulations is for example of particular interest when it comes to the field of in-vivo research. The opportunity to be able to replace in-vivo laboratory research at least partly by simulations is one aspect for the promising role of computational material science in future research. In order to capture the aims, abilities but also the shortcomings of molecular dynamics, it is vital to understand the fundamental theory it is based on. Therefore the following chapter provides a brief outline of the basic concepts behind molecular dynamics.

2.1.1. Born-Oppenheimer Molecular Dynamics

The equations of motion of the atoms, finally solved by numerical integration, are the classical Newtonian equations of motion. An understanding of the underlying approximations and assumptions can be obtained by deriving them from the exact ansatz of non-relativistic quantum mechanics, that means from the time-dependent Schrödinger equation for a system of N electrons and M nuclei, namely

$$i\hbar\frac{\partial}{\partial t}\Phi(\{\mathbf{r}_i\},\{\mathbf{R}_I\},t) = \hat{H}\Phi(\{\mathbf{r}_i\},\{\mathbf{R}_I\},t). \tag{2.1}$$

In this context i stands for the imaginary unit, $\hbar$ is the reduced Planck constant, $\mathbf{r}_i$ and $\mathbf{R}_I$ represent the positions of the electrons and nuclei respectively and $\Phi(\{\mathbf{r}_i\},\{\mathbf{R}_I\},t)$ is the total wave function. $\hat{H}$ stands for the Hamiltonian of the solid state and comprises the kinetic energies of the electrons and nuclei as well as the Coloumb potential energies of the electron-electron nucleus-nucleus and electron-nucleus interaction

$$\begin{aligned}\hat{H} = &-\sum_I \frac{\hbar^2}{2M_I}\nabla_I^2 - \sum_i \frac{\hbar^2}{2m_e}\nabla_i^2 \\ &+ \frac{1}{4\pi\varepsilon_0}\sum_{i<j}\frac{e^2}{|\mathbf{r}_i-\mathbf{r}_j|} + \frac{1}{4\pi\varepsilon_0}\sum_{I<J}\frac{e^2 Z_I Z_J}{|\mathbf{R}_I-\mathbf{R}_J|} \\ &- \frac{1}{4\pi\varepsilon_0}\sum_{I,i}\frac{e^2 Z_I}{|\mathbf{R}_I-\mathbf{r}_i|} \\ = &-\sum_I \frac{\hbar^2}{2M_I}\nabla_I^2 + \mathcal{H}_e(\{\mathbf{r}_i\},\{\mathbf{R}_I\}).\end{aligned} \tag{2.2}$$

Here M_I and Z_I refer to the mass and the atomic number of the I-th nucleus, while m_e and e stand for the mass and charge of an electron. Furthermore ε_0 denotes the vacuum permittivity.

System of Fixed Nuclei

The reduced Hamiltonian $\mathcal{H}_e$ in equation 2.2 describes the problem of N electrons in a potential of M fixed nuclei. If we regard the electronic system as solved and assume a discrete spectrum of energy eigenvalues (E_k) with corresponding orthonormalized eigenfunctions Ψ_k, we can expand the total wavefuction into

$$\Phi(\{\mathbf{r}_i\},\{\mathbf{R}_I\},t) = \sum_{\ell=0}^{\infty} \Psi_\ell(\{\mathbf{r}_i\},\{\mathbf{R}_I\}) X_\ell(\{\mathbf{R}_I\},t). \tag{2.3}$$

The $X_\ell(\{\mathbf{R}_I\},t)$ stand for the eigenfunctions of the nuclei. Thereby we assume adiabatic eigenfunctions Ψ_k as the solution of the electronic system, that means we only consider an electronic system that evolves slowly enough in order to stay in an equilibrium with its environment.

Adiabatic- and Born-Oppenheimer Approximation

Inserting the expanded total wave function into the time dependent Schrödinger equation (2.1) then gives

$$i\hbar\frac{\partial}{\partial t}X_k = \left[-\sum_I \frac{\hbar^2}{2M_I}\nabla_I^2 + E_k(\{\mathbf{R}_I\})\right] X_k + \sum_\ell C_{k\ell} X_\ell \tag{2.4}$$

$$\text{with} \quad C_{k\ell} = \int \Psi_k^* \left[-\sum_I \frac{\hbar^2}{2M_I}\nabla_I^2\right] \Psi_\ell d\mathbf{r} + \frac{1}{M_I}\sum_I \left(\{\int \Psi_k^* [-i\hbar\nabla_I]\Psi_\ell d\mathbf{r}\}[-i\hbar\nabla_I]\right). \tag{2.5}$$

The degree of approximation depends on the treatment of the factor $C_{k\ell}$. If we only take the diagonal terms C_{kk} into account we treat the system in an adiabatic approximation, since a limitation to the diagonal terms leads to an equation for determining X_k, where the motion of the nuclei is described without a change of the quantum state of the electronic system. If one goes one step further and also neglects the diagonal terms one obtains an equation for X_k in the Born-Oppenheimer approximation

$$[-\sum_I \frac{\hbar^2}{2M_I}\nabla_I^2 + E_k(\{\mathbf{R}_I\})]X_k = i\hbar\frac{\partial}{\partial t}X_k. \tag{2.6}$$

The Born-Oppenheimer approximation therefore describes the nuclei moving in an effective potential $E_k(\{\mathbf{R}_I\})$, which depends parametrically on the nuclei positions $\{\mathbf{R}_I\}$. Consequently the electron and the nuclei dynamics are totally separated in this case. The physical justification for the applicability of the Born-Oppenheimer approximation is the ratio of the masses of electrons and atomic nuclei. As the mass of a nucleus is in a range of 10^4-10^5 magnitudes larger than the electron mass, one can argue that the underlying time scales for the electronic and the nuclei dynamic are different. Therefore from the point of view of the fast electronic system, the

system of the nuclei can be seen as approximately static. Accordingly, the electronic system can be assumed to adapt to new nuclei positions almost instantaneously.

Newtonian Equations of Motion

Up to now the nuclei as well as the electrons are treated as quantum-mechanical particles. The next approximation necessary to derive the basic equations of motion for molecular dynamics is to consider the nuclei as classical particles. This is justified by the apparently large masses involved in the nuclei dynamics. In a first step, one describes the quantum-mechanical wave function of the nuclei as

$$X_k(\{\mathbf{R}_I\},t) = A_k(\{\mathbf{R}_I\},t)e^{iS_k(\{\mathrm{R}_I\},t)/\hbar}, \tag{2.7}$$

where A_k is a real and positive amplitude and S_k is the corresponding real phase. By inserting this ansatz into equation 2.6 and by separating the real and the imaginary part one can rewrite the equations of motion for the nuclei in terms of the amplitude and the phase. The classical limit is then imposed by setting $\hbar \longrightarrow 0$. In this limit the equation of the phase becomes

$$\frac{\partial S_k}{\partial t} + \sum_I \frac{1}{2M_I}(\nabla_I S_k)^2 + E_k = 0. \tag{2.8}$$

The structure of the description of the dependency of the phase, S_k, shows the same characteristics as the equations of motion in the Hamilton-Jacobi formulation. Therefore, in an analogy to the Hamilton-Jacobi methodology one can derive the underlying equations of motion for the nuclei

$$\begin{aligned} M_I\ddot{R}_I(t) &= -\nabla_I E_k(\{\mathbf{R}_I\}) \\ &= -\nabla_I \min_{\Psi_0}\langle\Psi_0|\mathcal{H}_e|\Psi_0\rangle. \end{aligned} \tag{2.9}$$

With Ψ_0 as the ground state wave function. Consequently one can derive a Newtonian formulation of motion for each electronic state k. The nuclei are seen to move in an effective potential based on the solution of the time independent Schrödinger equation for the electronic system in state k for the nuclei positions R_I. This ansatz to molecular dynamics is called Born-Oppenheimer molecular dynamics (BOMD).

Looking at the equation of motion it is obvious that a quantum-mechanical description of the time evolution of the electrons is not explicitly included in the description. More specifically the electronic dynamic is described to follow the nuclei dynamic by being parametrically dependent on the nuclei positions. This assumption allows one to choose a time step during a MD run that is adequate for the slower nuclei dynamic. As a consequence, large time steps and therefore longer simulation times are accessible. The prize that has to be paid for this useful property is

the minimization of the corresponding matrix element $\langle\Psi_0|H_e|\Psi_0\rangle$ at each minimization step to evaluate the corresponding energy surface. A different derivation of molecular dynamics, the Ehrenfest dynamics, takes into account the electronic dynamics so that, once the wave function is found that minimizes $\langle\mathcal{H}_{el}\rangle$, the electrons will stay in their ground state minimum as the nuclei move. This explicit inclusion makes it necessary to use time steps determined by the intrinsic electronic system dynamics, that means at least two orders of magnitude smaller than for BOMD.

2.1.2. Car-Parrinello Molecular Dynamics

The Car-Parrinello molecular dynamics (CPMD) is a concept that combines the approaches of BOMD and Ehrenfest. In CPMD the whole system is split into two purely classical problems (electronic and nuclei system), which exists on two different energy scales. This assumption is displayed in the corresponding Lagrangian

$$\mathcal{L}_{CP} = \sum_I \frac{1}{2} M_I \dot{R}_I^2 + \sum_i \frac{1}{2}\mu_i \langle\dot{\varphi}_i|\dot{\varphi}_i\rangle - \langle\Psi_0|\mathcal{H}_{el}|\Psi_0\rangle + constraints \tag{2.10}$$

postulated by Car and Parinello in 1985 [CP85]. Thereby the newly introduced variables μ_i can be interpreted as the fictitious masses of the orbitals φ_i with a unit of [energy $\cdot\, t^2$] to ensure the right dimensionality. In this context the orbitals φ_i that constitute the total electronic wave function are interpreted as a classical complex scalar field, therefore the "force" on these orbitals is simply given as the derivative of the Lagrangian with respect to these orbitals. The same is of course true for the nuclei system by substituting the orbitals with the nuclei position $\mathbf{R}$. Therefore the corresponding equations of motion are given with the use of the Euler-Lagrange equations as:

$$M_I \ddot{\mathbf{R}}_I(t) = -\frac{\partial}{\partial \mathbf{R}_I}\langle\Psi_0|\mathcal{H}_{el}|\Psi_0\rangle + \frac{\partial}{\partial \mathbf{R}_I} constraints, \tag{2.11}$$

$$\mu_i \ddot{\varphi}_i(t) = -\frac{\partial}{\partial \varphi_i}\langle\Psi_0|\mathcal{H}_{el}|\Psi_0\rangle + -\frac{\partial}{\partial \varphi_i}.constraints \tag{2.12}$$

The whole concept of CPMD is based on the assumption of separate energy scales for the electronic and the nuclei system, that means CPMD needs "hot" nuclei and "cold" electrons. To avoid energy transfer from one system to the other the power spectra from both dynamics should show no overlap, therefore

$$\frac{\omega_{el}^{min}}{\omega_n^{max}} >> 1 \tag{2.13}$$

should be fulfilled at all times, with ω_{el}^{min} (ω_n^{max}) being the minimal (maximal) frequency of the electronic (nuclei) system. The lowest possible electronic frequency is determined by the energy

gap E_{gap} present in the system

$$\omega_{el}^{min} \propto \left(\frac{E_{gap}}{\mu}\right)^{\frac{1}{2}}. \tag{2.14}$$

In order to well comply with equation 2.13 one therefore needs to keep μ small since E_{gap} and ω_n^{max} are characteristic and therefore fixed properties of the system. However, a small μ leads to a broadening of the whole frequency spectrum as well as to an increase of the maximum frequency through

$$\omega_{el}^{max} \propto \left(\frac{E_{cut}}{\mu}\right)^{\frac{1}{2}}, \tag{2.15}$$

with E_{cut} as the largest kinetic energy in the plane-wave formulation of CPMD (see chapter 2.2.1 for a more detailed description).

The introduction of the fictitious electronic dynamics in CPMD is advantageous, since it supersedes the time-consuming minimization of the matrix element (see equation 2.9) which is necessary in BOMD at every time step[1]. Although the time step complies with the fictitious electronic dynamic, and is therefore smaller compared to the one needed for BOMD, the overall computational time in CPMD is smaller. This is of particular interest considering the simulation of long trajectories. Nevertheless, since the maximum applicable time step is inversely proportional to the maximum electronic frequency in CPMD, the choice of the parameter of the fictitious mass is always a balance between the need for fully separated systems and the wish for a large time step.

2.1.3. The Velocity Verlet Algorithm

In order to use the equations of motion derived in the two previous sections for BOMD and CPMD in a computational simulation one needs to apply an algorithm that is able to integrate as accurately as possible. There are many different integration algorithms available to perform this task. Therefore the choice of the algorithm depends on the system and its properties. Since the major part of the calculation time is spent on the evaluation of the emerging interactions, algorithms that make the use of large time steps are the most efficient way to speed up the simulation. For BOMD the size of the time step is limited by the underlying vibrations of the system. To take all vibrations into account one has to make sure that the choice of the time step is smaller than the highest frequency of motion within the system. The highest vibrational frequencies are usually found for bonds between light and heavier atoms, for example between hydrogen and oxygen or carbon. For that reason it is possible to use constraints to inhibit these vibrations.

[1] In CPMD this minimization procedure is only needed at the first time step

Apart from a large time step, a good integration algorithm should guarantee an acceptable stability in energy. Thereby one can divide the available numerical integration schemes into two groups: one group that provides a good short term energy conservation and one that provides a long term energy conservation. The basis for the algorithm used in this work, called Verlet [Ver67], belongs to the latter. The long term energy conservation ensures that although the obtained trajectory instantaneously digresses from the true trajectory it stays close to the energy hyper surface and therefore still represents the microcanonical ensemble. Neglecting effects due to the finite machine precision of a computer the Verlet algorithm is symmetric in time, like the original equations that have to be solved. Therefore it follows the principle of detailed balance, which states that in a microscopic description each process is as likely as its reverse. The standard Verlet equations to determine the next position of the atoms are derived by expanding the position into a Taylor series.

$$\mathbf{R}(t+\Delta) = \mathbf{R}(t) + \Delta\dot{\mathbf{R}} + \frac{\Delta^2}{2}\ddot{\mathbf{R}} + \mathcal{O}(\Delta^3), \tag{2.16}$$

$$\mathbf{R}(t-\Delta) = \mathbf{R}(t) - \Delta\dot{\mathbf{R}} + \frac{\Delta^2}{2}\ddot{\mathbf{R}} - \mathcal{O}(\Delta^3). \tag{2.17}$$

Summation of equations 2.16 and 2.17 yields the verlet equations of motion:

$$\mathbf{R}(t+\Delta) \approx 2\mathbf{R}(t) - \mathbf{R}(t-\Delta) + \frac{\Delta^2}{M}\mathbf{F}(t) \tag{2.18}$$

The new positions are determined without the knowledge of the corresponding velocities. Once the positions are known, the velocity can be calculated using

$$\dot{\mathbf{R}}(t) \approx \frac{1}{2\Delta}(\mathbf{R}(t+\Delta) - \mathbf{R}(t-\Delta)). \tag{2.19}$$

Since the standard Verlet code does not calculate positions and velocities at the same time, kinetic and potential energy are not defined at the same time. An extended formulation of the Verlet algorithm, called the velocity Verlet algorithm [SABW82], eliminates this problem. The evaluation of the positions in the velocity Verlet algorithm is identical to the expansion of the positions as displayed in equation 2.19. The corresponding velocities are calculated as:

$$\dot{\mathbf{R}}(t+\Delta) = \dot{\mathbf{R}}(t) + \frac{\Delta}{2\mathrm{M}}(\mathbf{F}(t) + \mathbf{F}(t+\Delta)). \tag{2.20}$$

Mathematically the Verlet and the velocity Verlet algorithm are identical. They only differ in the way they work on a computer, that means in the way they are implemented.

2.1.4. Moleculardynamic Ensembles

One aim in the simulation of atomistic systems is to utilize microscopic properties to gain insight about the thermodynamic properties of the macroscopic system. The evaluation of these macroscopic quantities can be seen as the point of intersection between the microscopic and the macroscopic world, as only they build an link between virtual and real experiments.

The mathematical/theoretical tool that connects the microscopic and the macroscopic scale is statistical mechanics. In this concept we consider systems that consist of a large number of particles. Even if one fixes an extensive variable of this system (such as the energy E of a system with N non-interacting particles in a volume V) there are numerous ways to distribute the energies among the particles. Each possible way to do this is called a micro state. Thereby every micro state resembles the property (in this case the energy) assumed for the state of the whole system, the macro state. One fundamental assumption in statistical mechanics is the postulate of equal a priori probabilities. This means without additional constraints, the probability to find the system in one specific micro state is distributed equally among all possible micro states. The number of all possible micro states $\Omega(N,V,E)$ depends on the extensive variables of the system and is a key factor in the theory of statistical mechanics.

An equilibrated physical system will always adopt the macro state that is associated with the maximum number of micro states (i.e. max Ω). This argument leads to the relation that connects the number of possible micro states to the entropy S

$$S = k_B \ln \Omega. \tag{2.21}$$

Here k_B denotes the Boltzmann constant. In the course of time the various members of the ensemble representing the given macro state will switch between the possible micro states of the system. This fluctuation can be described by a motion of points in phase space, each representing one member of the ensemble. In the phase space this is described by a trajectory on a hyper surface corresponding to the energy of the system. The motion of this swarm[2] can be illustrated by the so called density function $\rho(q,p,t)$ which itself depends on the positions q and momentum coordinates p of the N particles. The ensemble average $\langle F \rangle$ of a quantity F(q,p) is therefore given by[3]

$$\langle F \rangle = \frac{\int F(q,p)\rho(q,p,t)d^{3N}qd^{3N}p}{\int F(q,p)d^{3N}qd^{3N}p} \tag{2.22}$$

Therefore if ρ is a function of time, $\langle F \rangle$ is dependent on the time t. The time evolution of the

[2] In this context swarm refers to the groups of points in phase space that are adopted by the members of the ensemble

[3] The formulation in this context is restricted to the case of classical statistical mechanics.

density function of the phase space is given by the Liouville equation

$$\frac{d\rho}{dt} = \frac{\partial\rho}{\partial t} + [\rho, H]. \tag{2.23}$$

H thereby stands for the Hamiltonian of the system. If one assumes a system in equilibrium, the density function does not depend explicitly on the time and therefore

$$\frac{\partial\rho}{\partial t} = 0. \tag{2.24}$$

Taking equation 2.23 into account this can only be true if the Poisson bracket $[\rho, H]$ vanishes, that means if

$$[\rho, H] = \sum_{i=1}^{3N} \left(\frac{\partial\rho}{\partial q_i}\dot{q}_i + \frac{\partial\rho}{\partial p_i}\dot{p}_i \right) = 0. \tag{2.25}$$

This is achieved for a density function ρ which is not a function of the position coordinates and the momentum coordinates on the hyper surface in the phase space. This assumption relates back to the postulate of equal a priori probabilities, as in the case of a constant ρ the probability of each system to be in one of the possible micro states is equally likely. An ensemble of systems that fulfills these conditions is called a micro canonical ensemble. The micro canonic ensemble is the simplest ensemble that is used in molecular dynamics simulations. It describes a macro state of a system with constrained particle number N, volume V and energy E, in the following called the NVE ensemble.

Equation 2.25 can also be fulfilled by considering a density function that depends on the phase space coordinates only through an explicit dependence on the Hamiltonian. If this dependence is of the type

$$\rho(q, p) \propto e^{[-H(q,p)/k_B T]} \tag{2.26}$$

the described ensemble is called the canonical ensemble (NVT). Compared to the micro canonical ensemble, it describes a system in which the energy is variable while the temperature is fixed.

In order to relate the observables of a molecular dynamics run to the above mentioned theory and therefore to an experimental value, another way to calculate ensemble averages has to be introduced. The junction between molecular dynamic and experimental observables relies on the assumption that the ensemble average (i.e. macroscopic quantities) can also be calculated by evaluating the time average of a quantity over a sufficiently long time. The equivalence between the ensemble average and the time average

$$\langle F \rangle = \lim_{t\to\infty} \frac{1}{t} \int_0^t dt' F(q, p, t') \tag{2.27}$$

is a description of the ergodic hypothesis which was originally stated by Ludwig Boltzmann [Pla91]. It assumes that all possible points of the phase space are adopted during the molecular dynamics run as long as the simulation time is long enough independent of the initial conditions. However, ergodicity cannot be seen as a general condition, since for example disordered systems such as spin-glasses do not display an ergodic behavior. Nonetheless for systems considered in this work the ergodic hypothesis holds.

Simulations at Constant Temperature: NVT-Ensemble

Adjusting the system parameters to an experiment is a lot easier using the NVT ensemble in molecular dynamics simulations, as the temperature can be easily controlled and measured during the execution. Experimentally temperature control is often realized by getting the sample into a thermal equilibrium with a heat bath, an idea that is also used in molecular dynamics, where thermostats are used to simulate a NVT ensemble. In this work the Nosé-Hoover thermostat is used in all NVT simulations [Hoo85]. The Nosé-Hoover thermostat is included in the formulation of molecular dynamics by introducing an additional coordinate s and a corresponding effective mass Q. As the Nosé-Hoover thermostat does not ensure ergodicity for all sorts of Hamiltonians, in an extended formulation, called the Nosé-Hoover-Chain thermostat [MTTK96], a chain of thermostats is added to the original thermostat to avoid that problem. The adapted equations of motion for the nuclei and the thermostats are then given by

$$
\begin{aligned}
M_I \ddot{\mathbf{R}}_I &= -\nabla_I E - M_I \dot{s}_1 \dot{\mathbf{R}}_I, \\
Q_1^n \ddot{s}_1 &= \Big[\sum_I M_I \dot{\mathbf{R}}_I^2 - g k_B T\Big] - Q_1^n \dot{s}_1 \dot{s}_2, \\
Q_k^n \ddot{s}_k &= \big[Q_{k-1}^n \dot{s}_{k-1}^2 - k_B T\big] - Q_k^n \dot{s}_k \dot{s}_{k+1}(1-\delta_{kK}), \\
&\qquad \text{with} \quad k = 2,,K.
\end{aligned}
\tag{2.28}
$$

Thereby K accounts for the number of thermostats in the chain, g is the degree of freedom of the nuclei and T stands for the target temperature. The mode of operation of the thermostat can thereby be described as followed. The newly introduced coordinate s acts like a dynamic friction coefficient in the equation of motion for the nuclei, as is can be negative or positive depending on the target temperature, . For the case of CPMD a similar procedure is introduced to define extended equations of motion for the fictitious orbital dynamics. The Nosé-Hoover-Chain thermostat is able to simulate a NVT ensemble where the original MD energy is not conserved but the extended energy is a constant in time.

2.2. Ways of Describing the Atomic Interaction

In the derivation of the equations of motion for the BOMD and CPMD in chapter 2.1.1 and 2.1.2, a separation of the system into an electronic problem and a nuclei problem is described. While for the BOMD only the nuclear system is treated dynamically, CPMD also includes equations of motion for a fictitious orbital dynamics. The calculation of the matrix element $\langle\Psi|\mathcal{H}_{el}|\Psi\rangle$ which defines the forces is of fundamental importance in both methods. There are numerous possibilities to solve the underlying electronic problem. The choice of the method is thereby dependent on the desired accuracy and the available computer resources. The following chapters focus on various approaches to treat the electronic problem by giving an introduction starting from full ab-initio methods like density functional theory (DFT) to more approximate methods like DFT-tight binding (DFTB) and classical force fields.

2.2.1. Ab-initio approaches: Hartree-Fock, Density Functional Theory and beyond

The fundamental electronic problem concerns the system of N electrons moving in an effective potential induced by M nuclei. The corresponding Hamiltonian is given by [4]

$$\begin{aligned}\hat{\mathcal{H}}_e &= -\sum_i \frac{\hbar^2}{2m_e}\nabla_i^2 - \frac{1}{4\pi\varepsilon_0}\sum_{I,i}\frac{e^2 Z_I}{|\mathbf{R}_I-\mathbf{r}_i|} + \frac{1}{4\pi\varepsilon_0}\sum_{i<j}\frac{e^2}{|\mathbf{r}_i-\mathbf{r}_j|} + \frac{1}{4\pi\varepsilon_0}\sum_{I<J}\frac{e^2 Z_I Z_J}{|\mathbf{R}_I-\mathbf{R}_J|}\\ &= \hat{T}+\hat{V}_{Ne}+\hat{V}_{ee}+\hat{V}_{NN}\\ &= \hat{H}_{el}+\hat{V}_{NN}. \end{aligned} \tag{2.29}$$

As the nucleus-nucleus repulsion is in principle just an added constant, the time independent Schrödinger equation to solve the electronic problem is

$$\hat{H}_{el}\Psi_{el} = E_{el}\Psi_{el}. \tag{2.30}$$

Up to now a solution of this equation, and therefore a way to determine Ψ_{el} and with that all system relevant properties is not known. [5]

Hartree-Fock Approximation

The variational principle is a theorem used to systematically determine the ground state wave function and its energy. It states that the ground state energy calculated as the expectation value of the electronic Hamiltonian with the correct wave function will be a lower bound to any

[4] The assignment of the variables is consistent with the one introduced in the preceding chapter
[5] To improve clarity in the following the index *el* will be dropped.

energy calculated using a trial wave function, thus

$$\langle \Psi_{trial} | \hat{H} | \Psi_{trial} \rangle = E_{trial} \geq E_0 = \langle \Psi_0 | \hat{H} | \Psi_0 \rangle. \tag{2.31}$$

Therefore in order to find the ground state wave function one basically has to minimize the functional E[Ψ] with respect to all allowed N-electron wave functions. The Hartree-Fock (HF) approximation is a fundamental concept in quantum chemistry that makes use of the variational principle. Instead of searching through all possible N-electron wave functions (which is impossible) it considers only a subset of wave functions. The total N-electron wave function is approximated as an antisymmetrized product of N one-electron wave functions $\varphi_{k_\alpha}(\mathbf{r}_i) = |k_\alpha\rangle^{(i)}$

$$\Psi_0 \approx \Phi_{SD} = \frac{1}{\sqrt{N!}} \begin{vmatrix} |k_1\rangle^{(1)} & \dots & |k_1\rangle^{(N)} \\ . & . & . \\ |k_N\rangle^{(1)} & \dots & |k_N\rangle^{(N)} \end{vmatrix} \tag{2.32}$$

called the Slater determinant Φ_{SD}. Thereby the k_α account for a complete set of one-electron quantum numbers and can be split into an orbital and a spin part: $|k_\alpha\rangle = |\tilde{k}_\alpha\rangle|\sigma\rangle$. The one-electron wave functions are for simplicity chosen to be orthonormal, i.e.

$$\int \varphi^*_{k_\alpha}(\mathbf{r}) \varphi_{k_\beta}(\mathbf{r}) d\mathbf{r} = \delta_{\alpha\beta}. \tag{2.33}$$

Assuming a Slater determinant as the total wave function the energy matrix element is given by

$$\begin{aligned} E_{HF} &= \langle \Phi_{SD} | \hat{H} | \Phi_{SD} \rangle \\ &= \sum_{\alpha,\sigma} \langle \tilde{k}_\alpha | \hat{h} | \tilde{k}_\alpha \rangle + \frac{1}{2} \sum_{\alpha,\beta,\sigma} \left((\tilde{k}_\alpha \tilde{k}_\alpha | \tilde{k}_\beta \tilde{k}_\beta) - (\tilde{k}_\alpha \tilde{k}_\beta | \tilde{k}_\alpha \tilde{k}_\beta) \right). \end{aligned} \tag{2.34}$$

Thereby the first term describes the contribution of the kinetic energy and the electron-nucleus interaction to the total energy, thus

$$\langle \tilde{k}_\alpha | \hat{h} | \tilde{k}_\alpha \rangle = \int \varphi^*_{\tilde{k}_\alpha}(\mathbf{r}) [-\frac{1}{2}\nabla^2 - \sum_I^M \frac{Z_I}{r_{\alpha I}}] . \varphi_{\tilde{k}_\alpha}(\mathbf{r}) d\mathbf{r} \tag{2.35}$$

This matrix element is independent of the electron index i. That means it acts like a single particle operator and the corresponding single particle energies are just added up. The second and third term in equation 2.34 represent the part of the Hartree-Fock energy that arises from

the electron-electron interaction. They are given in detail as

$$(\tilde{k}_\alpha \tilde{k}_\alpha | \tilde{k}_\beta \tilde{k}_\beta) = \sum_{\sigma'} \int\int |\varphi_{\tilde{k}_\alpha}(\mathbf{r})|^2 \frac{e^2}{|\mathbf{r}-\mathbf{r}'|} |\varphi_{\tilde{k}_\beta}(\mathbf{r}')|^2 d\mathbf{r} d\mathbf{r}' \tag{2.36}$$

$$(\tilde{k}_\alpha \tilde{k}_\beta | \tilde{k}_\alpha \tilde{k}_\beta) = \int\int \varphi_{\tilde{k}_\alpha}(\mathbf{r}) \varphi^*_{\tilde{k}_\beta}(\mathbf{r}') \frac{e^2}{|\mathbf{r}-\mathbf{r}'|} \varphi_{\tilde{k}_\alpha}(\mathbf{r}') \varphi^*_{\tilde{k}_\beta}(\mathbf{r}) d\mathbf{r} d\mathbf{r}'. \tag{2.37}$$

Hatree-Fock uses the Slater determinant ansatz for the total energy functional to find the minimal expectation value of the Hamiltonian by varying the Slater determinant with respect to the one electron wave functions. For the optimal wavefuntion the variation of the energy functional therefore has to be zero. The variation is done for a fixed $\tilde{k}_\gamma$. The orthonormality of the φ_{k_α} is taken into account by introducing the Lagrange multipliers ε_γ. This variation leads to the so called Hartree-Fock equations

$$\begin{aligned} &\hat{h}(\mathbf{r}) \varphi_{\tilde{k}_\gamma}(\mathbf{r}) + \sum_{\beta,\sigma'} \int \frac{e^2 |\varphi_{\tilde{k}_\beta}(\mathbf{r}')|^2}{|\mathbf{r}'-\mathbf{r}|} \varphi_{\tilde{k}_\gamma}(\mathbf{r}) d\mathbf{r}' - \sum_{\beta} \int \varphi^*_{\tilde{k}_\beta}(\mathbf{r}') \frac{e^2}{|\mathbf{r}-\mathbf{r}'|} \varphi_{\tilde{k}_\gamma}(\mathbf{r}') \varphi_{\tilde{k}_\beta}(\mathbf{r}) d\mathbf{r}' \\ &= (\hat{h} + V_{HF_\alpha}) \varphi_{\tilde{k}_\gamma}(\mathbf{r}) \\ &= \varepsilon_\gamma \varphi_{\tilde{k}_\gamma}(\mathbf{r}). \end{aligned} \tag{2.38}$$

The Hartree-Fock equations describe a pseudo eigenvalue problem as the so called Fock operator $\hat{F} = \hat{h} + V_{HF_\alpha}$ itself depends on the spin orbitals due to the Hartree-Fock Potential V_{HF_α}. In order to obtain the Slater determinant of the ground state the HF equations have to be solved self-consistently. The electron-electron interaction in the Hartree-Fock approximation is described as an average repulsive potential that acts on the i-th electron due to the presence of the remaining N-1 electrons. This potential can therefore be split into two different parts which differ fundamentally in their effect. The first term in the HF potential, the Coulomb or Hartree part, describes the potential on one electron in the average charge distribution caused by the other electrons. As this Hartree part only depends on the value of $\varphi_{\tilde{k}_\gamma}$ on the position of the i-th electron this potential is said to be local. In contrast the second term of the HF potential, called the Fock or exchange part, is found to be non-local as it includes an integration over all positions of the required single particle wave function. By definition the potential described by this second part only exists for electrons of like spin. It arises directly from the indistinguishability of the electrons and is therefore a purely quantum mechanical effect.

As only wave functions from the subset of Slater determinants are considered in the variation of the energy, the final total energy obtained in a self-consistent evaluation has to be larger than the ground state energy

$$E_C = E_0 - E_{HF}. \tag{2.39}$$

The difference E_C between the real ground state energy and the Hartree-Fock energy is due to

effects not described by the simplified Hartree-Fock ansatz. All these effects are summarized in the generic term "correlation". As both effects, exchange and correlation, keep the electrons away from each other, the phrase exchange-correlation hole is often introduced when referring to this context. One can think of these effects as holes surrounding each electron. The practicability of this concept is emphasized by looking at the full exchange-correlation energy, accounting for all non-classical contributions to the potential energy formulated in terms of the charge density and the corresponding exchange-correlation hole density

$$E_{xc} = \frac{1}{2} \int \int \frac{\rho_r h_{xc}(\mathbf{r},\mathbf{r}')}{|\mathbf{r} - \mathbf{r}'|} d\mathbf{r} d\mathbf{r}'. \tag{2.40}$$

As will be seen later in the discussion of the exchange-correlation functionals used in density functional theory, the characteristics of the density h_{xc} influence the exchange-correlation functional and which is therefore used to design well performing approximations of the latter. The different parts of the correlation introduced in the Hartee-Fock approach can be separated into three different groups. The first correlation effect not described by Hartree-Fock is the so called dynamical electron correlation and constitutes the largest contribution. As the Hartree-Fock approximation only considers electrons to move in an average field of the other electrons, that means it is a mean-field theory, the electrons get too close to each another. Therefore the electron-electron interaction is overestimated as this part is inversely dependent on the electron-electron distances. This fact results in a larger ground state energy. The non-dynamical correlation constitutes the second part and is effected by the approximation of a Slater determinant as the total wave function ansatz. A simple model in which a Slater determinant is not a good choice is the F_2 molecule or the dissociation of an H_2 molecule. The third and smallest part of the correlation is the error due to the deviation of the assumed kinetic energy and the electron-nucleus interactions. Despite the missing correlation the basic ideas given in the Hartree-Fock approximation constitute a good starting point in the description of another commonly used scheme to handle many electron problems, namely the density functional theory.

Density Functional Theory

The fundamental quantity in the concept of density functional theory (DFT) is the electron density $\rho(\mathbf{r})$ given by

$$\rho(\mathbf{r}) = N \int |\Psi(\mathbf{r}_1,...,\mathbf{r}_N)|^2 d\sigma_1 d\mathbf{r}_2,...,d\mathbf{r}_N. \tag{2.41}$$

Here $\Psi(\mathbf{r}_1,...,\mathbf{r}_N)$ stands for the total wave function of the N-electron system, while $\{\mathbf{r}_i\}$ accounts for the 3N spatial coordinates $\{\tilde{\mathbf{r}}_i\}$ and the N spin coordinates $\{\sigma_i\}$. $\rho(\mathbf{r})$ describes the probability to find one electron with arbitrary spin in the volume element $d\tilde{\mathbf{r}}_1$ while the other N-1 electrons have the spin and position described by the total wave function Ψ. The unique properties of this

electron density, that are utilized in the concept of DFT, are summed up in two postulates, the Hohenberg-Kohn theorems [HK64]. The first one states:

> *"The external potential $V_{ext}(\mathbf{r})$ is (to within a constant) a unique functional of $\rho(\mathbf{r})$; since, in turn $V_{ext}(\mathbf{r})$ fixes $\hat{H}$ we see that the full many particle ground state is a unique functional of $\rho(\mathbf{r})$"*

This conclusion made by Hohenberg and Kohn in the year 1964 changes the method of approach in the solution of the N-electron problem. Instead of determining the many particle ground state wave function which depends on the 3N spatial and N orbital coordinates of the electrons, they suggest that it is sufficient to know the ground state electron density ρ_0 which only depends on three spatial coordinates. Since, if we know the ground state electron density, we know the external potential, which in this underlying case is defined by the attractive interaction between N electrons and M nuclei. As the external potential itself determines the corresponding Hamiltonian $\hat{H}$ and therefore among other properties the ground state energy E_0, one can also rewrite the latter to

$$E_0[\rho_0] = T[\rho_0] + E_{ee}[\rho_0] + E_{Ne}[\rho_0] \tag{2.42}$$

$$= F_{HK}[\rho_0] + E_{Ne}[\rho_0]. \tag{2.43}$$

The whole information about the kind of system investigated is described by the external potential and thereby by the functional $E_{Ne}[\rho_0]$. In the case of electrons moving in a potential of fixed nuclei, the potential is based on the attractive Coulomb interactions between electron and nuclei and is given by

$$E_{Ne}[\rho_0] = \int \rho_0(\mathbf{r}) V_{Ne} d\mathbf{r}. \tag{2.44}$$

The remaining part of the energy functional, summed up in the so called Hohenberg-Kohn functional, $F_{HK}[\rho_0]$ is basically system independent. Its importance is described in the second Hohenberg-Kohn theorem which states [HK64]:

> *$F_{HK}[\rho]$, the functional that delivers the ground state energy of the system delivers the lowest energy if and only if the input density is the true ground state density ρ_0.*

So if the functional $F_{HK}[\rho_0]$ was exactly known, the corresponding Schrödinger equation would be solvable. In principle the second Hohenberg-Kohn theorem suggests that it is sufficient to minimize the energy functional with respect to the ground state density as it is a direct functional of the system defining external potential. Therefore only densities are considered which are V_{ext}-representable, that means those who are associated with an antisymmetric wave function and a Hamiltonian defining external potential.

This constraint can be lifted by choosing a slightly different point of view as introduced by Levy in the year 1979 and is called the Levy constrained search formulation. The starting point

is the variational principle introduced in the previous section. In this case the minimization of the energy functional is split into two parts, and the ground state energy is determined by

$$\begin{aligned} E_0 &= \min_{\rho \to N} \left(\min_{\Psi \to \rho} \langle \Psi | \hat{T} + \hat{V}_{ee} | \Psi \rangle + \int \rho(\mathbf{r}) V_{Ne} d\mathbf{r} \right) \\ &= \min_{\rho \to N} \left(F[\rho] + \int \rho(\mathbf{r}) V_{Ne} d\mathbf{r} \right). \end{aligned} \tag{2.45}$$

For the first, i.e. the inner minimization, the search is done in a subset of infinitely many antisymmetric wave functions that give rise to a density ρ. The subsequent outer minimization is performed on the subset of the density obtained in the first minimization to evaluate the density that gives the lowest energy. The difference between the Hohenberg-Kohn based density functional theory and the one defined by the Levy constrained search formulation lies in the definition of the density and the systems requirements. While the Hohenberg-Kohn approach is valid only for a non-degenerate ground state and for a density that is V_{ext}-representable these two conditions are lifted in the definition of the Levy constrained search approach. The energy functional $F[\rho]$ in the latter case is defined for all densities that originate from an antisymmetric wave function, therefore they are called N-representable. Both approaches show a new perspective of how to treat the many particle problem. But none of the two describes a way how to define the energy functional nor how to actually identify the right wave function, since unlike in the Hartree-Fock approach a lower energy does not correspond to a 'better' wave function.
One approach based on these fundamental concepts of density functional theory, that identifies an approximate but soluble concept, is the Kohn-Sham approach. The main idea is to evaluate as many parts as possible exactly. To do this the energy functional $F[\rho]$ is split into known and unknown parts

$$\begin{aligned} F[\rho] &= T[\rho] + E_{ee}[\rho] \\ &= T[\rho] + J[\rho] + E_{ncl}[\rho]. \end{aligned} \tag{2.46}$$

In this context $J[\rho]$ refers to the Coulomb part of the electron-electron interaction introduced in the Hartree-Fock approach. The structure of the kinetic energy $T[\rho]$ and the nonclassical parts $E_{ncl}[\rho]$ are unknown. In order to get a good approximation of the energy functional the Kohn-Sham approach introduces a system of N non-interacting electrons as an auxiliary model, since for this system the exact form of the kinetic energy is known and identical to the kinetic energy of the Hartree-Fock approach in equation 2.34. The Hamiltonian describing a system of N non-interacting electrons in an external potential V_S is given by

$$\begin{aligned} \hat{H}_s &= T_S + V_S \\ &= -\frac{1}{2} \sum_i^N \left(\nabla_i^2 + V_S(\mathbf{r}_i) \right), \end{aligned} \tag{2.47}$$

For this kind of system the exact wave function is given by a Slater determinant or by a linear combination of these in the case of a non-degenerate ground state. The spin orbitals specifying the Slater determinant are determined by:

$$\left(\nabla_i^2 + V_S(\mathbf{r}_i)\right)\varphi_{k_\alpha} = \varepsilon_{k_\alpha}\varphi_{k_\alpha}. \tag{2.48}$$

If one includes the kinetic energy T_S into the definition of the energy functional $F[\rho]$ one obtains

$$F[\rho] = T_S[\rho] + J[\rho] + E_{xc}[\rho]. \tag{2.49}$$

The newly introduced exchange-correlation functional $E_{xc}[\rho]$ contains the effects due to exchange and correlation of the electronic system as well as the part of the kinetic energy that accounts for the interacting electronic system. The total energy functional is then given by

$$\begin{aligned} E[\rho] &= T_S[\rho] + J[\rho] + E_{xc}[\rho] + E_{Ne}[\rho] \\ &= -\frac{1}{2}\sum_{\alpha\sigma}^{N}\langle\varphi_{k_\alpha}|\nabla^2|\varphi_{k_\alpha}\rangle + \frac{1}{2}\sum_{\alpha,\beta,\sigma,\sigma'}^{N}\int\int|\varphi_{k_\alpha}(\mathbf{r})|^2\frac{e^2}{|\mathbf{r}-\mathbf{r}'|}|\varphi_{k_\beta}(\mathbf{r}')|^2 d\mathbf{r}d\mathbf{r}' \\ &\quad + E_{xc}[\rho] - \sum_{\alpha,\sigma}\int\sum_{I}^{M}\frac{e^2 Z_I}{|\mathbf{r}-\mathbf{R}_I|}|\varphi_{k_\alpha}(\mathbf{r})|^2 d\mathbf{r} \end{aligned} \tag{2.50}$$

The only unknown part of the total energy left is the exchange-correlation part. If one now applies the variational principle by minimizing the energy expression under the constraint that $\langle\varphi_{k_\alpha}|\varphi_{k_\beta}\rangle = \delta_{k_\alpha k_\beta}$, similar to the minimization done in the Hartree-Fock approach one obtains

$$\Big(-\frac{1}{2}\nabla^2 + \underbrace{\left[\int\frac{\rho_{\mathrm{r}'}|\mathbf{r}-\mathbf{r}'|}{d}\mathbf{r}' + V_{XC}(\mathbf{r}) - \sum_{I}^{M}\frac{Z_I}{|\mathbf{r}-\mathbf{R}_I|}\right]}_{V_{eff}(\mathrm{r})}\Big)\varphi_{k_\alpha} = \varepsilon_{k_\alpha}\varphi_{k_\alpha} \tag{2.51}$$

Thereby the effective potential contains the effects present in the interacting electronic system. The comparison with the non-interacting electronic problem yields that V_{eff}=V_S. The equality between the two potentials means that once the substantial parts of V_{eff} are either known or approximated one can use it in the one particle equations to determine the orbitals. The Kohn-Sham approach is based on the assumption that the effective potential of a non-interacting system can be chosen in such a way that the density obtained from the single particle wave functions of the Slater determinant is identical to the ground state density of the interacting electronic system

$$\rho_S(\mathbf{r}) = \sum_{\alpha\sigma}^{N}|\varphi_{k_\alpha}(\mathbf{r})|^2 = \rho_0(\mathbf{r}), \tag{2.52}$$

which can then be used to determine the ground state energy according to equation 2.50.

Similar to the Hartree-Fock approach the potential itself depends on the density, therefore the equations have to be solved self-consistently. Although there are many similarities between the Hartree-Fock approach and DFT there are major differences in the underlying assumptions and definitions. The potential of the non-interacting system in the Kohn-Sham approach is local, that means, it is a function of only one spatial coordinate $\mathbf{r}$, this equality also means that it must be also true for V_{eff}. As V_{eff} includes the exchange-correlation effects V_{xc} must be local in contrast to the non-local exchange obtained in the Hartree-Fock approximation. More likely is has very complex and non-local dependence on the density. The exchange-correlation energy defined within the Hartee-Fock approach and the one obtained in the Kohn-Sham approach are therefore fundamentally different. In detail the HF orbitals result in a ground state density that does not equal the exact ground state density while this is the case by definition in the Kohn-Sham approach. Therefore the closer the Hartree-Fock ground state density resembles the true density the smaller are the differences in the exchange-correlation parts of these two methods.

Exchange-Correlation Functionals

Assuming that one knows the exact exchange-correlation functional, the Kohn-Sham approach would constitute an exact and solvable concept. Since this is not the case, the approximation of the exchange-correlation functional is the only impreciseness used in Kohn-Sham based DFT. To find an accurate description of the exchange-correlation functional is an ongoing field of research. Since there is not a systematical way to improve the functional, a good share of the work is based on intuition. Nevertheless there are a few basic constraints a "good" functional should fulfill, namely the sum rule, the one electron limit, the derivative discontinuity and the Lieb-Oxford bond[6]. These constraints can only be seen as trend-setting and a violation of these constraints by a functional does not imply that it is of no use. A good example of an approximation that does not fulfill all mentioned requirements but still has its place in DFT is the local density approximation (LDA). The concept behind the local density approximation is the approximation of the exchange-correlation energy using the electron density $\rho(\mathbf{r})$ at the position $\mathbf{r}$ of a homogeneous electron gas. The same procedure is repeated for each point in the corresponding volume and the obtained energies are added up. This approximation is embodied by the equation for the exchange-correlation functional in LDA which is given by

$$E_{xc}^{LDA} = \int \rho(\mathbf{r})\varepsilon_{xc}(\rho(\mathbf{r}))d\mathbf{r}. \tag{2.53}$$

In this context ε_{xc} denotes the exchange-correlation energy per particle of the uniform electron gas. Due to the underlying structure the described exchange-correlation effects only depend on

[6] The list is not intended to be complete and should only serve as a short summary as the validation of different functional does not constitute a part of this work. See [KH01] for a more thorough discussion.

the local values of $\rho(\mathbf{r})$.

The reason for the choice of a homogeneous electron gas (HEG) as the model system is the fact that the exact form of the exchange part is known, as well as the correlation part for the limiting cases of high and low densities. Therefore the HEG model is the system where the exchange-correlation is described most accurately[7]. In detail the exchange part of the exchange-correlation function ε_x is found to be proportional to $\rho(\mathbf{r})^{\frac{1}{3}}$, which results in an integrand of $\rho(\mathbf{r})^{\frac{4}{3}}$ for the full exchange part. Quantum Monte-Carlo simulation of intermediate densities are then used to interpolate the known results and obtain an expression for the correlation part. There are various approaches available to describe the correlation, for example VWN [VWN80], PZ81[PZ81a] or PW92 [PW92]. The extension to an unrestricted formulation of the exchange-correlation functional within LDA, that means the inclusion of spins, is done by taking into account the spin densities instead of solely the electron density, and is called the local spin-density approximation LSDA[8]. Although the approximations underlying LDA are very restricting, its performance describing equilibrium structures, harmonic frequencies or charge moments is very good in Kohn-Sham DFT. This is the case because the implied exchange-correlation hole functions introduced earlier fulfill most of the constraints valid for the exact formulation despite the strong approximations applying the HEG formalism. Nevertheless, due to the lack of flexibility of the exchange hole in LDA energetic details are in general not well described and the calculations performed with LDA are subject to a large overbinding. Owing to the assumption made in LDA, it is a good approximate functional for the description of systems with no or just very slow change in density, while it fails for systems that have a considerably varying charge density.

If one thinks of LDA being just the first term of a Taylor expansion of the uniform electron gas density, one way to improve the performance will be the inclusion of the next term in the expansion. This means to take into account the gradient of the density, and therefore constitutes a first step on the way to describe the inhomogeneity of the real density. But as mentioned earlier there is no such thing as a recipe of how to improve functionals, therefore the performance of such an extended formulation of the exchange-correlation functional is found to be worse than for LDA. This poor performance can be understood as the associated hole functions do not comply with the rules found for the exact holes. The method that solves this dilemma and takes into account the density gradient but also imposes the hole functions to fulfill the constraints is called the generalized gradient approximation (GGA). The exchange-correlation functional in this case is given by

$$E_{xc}^{GGA}[\rho] = \int f(\rho, \nabla\rho) d\mathbf{r}. \tag{2.54}$$

Again the exchange and the correlation part are treated separately. To approximate the exchange

[7] The ansatz for the exchange part was first derived by Bloch and Dirac.
[8] from now on only LSDA is mentioned as the following always applies to LDA and LSDA

part, the energies belonging to a HEG are again used as a basis and E_x^{GGA} is described as

$$E_x^{GGA}[\rho] = \int \rho(\mathbf{r})\varepsilon_x^{HEG} F_x(s) d\mathbf{r}. \tag{2.55}$$

The variable s thereby is a dimensionless density gradient given by $s = |\nabla\rho(\mathbf{r})|/\rho^{\frac{4}{3}}(\mathbf{r})$. The function F is fitted to the desired constrains. The functional used in this thesis to describe ZnO in various environments is the GGA functional derived by Perdew, Burke and Ernzerhof [PBE96] and is referred to as PBE. For this GGA functional the function F_x is given by

$$F_x(s) = 1 + \kappa - \frac{\kappa}{1 + \frac{\mu s^2}{\kappa}} \tag{2.56}$$

where $\mu \approx 0.21951$ is the effective gradient coefficient for exchange and κ is set to 0.804. The treatment of the correlation part by Perdew, Burke and Ernzerhof is done in a similar way by introducing a function that fits the required constraints.

The LDA as well as the GGA approach approximate both the exchange and the correlation part. An alternative ansatz to approximate the exchange-correlation energy functional exploits the fact that the exchange functional for a Slater determinant is known exactly. The straightforward ansatz to use the exact correlation from the Hartree-Fock approximation and just fit the correlation fails for systems larger than one atom, as the combination of a delocalized exchange and a localized correlation does not account for the localized behavior of the exact exchange-correlation. A more sophisticated concept is used in the so called hybrid functionals, also called the adiabatic connections method as it approximates the exchange-correlation energy by introducing a coupling constant that depicts the transition from a fully interacting to a non-interacting system. A very popular example of such a functional is B3LYP [SDCF94]. In this case the exchange-correlation function with the coupling constant is fitted by introducing three semi-empirical parameters which are set to give the right mixing between exact exchange and exchange-correlation gradient corrections. Thereby the fraction of exact exchange is 20 %.

Since the quality of the DFT calculations is to a large extend dependent on the approximation of the exchange-correlation functional the choice of the latter for a simulation set up is of tremendous importance. In this work the PBE functional is chosen for all ab-initio simulation set ups. PBE in combination with ZnO has the advantage that geometries as well as energies (adsorption energies, surface energies and the like) are well described [MM03]. Nevertheless when it comes to the electronic structure, PBE fails to predict the right band gap. This shortcoming is a feature of DFT in combination with a LDA or GGA approximation and is due to a deficient description of strongly correlated materials like ZnO. In this case the strong correlations lead to a distinct localization of the zinc 3d states in the case of ZnO. The homogenous electron gas model system, as inherent in the LDA and GGA approximations, turns out to be a poor ansatz in cases like this. The inadequate treatment (of these localized states) of the exchange-correlation

problem leads to a significant increase in the self-interaction error as well as an underestimation of the on-site electron-electron repulsion. There are several methods described in the literature to partly correct for this problem, like for example the GW concept [Hed65] [9], the self-interaction correction (SIC) [10] [PZ81b] or even the hybrid functional B3LYP[SDCF94]. But the problems of this work require molecular calculations using time scales and system sizes, which are not possible using computationally "expensive" corrections like hybrid functionals.

LDA+U Approach

A brute force and less costly way to improve the band structure for cases like ZnO is the so-called LDA+U[11] approach. In order to improve the description of the on-site electron-electron repulsion of the localized states an additional term, E_{Hub}, is introduced to the original energy functional [AZA91]:

$$E_{LDA+U}[\rho(\mathbf{r})] = E_{LDA}[\rho(\mathbf{r})] + E_{Hub}[\{f_m^{I\sigma}\}] - E_{DC}[\{f^{I\sigma}\}] \tag{2.57}$$

In this context $\{f_m^{I\sigma}\}$ are the atomic-orbital occupations for the site I considered in the Hubbard correction. The index m stands for the separate orbitals within each set (the five orbitals of the d-state). In other words the too approximate treatment of correlation effects in the LDA approach is corrected by introducing an energy, based on a Hubbard-type Hamiltonian for the strongly localized stated, to the total energy of the system. The subtracted energy E_{DC} accounts for the double counting of the effects included in E_{Hub} as well as in an average way in E_{LDA} with $f^{I\sigma}$ being the total and spin-projected occupations of $\{f_m^{I\sigma}\}$. The occupations are in a general basis description given by [CG05]:

$$n_{mm'}^{I\sigma} = \sum_{n\mathbf{k}} f_{n\mathbf{k}}^{\sigma} \langle \Psi_{n\mathbf{k}}^{\sigma} | P_{mm'}^{I} | \Psi_{n\mathbf{k}}^{\sigma} \rangle \tag{2.58}$$

Here $\Psi_{n\mathbf{k}}^{\sigma}$ is the valence electronic wave functions of the state specified by $n\mathbf{k}$ with spin σ and a corresponding occupation of $f_{n\mathbf{k}}^{\sigma}$. The generalized projection operators $P_{mm'}^{I}$, determine the choice of the underlying basis, for example projection on normalized atomic orbitals or projection on Wannier functions. In the approach of a rotationally invariant scheme[12] the Hubbard

[9] The GW concept introduced by Hedin [Hed65] is based on the estimation of the self-energy operator with the help of single particle Green's functions.

[10] In SIC-DFT the self-energy is explicitly taken into account for each electron.

[11] The expression LDA+U is an umbrella term for a special kind of post-LDA calculations. The first term LDA is thereby only a placeholder and does not means that a LDA-type exchange-correlation function is applied. In matters of this work this concept is used with a GGA ansatz.

[12] That means one neglects higher terms in the Coulomb interaction as well as an explicit magnetic description [CG05].

correction is given by [CG05]:

$$\begin{aligned} E_U[\{n^{l\sigma}_{mm'}\}] &= E_{Hub}[\{f^{l\sigma}_m\}] - E_{DC}[\{f^{l\sigma}\}] \\ &= \frac{U}{2}\sum_l \sum_{m,\sigma}\left(f^{l\sigma}_{mm} - \sum_{m'} f^{l\sigma}_{mm'} f^{l\sigma}_{m'm}\right) \\ &= \frac{U}{2}\sum_{l\sigma} Tr[\mathbf{f}^{l\sigma}(1-\mathbf{f}^{l\sigma})] \end{aligned} \tag{2.59}$$

The correction can therefore be tuned by the choice of the parameter U. Thereby this parameter can be seen as the correction factor for the curvature found in the total energy for non-integer occupation numbers, due to the self interaction of latter. An elaborate discussion of the interpretation of this parameter can be found in [CG05], together with a concept on how to calculate the appropriate U.

Relevant Implementations of the CPMD Code

To implement the DFT approach in an algorithm one has to expand the Kohn-Sham orbitals into a specified basis set in order to be able to evaluate the iterative solution computationally. The approach of "linear combination of atomic orbitals" (LCAO) as a basis set is used for DFTB calculations which will be introduced in detail in chapter 2.2.2. Since all *ab-initio* MD calculations in this work are done using CPMD in combination with DFT as described in the code CPMD[13] [CPM], this chapter will outline a rough sketch of the most important features included in this implementation. CPMD describes the system as a periodically repeated supercell, with a unit cell defined by the three Bravais lattice vectors $\mathbf{a}_1$, $\mathbf{a}_2$ and $\mathbf{a}_3$ and the corresponding volume $\mathcal{V}$. Therefore a translation of the system by the vector $\mathbf{R} = n\mathbf{a}_1 + m\mathbf{a}_2 + l\mathbf{a}_3$ will transfer the system onto itself, that means the corresponding periodic potential $V(\mathbf{r})$ is translation invariant regarding the vectors $\mathbf{R}$. This periodicity is especially of interest when simulating crystal bulk structures since the properties of the infinite number of electrons present in a realistic material, can be expressed by the electrons of the supercell. The theoretical instrument to describe the wave function of the problem of N nuclei in a periodically repeated formation is Bloch's theorem [Blo29]. It states that in this case the normalized wave functions can be expressed as a product of a function resembling the periodicity of the potential u_k and a plane wave $e^{i\mathrm{kr}}$:

$$\nu_\mathrm{k}(\mathbf{r}) = \frac{1}{\sqrt{\mathcal{V}}} e^{i\mathrm{kr}} u_\mathrm{k}(\mathbf{r}). \tag{2.60}$$

Here $\mathbf{k}$ stands for the Bloch wave vector. For a finite system with periodic boundary conditions the $\mathbf{k}$'s can be restricted to the first Brillouin zone. They form a discrete set and their number is dependent on the total number of primitive unit cells in the system [Czy07]. $u_\mathrm{k}(\mathbf{r})$ is called

[13] From now on, CPMD will always refer to the code CPMD and not to the theoretical concept.

the Bloch factor for which holds:

$$u_{\mathrm{k}}(\mathbf{r}) = u_{\mathrm{k}}(\mathbf{r}+\mathbf{R}). \tag{2.61}$$

That means the wave functions do not have to strictly reflect the lattice periodicity since they can differ in a phase factor represented by the plane wave. If one now applies this Bloch ansatz in the corresponding Schrödinger equation, the initial problem of finding an infinite number of wave functions representing an infinite number of electrons is reduced to finding for every discrete value of $\mathbf{k}$ the corresponding n eigenvalues $\varepsilon_n(\mathbf{k})$ and eigenfunctions $u_{n\mathrm{k}}(\mathbf{r})$. The index n is referred to as the band index.

This theoretical concept of the Bloch theorem can also be applied to the quantities described in the Kohn-Sham approach of DFT. For the case of a periodic system the Kohn-Sham potential displays the same periodicity as the underlying lattice. Consequently the Kohn-Sham orbitals can be written in the Bloch-representation. In order to implement this Bloch-ansatz of the Kohn-Sham equations as well as its iterative solution into an algorithm the Bloch factor $u_{n\mathrm{k}}(\mathbf{r})$ is expanded into a plane wave basis. This is a reasonable expansion since this representation follows directly from the derivation of the Bloch theorem [Czy07]. Accordingly the Kohn-Sham orbitals can be written in the plane wave basis as [MH09]:

$$\Psi_n^{KS}(\mathbf{r},\mathbf{k}) = \frac{1}{\mathcal{V}} \sum_{\mathrm{G}} c_n(\mathbf{G},\mathbf{k}) e^{i(\mathrm{G}+\mathrm{k})\mathrm{r}}. \tag{2.62}$$

Here $\mathbf{G}$ stands for the reciprocal lattice vectors and the $c_n(\mathbf{G},\mathbf{k})$ are complex coefficients. Applying this description effectuates that the sum over states in expression like for example for the total energy in equation 2.50 convert into integrals over the Brillouin zone and a sum over the band index. In order to evaluate this expression the integrals are superseded by a finite sum over a set of $\mathbf{k}$-points [MH09], since wanted quantities like the wave functions vary only evenly in the first Brillouin zone. In this respect there are different ways to efficiently place the integrations points, reviewed for example in [ES83]. Since the volume of the supercell is inversely proportional to the volume of the first Brillouin zone, the latter becomes smaller the larger the super cell. In this work only very large super cells are considered. Therefore in most simulations the wanted quantities are only calculated at $\mathbf{k} = 0$, which is the so called Γ-Point approximation. In cases where very accurate energies are needed, the choice of the $\mathbf{k}$-points was done using the Monkhorst-Pack approach [PM77].

Apart from the choice of the $\mathbf{k}$-point sampling, the plane-wave description of quantities, like for example the density in equation 2.62, make it necessary to truncate the sum over the reciprocal lattice vectors $\mathbf{G}$. This truncation can be defined by including only those plane waves in the

basis with a **G** which complies with:

$$\frac{1}{2}|\mathbf{k}+\mathbf{G}|^2 \leq E_{cut}. \tag{2.63}$$

The advantage of the plane wave basis set compared to an atomic orbital based basis set is therefore the simplicity in increasing the accuracy of a calculation by adjusting just one parameter, E_{cut}, in the input file.

Apart from being a plane wave code, CPMD also includes a pseudopotential approximation. The core electrons are highly localized electrons and strongly bound to the nuclei. By construction the wave function of the valence electrons have to be orthogonal regarding the core states which leads to short-wave oscillations, which require a large plane wave basis set to be described properly. Since for most cases the core electrons are unaffected by different chemical environments, that means they do not participate in chemical reactions such as bond forming or bond breaking, they can be treated in a more approximate way than the valence electrons. Consequently one way to minimize the required basis set is by treating the core electrons together with the nuclei as rigid non-polarizable ion cores. The different kind of interactions between valence electrons and these core electrons are then replaced by a so called pseudopotential. They are constructed so that for regions with $r \geq r_c$ they resemble the true potential ,while they are smooth functions in the core region. Thus only the valence electrons are treated explicitly. In the pseudopotential scheme they are described by smooth and nodeless pseudo wave functions, which only require a "small" plane wave basis set. These wave functions for one atom are solutions of a modified Schrödinger equation[Czy07]:

$$[\hat{H}+V_{PS}]|\Psi^V_{\mathrm{k}}\rangle = \varepsilon_n(\mathbf{k})|\Psi^V_{\mathrm{k}}\rangle, \tag{2.64}$$

with an effective pseudopotential given by

$$V_{PS} = \sum_{l_c}(\varepsilon_n(\mathbf{k}) - E_{l_c})|\Psi^c_{l_c\mathrm{k}}\rangle\langle\Psi^c_{l_c\mathrm{k}}|. \tag{2.65}$$

Here $\varepsilon_n(\mathbf{k})$ are the eigenenergies, E_{l_c} are the eigenenergies of the core states described by the core wave function $\Psi^c_{l_c\mathrm{k}}$. The pseudo wave function of the valence electrons $|\Psi^V_{\mathrm{k}}\rangle$ have identical eigenvalues with the not-pseudodized system. In the pseudopotential the strong Coulomb potential parts are eliminated by substracting the projection of the core states from the true potential. Hence the pseudopotential is weaker than the trial potential. Moreover it is also indifferent to further approximations like the one usually applied when going from the one-atom-picture to solids. This transition will for sure change the corresponding eigenenergies, $\varepsilon_n(\mathbf{k})$, nevertheless it is sufficient to substitute this value with a constant suitable energy [Czy07].

There are different classes for the pseudopotentials described in the literature such as norm-conserving [HSC79] or ultrasoft pseudopotentials (USPP) [Van90]. The latter ones are used in

this work. In the USPP approach the number of projectors used to describe the pseudopotential described in equation 2.65 is increased, so that the transferability of the potential is generalized and able to reproduce the all-electron energy values with arbitrary accuracy [Van90]. Furthermore in contrast to the norm-conserving pseudopotentials the USPP do not have the same norm as the all-electron wave function inside the core radius. The difference in charge is leveled out through the introduction of localized atom-centered augmentation charges Q_{ij} [MH09] into the valence charge density. These charges are defined as the difference in charge between the all-electron and pseudo picture:

$$Q_{ij} = \langle \Psi_i^{all-e} | \Psi_j^{all-e} \rangle_R - \langle \Psi_i^{PS} | \Psi_j^{PS} \rangle_R \tag{2.66}$$

Here the index R accounts for an integration within a sphere of radius R, and the index i and j are quantum numbers. The calculation of the augmentation charges is in practice done on a regular grid in real space, with cut-off radius comparable to the ones for norm-conserving potentials. Nevertheless, due to the cutback of norm conservation in requirements for the pseudo wave function, freedom in the choice of the cut-off radius is gained in this case. This allows for the construction of even smoother wave functions and thereby the use of low cut-off energies (equations 2.15 and 2.63), which has a significant influence on the computer performance. As a result of the introduction of the augmentation charges the system-relevant quantities and relations, such as the charge density, the total energy or the Kohn-Sham equations have to be adapted regarding these. A detailed description of these modifications as well as the integration of the CPMD equations of motion for this case can be found in [MH09].

2.2.2. Density Functional Theory based Tight Binding: DFTB

DFT is a well-functioning and widely spread electronic structure method nowadays. However, in spite of the constant improvement of the computational performance, DFT is still too cost-intensive (speaking of simulation time) to handle larger scale systems (>1000 atoms) in ab-initio molecular dynamics simulations. Although there are classical force fields available (see chapter 2.2.3) that can handle up to millions of atoms, they are only of use in situations when no chemical reactions like bond formation/breaking or the underlying electronic structure is of interest.

One approach that fills this gap is called *tight-binding* method. In standard tight binding the eigenstates of the Hamiltonian are expanded in a basis composed of a linear combination of atomic orbitals (LCAO-ansatz), therefore accounting for a description of tightly bound electrons to an atom or within a solid, that means:

$$\phi_i(\mathbf{r}) = \sum_I \sum_{\mu \in I} c_{\mu i} \Phi_\mu(\mathbf{r} - \mathbf{R}_I) \tag{2.67}$$

The eigenstates are expanded in a so called minimal basis, that means they are expanded using

one basis function $\Phi_\mu(\mathbf{r}-\mathbf{R}_I)$ for each orbital μ at atom I. The coefficients $c_{\mu i}$ are considered to be real. The use of an ansatz of linear combination of atomic orbitals (LCAO) for the eigenstates (equation (2.67)) is reasonable as it transforms the solution of the Kohn-Sham equations from a non-linear optimization problem to a set of linear equations for the coefficients $c_{\mu i}$:

$$\sum_I \sum_{\nu \in I} c_{\nu i}(H_{\mu\nu} - \epsilon_i S_{\mu\nu}) = 0. \tag{2.68}$$

Here the overlap matrix $S_{\mu\nu}$ and the Hamilton matrix elements $H_{\mu\nu}$ are defined as:

$$H_{\mu\nu} = \langle \Phi_\mu | \hat{H} | \Phi_\nu \rangle = \langle \Phi_\mu | \hat{T} + V_{eff} | \Phi_\nu \rangle, S_{\mu\nu} = \langle \Phi_\mu | \Phi_\nu \rangle \tag{2.69}$$

The background for the tight-binding method used in this work is the DFT-based tight binding (DFTB)[PFK+95, AHF07]. The DFTB representation of the total energy has its starting point in the total DFT energy derived in chapter 2.2.1. Thereby the density is described as the sum of a reference density ρ_0 and a fluctuation $\Delta\rho$:

$$\rho(\mathbf{r}) = \rho_0(\mathbf{r}) + \Delta\rho(\mathbf{r}). \tag{2.70}$$

This ansatz is justified, since the total DFT energy is variational regarding density variations. Consequently the energy can be calculated from this approximate density, which nevertheless should be sufficiently close to the true ground state density [SJ12].

If one now substitutes this into the equation for the total DFT energy (equation 2.50) taking also into account the nucleus-nucleus interaction and expanding the exchange-correlation potential up to the second order for the density[14]one obtains the following expression for the total DFTB energy[15]:

$$\begin{aligned} E_{DFTB}[\rho_0 + \Delta\rho] = \sum_i \langle \varphi_i | \frac{\nabla^2}{2} + V_{Ne} + \int \frac{\rho_0'}{|\mathbf{r}-\mathbf{r}'|} d\mathbf{r}' + V_{xc}[\rho_0] | \varphi_i \rangle \\ + \; E_{rep} \\ + \; \frac{1}{2} \int' \int \Big(\frac{1}{|\mathbf{r}-\mathbf{r}'|} + \frac{\delta^2 E_{xc}[\rho]}{\delta\rho\delta\rho'}\Big|_{\rho_0\rho_0'} \Big) \Delta\rho\Delta\rho' d\mathbf{r} d\mathbf{r}' \\ + \; \frac{1}{6} \int \int \frac{\delta^3 E_{xc}[\rho]}{\delta\rho\delta\rho'\delta\rho''}\Big|_{\rho_0\rho_0'\rho_0''} \Delta\rho\Delta\rho'\Delta\rho'' \\ + \ldots \quad . \end{aligned} \tag{2.71}$$

The first line in equation 2.71 comprises all the energy contributed from the reference density ρ_0. The term in the second line (E_{rep}) represents the parts of the energy that result from double

[14] A detailed derivation is given in [Gau11].
[15] to improve clarity in the following $\rho_0(\mathbf{r}) = \rho_0$, $\rho_0(\mathbf{r}') = \rho_0'$ and $\rho_0(\mathbf{r}'') = \rho_0''$ and $k_\alpha = i$

counting in the first line, the nucleus-nucleus interaction and exchange-correlation contributions. The sum of these terms is approximated in DFTB by a repulsive energy term characterized through short-ranged two center potentials[Gau11]:

$$E_{rep} = \frac{1}{2}\sum_{I,J} V_{IJ}^{rep}[\rho_{0I}, \rho_{0J}, |\mathbf{R}_I - \mathbf{R}_J|] \tag{2.72}$$

where ρ_{0I} corresponds to the reference density of atom I. These pair potentials are determined using DFT calculations of suitable reference systems. In detail DFTB calculations excluding the repulsive energy part are fitted to the results of self-consistent DFT calculations[PFK$^+$95]. The two remaining contributions to the energy (line two and three in equation 2.71) contain the information about the density fluctuations up to second and third order respectively.
Which level of DFTB is used depends on where the energy is truncated. If just the first two lines are used to approximate the total energy the scheme corresponds to a non-selfconsistent DFTB approach. The non-selfconsistent approximation is only an appropriate description for homogeneous systems with negligible charge flow. As this is not a suitable model system for the fundamental material of this work, ZnO, the second order approximation of the energy is used, corresponding to the first three lines of equation 2.71, namely:

$$E_{DFTB}[\rho] = \sum_{iIJ}\sum_{\nu\in I}\sum_{\mu\in J} n_i c_{\nu i} c_{\mu j} H^0_{\nu\mu} + E_{rep}[\rho_{0I}, \rho_{0J}, |\mathbf{R}_I - \mathbf{R}_J|] + E^{2nd}[\rho_0, \Delta\rho] \tag{2.73}$$

In DFTB the basis orbitals are described as Slater type orbitals (STO) and spherical harmonics of the form of [PFK$^+$95]:

$$\Phi_\mu(\mathbf{r}) = \sum_{n,\alpha,\ell_\mu,m_\mu} a_{n\alpha} r^{\ell_\mu + n} \exp(-\alpha) Y_{\ell_\mu m_\mu}(\frac{\mathbf{r}}{r}). \tag{2.74}$$

The ℓ and m refer to the azimuthal and the magnetic quantum number and Y to the spherical harmonic. Five different values of α and n= 0,1,2,3 were found to constitute a sufficiently accurate basis set for all element up to the third row [PFK$^+$95]. The coefficients, $a_{n\alpha}$, for the composition of the STO-basis set are determined through self-consistent solution of the atomic Kohn-Sham equations:

$$(-\frac{1}{2}\nabla^2 + V_{psat}(\mathbf{r}))\Phi_\mu(\mathbf{r}) = \epsilon_\mu \Phi_\mu(\mathbf{r}). \tag{2.75}$$

Here the atomic potential,V_{psat}, is expanded by a term $\frac{r}{r^c}^2$ accounting for the compression of the potential due to interatomic interaction, but leaving the relevant bonding region of the wave function unchanged. In this context r^c its chosen to be 1.85 times the covalent radius of the

considered element[16], as a result of several calculations[FSE+00].

The effective potential included in the Hamilton matrix element, $H^0_{\nu\mu}$ (see equation 2.69), is assumed to be describable by a sum over atomic contributions [FSE+00]. Similar to the pseudopotential ansatz described in chapter 2.2.1 DFTB only uses the LCAO basis set to describe the chemically active valence electrons. In the need to construct these valence basis function orthogonal to the core states of other atoms, one finds that the potential contained in the matrix element is approximately made up of two-center contributions. These two center potentials are then approximated taking the density overlap into account, where the atomic densities ρ_{0I} and ρ_{0J} are evaluated for isolated atoms[17] [FSE+00]. Applying these assumptions the matrix element is given by:

$$H^0_{\mu\nu} = \begin{cases} \epsilon_{\text{free neutral atom}} & \text{if } I = J, \mu = \nu \\ \langle \phi_\mu | T + V[\rho_{0I} + \rho_{0J}] | \Phi_\nu \rangle & \text{if } I \neq J \\ \approx 0 & \text{if } I = J, \mu \neq \nu. \end{cases} \tag{2.76}$$

That means that for the diagonal terms the corresponding free energy without the compression factor $(\frac{r}{r_c})$ is assumed. Whereas the non diagonal factors are treated in a two-center approximation [Sei07].

For the second order energy terms the density fluctuations are assumed as a superposition of atomic contributions, which are approximated using Mulliken analysis to evaluate the charge q_I that is centered at atom I. The second order expression for the energy is then written as:

$$E^{2nd} \approx \frac{1}{2} \sum_{IJ} \Delta q_I \Delta q_J \gamma_{IJ}(|\mathbf{R}_I - \mathbf{R}_J|). \tag{2.77}$$

The newly introduced parameter γ_{IJ} resembles in the limit of two charges at two distant atoms the characteristics of the pure Coulomb interaction. In the opposite case where the two charges are localized at the same atom it accounts for the on-site self-repulsion, which is approximated by the Hubbard parameter U_I. These can be obtained for each type of atom by evaluating the curvature of the total energy with respect to the occupation number of the highest occupied atomic orbital (HOMO). A more detailed discussion of the approximation in the second order term as well as the exact expression for the parameter γ_{IJ} can be found in [Els98].

With these assumptions the corresponding Kohn-Sham equations (2.68) have to be solved in order to calculate the coefficients included in the LCAO expansion. Due to the occurrence of the Mulliken charges in the second order energy term, which itself depend on the expansion coefficient, these equations have to be solved self-consistently [SJ12].

[16] For the self-consistent charge implementation of DFTB the introduction of a second parameter r^{dens} is needed for the compressed density evaluation in order to obtain accurate results[Els98].

[17] see equation 2.75 without the compression part.

The reason why DFTB allows the simulation of larger systems is that a lot of time-consuming calculations can be performed in advance and re-invoked during later calculations. Elementary for every DFTB calculation are therefore the so called Slater-Koster files. In these files the overlap matrix element $S_{\mu\nu}$ and the Hamilton matrix elements $H^0_{\mu\nu}$ are tabulated for every type of atom pairs for various interatomic distances. Furthermore information about the repulsive potential is also included in these parameter files. This tabulation effects a decrease in computational time up to magnitudes faster than *ab-initio* DFT.

2.2.3. Classical Approaches

A different approach to describe the electronic system is by assuming a purely empirical potential energy function. The first approaches using an empirical force field in computational simulations date back to the 1970s and were motivated by the insufficient computational performance of quantum chemistry based methods. In the so called force field molecular dynamics, or molecular mechanics (MM), the potential energy term of the nuclei system is split into different parts describing the bonding and non-bonding interactions:

$$\begin{aligned} E &= E_{bonding} + E_{non-bonding} \\ E_{bonding} &= E_{bond} + E_{angle} + E_{dihedral} + E_{improper} \\ E_{non-bonding} &= E_{vdw} + E_{Coulomb}. \end{aligned} \tag{2.78}$$

The bonding part is thereby usually subdivided into part accounting for the bond, angle, dihedral and improper energies involved. The non bonding part consist of the sum of van der Waals and Coulomb interaction between different atoms. In this concept the electronic system is not treated explicitly, rather the focus of this concept is the correlation between conformation and energy. Since the classical force field is a purely empirical method the effective parameters defining each potential energy term are chosen to reproduce results produced by more sophisticated theoretical approaches or even experiments. Therefore prior to every force field calculation the user has to decide about an appropriate parametrization. Various different parametrizations are used nowadays to describe system of up to millions of atoms, for example the CHARMM [BBO$^+$83] or the amber force field [WWC$^+$04]. The implementation and parameters used in this work for the parametrization of a force field for the hydrated ZnO surface in contact with water and/or biomolecules is the OPLS all-atom force field [JMTR96]. In the OPLS force field the potentials representing the bond and angle energies are chosen to be of a simple harmonic form, while for the dihedrals and impropers a different type of function is used to account for all accessible

angles of the system [Fie07]

$$V_{bond} = \sum_{bonds} k_b(b - b_0)^2 \tag{2.79}$$

$$V_{angle} = \sum_{angles} k_\theta(\theta - \theta_0)^2 \tag{2.80}$$

$$V_{\substack{dihedral \\ improper}} = \sum_{\substack{dihedral \\ improper}} \left(\frac{V_1}{2}(1 + \cos\Phi) + \frac{V_2}{2}(1 - \cos 2\Phi) + \frac{V_3}{2}(1 + \cos 3\Phi) \right). \tag{2.81}$$

Here (b-b_0) and ($\theta - \theta_0$) stand for the deflection of the bond and angle out of the equilibrium respectively. The potential function for the dihedral and improper angles are formally identically and just differ in the considered angle. The amplitude of the contribution is altered by the choice of the V_i's.

The parametrization of the OPLS force field is based on its performance regarding the non-bonded interactions, since the bonded parameters were taken nearly unchanged from the Amber force field. In detail the intermolecular, non-bonded interactions for two molecules a and b are given by:

$$E_{ab} = \sum_{i \in a} \sum_{j \in b} \left(\frac{Z_i Z_j e^2}{r_{ij}} + 4\varepsilon_j \left[\left(\frac{\sigma_{ij}}{r_{ij}} \right)^{12} - \left(\frac{\sigma_{ij}}{r_{ij}} \right)^{6} \right] f_{ij} \right). \tag{2.82}$$

Z_i (Z_j) stands for the atomic number of atom i (j). r_{ij} represents the interatomic distance. The variable ε describes the potential well while σ_{ij} accounts for the zero cross point of the potential curve given by the Lennard-Jones potential. The factor f_{ij} guarantees that this form of non-bonded interaction can be applied to describe intermolecular as well as intramolecular non-bonded interactions between atom pairs. A detailed discussion about the performance of the OPLS force field can be found in [JMTR96].

A classical description of the underlying electronic potential offers the possibility of fast calculation of large systems, on the other hand the parametrization does not yields certain necessities to describe chemical reactions like bond breaking or forming. One approach, that is based on the basic idea of a classical force field but is also able to describe chemical reactions, is called a reactive force field. The central quantity of this ansatz is the bond order as a factor to describe the current coordination status of every atom in the system. Consequently the potential energy is split up into bond-order dependent (BO) and independent (non-BO) parts [DDLG01][18]:

$$\begin{aligned} E &= E_{BO} + E_{non-BO} \\ E_{BO} &= E_{bond} + E_{over} + E_{under} + E_{val} + E_{lp} + E_{tors} + E_{conj} \\ E_{non-BO} &= E_{vdw} + E_{Coulomb}. \end{aligned} \tag{2.83}$$

[18] Only system relevant energy components are used in the fitting procedure.

The BO dependent part is subdivided into parts describing energy stemming from the bonds, corrections for the over/under coordination, valence angle, lone pairs, torsion angles and conjugations effects. The different parts are constructed in such a way, that the single contribution smoothly approaches zero for a vanishing BO (that means for bond dissociation). Similar to the classical force field the BO independent energy is a sum of the van der Waals (vdW) and Coulomb interactions and parametrized for each pair of atoms in the system. However in this case, the vdW interactions are expressed through a distance corrected Morse-potential, while the shielded Coulomb potential is used to account for the Coulomb interaction. Thereby the atomic charges are calculated via the electron equilibration method (EEM) described in [JBT$^+$95].

Like for the classical force field, the reactive force field relies on a prudential parameterization. The parametrization used in this work for ZnO in contact with water was published by Raymand et. al. [RDS$^+$10]. They first decided on a minimal set of energy terms from equation (2.83) and fitted the included parameters to match DFT-B3LYP calculations on assorted test systems. Subsequently they extended their energy expression and repeated the fitting procedure. A detailed discussion of the used expression and the set of chosen parameters can be found in [DDLG01] and [RDBH08, RDS$^+$10] respectively.

2.2.4. Opportunities and Limitations

The four different methods (DFT, DFTB, force fields, reactive force fields) are all tailored for a different areas of application and problems. In order to apply the methods correctly, it is vital to properly define these areas since, despite of the great success of implementations based on the approaches each method is also limited in its possibilities. In the case of Kohn-Sham density functional theory the performance is determined by the choice of the approximation for the exchange-correlations functional. In this work a GGA representation of the exchange-correlation functional is chosen for all simulations. One feature that results from this approximation has already been discussed in the introduction of the GGA+U formalism: The described underestimation of the band gap can be tracked back to a false description of the fractional charge behavior in GGA. Furthermore the semi local structure of GGA does not include the long range interactions properly. This deficient description of the dispersion can only be improved through very sophisticated approaches for the exchange-correlation functional [KB09]. Since these are computationally very demanding, DFT implementations often provide a flag to add an empirical parameter ($\propto \frac{1}{r^6}$) to improve the performance of semi local functions like GGA in the description of the dispersion forces. Overall a lot of progress has been made to develop exchange-correlation functional with improved properties and performance[19]. A review of the performance of different exchange-correlation functional can be found in [SFR07]. The employment of DFT in electronic structure methods therefore demands a careful weighting of the needed properties in

[19] Often compared to the Jacobs ladder illustrated in the book of Genesis.

an exchange-correlation functional regarding the computation resources available.

DFTB constitutes a reliable and transferable DFT based method.It is very efficient regarding computational time, as it makes use of the pre-tabulated matrix element $H^0_{\nu\mu}$ and overlap matrix $S_{\nu\mu}$. This makes it up to magnitudes faster than corresponding full DFT calculations and therefore especially expedient regarding long molecular dynamics runs. But DFTB in its second order expansion also has some deficiencies. As it is a DFT-based method it exhibits similar problems as for example the missing description of dispersion interaction[20]. Apart from this DFTB proton affinities are not well described, proton transfer barriers underestimated and most important in this work hydrogen binding energies are typically underestimated by 2-3 kcal/mol per hydrogen bond[21] [YYY+07]. Yang and co-workers have stated that the expression for the parameter γ_{IJ} in DFTB, which implies that there is an inverse correspondence between the size of an atom and the corresponding chemical hardness, is not a good description for the hydrogen atom. Furthermore they showed that the inclusion of an additional damping factor γ_{IH} added for all X-H atom pairs is able to correct for this inaccuracy. This damping term is characterized by a parameter ξ and used for all DFTB calculations in this work including hydrogen[22]. Therefore a meticulous validation of selected system properties against reference DFT and experimental results is necessary in order to benefit from the convenient computational performance.

The same exigency for a thorough validation is true for the application of classical and reactive force fields. Like DFTB, the reactive force field constitutes a method in-between a full quantum mechanical and a classical description of the electronic potential and offers an accuracy in the range of other semi-empirical methods. Due to the bypassing of the quantum mechanical description this method is able to simulate up to thousands atoms on a nanosecond timescale. Since the electrons are not explicitly treated in classical force fields, these approaches fail to describe phenomena like proton transfer and other chemical reactions. In turn they are capable to handle systems up to millions of atoms up to the millisecond timescale making complex systems feasible with molecular dynamics. Since the parametrization of classical and reactive force fields (OPLS and ReaxFF in this work) is based on fitting properties of selected reference structures to DFT results, the inherent limitations are basically dependent on the variety and realization of this fitting procedure. Therefore a general error regime in the description of system properties like minimum energy structures or barrier heights cannot be made, since it can vary for each different implementation. Furthermore like DFTB, both force fields requires a pre-parametrized complete set of parameters for each element present in the system. For the case of a reactive force field of ZnO this is only available for ZnO surfaces in contact with water, the introduction of additional, e.g. small bio molecules into the system, is only possible if one does

[20] There exists an add-on flag in the input file.

[21] Which is reasonable but can also be of tremendous importance in simulations concerning biological environments like done in this work.

[22] Throughout the work we will refer to DFTB always meaning the second order expansion plus the damping in the γ-function. In some literature this is already named DFTB3, while in this work only the inclusion of the expansion of the total energy up to third order in addition to the damping will be referred to as DFTB3.

a time-consuming reparametrization of the extended system. A classical force field comprising an identical set-up is currently not available at all.

To summarize, careful consideration is necessary to match problem and method in order to achieve an optimal performance. Within this work the application of different methods going from full DFT to classical force fields is demonstrated for different aspects. For the specific cases the abilities and also the limitations of the applied methods are evaluated and thoroughly discussed.

3 Chapter 3. From Bulk ZnO to a reliable ZnO/water interface

The description of the solid/liquid ZnO/bio interface is the main focus in this work. This chapter constitutes the first puzzle piece on our way to a more complete picture of the considered interface. To account for the complexity of this system is it necessary to methodically establish this system through deliberately chosen sub-steps. Hence, in order to build reliable surface models and computational set ups for ZnO, the first sub-step of this work is the validation of the employed simulation methods and corresponding parameters for a bulk model of the wurtzite crystal of ZnO, which is described in the first part of this chapter.

Since the surface of zinc oxide nanostructures under atmospheric conditions is dominated by the two non-polar surfaces of ZnO (80% non-polar, 20% polar surfaces [SSB$^+$92]), the emphasis in this work is on a correct description of the two non-polar surfaces. The interaction of the non-polar ZnO surfaces in a biological environment will be dominated by their interactions with water. It has been shown for other oxides like TiO_2 [ML10], that the first water layer is very strongly bound and can often only be removed in repeated cleaning cycles. Moreover, the first water layer has shown to influence the adsorption of larger molecules to a great extent [SC12, KL10, MW11]. These findings emphasize the necessity to analyze the first hydration layer and its properties in detail to obtain a reliable water structure as a next step on the way to a description of the ZnO/bio interface. For that reason in a second validation step the water adsorption of the ZnO $(10\bar{1}0)$ surface, which has been described in various publications [MRM06, MMD$^+$04, CC09], is used to validate the computational set-ups for ZnO in contact with water for CPMD, DFTB and ReaxFF (see chapter 3.2). The description of the interface between non-polar interfaces of ZnO and water is continued by a detailed analysis of water adsorption on the $(1\bar{2}10)$ ZnO surface going from a single water molecule to a completely hydrated system [HKFCC12]. Lastly the investigation of the ZnO/water interface is completed by the analysis of the water adsorption on a $(10\bar{1}0)$ ZnO surface comprising two surface kinks.

3.1. Validation of the Computational Set Up for CPMD, DFTB and ReaxFF

In order to compile a reliable computational set up, the three methods (and therefore codes) employed in this part of the work, namely CPMD, DFTB and ReaxFF are used to reproduce well known literature data for bulk ZnO (CPMD) as well as for ZnO surfaces. The set of variables determined in these calculations is then used in all following simulations. Nevertheless for ease of reference, relevant simulation parameters applied in the various calculations are listed at the beginning of the the corresponding subchapters.

3.1.1. Allocation of the CPMD Specific Variables

In order to enhance the validity in subsequent MD simulations long trajectories are needed. Therefore the *ab-initio* DFT molecular dynamic simulations are all performed using Car-Parinello MD as implemented in the code CPMD [CPM]. In order to assign the various values of CPMD to a parameter, a model of a bulk ZnO supercell consisting of 72 atoms is used for validation. Ultrasoft pseudopotentials [PP] are used to describe the influence of the core electrons. [1] The size of the required basis set can be adjusted by variation of the parameter E_{cut} introduced in chapter 2 in equation 2.63. Since an increase in E_{cut} is directly connected to an increased computational time, the cut-off energy should be chosen large enough to achieve a convergence in the corresponding energy but small enough to ensure a feasible computational performance. To identify the best choice for E_{cut} the positions of the atoms of the wurtzite bulk ZnO supercell are optimized using the limited-memory Broyden-Fletcher-Goldfarb-Shanno (BFGS) algorithm [LN89] until the force reached a threshold of $1.0 \cdot 10^{-4}$ a.u. The results for fixed cut-off energies in the range between 16 to 40 Rydberg are displayed in figure 3.1 (a). With increasing E_{cut} the energy values converge rapidly against a fixed energy value. The change in energy for cut-off energies larger than 30 Ryd is less that 0.001 %. Therefore for all following CPMD calculations the cut-off is set to 30 Ryd (300 Ryd) for the wave function (densities) which is in accordance with ZnO calculations done by Meyer and Marx [MM03].

In order to identify the right set up for the molecular dynamics calculations, the influence of the chosen parameters on the corresponding fictitious energy is investigated. Since later in this work the water/ZnO interface is of special interest, a model system comprising of the $(10\bar{1}0)$ ZnO surface with a surface area of 10.56x0.89 Å^2 and 52 water molecules is used. For this test system the increase in the kinetic energy of the electronic subsystem, E_kinc, is analyzed regarding various combinations of the electronic mass and time step. The results are displayed in figure 3.1 b). Five different masses are tested in combination with 4 different time steps. For the two lowest masses not all time steps are possible, since they lead to a crash of the molecular

[1] Test calculations performed with norm-conserving pseudopotentials (Troullier-Martin) were not able to reproduce literature data. CPMD uses a plane wave basis to describe the electronic wave functions.

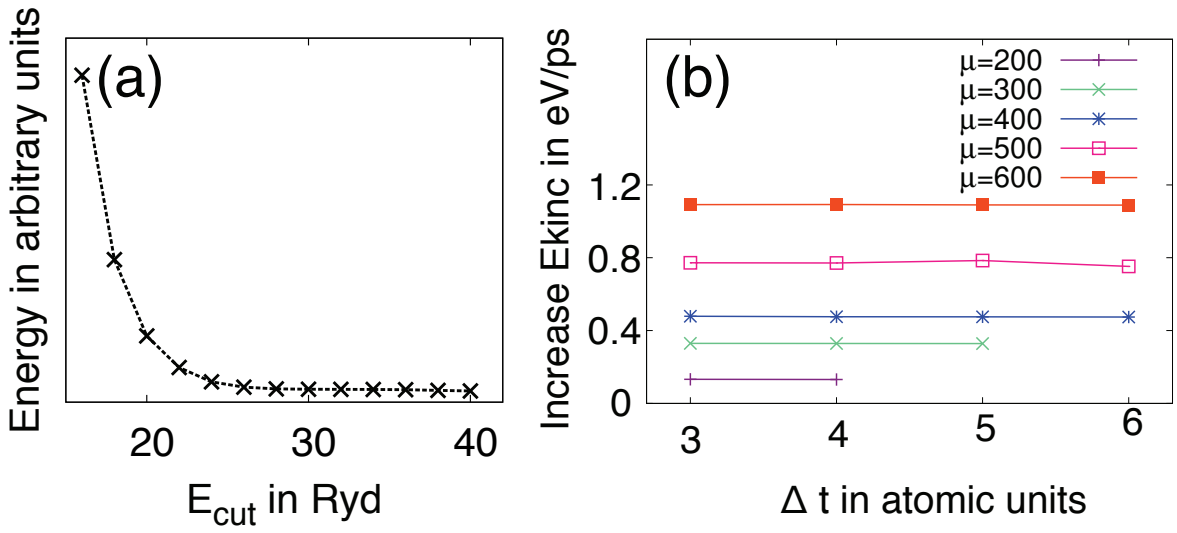

Figure 3.1.: In (a) the dependence of the energy on the chosen energy cut-off is shown. Figure (b) depicts the increase of the kinetic energy of the electronic subsystem per ps for different choices of electronic masses and time steps.

dynamics run. As expected the rate of increase grows with enlargement of the fictitious mass. Since the aim is to keep the increase as small as possible while at the same time use a time step which enables us to simulate long trajectories, an electron mass of 300 a.u. and a time step of 5 a.t.u is chosen for all molecular dynamics runs performed with CPMD in this work.

3.1.2. Validation of the CPMD Set Up for Bulk ZnO

In a first step the CPMD set-up is tested regarding the performance to reproduce reasonable equilibrium lattice constants. According to the 3rd order Birch-Murnaghan equation of state the relation between the volume and the corresponding obtained energies is given by:

$$E(V) = E_0 + \frac{9V_0B_0}{16}\left\{\left[\left(\frac{V_0}{V}\right)^{\frac{2}{3}} - 1\right]^3 B_0' + \left[\left(\frac{V_0}{V}\right)^{\frac{2}{3}} - 1\right]^2 \left[6 - 4\left(\frac{V_0}{V}\right)^{\frac{2}{3}}\right]\right\}. \quad (3.1)$$

In this context V_0 refers to the reference and V to the distorted Volume. B_0 stands for the bulk modulus, while B_0' corresponds to the derivative of the latter with respect to the pressure. The structure of equation 3.1 implies that E(V) reaches its minimal value if $V_0 = V$. Hence calculations are performed in which the values of the lattice constants, a, b and c (introduced in chapter 1.1) were varied. For this purpose the c/a ratio is held constant at the experimental value of 1.602 [AB69]. The results for the corresponding volumes (crosses) and a fit according to equation 3.1 are displayed in figure 3.2. The minimal energy is found for a volume of 337.16 Å^3 which equates to a lattice parameter a of 3.30 Å. This lattice parameter is in good agreement

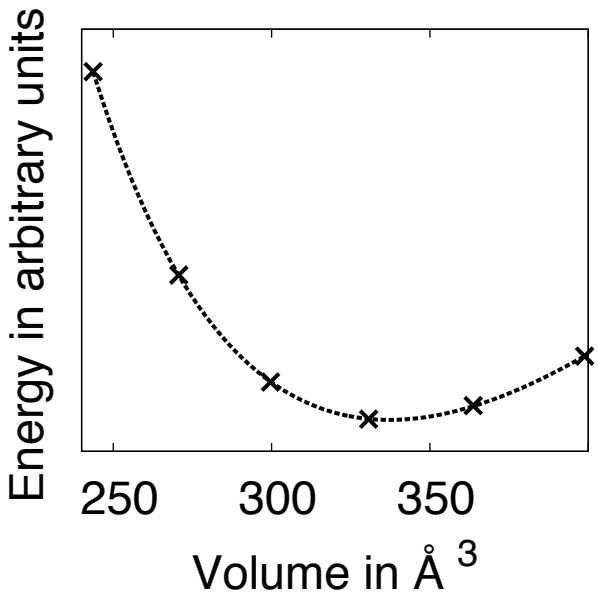

Figure 3.2.: Calculated (crosses) and fitted (line) plot of the relation between the considered volume of the primitive cell and the corresponding total energy.

with previously published data being only by 1.5 % larger compared to the experimental findings by Abraham and co-workers [AB69] and by only 0.6 % regarding DFT results from Meyer et al. [MM03].

Furthermore the CPMD set-up is tested regarding the description of the binding energy of bulk ZnO. The binding energy (E_{bin}) was calculated using the total DFT energy of a single zinc atom ($E_{Zn-single}$) and a single oxygen atom ($E_{O-single}$) in a periodic box respectively.

$$E_{bin} = E_{bulk} - n \cdot (E_{Zn-single} - E_{O-single}) \tag{3.2}$$

In this context n accounts for the number of ZnO dimers in the bulk ZnO supercell. A binding energy of 7.28 eV is obtained for the wurzite phase of ZnO, which reproduces well the binding energy found by Schleife et al.[SFFB06] who calculated a binding energy of 7.20 eV.

In order to check the set up for electronic properties, the band structure of wurzite ZnO is calculated and plotted. Since the CPMD code has its main focus on the analysis of biological systems, the calculations of electronic properties in this work are done using the PWscf code as implemented in the Quantum Espresso package [GBB$^+$09]. Identical pseudopotentials can be employed in PWscf, therefore CPMD and PWscf can be used equivalently. The obtained band structure for wurzite ZnO is displayed in figure 3.3 for a high symmetry k point path in the hexagonal Brillouin zone. The results characterize ZnO as a direct semiconductor, displaying the valence band maximum and the conduction band minimum at the Γ point. The corresponding

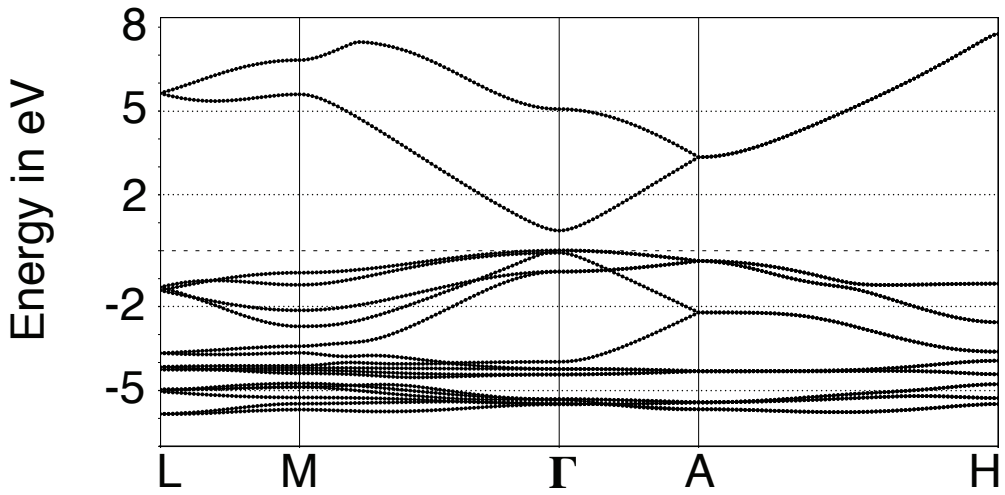

Figure 3.3.: Depiction of the band structure of wurzite ZnO along the high symmetry k point path in the hexagonal Brillouin zone.

band gap is 0.72 eV and therefore strongly underestimated compared to the experimentally determined gap at room temperature of 3.3 eV[SC98]. However the calculated band gap is in agreement with previous theoretical work on ZnO applying a DFT PBE ansatz [MM03]. The underestimation of the band gap is due to an incorrect description of the low lying valence bands (not shown in figure 3.3) which correspond to the Zn 3d levels. One way to improve the PBE description is the so called LDA+U ansatz. A more detailed discussion about the parameter U and its influence on the band gap can be found in chapter 5. Despite the well known discrepancy in the band gap the band structure obtained with this computational set up exhibits the characteristic features of a ZnO band structure. Overall this set up for CPMD is found to adequatly reproduce literature data concerning geometric, energetic and electronic properties of bulk ZnO.

3.2. Validation of DFT, DFTB and ReaxFF Set Up: Interactions with Water

Water monolayer adsorption on ZnO ($10\bar{1}0$)

The water adsorption at the non polar ZnO surfaces constitutes the basis for further analysis of the adsorption of various organic compounds like amino acids or small peptide chains. In particular, the precise structure of the water layers in proximity of oxide/water interfaces has been observed to be a very important component of the driving force for the adhesion of proteins [HSG$^+$08, CVTG09, MW11, KL06, KL10]. It has also been suggested that the specific

recognition of materials by short peptide sequences arises, at least in part, from the sensing of the local density variation of water at the solid/liquid interface at the molecular level [SC12]. Moreover, the dissolution of ZnO nanoparticles, which is most probably the cause of their toxicity both in single cells and higher animals [XKL$^+$08], obviously depends on the hydration structure of the solvent-exposed surface.

The interaction of a single water molecule with the ZnO $(10\bar{1}0)$ surface has been extensively investigated by DFT by Meyer et al. [MRM06], identifying a surface pattern with (2x1) periodicity at a water coverage of one monolayer (ML), in agreement with STM observations [MMD$^+$04]. While at lower coverages a molecular adsorption mode is preferred, the formation of a strongly bound hydrogen-bonding network promotes the dissociation of every second water molecule in the ML structure. The occurrence of an equilibrium between molecularly and dissociatively adsorbed water at 1 ML coverage on the $(10\bar{1}0)$ was also predicted by Raymand et al. [RDS$^+$10] using MD simulations within the ReaxFF approach. The code ReaxFF is based on the reactive forcefield approach introduced in chapter 2.2.3. That means the energy surface is calculated by the energy functional described in equation 2.83. The parametrization has to be done for each atom pair present. In the case of ZnO, the interaction with water was parametrized by Raymand and co-workers [RDBH08].

Accurate tight-binding schemes such as DFTB [EPJ$^+$98] also appear to be very promising for simulations where chemical interactions such as water dissociation, proton transfer reaction or dissolution events cannot be neglected. The parametrization of ZnO has been done by Moreira and co-workers [MDA$^+$09] within the *mio*[2] set. The parametrization of DFTB was not validated against the ZnO/water interaction. Thus the model system ZnO $(10\bar{1}0)$/water is a good test set up to validate the performance of the methods applied in this work in a scenario similar to the model systems used later on.

On that account 5 different model structures ((1x1),HD(2x1),(2x1),(1x2),(2x2),c(2x2)) described in the work of Meyer et al. [MRM06] are relaxed with all three methods. The nomenclature of these structures is derived from the adsorption periodicity of water molecules on the surface, that means e.g. (1x1) corresponds to a configuration with one molecular adsorbed water per surface unit cell. The special case of HD(2x1) decribes a configuration which comprises alternating adsorption states (either molecular or dissociatively adsorbed) of the water molecules in x-direction. The volume of the (4x2) super cells is set to (13.13x10.52x53) Å^3. The plain surface slab contained 256 atoms. All geometries were relaxed up to a force threshold of $1.0 \cdot 10^{-4}$ a.u. with the BFGS (CPMD) or the conjugate gradient method (DFTB,ReaxFF) respectively. All calculations were done in the Γ-point approximation.

The obtained binding energies per water molecule for the three different half monolayer and two full monolayer configurations are displayed in table 3.1. All three methods display the same trend in the obtained energies, since they all predict the half dissociated HD(2x1) structure to

[2]Included elements are H - C - N - O - S - P

Table 3.1.: Validation of applied methods: Binding energy per water molecule for the ZnO $(10\bar{1}0)$ surface
.

	Binding energy per H_2O in eV			
	CPMD	DFTB	ReaxFF	Reference *
(1x1)	1.06	1.30	1.18	1.03
HD(2x1)	1.16	1.35	1.21	1.13
(2x1)	1.01	1.30	1.16	0.97
(1x2)	1.00	1.27	1.19	0.97
(2x2)	0.96	1.28	1.15	0.93
c(2x2)	0.98	1.28	1.10	0.94

*DFT reference from [MRM06]

be the energetically favored. The CPMD results only show a constant shift of 0.03 eV/ H_2O compared to the reference values. This negligible difference is to be expected as an identical set-up was used in the work published by Meyer et al. [MRM06]. DFTB shows an overbinding of the water molecules by about 0.3 eV. Despite the inequality of the binding energies for the configuration (2x1) and (1x2), it is able to identify the general trend in stabilities. ReaxFF also overestimates the water binding energies by approximately 0.15 eV/ H_2O. Like DFTB it shows a difference in energies between the (1x2) and (2x1) configurations which is not observed using full DFT calculations. Nevertheless ReaxFF is able to reproduce binding energies in the same regime as DFT and is able to determine the energetically favored structure.

Solvated Zn^{2+} Ion

To get another indication of the performance of the DFT, DFTB and ReaxFF approaches in describing the interaction between zinc and water, a single, solvated Zn^{2+} ion is considered[3]. The ion is placed in a cubic box with edge-length of 12 Å filled with 66 water molecules for DFT and DFTB calculations and an edge-length of 24 Å filled with 548 water molecules for the reactive forcefield calculations. The system is heated up to 300 K and a 4 ps constant-temperature MD simulation is carried out for each of the three methods. For each method a Nosé-Hoover thermostat was used and a time integration step of 5 a.u (CPMD), 1 fs (DFTB) and 0.25 fs ReaxFF is chosen respectively. Radial distribution functions (RDF) of the Zn-O and Zn-H atom pairs are then calculated (3.4 (a) and (b)) from each MD simulation.

The first peak in the Zn-O RDF is centered at 2.15 Å for both the DFT and DFTB simulations, whereas it is shifted 0.2 Å away from the Zn ion when using ReaxFF. The experimentally determined Zn-O distance for the first hydration shell around a single Zn^{2+} ions is 2.09 Å [OR93].

[3]This part of the thesis was published in [HKFCC12].

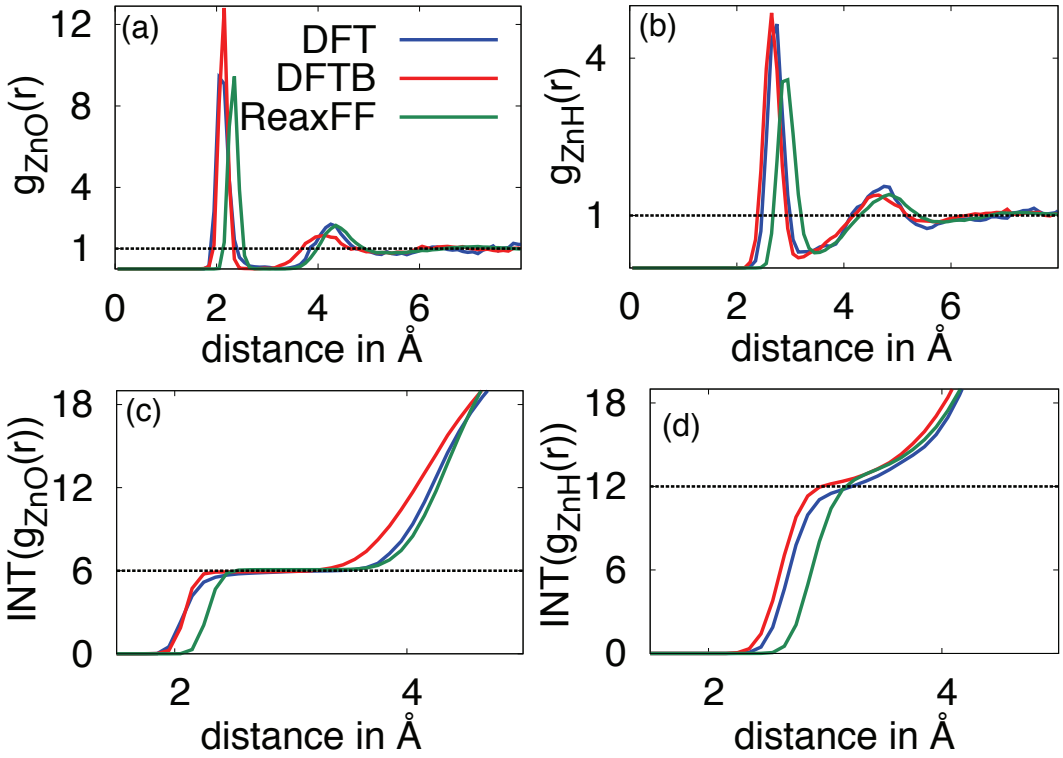

Figure 3.4.: Radial distribution functions (RDF) for (a) Zn^{2+}-O(H_2O) and (b) Zn^{2+}-H(H_2O) obtained in DFT, DFTB and ReaxFF MD simulations. The corresponding RDF integrals are depicted in (c) and (d).

All three theoretical results therefore slightly underestimate the Zn-O interaction resulting in a 3-4% longer bond distance. The position of the second RDF peak, corresponding to the second hydration shell around the ion is, as expected, less intense but wider for all three methods. While for DFT and ReaxFF simulations the second peak lies at about 4.3 Å, DFTB predicts a second maximum located 0.2 Å closer to the Zn ion. Similar trends in the RDFs can be observed taking into account the Zn-H pair. The peaks are located at 2.76 Å and 2.65 Å for DFT and DFTB, whereas ReaxFF predicts a slightly larger distance of 2.9 Å for the Zn-H bond in the first hydration shell, similarly as for the Zn-O bond. In the second hydration shell, again DFTB leads to a 0.2 Å smaller Zn-H distance than DFT and ReaxFF. The integrals of the RDFs, corresponding to the number of coordinating water ligands around the Zn^{2+} ion, are reported in 3.4 (c) and (d) for Zn-O and Zn-H, respectively. All three methods show a distinct plateau at a coordination of 6 water molecules, especially visible taking into account the Zn-O RDF. This agrees well with the diffraction and EXAFS experiments performed for solvated Zn^{2+} ions by Ohtaki and Radnai [OR93], which reveal the presence of 6 water molecules in the first hydration shell. In conclusion, in spite of the small differences highlighted above, all three simulation methods give

a reliable description of the bonding interactions between single Zn^{2+} ions and water.

Summing up the results obtained for the water ML on ZnO (10$\bar{1}$0), the ones for the solvated Zn^{2+} ion and the previously published data for ZnO for CPMD [MMD$^+$04, MM03, MRM06], DFTB [MDA$^+$09] and ReaxFF [RDG$^+$11, RDS$^+$10, RDBH08] they constitute a good basis to proceed with new and more detailed study of the hydration of the ZnO (10$\bar{1}$0) and ZnO (1$\bar{2}$10) surfaces, as presented in the remaining sections of this chapter.

3.3. Atomistic Simulations of the ZnO(1$\bar{2}$10)/Water Interface

Compared to the non-polar (10$\bar{1}$0) surface of ZnO, the water adsorption of the second non-polar ZnO surface has only been the focus of interest of very few studies. Considering non-stoichiometric models of the two non-polar surfaces under varying external conditions, Cooke et al. [CMP06] proposed that, in contrast to the (10$\bar{1}$0) surface, a fully dissociated monolayer with (1x1) periodicity should be the favorable adsorption mode on the (1$\bar{2}$10) surface. This finding is in agreement with ReaxFF results for the same surface [RDS$^+$10]. However the results obtained by Cooke et al. also predict only a very small difference in energy (0.06 eV) between a hydrated and a hydroxylated structure. This suggests that both adsorption modes could be present, especially over larger surface areas [CMP06]. Following the analysis of Meyer et al. [MRM06] of the (10$\bar{1}$0) surface, this part of the thesis is aimed at a thorough analysis of the characteristics of the ZnO(1-210)/water interface. The working schedule is based on a step-by-step investigation of this interface starting from the adsorption of single water molecules, going through the formation of a monolayer and finishes by evaluating the influence of bulk liquid water in contact with the surface. The results obtained in this part of the work constitute another puzzle piece on our way to a description of the more complex ZnO/bio interface, since a detailed knowledge of the ZnO(1-210)/water interface is essential in the assembly of a more elaborate model system. In this context DFT-based simulations can be considered as a reliable tool to predict the hydration structure of surfaces, although the choice of the xc functionals may have a non-negligible influence on the simulations' outcome [LZTM10]. However, the small system size and especially the limited simulation time accessible with DFT-based MD prevent a statistically relevant exploration of the phase-space, as required in investigations of protein adsorption or surface dissolution processes. Thus in the following chapters a thorough comparison between a standard DFT implementation (plane-wave, ultrasoft pseudopotentials, PBE xc functional), the DFT-based tight-binding approach DFTB, and a recently published reactive force field [RDBH08] for ZnO/water interfaces (ReaxFF) is performed in order to assess their performance in describing the non-polar ZnO(1$\bar{2}$10) surface in contact with water vapor and liquid water. Indeed selective DFTB and ReaxFF calculations of the (10$\bar{1}$0) surface indicate a promising performance of the two methods, nevertheless a more elaborate judgement requires

a more systematic approach. Therefore this chapter of the thesis will focus on the structures, energetic stabilities and electronic structure features of different adsorption configurations at increasing coverage, with the aim to highlight the differences between the three simulation methods.

3.3.1. Calculation Protocols

Ab-initio molecular dynamics simulations at room temperature (300 K) are performed with the CPMD code [CPM] at the Γ point. No corrections to the standard GGA formalism are necessary to reliably reproduce the basic physical properties of non-polar ZnO surfaces, as shown by Calzolari et al. [CC09] The PWscf code [GBB+09], already employed for the calculation of the bulk ZnO band structure, is used for all static calculations with geometry optimizations, integrating the Brillouin zone at the Γ point only, except for the projected density of states (PDOS) analysis, in which a denser $(4\times4\times1)$ k-point grid is used. All structures are relaxed until forces are below a threshold of 10^{-5} eV/Å. All systems are heated up using a Nosé-Hoover thermostat applying a previously employed heating procedure [KBL08].

The DFTB calculations are performed with the DFTB+ code [AHF07], using the tight-binding parameter set *znorg* introduced in ref. [MDA+09]. To improve the performance of DFTB a γ-correction factor as introduced by Elstner and coworkers [Els07] is used in calculations to improve the polarization of hydrogen bonded complexes. The geometry optimizations at the DFTB level are performed using the conjugate gradient method on a (2×2×2) Monkhorst-Pack grid for the k-point sampling, using a force error tolerance of 10^{-6} eV/Å. In the MD simulations only the Γ point is included and a Nosé-Hoover thermostat with an integration time step of 1 fs is applied. The ReaxFF calculations are performed with the LAMMPS code [Pli95], using the potential parametrization introduced by Raymand et al. [RDBH08]. The conjugate gradient method with a tolerance of 10^{-6} eV/Å for the geometry optimizations is employed, and the Nosé-Hoover thermostat is used with an integration time step of 0.25 fs for the MD simulations.

3.3.2. ZnO $(1\bar{2}10)$ Surface Model and Coverage Factor

Slab Model

The $(1\bar{2}10)$ surface is modeled as a periodically repeated slab with a thickness of 12 Å, which corresponds to 4 layers of ZnO, separated by vacuum or a bulk liquid water layer of 15 Å in the *z* direction perpendicular to the surface. For the DFT and DFTB simulations a (2×2) surface cell in the *xy* plane, with a surface area of 11.4×10.6 Å^2 is used. For the ReaxFF simulations a surface cell twice that size (4×4) is utilized. In a first step a geometry optimization using DFT of the $(1\bar{2}10)$ surface slab results in an inward relaxation of the zinc surface ions involving a decrease of the zinc oxygen bond length from 2.00 to 1.89 Å, leading to a tilted Zn-O dimer structure, already described earlier by Meyer and co-workers [MM03](see also figure 1.4

in the introduction). The slab model is further validated by evaluating the corresponding surface energy. The surface energy in the absence of any additional water molecule is 0.84 J/m^2 (see table 3.2), in close agreement with the previously computed PBE value of 0.85 J/m^2 [MM03]. The corresponding surface energies at the DFTB and ReaxFF levels are 0.73 and 1.45 J/m^2,

Table 3.2.: Surface energy of the (1$\bar{2}$10) crystal facet (γ) calculated using DFT, DFTB and ReaxFF.

	DFT	DFTB[a]	ReaxFF[b]
γ [J/m^2]	0.84	0.73	1.45

[a] Reference [MDA+09], [b] Reference [RDBH08]

respectively (table 3.2). The large deviation of the ReaxFF from the PBE value may be in part explained by the fact that the force field parameters were fitted to DFT calculations using the B3LYP xc functional (unlike the DFTB parametrization, which is based on PBE references). In fact, it is well known that GGA calculations tend to underestimate surface energies compared to LDA or B3LYP values.

Coverage Definition

Since this approach of the analysis of the (1$\bar{2}$10) surface is based on a subsequent increase of the water coverage, a factor to describe the degree of coverage is introduced to enhance clarity. This coverage factor of water on the (1$\bar{2}$10) surface is defined as $\theta = \frac{N_{H_2O}}{N_{\mathrm{Zn}}}$, where N_{H_2O} and N_{Zn} denote the numbers of adsorbed water molecules and of possible Zn binding sites on the surface area of the simulation cell. With this definition, a coverage $\theta = 1.0$ ML corresponds to 8 water molecules for the (2×2) surface model (DFT and DFTB simulations) and of 32 molecules for the (4×4) model (ReaxFF simulations).

3.3.3. Monolayer Adsorption

The investigation of the ZnO(1$\bar{2}$10)/water interface has as an initial step DFT calculations to determine the most stable configurations of adsorbed water, from a single molecule to a full monolayer (ML). The obtained ML geometries and adsorption energies are then compared with the results of the DFTB and ReaxFF methods. In doing this, an ab-initio thermodynamics approach is applied that allows to predict the most stable adsorption coverages as a function of temperature and water vapor pressure.

DFT Results

To determine the stable adsorption configurations of water molecules on the (2×2) surface cell, five independent initial configurations of one water molecule on the surface (corresponding to

a coverage of $\theta = 0.125$) are taken into account. For each configuration a short (2 ps) MD simulation at 300 K is performed in order to enable the water molecule to proceed to a more stable adsorption position. The final configuration is then relaxed using a geometry optimization. Subsequent to this procedure two (meta)stable adsorption configurations (see figure 3.5) were obtained for a single H_2O molecule on the surface (whose cell size is chosen large enough as to prevent interactions with its neighbor images through the periodic boundary conditions). Both

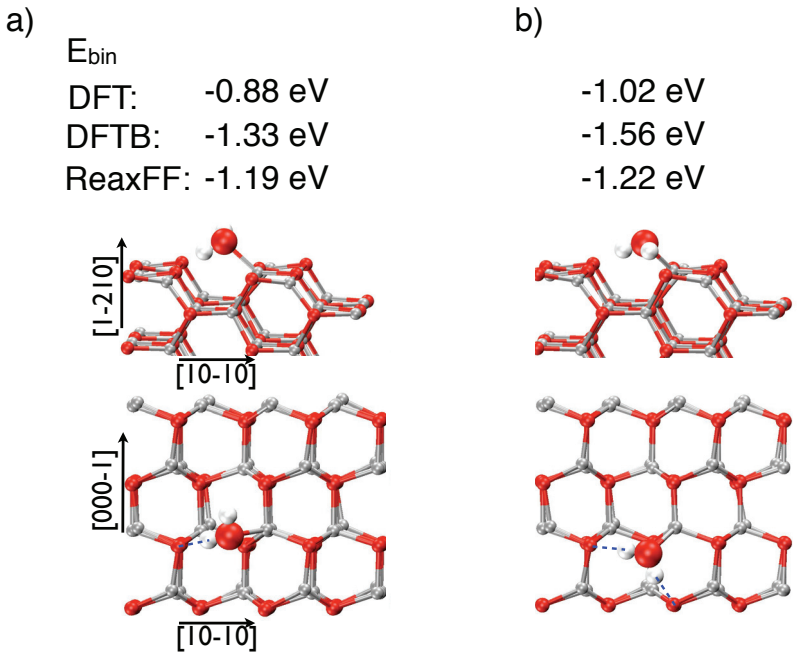

Figure 3.5.: The two adsorption configurations and corresponding binding energies (DFT, DFTB, ReaxFF) of a single water molecule ($\theta = 0.125$) on ZnO $(1\bar{2}10)$ (side and top views) .

adsorption modes exhibit a strong bond to a surface Zn atom via the O atom of the water molecule (OW). However, the two configurations differ in the number of hydrogen bonds to the surface, marked by the blue dashed lines in figure 3.5. In the configuration on the left side of figure 3.5, the water molecule bridges two rows of Zn-O dimers on the ZnO surface by forming a hydrogen bond between one of the water hydrogen atoms (HW) and a surface oxygen atom (OS) across the trench. In the second single water molecule configuration (figure 3.5 b)) the adsorption is further stabilized by a second hydrogen bond to another OS atom along the row of Zn-O dimers. Comparison with the clean surface slab and the energy of a single water molecule yielded adsorption energies of 0.88 eV and 1.02 eV per molecule, respectively. Therefore the formation of the second hydrogen bond can be directly linked to the higher adsorption energy of the second configuration. Upon adsorption, the overall surface morphology remains unchanged, while the tilt angle of the Zn-O dimer at the OW-Zn interaction site is relaxed back to its bulk

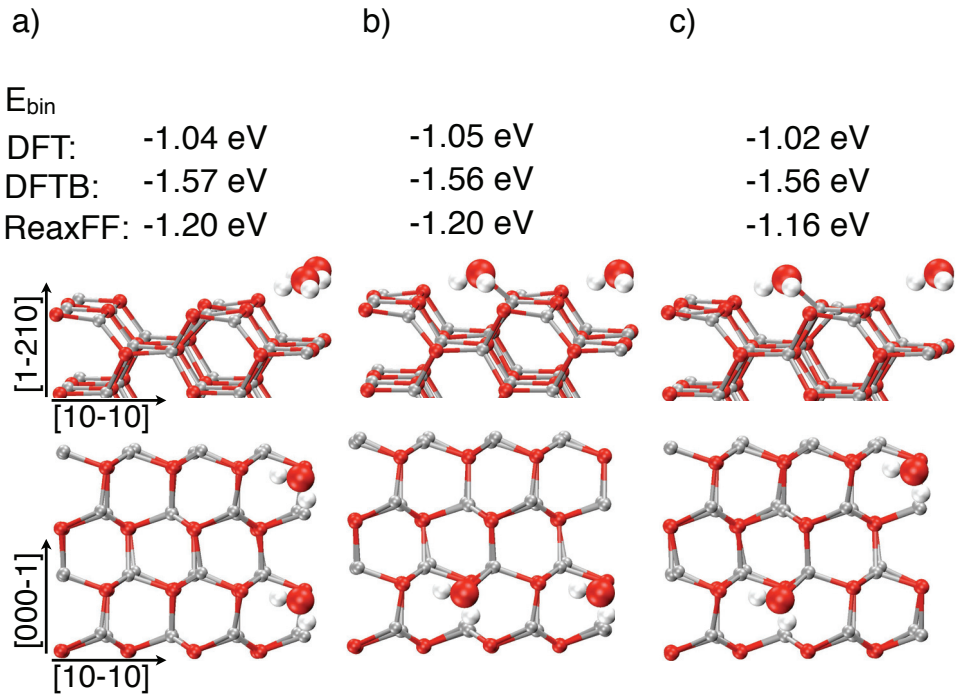

Figure 3.6.: The three adsorption configurations and corresponding binding energies (DFT, DFTB, ReaxFF) for a coverage of $\theta = 0.25$ on ZnO (1$\bar{2}$10) (side and top views) .

position. This is easily explained in terms of the recovered tetrahedral coordination of the Zn surface atom by three OS and one OW atoms, as in bulk ZnO.

In a next step a second water molecule is inserted onto the surface thereby increasing the coverage from $\theta = 0.125$ to $\theta = 0.25$. The adsorption configurations obtained after a 2 ps MD run followed by a geometry optimization are depicted in figure 3.6. Irrespective of the water arrangement on the surface, the water molecules are found to adsorb in a two-hydrogen-bonds mode (compare to figure 3.5 b)) [4]. All three calculated binding energies correspond to the ones found for the single water molecule adsorption and therefore suggest that no notable interaction between water molecules is observed.

The same two configurations as in the single water molecule adsorption are retained increasing the coverage θ further from 0.25 to 0.5 ML, i.e. including water 4 molecules (per surface) in the simulation cell (figure 3.7) applying the same procedure mentioned before. The binding energies vary only negligibly with respect to $\theta = 0.125$, amounting to 0.89 and 1.05 eV/H_2O for A and B, respectively, indicating that like for the $\frac{1}{4}$ ML , no intermolecular interactions occur at this small coverage (see figure 3.7 A,B, figure 3.5 a), b) and figure 3.5 a),b) and c)). Increasing the coverage further to 1 ML, a partial or complete dissociation of the adsorbed water molecules is

[4] All three arrangements were started using both single water adsorption modes, however a switching from the one-hydrogen-bond to the two-hydrogen-bonds mode is observed in the simulations.

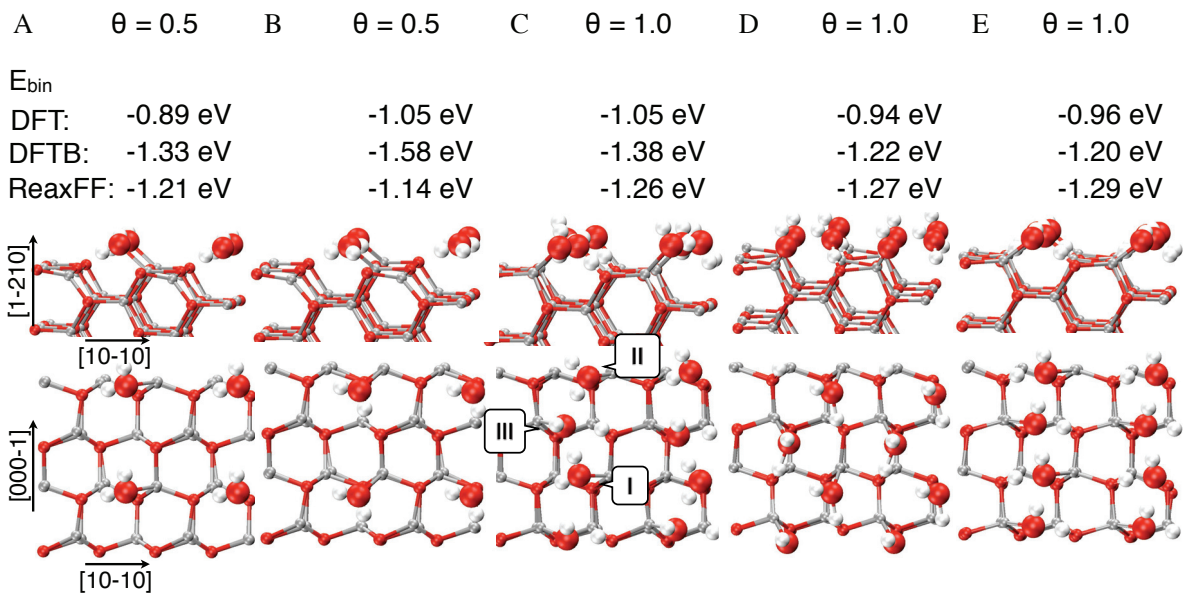

Figure 3.7.: Five adsorption configurations and corresponding binding energies (DFT, DFTB, ReaxFF) of water on ZnO $(1\bar{2}10)$ (side and top views) at different water coverages θ. Configurations A and B correspond to a coverage of $\theta = 0.5$. Configurations C, D and E correspond to half-dissociated, undissociated and fully dissociated water monolayers ($\theta = 1.0$). In C, different adsorbing states of water are labelled with roman numerals (for further explanation see text).

observed. In particular, we obtain three different adsorption configurations of the ML, depicted in 3.7 C,D,E. In the most stable configuration C (average adsorption energy of 1.05 eV/H_2O), every second water molecule is dissociated, leading to a shortening of the OW-Zn distance by about 0.1 Å. This dissociative adsorption mode (indicated by III in 3.7 C) leads to an OH group bound to a Zn site and a proton bound to a neighbor OS atom across the trench in the $(10\bar{1}0)$ direction. The molecularly adsorbed molecules adopt two different geometries (indicated by I and II in 3.7 C). Geometry I resembles the configuration A at low coverage, with one additional hydrogen bond to a next-neighbor adsorbed OH group. In geometry (II) the water molecule forms two hydrogen bonds to its two neighboring OH groups. The adsorption configuration C can be thus described as a stacking order of dissociated and molecularly adsorbed water, in which two different molecularly adsorbed geometries alternate.

In the two further configurations, lying about 0.1 eV/H_2O higher in energy, all water molecules building the ML are dissociated (3.7 D,E). In D the molecules dissociate along the Zn-O dimer trenches, and the two resulting OH groups are bridged by one H bond without further interactions between different dissociated molecules. In E the dissociation occurs across the trenches, leading to the formation of a fully developed hydrogen bond network between the adsorbed OH groups. This fully dissociated H-bond network has been proposed by Raymand et al. [RDS+10] to be

the most stable adsorption configuration at $\theta = 1.0$ ML.[5] However the DFT binding energies calculated as part of this work instead suggest that the half-dissociated configuration C is the most stable at the level of PBE-DFT.

In a last step the DFT analysis of the water adsorption up to a monolayer is completed by looking at the electronic properties of occurring adsorption modes. On that account the different types of chemical bonds that occur at the ZnO(1$\bar{2}$10)/water interface are investigated by plotting the projected density of states (PDOS) of two different adsorption scenarios (C and E) in comparison with the clean surface and an isolated water molecule (Fig. 3.8). To improve

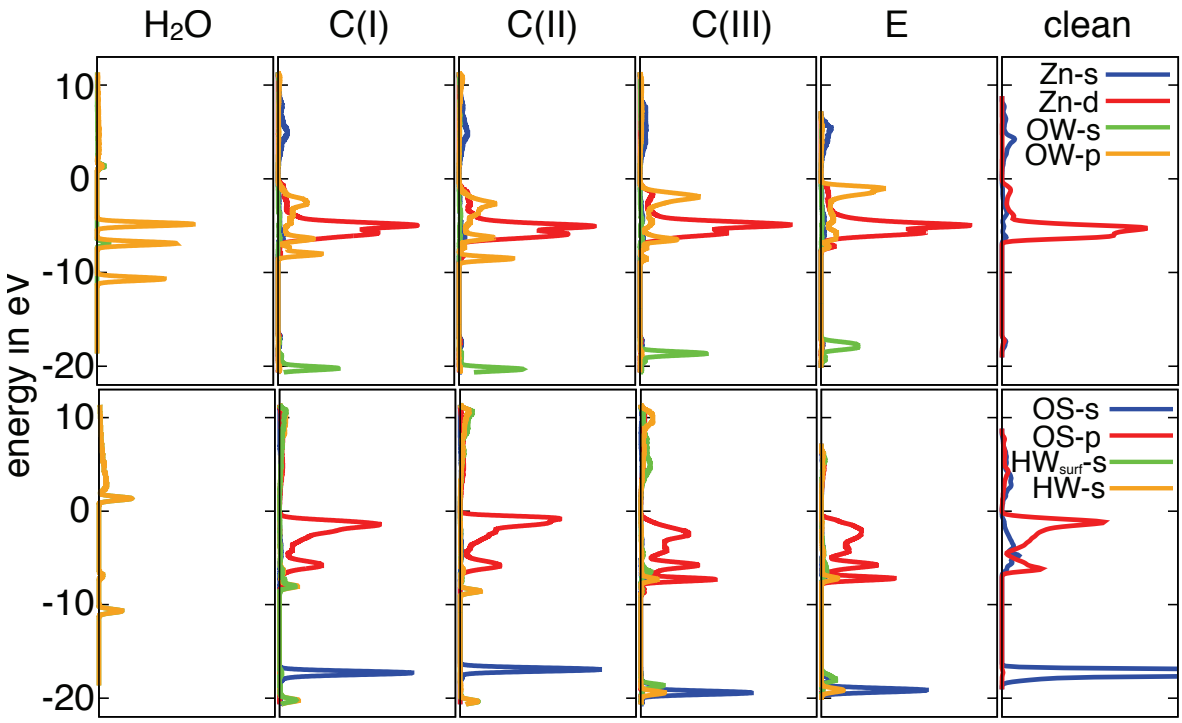

Figure 3.8.: Projected density of states (pdos) of selected monolayer configurations C and E (see 3.7) compared with the isolated water molecule and the clean ZnO(1$\bar{2}$10) surface.

clarity the projected densities are separated into a depiction of the bonds between surface zinc and water oxygen (upper part of figure 3.8) and an illustration of the bonds between surface oxygen and water hydrogen (lower part of figure 3.8). For the Zn-OW bonds, the DOS is projected on the s and p orbitals of the OW atoms along with the projections on the s and d orbitals of Zn. Compared to free water molecules, the bonding OW-s orbital of an adsorbed water is pushed down in energy by about 13 eV for all configurations but it remains quite localized at about -20 eV. Evident is also a large overlap between the Zn-d and the OW-p orbitals at about -5 eV. The latter leads to a more pronounced splitting of the Zn-d peak with respect to the clean

[5] This is confirmed by the comparison of binding energies calculated with ReaxFF.(see figure 3.7)

surface and to a broadening of the OW-p peaks over the whole valence band, as a consequence of the Zn-O bond formation. It is interesting to note the differences between the molecularly adsorbed water in C(I) and C(II) and the dissociatively adsorbed water in C(III) and E. In the dissociative adsorption case, the OW-s orbital is localized at about 1.3 eV higher energy, and a pronounced OW-p peak appears at the top of the valence band, as expected from the presence of an electron lone-pair on the adsorbed OH group. The lowest empty states of the two adsorption configurations are mostly composed of Zn 4s, a feature also found for the clean surface.

Differences between the molecularly and dissociatively adsorbed modes are also visible from the analysis of the OS-s and OS-p together with the HW-s orbitals (lower part of figure 3.8). No evident changes in the PDOS are associated with the molecular adsorption of a water molecule (panels C(I) and C(II) compared with the clean surface), this is expected, as in these cases the hydrogen and the oxygen atom only form a hydrogen bond. However the dissociative adsorption, which includes at transfer of a proton from the water to the surface, leads to a restructuring of the OS-p band, that means to a downwards shift in energy for the latter. This observed decrease of the peak at the valence-band edge as a consequence of (partial) saturation of the dangling bond of the surface O atom, and appearance of a sharp double-peak at the bottom of the valence band, is indicative of the formation of a covalent OS-H bond. This also causes a shift of the OS-s peak to lower energy values (analogous to the shift of the OW-s peak between the dissociated and molecular case, as described above).

Comparison of the DFT Results to DFTB and ReaxFF

Subsequent to the in-depth DFT analysis of the water adsorption on ZnO($1\bar{2}10$) up to a ML of water, the results are from now on used as reference points for the calculations using the two approximate methods. Hence, starting from the adsorption configurations obtained with DFT, further geometry optimizations are performed with DFTB and ReaxFF and compared to the DFT reference. A detailed overview of the obtained relaxed geometries for selected coverages is shown in figure 3.9 and table 3.3[6]). In all systems, the Zn-OW bond lengths calculated with DFTB nicely match the DFT results, with only small deviations of about 0.02 Å. The average Zn-OW distance of 2.14 Å agrees well with the peak position of the RDF of the hydrated Zn^{2+} ion (2.15 Å) discussed in chapter 3.2. At the ReaxFF level, the computed Zn-OW bond lengths are systematically longer by 0.2 Å, which also corresponds to the results of the RDF analysis (3.4). The lengths of the hydrogen bonds formed between the HW and OS atoms exhibit larger deviations from the DFT reference, of the order of 0.1 Å for DFTB and up to 0.3 Å for ReaxFF. In particular, ReaxFF tends to overestimate the hydrogen bond strength between surface and adsorbed water with respect to PBE-DFT, which may be consistent with the larger surface energy of the clean ($1\bar{2}10$) plane (see table 3.2). Accordingly, as a consequence of the stronger H-bonds, the angles between the Zn-OW bonds and the surface plane (defined as α and β

[6]The table can be found on the last page of the chapter (page 78

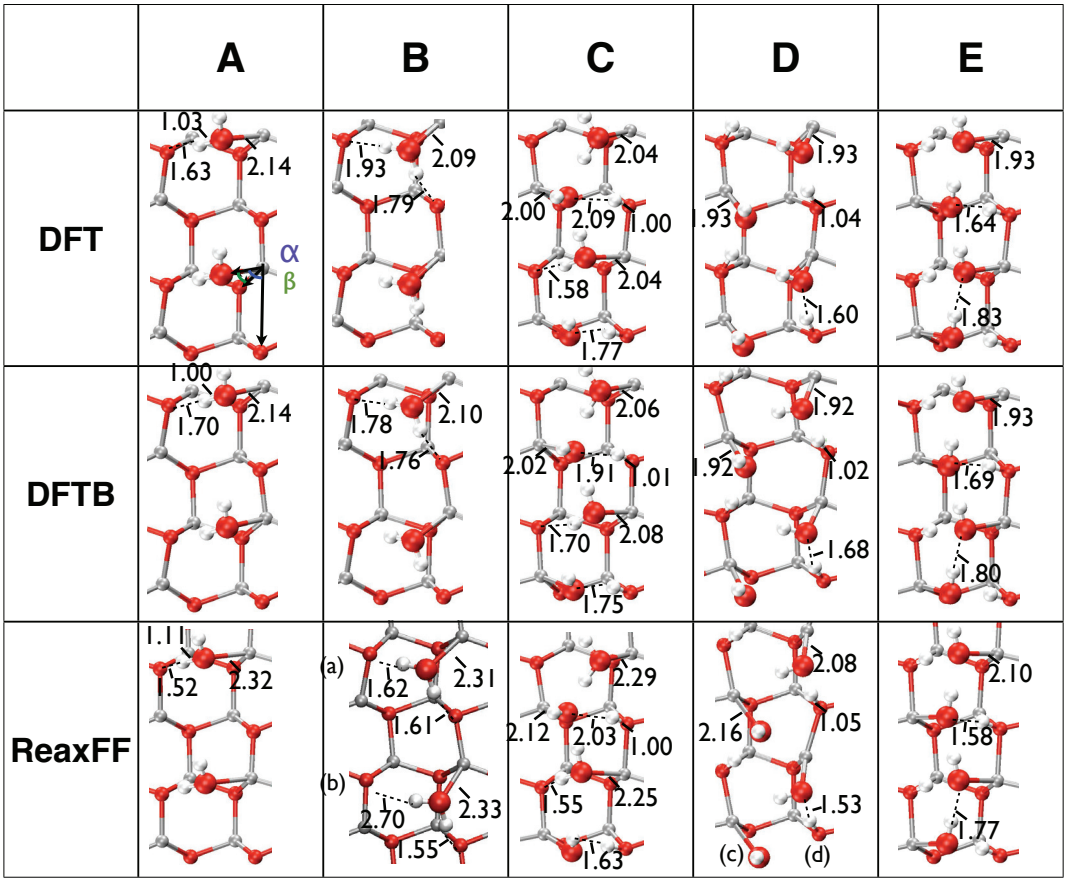

Figure 3.9.: Overview of the average bond lengths of the thermodynamically most stable (half) monolayer geometries as introduced in 3.7 calculated with DFT, DFTB and ReaxFF molecular dynamics simulations (top view). The values of the angles α and β are reported in table 3.3.

in figure 3.9 and table 3.3) also present considerable deviations from the corresponding DFT values. This results in slightly different ordering and alignment of the adsorbed water molecules over the surface at low coverage ($\theta = 0.5$), especially for the ReaxFF approach. In particular, in the adsorption configuration B, ReaxFF yields two geometries of molecularly adsorbed water (labelled with (a) and (b) in figure 3.9 and table 3.3). One of the molecules (a) forms two hydrogen bonds with the surface, as in the DFT reference and in the DFTB structure. The second molecule (b) adopts a configuration where only one hydrogen bond forms along the row of Zn-O dimers. Due to the short H-bonds, the two molecules bend considerably towards the surface plane, leading to a highly distorted coordination of the surface Zn atoms they are bound to. At $\theta = 1.0$, the hydrogen-bonding networks in C, D, E do not change their overall patterns after DFTB or ReaxFF optimization, although their relative energetic stability does change, as explained below.

Futhermore the three different methods are compared by quantifying the relative energetic

stability of the various adsorption scenarios by means of differences in the Gibbs free energy $\Delta\gamma$ of the water-adsorbed surfaces with respect to the clean surface. This can be computed as [MRM06]:

$$\Delta\gamma = \frac{1}{N_C A}\left(E_{slab}^{H_2O/ZnO} - E_{slab}^{ZnO} - N_{H_2O}(E_{single}^{H_2O} + \Delta\mu_{H_2O})\right) , \tag{3.3}$$

where N_C is the number of surface unit cells, A their surface area, and N_{H_2O} the number of water molecules. E_{slab}^{ZnO} and $E_{slab}^{H_2O/ZnO}$ are the computed total energies of the slab in the clean and adsorbed states. $\Delta\mu_{H_2O}$ defines the chemical potential of the water vapor with respect to an isolated water molecule with computed energy $E_{single}^{H_2O}$:

$$\Delta\mu_{H_2O} = \Delta\tilde{\mu}_{H_2O} + k_B T \ln\frac{p}{p_0} , \tag{3.4}$$

where p and T are the vapor pressure and temperature, k_B the Boltzmann constant and $\Delta\tilde{\mu}_{H_2O}$ contains the entropy and enthalpy variation of the vapor at the reference pressure p_0, as available in standard thermodynamical tables [Lid09]. In order to analyze the influence of the water condition, two constant water vapor pressures of $p = 1.0$ bar and $p = 10^{-10}$ bar are assumed in the calculation of the corresponding Gibbs free energies. In figure 3.10 the results of the surface energy values as a function of the temperature for the DFT, DFTB and ReaxFF calculations at $\theta = 0.5$ and $\theta = 1.0$ ML are depicted.

The DFT results predict a coverage of 1.0 ML with adsorption configuration C to be the most stable surface structure at temperatures lower than 520 K for $p = 1.0$ bar and lower than 291 K for $p = 10^{-10}$ bar (Fig. 3.10 a). At higher temperatures, desorption of the whole ML takes place leaving a clean surface. The coverage of 0.5 ML is never favorable and the corresponding free energy curve intersects the one associated with the clean surface at the same point as the 1.0 ML curve. This is a consequence of the equal average adsorption energies per molecule computed for $\theta = 0.5$ and 1.0 ML (see 3.7).

The DFTB approach likewise predicts the monolayer configuration C to be the most stable structure at low temperatures. However, differently from the DFT reference, it also predicts an interval of stability for the 0.5 ML structure (between 600 and 780 K at 1.0 bar, or between 330 and 438 K at 10^{-10} bar (3.10 b). This discrepancy is also reflected in the corresponding adsorption energies (see figure 3.7), which comply with the intercept point of the x-axis. With a value of 1.58 eV/H_2O the adsorption energy of the half ML structure B is 0.2 eV higher in energy compared to the half-dissociated ML structure C found lowest in energy using DFT. Furthermore all adsorption energies determined with DFTB overestimate the binding strength, as already described for the $(10\bar{1}0)$ in chapter 3.2. Hellström and co-workers show in a recent work [HJB+13], that this over-binding can be partly corrected by reparametrization of the corresponding zinc and oxygen repulsive potential used in DFTB. However as the focus of this work is not on single point calculations but on molecular dynamics simulation at room temperature

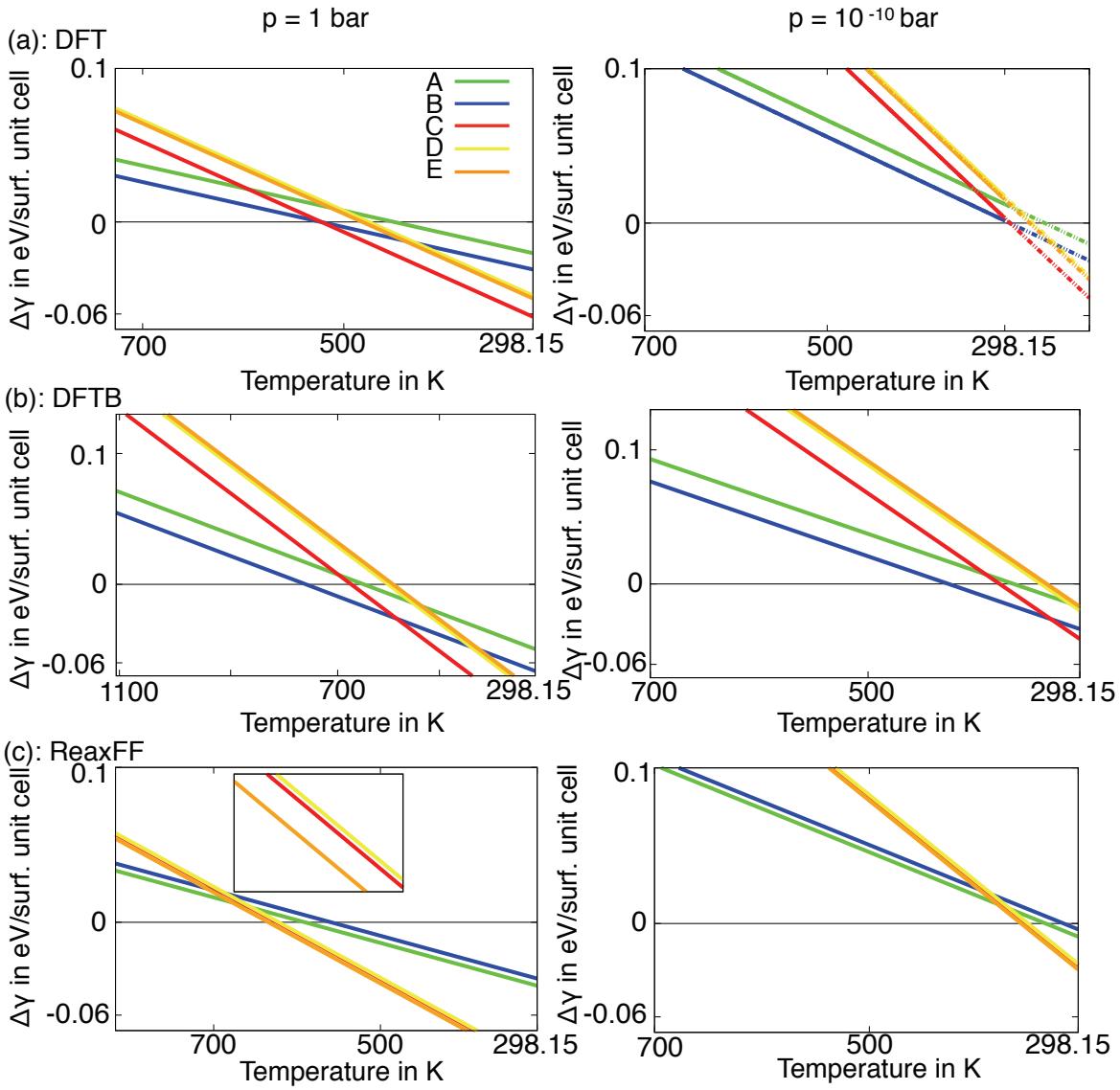

Figure 3.10.: Dependencies of the Gibbs free energy of the ZnO(1$\bar{2}$10) surface at various water coverages on the water vapor chemical potential obtained with (a) DFT, (b) DFTB and (c) ReaxFF. The blue and green lines correspond to configurations A and B in 3.7 (0.5 ML), the red, yellow and orange lines to configurations C, D, E (1.0 ML). The data below 298 K in the top-right panel (dotted lines) are obtained from a linear extrapolation of the higher temperature curves.

the obtained results show DFTB to be capable of a sufficiently accurate description.

At the ReaxFF level of approximation, as in the DFT case, a direct transition from the full ML to the clean surface, with transition temperatures of 620 K and 360 K at 1.0 bar and 10^{-10} bar, respectively is obtained. The 0.5 ML structure is less stable than in the DFT case, due to the lower average adsorption energy per molecule obtained at the lower coverage. Moreover, the free energy curves corresponding to the three ML configurations C, D and E are almost

degenerate, with a slight preference for the fully dissociated structure (see insert of Fig. 3.10 c). The adsorption energies computed with ReaxFF are as well overestimated compared to the ones obtained by DFT calculations (see figure 3.7).

3.3.4. Influence of Bulk Water

After the investigation of the interface between ZnO($1\bar{2}10$) and water vapor up to a coverage of 1 ML, the next step in this study is the dynamical behavior of the surface placed in contact with bulk liquid water. To this aim, the vacuum region between the periodically repeated surface slabs is filled with H_2O molecules at the normal density of about 1g/cm^3. As a first investigation, the surface is decorated with only 0.5 ML of adsorbed water and randomly placed water molecules in the bulk liquid. In an MD simulation the time evolution of the average coordination number (CN_{Zn-OW}) of the surface Zn atoms is then monitored using the three simulation methods, DFT, DFTB, ReaxFF. Since at the beginning of the simulations only half of the Zn sites are

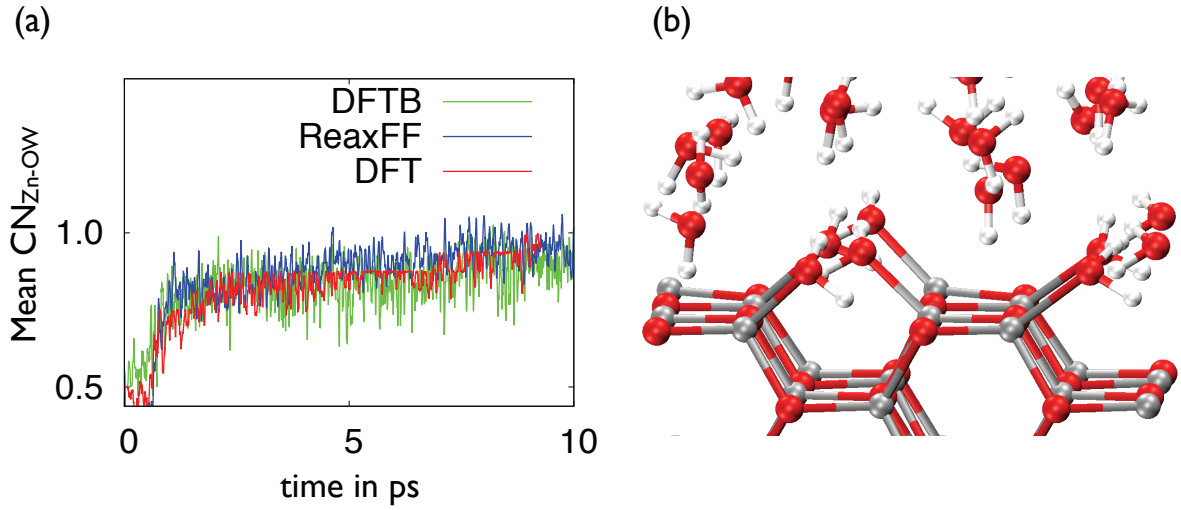

Figure 3.11.: The left side (a) depicts the time evolution of the mean coordination number for surface zinc and water oxygen calculated from a MD run of 10 ps performed with all three methods. In (b) the additional initial configuration used to study the effect of bulk water on a molecular adsorbed monolayer is shown.

bound to water molecules, CN_{Zn-OW} starts at the value of 0.5 (see figure 3.11 a)). The time evolution of the coordination number, CN_{Zn-OW} shown in figure 3.11 a), increases and stabilizes at about 1.0 for all three methods within a few ps of MD at 300 K. This indicates that full occupation of the Zn surface site by one (and only one) water molecule is found for all three methods. Importantly, no further increase of the coordination number is observed over a much longer simulation time (tens of ps) in DFTB and ReaxFF simulations.

The finding that full coverage of Zn binding sites for all three methods suggest that a ML coverage should be used as initial configuration for further analysis of the influence of bulk

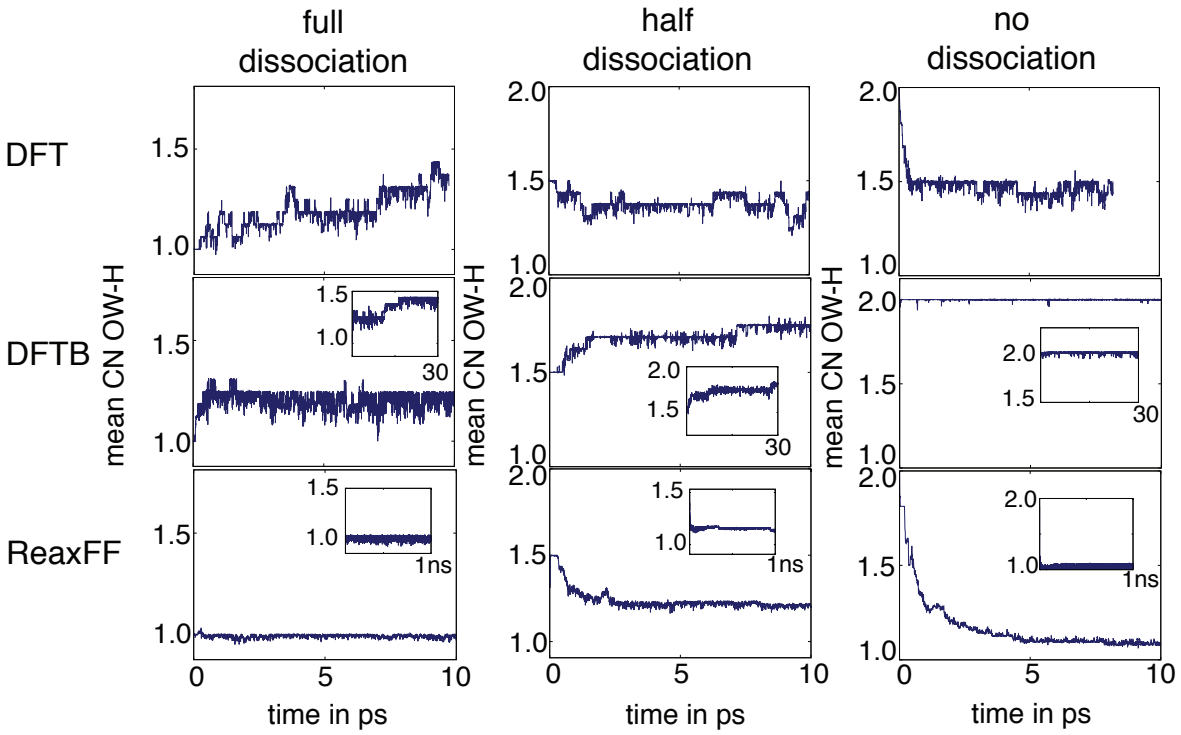

Figure 3.12.: Time evolutions of the mean coordination numbers of water oxygen and hydrogen over the ZnO(1$\bar{2}$10) surface obtained in MD simulations starting from three different initial structures: full dissociation (left), half dissociation (center) and no dissociation (right). Each row shows the results of the DFT, DFTB and ReaxFF methods (top to bottom).

water. For that reason the propensity of dissociative versus molecular water chemisorption in the presence of bulk liquid water is evaluated with the three methods, which predicted different adsorption configurations at the coverage of 1 ML (see Fig. 3.7). Apart from the two ML configurations already analyzed in chapter 3.3.3, to complete the case an additional third arbitrary configuration shown in figure 3.11 b) is taken into account. The distinguishing feature of this configuration is that all water molecules are molecularly adsorbed to the Zn surface sites. Therefore starting from three different initial configurations of the chemisorbed layer, namely (i) fully dissociated, (ii) half-dissociated and (iii) non-dissociated, at least 10 ps long MD runs of the systems in contact with bulk water are performed and analyzed. Longer simulations are performed for DFTB (30 ps) and ReaxFF (1000 ps), since these require less computational resources. The time evolutions of the average coordination number $CN_{OW(s)-HW}$ of the chemisorbed OW atoms to hydrogen atoms are shown in figure 3.12 for all investigated cases. The three initial conditions used correspond to $CN_{OW(s)-HW}$ equal to (i) 1.0, (ii) 1.5 and (iii) 2.0, respectively, at the beginning of the MD simulations.

At the DFT level, irrespective of the initial conditions, within 10 ps an equilibrium configuration of half-dissociated water molecules is reached. Notably, the recombination of the initially fully

dissociated water (increase of $CN_{OW(s)-HW}$ from 1.0 to 1.5) takes much longer than the (half) dissociation of the molecularly adsorbed layer, which is completed in less than 100 fs (Fig. 3.7, top three panels). The structure of the chemisorbed water layer at the end of the simulations corresponds to the adsorption configuration C in figure 3.7, i.e. every second water molecule is dissociated.

The ReaxFF simulations show a different trend, in which complete dissociation of the adsorbed water molecules ($CN_{OW(s)-HW} = 1.0$) is obtained at the end of the simulations. Only starting from a half-dissociated chemisorbed layer an average value $CN_{OW(s)-HW} = 1.2$ is obtained after 1000 ps, most probably indicating the presence of a local energy minimum in which a few of the adsorbed molecules remain undissociated. Interestingly, however, when starting from undissociated water complete dissociation takes place very rapidly, within 10 ps. Therefore, ReaxFF predicts the same adsorption configuration to be stable both at 1 ML of water vapor (see figure 3.10 c)) and in the presence of liquid water (fully dissociated configuration E in 3.7). This result is consistent with previous ReaxFF investigation of the water adsorption on the $(1\bar{2}10)$ ZnO surface performed by Raymand et al. [RDG+11].

DFTB predicts the opposite scenario. Namely, the molecularly adsorbed layer is remarkably stable over more than 30 ps of MD ($CN_{OW(s)-HW} = 2.0$). Also starting with a half-dissociated or fully dissociated chemisorbed layer, a slow but evident increase of $CN_{OW(s)-HW}$ towards values higher than 1.5 is observed on the time scale of the simulation (which would probably end up with $CN_{OW(s)-HW} = 2.0$ at longer times). The MD simulations thus indicate a net preference of the DFTB method for molecular adsorption in the presence of bulk water, which is in contradiction with the results at $\theta = 1.0$ ML, where a half-dissociated structure is favorable (see 3.7 and 3.10). Therefore, the stabilization of molecular water in the chemisorbed layer must be due to the formation of a developed hydrogen-bonding network above the surface, resulting in different dissociation equilibria within the DFTB formalism.

A possible explanation for this behavior may be associated with the changes of the self-consistent charges (SCC) of the atomic species under the different adsorption conditions. Consistently with typical literature values [JM83], the SCC on the O atoms amounts to -0.78 e in bulk water, and *decreases* in value to -0.60 e after molecular adsorption on the surface, becoming closer to the SCC of surface O atoms (-0.5 e). Instead, the Zn-O bonds in the ReaxFF formalism are more strongly polarized, with a surface O point charge of -0.90 e, consistently with the high surface energy values computed in Section 2.3. It can be thus inferred that the markedly different behavior of water on the ZnO surface in the DFTB and ReaxFF formalism may arise, at least in large part, from the large difference in the electrostatic interactions between atomic charges in the two cases.

An important consequence of different dissociation equilibria at the interface is the different structuring of water layers in surface proximity predicted by the three formalisms. In figure 3.13 the density of OW and HW atoms averaged over 10 ps MD simulations performed with the

equilibrium structures of figure 3.12 is plotted against the height z above the surface plane. For

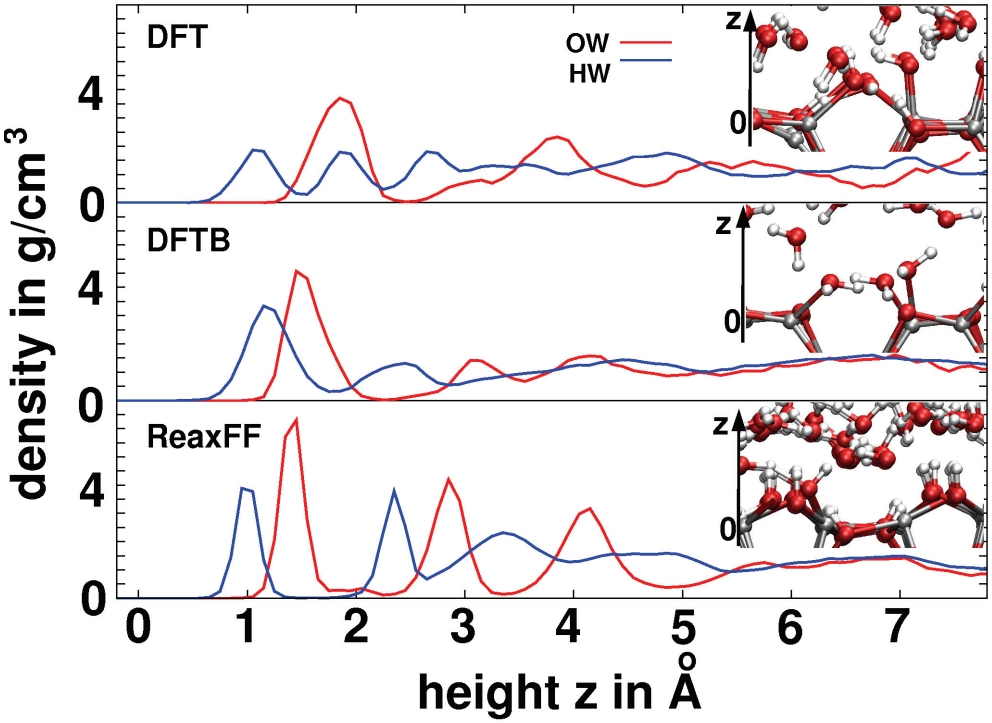

Figure 3.13.: Density of OW and HW atoms of liquid water against the height z above the ZnO (1$\bar{2}$10) surface obtained in MD simulations using DFT (top), DFTB (middle) and ReaxFF (bottom). To improve the comparison the HW density is multiplied by a factor of ten. The zero point of z is set at the position of the surface Zn atoms. For each method the inset displays a snapshot of the equilibrium interface structure.

ReaxFF the first HW peak at 1.0 Å corresponds to the dissociated protons covalently bond to the OS atoms. The first OW and the second HW peaks (at 1.5 and 2.3 Å) arise from the adsorbed OH groups in an almost vertical orientation. The two further well-defined OW peaks and the associated HW peaks between 2.8 and 4.5 Å indicate the presence of a second and a third strongly structured water layers over the surface. This structuring is much less pronounced at the DFTB level, where the first HW and OW peaks at 1.2 and 1.5 Å reflect the presence of water molecules bent with the hydrogen atoms towards the surface in the molecularly adsorbed layer. The second HW peak at 2.4 Å arises both from molecules adsorbed in an upright geometry and from H atoms of the second water layer. Both this second and a third water layer are visible in the OW density distribution, although with very small density maxima. The density obtained from DFT MD shows two distinct maxima and an intermediate subsidiary peak for OW, and three distinct peaks for HW. The first OW peak at 2.0 Å is broadened, as it represents both the molecular and dissociated adsorbed water molecules of the interface layer. The HW peaks

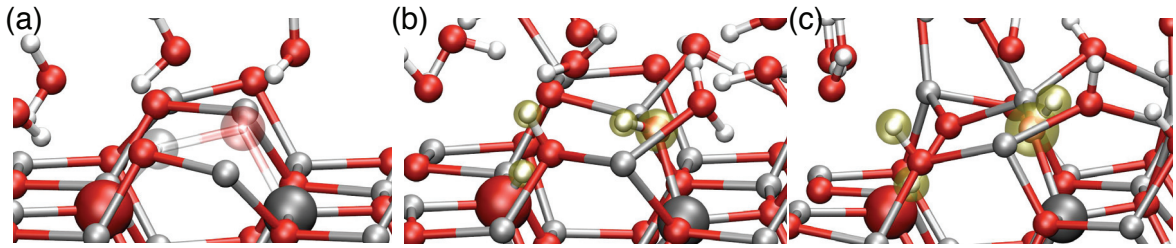

Figure 3.14.: Snapshots from MD simulations of the reaction between the ZnO $(1\bar{2}10)$ surface and liquid water, including a missing Zn-O dimer as a surface defect. (a) Initial configuration. The missing Zn and O atoms are rendered as semi-transparent and the resulting under-coordinated subsurface atoms are highlighted as larger spheres. (b) Final configuration after 15 ps of MD using DFTB. (c) Final configuration after 15 ps of MD using ReaxFF. Both simulation methods show the same qualitative reaction mechanism, namely dissociative adsorption of a water molecule at the uncoordinated subsurface sites and protonation of one of the surface O atoms neighboring the initial defect. The newly adsorbed H and OH groups are highlighted with a yellow halo.

at 1.1 Å, 2.0 Å, and 3.7 Å depict the HW atoms bonded directly to the surface, forming a hydrogen bond to a OS or a neighboring OW and pointing away from the surface, respectively. The overall amount of structuring predicted by DFT extends up to about 4.5 Å over the surface, with intensities intermediate between the ReaxFF and the DFTB methods.

As a final test of the performance of the two approximate methods using the $(1\bar{2}10)$ surface as a model system, the reaction between liquid water and a neutral surface vacancy defect, obtained upon removal of a Zn-O dimer from the $(1\bar{2}10)$ surface is analyzed . Starting from randomly placed water molecules over the dry defective surface (Fig. 3.14 (a)), MD simulations performed with either DFTB or ReaxFF predict the same reaction mechanism and final outcome (Fig. 3.14 (b) and (c), respectively). Namely, within a few ps the under-coordinated subsurface Zn and O atoms become saturated by an OH and an H group, respectively, as a consequence of the dissociative adsorption of a water molecule. Moreover, one of the O atoms neighbor to the Zn vacancy receives a proton from the bulk liquid. Notably, in this case also DFTB, not only ReaxFF, predicts water dissociation at the vacancy site and increased reactivity (basicity) of the O atoms nearby, indicating that the subtle differences between the methods in the case of protonation equilibria of defect-free surfaces are not as substantial as to predict a different behavior in the case of obvious defects.

3.4. The Influence of Two Different Surface Kinks on the Formation of a First Adsorption Layer

As mentioned earlier several experimental studies so far have linked the toxicity of ZnO directly to solvated zinc ions. In order to understand why different environments influence the solubility of ZnO, it is crucial to understand where and how dissolution happens. Therefore the next puzzle piece on our way to a reasonable description of reactions occurring at the ZnO/water/bio interface is an analysis of different starting points of the dissolution process. Intuitively dissolution will start at regions, where atoms display the largest contact surface, that means at region wheres the surface exhibits defects. This assumption is confirmed by an experimental study focusing on the chemical dissolution of zinc oxide single crystals [GS92]. The results of this work suggested that the rate of dissolution is dependent on the bond breaking reactions at surface kink sites. Furthermore they found that the corresponding activation energy is similar for the three surfaces studied, namely the two polar surfaces and the non-polar $(10\bar{1}0)$ surface. Therefore only defects at the non-polar $(10\bar{1}0)$ ZnO surface are considered. Similar to the perfect surface, the first step in order to analyze more complex reactions at a defect surface is the evaluation of the ZnO-defect/water interface.

Computational Details and Model System

The dimer-defect geometries obtained with ReaxFF in the previous sections showed a good agreement with DFT result. This and the fact that sufficiently large model systems are needed in order to reasonably describe a surface defect the method of choice for this part of the work is ReaxFF. The calculations are performed with the LAMMPS code [Pli95], using the potential parametrization introduced by Raymand et al. [RDBH08]. The Nosé-Hoover thermostat is used with an integration time step of 0.25 fs for the MD simulations to sample a NVT ensemble at 350K.

The slab model was built using a perfect model of the $(10\bar{1}0)$ surface. A zinc kink and an oxygen kink are cut into one side of the surface slab respectively (see figure 3.15 a) and c)), according to the kink models reported in [GS92]. The supercell comprised a volume of $(15.78 \times 16.41 \times 22)\text{Å}^3$. The simulation cell was filled up with bulk water up to a density of 1 g/cm^3 and contained 537 atoms in total .

Adsorption Geometries of Water at the Kink Sites

During the first femto seconds of the 20 ps MD run a water molecule dissociates at the Zn kink site (see figure 3.15 a)). The oxygen of the resulting hydroxyl group forms a bond to the zinc of the kink site with a bond length of approximately 2.1 Å. Bulk water additionally settles on the zinc kink and on the neighboring surface zinc atoms restoring the tetrahedrally conformation

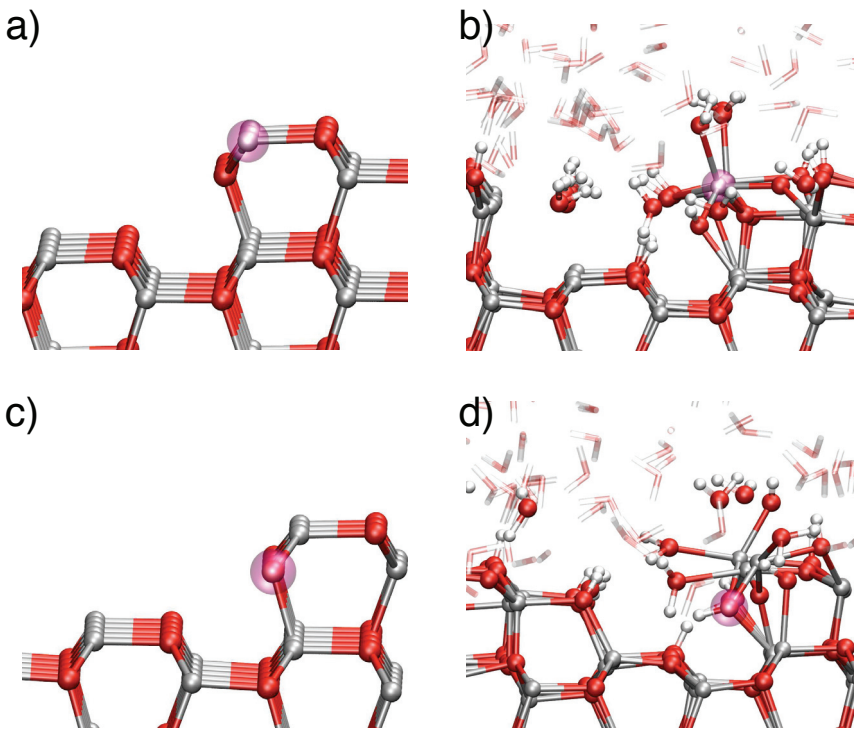

Figure 3.15.: Initial (a) and final snapshot (b) of the zinc kink model used in the calculation.Figures (c) and (d) show the corresponding snapshots for the considered oxygen kink model. Only bulk water that interacts with the surface is displayed by a ball and stick model. To improve clarity the remaining water is depicted by transparent dynamic bonds.

also found in bulk ZnO. Additionally water dissociates at the one edge of the kink. The resulting hydroxyl group settle at an intermediate position in between two zinc atoms forming bonds of 2.2 Å and 2.5 Å respectively. During this process the zinc oxygen bond of the surface dimers are elongated and even a bond breaking can be observed. An evaluation of the corresponding charges yields a charge of 0.84 e at the zinc kink site at the end of the 20 ps MD run. However comparison with the charges of the next neighbor zinc atoms show no significant difference.

The oxygen kink is also very reactive already during the first femtoseconds of the MD run. It promotes the dissociation of a water molecule, thereby forming a stable O-H bond to the transferred hydrogen atom (see figure 3.15 d)). The neighboring zinc binding sites of the surface are saturated by water molecules during the MD run. Bulk water also dissociates at the oxygen atoms belonging to one border of the kink. Additional bulk water forms bonds to the bordering zinc atoms, however unlike in the previous case, these water molecules adsorb in a molecular mode on one zinc atom, displaying bond lengths of approximately 2.3 Å. The zinc-oxygen bonds of the surface dimers are elongated by about 0.1 Å but remain intact. Similar to the case of the zinc kink, an analysis of the charges does not yield a distinct difference for

the oxygen atom at the kink site and nearby oxygen atoms.

The results for both kinks therefore suggest that surface reconstruction of the defect site is to be expected under the influence of bulk water. This is found to be more pronounced for the case of the zinc kink. Gerischer et al. [GS92] concluded in their work that the dissolution process at kink sites can be catalyzed by the addition of acids and certain ligands. They assumed that the formation of complexes with Zn^{2+} ions might be the triggering factor of this effect. This analysis of the water formation on the two types of kinks is therefore an excellent vantage point for the analysis of the adsorption behavior of a small bio molecule on a kinked surface (see chapter 4.1.8).

3.5. Discussion

In this chapter I have described the process to obtain a reliable model of the first water layer on the ZnO $(1\bar{2}10)$ surface and on a kink defect model. Starting from a thorough validation of the applied methods using already published reference values (experimental and theoretical), I have shown that the chosen set-ups are able to reproduce these literature data. The CPMD set up showed a good agreement regarding geometric, energetic and electronic issues. Despite the over interpretation of the binding energies per water molecule for the $(10\bar{1}0)$ surface using DFTB and ReaxFF, both methods were able to reproduce DFT results by yielding a very similar general ordering of the different considered configurations. All three methods describe the interactions between a single Zn^{2+} ion and liquid water in acceptable agreement with experimental results. Since an elaborated study of the interface between the non-polar $(1\bar{2}10)$ surface and water had not been reported, the subsequent part of the work focused on this system. In the analysis of coverages up to a water ML on the $(1\bar{2}10)$ surface, results showed that CPMD, DFTB and ReaxFF are found to predict different adsorption structures for a water monolayer adsorbed on the surface. DFT and DFTB predict a half-dissociated structure to be most stable, while ReaxFF predicts a fully dissociated (hydroxylated) structure. In contact with bulk liquid water, the half-dissociated and the fully dissociated structures remain stable within DFT and ReaxFF, respectively, while recombination of the dissociated water with formation of a molecularly adsorbed first water layer takes place at the level of DFTB. This finding is peculiar, since previous theoretical studies on ZnO and other metal oxides indicate, generally, a tendency toward dissociation of the chemisorbed layer promoted by higher water coverages [RDG+11]. The obtained tendency of the water to recombine in the DFTB simulations might be due to the intrinsic shortcomings of the used self-consistent-charge approach to describe proton affinities and binding energies. In this approach, the Taylor series of the total energy of the system expanded in terms of the density is truncated after the second term (second-order Tight-Binding). As a consequence of this approximation, the proton affinities of negatively charged molecules are overestimated due to an overbinding of the O-H bond of about 6-7 kcal/mol [GCE11]. Gaus

et al. suggested that the problem can be solved when third-order terms are included in the series expansion of the tight-binding energy [GCE11](see equation 2.71), which could be performed in future works for the whole ZnO/water interface system.

The ReaxFF approach offers in principle a viable alternative to both DFT and DFTB, with a nice compromise between accuracy and computational cost. In the case of the ZnO($1\bar{2}10$) surface, however, ReaxFF predicts a different water structure with respect to our DFT reference, as mentioned above. In the absence of specific experimental information, which is available only for the other non-polar surface ($10\bar{1}0$),[MMD$^+$04] it remains unclear what is the correct adsorption structure, and what is the influence of the chosen xc functional on the DFT results. In the case of the ($10\bar{1}0$) surface, the ReaxFF results available in the literature nicely match both PBE-DFT and experiments findings, predicting 50% of the adsorbed water molecules to dissociate at $\theta = 1.0$ ML. At higher coverages, the amount of dissociation increases to about 80% for the ($10\bar{1}0$) surface and 100% for the more stepped ($1\bar{2}10$) surface [RDG$^+$11]. A reason for the observed behavior may be the much stronger polarization of the ZnO bond in ReaxFF than in DFTB, as evident from the analysis of point charges presented in Section 3.3. This difference, together with the different polarizabilities of the first water layer, may shift the hydroxylation equilibrium towards dissociative adsorption. In line with these observations, we note that the overestimated ReaxFF surface energy of the clean ($1\bar{2}10$) surface with respect to PBE-DFT (1.45 vs. 0.84 J/m^2, see Table 3.2) is also an indication of overestimated surface reactivity. In fact, surfaces with lowest surface energies show a tendency for molecular adsorption, whereas surfaces with higher energy show a stronger hydroxylation equilibrium caused by water dissociation [BZ04, Die03]. Consistently, DFTB predicts both the lowest surface energy (0.79 J/m^2) and stable molecular adsorption.

Despite the shortcomings and inconsistencies highlighted above, one has to note that the energy differences associated with the different adsorption structures are rather small (less than 0.1 eV for a binding energy per molecule of about 1 eV). Therefore, little changes of the computational parameters (xc functionals and pseudopotentials in DFT, Slater-Koster parameters in DFTB, numerical parameters in ReaxFF) may easily result in an altered hydroxylation equilibrium, especially in the presence of bulk water. This might point towards nearly equal stabilities of the molecularly adsorbed and dissociated water molecules of the ZnO($1\bar{2}10$) surface. An important consequence of the different hydroxylation equilibria is the different structuring of the water layers up to about 5.0 Å far from the surface (see 3.13). As this structure has been found to considerably influence the geometry, adsorption energy and adhesion forces of biomolecules at solid/liquid interfaces [SC12, SLW09, HSG$^+$08], the choice of the simulation method may heavily affect atomistic simulations between ZnO and dissolved biomolecules.

The results about the reaction of liquid water with a neutral surface defect (see 3.14) are however encouraging, demonstrating qualitatively the same outcome of MD simulations performed with either DFTB or ReaxFF. These results motivated the use of ReaxFF to evaluate the water

adsorption at two different kink sites. No unexpected reactions or major reconstruction were observed during the corresponding MD runs of the kink interfaces. However the geometries obtained from these simulations are an excellent starting point for further analysis focusing on the adsorption of small molecules on these defect site or even for future free energy calculations regarding the dissolution of ZnO.

Table 3.3.: Average bond angles (as defined in figure 3.9) for the thermodynamically most stable (half) monolayer geometries of water over ZnO($1\bar{2}10$) (see figure 3.7) calculated with DFT, DFTB and ReaxFF.

	A		
	DFT	DFTB	ReaxFF
α	96.88	96.65	102.74
β	81.03	75.46	88.20
	B		
	DFT	DFTB	ReaxFF
α	90.67	88.25	(a)89.98 (b)97.56
β	55.29	53.86	(a)52.33 (b)50.08
	C(i)		
	DFT	DFTB	ReaxFF
α	101.87	99.99	109.05
β	92.30	86.41	93.66
	C(ii)		
	DFT	DFTB	ReaxFF
α	106.09	100.83	117.19
β	83.53	79.58	79.79
	C(iii)		
	DFT	DFTB	ReaxFF
α	102.97(1HB) 105.33(2HB)	103.08	108.87(1HB) 117.73(2HB)
β	83.45	80.83	88.93
	D		
	DFT	DFTB	ReaxFF
α	107.18	105.42	(c) 98.05 (d)118.45
β	50.42	53.47	(c) 53.55 (d) 51.84
	E		
	DFT	DFTB	ReaxFF
α	101.95	104.64	111.37
β	89.52	88.02	91.24

Chapter 4.

4 Adsorption of organic compounds on ZnO

The interactions at zinc oxide surfaces in biological environments are very complex, involving the surface adsorption and reactions of water, metal ions and biomolecules. The pure ZnO/water interfaces have been studied in a number of theoretical studies (see e.g. [HKFCC12, MMD$^+$04, MRM06, CC09] in the previous chapter of this thesis). In this part of the work the model is extended a level further in complexity, addressing the adsorption of organic molecules on ZnO surfaces. In addition to the adsorption on perfect surfaces, a surface exhibiting an oxygen kink is also considered in this context. In addition to the initial motivation for this work, that means reactions occurring at the ZnO/water/bio interface that might enhance the solubility of ZnO, molecular dynamics studies on closely related research fields like GEPI or the functionalization of nano wires conclude this part of the thesis.

4.1. Analysis of the Adsorption Behavior of Four Different Amino Acids on the ZnO (10-10)/water Interface

So far only very few theoretical and experimental studies have focused on the adsorption of amino acids on ZnO. In a combined XPS and DFT study of the adsorption modes of alanine on the non-polar ZnO(10$\bar{1}$0) surface in vacuo, a dissociated bidentate adsorption configuration in neutral (and not zwitterionic) form was found to be stable [GTS$^+$09]. Irrera et al. investigated the adsorption of glycine on the polar, zinc terminated (0001) surface by means of density functional theory [ICM09]. In the most stable binding mode, the glycinate ion form induces a stabilization of flat Zn-ZnO terraces binding to the surface through both the amino and the carboxylate functional groups. A similar adsorption configuration was determined for the adsorption of glycine on ZnO(10$\bar{1}$0) [DMD$^+$11]. While these studies represent valuable contributions to our understanding of the interactions of amino acids with bare ZnO surfaces, they do not consider

hydrated surfaces in an effort to mimic biological conditions. However, as stressed, before the presence of water at oxide surfaces is known to have a direct influence on the biomolecular adsorption modes [SC12, KL10, MW11].

Results from the previous chapter and other works have proven that on ZnO, the first interfacial water layer presents an equilibrium between dissociated and molecularly adsorbed water [MMD$^+$04, MRM06, HKFCC12], which is likely to have a strong impact on the adsorption of other molecules. In order to study these effects theoretically, it is necessary to employ methods that are capable of predicting possible chemical reactions between the hydrated surface and adsorbing molecules (e.g. the exchange of protons or the formation of covalent bonds to surface atoms). At the level of single amino acids, full quantum methods such as DFT can be employed. For that reason in this part of the thesis, the adsorption of four single amino acids (glutamine, glutamic acid, cysteine and serine) on the ZnO($10\bar{1}0$) surface in a water environment is investigated theoretically. However, due to increasing system sizes, studies of more complex bio-hybrid ZnO interfaces require much longer simulation times and larger system sizes than accessible by DFT. Contrary to the analysis of the ZnO/water interface the reactive force field ReaxFF cannot be applied in these kind of systems. This is due to the fact that atom types occurring in organic compounds, like carbon or nitrogen were not part of the specific paramterization set of ZnO [RDG$^+$11]. Therefore, in the absence of an reactive force field to describe at the same time the chemistry of dissolved amino acids and ZnO surfaces, tight-binding methods such as DFTB [EPJ$^+$98] are a presently available compromise between computational accuracy and efficiency. Consequently, additionally to the analysis of the adsorption modes a thorough comparison between simulations performed with DFTB and reference molecular dynamics (MD) simulations performed with DFT, is carried out in this part of the work. In particular, DFTB simulation settings are validated in terms of reproducing the adsorption modes predicted by DFT. Furthermore the corresponding energetics of the two methods on the basis of computed adsorption energies are compared.

4.1.1. Methods and Model Systems

The benchmark DFT calculations for the amino acid adsorption were performed with Car-Parinello MD as implemented in the CPMD code [CPM]. Constant-temperature MD simulations of 6.5 ps at 350 K were performed using a Nosé-Hoover thermostat after heating and equilibration of the system as introduced in ref. [KBL08]. The temperature was thereby set to a slightly higher value than room temperature to promote interactions at the surface. The Brillouin zone integration was performed in the Γ-point approximation. The DFTB calculations were conducted using the DFTB$^+$ code [AHF07]. The parametrization set *znorg* introduced in ref. [MDA$^+$09] was used to describe the hybrid interface. The nitrogen-hydrogen interaction was replaced by the modified set *miomod:nh* by Gaus et al[GCE11]. For the molecular dynamics simulations with DFTB$^+$ a (1x1x1) Monkhorst-Pack grid, a time step of 1 fs and a Nosé-Hoover

thermostat were used for the 15 ps MD simulations at 350 K. Since all simulations are done in a simulation cell filled with bulk water, the considered interactions are dominated by their electrostatic component. Therefore all simulations are done without any added van der Waals corrections.

The slab model of the $(1\bar{0}10)$ surface was generated by carving out of the optimized bulk structure (see 3.1.2) a (4x2) supercell with dimensions of (13.15x10.60) $Å^2$ in the periodically repeated (x,y) plane. In z direction the cell parameter was set to 24.79 Å to keep the slab separated from its periodic images by 15 Å. Subsequently a water monolayer was positioned on the slab surfaces. Starting point for this purpose were the DFT calculations of Meyer and co-workers [MRM06], which identified an equilibrium between dissociatively and molecular adsorbed water molecules. In DFT-based MD simulations prior to this work the introduction of bulk water to this system did not show an influence on the ratio of hydroxylation of the first water monolayer. The initial structures for the amino acids were relaxed in 2 ps MD runs of each single amino acid placed in a cubic box with edge-length of 15 Å filled with water molecules according to the standard water density. The relaxed amino acids were then placed in proximity of the ZnO $(10\bar{1}0)$, which was saturated with a water monolayer, while the simulation cell was filled with water molecules according to the standard water density.

4.1.2. DFT Adsorption Geometries

Different adsorption modes of each of the four selected amino acids are explored starting from the three different initial configurations depicted in figure 4.1. These differ in the mutual orientations of the amino acid backbone and sidechain with respect to the ZnO surface. Namely, in configuration (I) the backbone faces the surface; in configuration (II) the amino acid lies with both the sidechain and the backbone close to the surface; and in configuration (III) the sidechain faces the surface. Although the composition of the backbone is identical for all amino acids, the adsorption of the latter is explicitly taken into account for all amino acids to account for possible influences of the side chain.

Final snapshots of the trajectories of all four amino acids for the three initial configurations are depicted in figure 4.2. In the starting configuration (I) the amino acid backbone is positioned within the first water layer with both functional groups in proximity of the surface atoms. During the course of the MD runs (each lasting about 6 ps), often the amino acids move farther from the surface and remain anchored to the first water layer via a network of stable hydrogen bonds according to two main characteristic binding modes. In one mode, both the carboxylate and the amino group bind above the same row of adsorbed water molecules (see *e.g.* the final snapshot of glutamine in Fig. 4.2 a). In the second mode, the two backbone functional groups take a bridging position between two neighboring rows of adsorbed water (see Fig. 4.2 d), g) and j)). In this case the backbone is stabilized closer to the ZnO surface. These two modes do not seem to depend on the different sidechains. For instance, in an additional MD run starting with

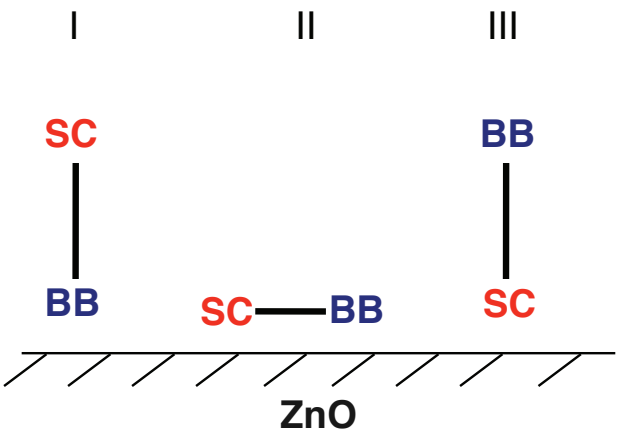

Figure 4.1.: Set up of the initial configurations for the analysis of different adsoption modes: backbone (I), backbone/sidechain (II), sidechain (III).

the same bridging adsorption mode spontaneously taken by glutamate, glutamine also remains stable therein.

Starting with the parallel adsorption configuration (II), in general hydrogen bonds form between both the sidechains or the backbones and the first water layer, keeping the amino acids flat above the surface. Which functional group remains closer to the surface appears to depend more on the instantaneous water structure at the beginning of the different simulations rather than on the amino acid type. Evident, however, is the tight H-bond (average length of 1.7 Å) that the OH sidechain group of serine form with the first water layer (figure 4.2 h)). Moreover, in the case of cysteine the H atom of the thiol group is transferred to a hydroxyl group of the first water layer after approximately 4 ps of simulation. Afterwards, the S atom remains bound to its former H atom via a tight hydrogen bond. In all other cases no stable proton transfer takes place between the amino acids and the surface, although in some cases H atoms involved in tight surface-molecule H-bonds occasionally switch back and forth between the donor and acceptor sites.

When starting with the amino acid sidechains pointing towards the surface in configuration (III), while most interactions again take place via H-bonding to the surface hydration layer, in some case ionic or H-bonds form directly with the surface. Direct H-bonds to surface O atoms involve for instance the NH_2 group of glutamine (Fig. 4.2 c) and the OH group of serine (Fig. 4.2 i). The carboxylate group of glutamate binds in a bidentate mononuclear configuration (via both oxygens) to a surface Zn atom, displacing a water molecule of the first hydration layer sideways (Fig. 4.2 f). The Zn-O bond length varies between 2.0 and 2.5 Å, being on average larger than the 2.0 Å Zn-O distance in bulk ZnO.

To investigate whether similar direct bonds to surface atoms can occur also with the amino acid backbone, two additional MD runs are performed with glutamine starting in configuration

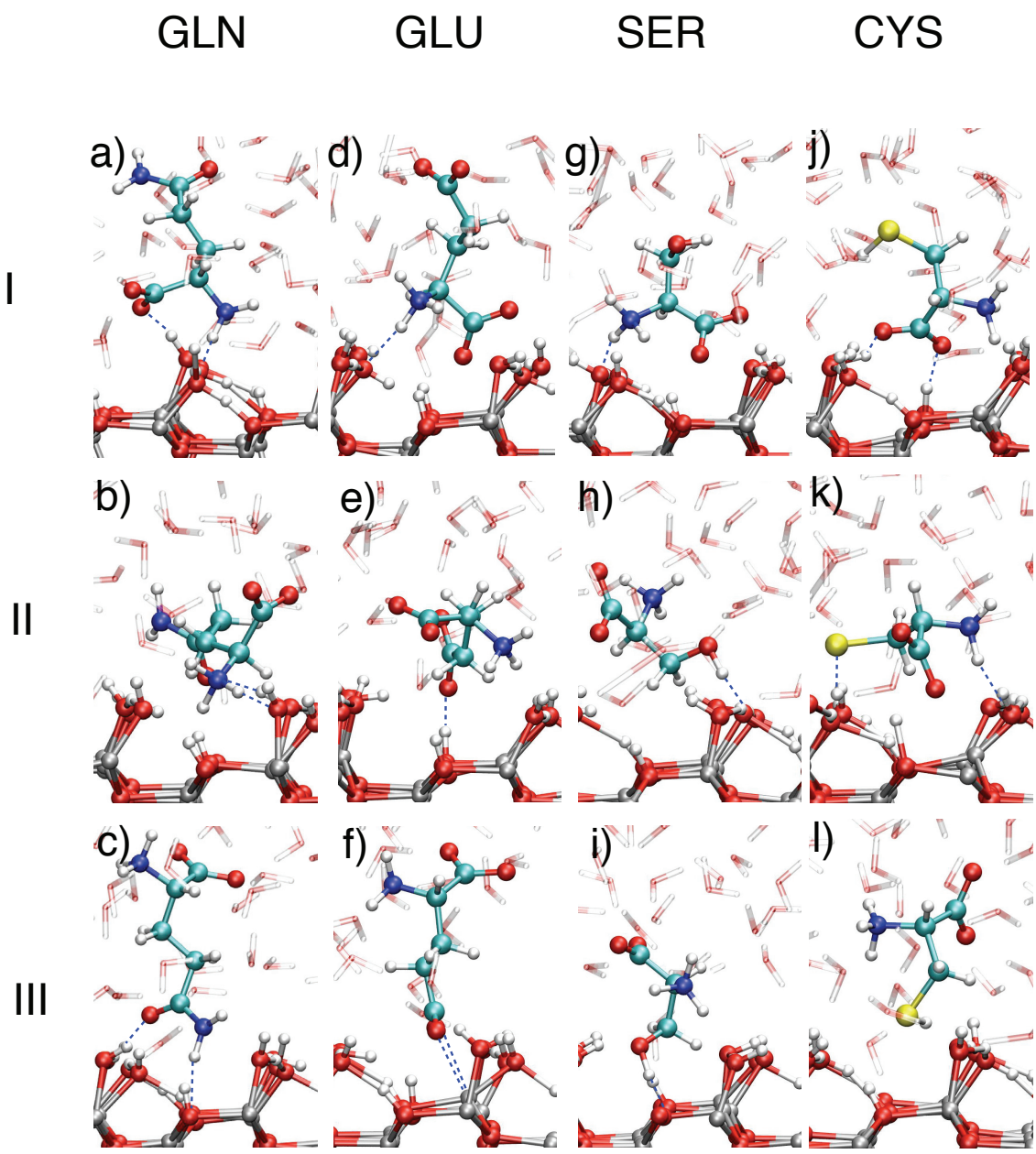

Figure 4.2.: Final snapshots of the adsorption configurations of glutamine (a-c), glutamate (d-f), serine (g-i) and cysteine (j-l) obtained in DFT-based MD runs starting with the configurations I (left), II (middle) and III (right), as defined in Fig. 4.1. Zn, O, H, C and N atoms are represented by grey, red, white, cyan and blue spheres, respectively. Bulk water is displayed by transparent dynamic bonds.

(I), in which either one or two neighboring water molecules are removed from the first surface hydration layer and placed in the liquid bulk. The obtained adsorption configurations are displayed in Fig. 4.3 a) and b). In the first case one O atom of the carboxylate group binds to a surface Zn atom with an average bond length of 2.0 Å. In the second case an H atom of the amino

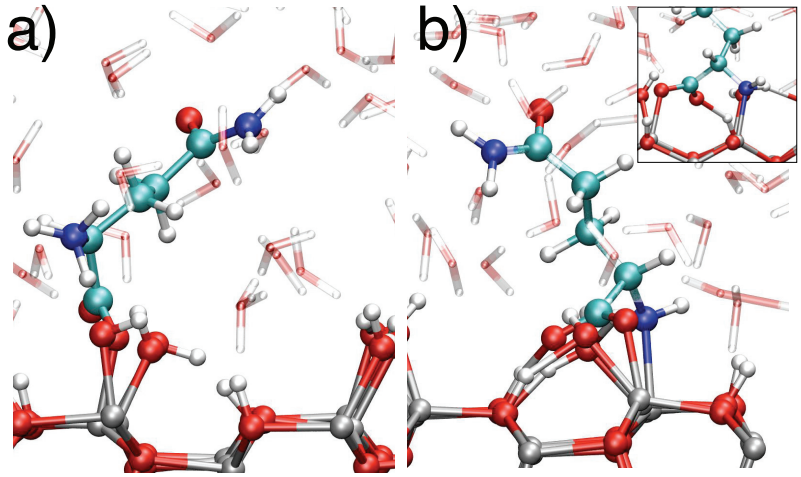

Figure 4.3.: Final snapshots of the adsorption configurations of glutamine obtained in DFT-based MD runs starting with configuration I after moving one (a) or two (b) water molecules from the first hydration layer into the water bulk. The insert shows an alternative side view of the system in b). The same color coding for the atoms as in Fig. 4.2 is applied.

group is transferred to a surface O atom while a direct Zn-N bond with average length of 2.1 Å is formed, and the second undercoordinated Zn atom becomes bound to one O atom of the carboxylate group (average Zn-O length of 2.0 Å).

Taking into account the obtained adsorption configurations for the four amino acids, it is striking that the adsorption onto the hydrated $(10\bar{1}0)$ surface is to a large extend dominated by the formation of hydrogen bonds to the first water layer.

4.1.3. DFT Adsorption Energies

In an attempt to evaluate the relative stabilities of the obtained adsorption geometries, the time evolution of the potential energies is analyzed in each of the MD runs. As a representative case, the energy evolutions of glutamine in the three different starting configurations as well as of a reference structure where the desorbed amino acid is placed in the bulk water between the surface slabs are displayed in Fig.4.4. For clarity of presentation, the zero-energy values are shifted by 3, 6 and 9 eV for the configurations I, II and III respectively, with respect to the non adsorbed case. Unfortunately, even after more than 6 ps of simulation (which is a relatively long time for the system sizes considered here with include nearly 400 atoms), no reliable convergence

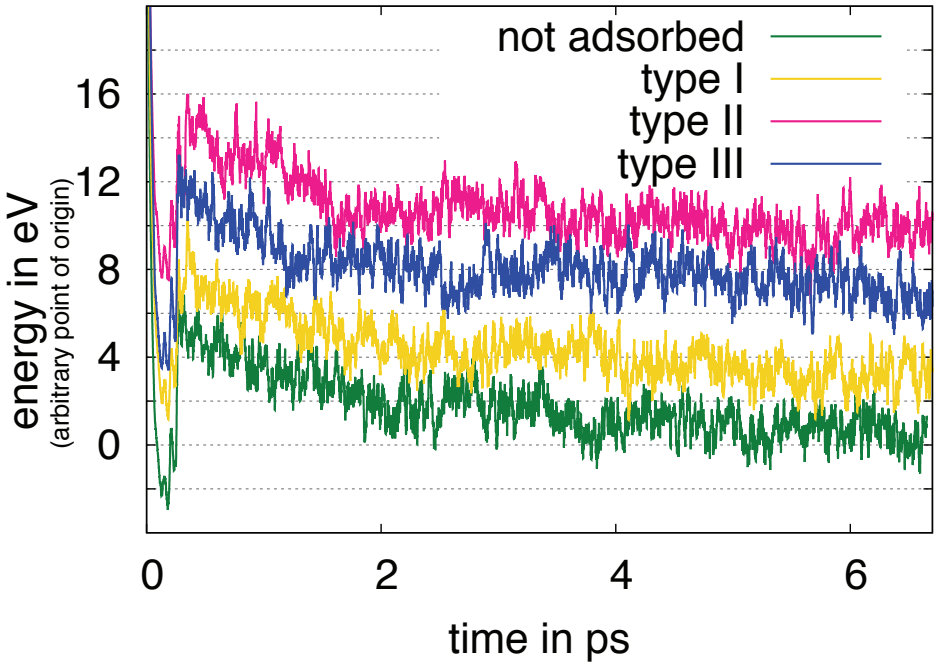

Figure 4.4.: Time evolution of the potential energy of glutamine in one non-adsorbed and three adsorbed configurations obtained from DFT-based MD runs. The zero-energy value is chosen arbitrarily for the non-adsorbed case and shifted by multiples of 3 eV for the other cases, for clarity.

of the potential energy could be reached. Moreover, fluctuations of the averaged potential energy of the order of 2 eV are observed, *i.e.* one order of magnitude larger than the relative energy differences. The situation is qualitatively the same for all amino acids investigated. This lead to the conclusion that, in order to compute reliable average potential energy values and draw a conclusion about the relative stabilities of the obtained adsorption geometries, much longer simulations than accessible by full DFT should be performed. This motivates the use of approximate methods such as DFTB for these ZnO/water/adsorbant systems, as presented in the next sections of this thesis.

4.1.4. Validation of the N-H DFTB Parametrization Set

It is known that the neutral form of glycine is stable in the gas phase, while the zwitterionic form is stable in the solid phase or in aqueous solution. This dependency on the surrounding environment is due to a stabilization of the zwitterion through H-bond formation. The neutral-to-zwitterionic transition has been extensively studied by DFT, obtaining results in agreement with experimental findings [TSRL00]. However, when computed with standard DFTB, the proton affinities of sp^3 N atoms are wrong by about 10 kcal/mol [BFS$^+$04, YYY$^+$07]. To correct for this error, in the

special DFTB parametrization set *miomod:nh* [GCE11] a constant shift of 10 kcal/mol to the N-H repulsive energy pair potential has been added. In order to verify the performance of this modified parametrization for the case of a single amino acid in aqueous solution an MD simulation of a single glycine in a 15 Å cubic cell filled with water molecules is performed. The transition of a hydrogen from the backbone amine group to the backbone carboxylate group is followed using metadynamics as implemented in the plumed plugin [BBB+09] [1]. The initial configuration for the two parametrization sets is chosen to be in the most stable state, *i.e.* zwitterionic for the *miomod:nh* set and neutral for the standard *mio:nh* set. Since the underlying intention is not the aim for exact values of the free energy barrier, only one collective variable, namely one N-H distance, is chosen to explore the free energy surface. The two free energy profiles obtained with the two parametrization sets are displayed in figure 4.5. The standard parametrization

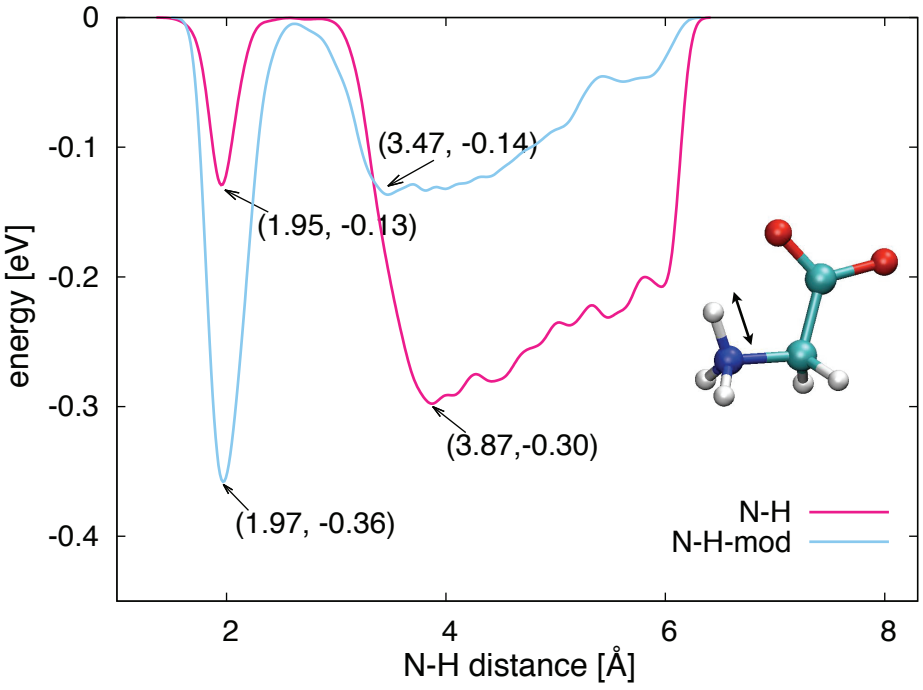

Figure 4.5.: Free energy profiles of the tautomerization process of glycine (neutral-to-zwitterion transition) in liquid water obtained using the *mio:nh* and *miomod:nh* parametrizations of the N-H interaction.

predicts a broad minimum of the free energy at a N-H distance of about 4 Å. Analysis of the trajectory yields that this N-H distance corresponds to the neutral glycine form. A 0.17 eV higher local minimum at a distance of about 2 Å of the *mio:nh* curve therefore corresponds to the zwitterionic form. The barrier for escaping the local minimum and reach the neutral state

[1] A very nice review of the principles behind metadynamics can be found in [LG08]

is about 0.13 eV. This implies that zwitterionic glycine will not be stable in liquid water and wrongly convert to the neutral form when performing DFTB simulations using the *mio:nh* set. In contrast, the *miomod:nh* set correctly predicts a free energy curve with a global minimum at a N-H distance of about 2 Å, corresponding to the zwitterionic form, and a 0.22 eV higher local minimum corresponding to the neutral form. This reaction free energy agrees with previous calculations of Tuñón et al. [TSRL00] for the transition between the zwitterionic state and one intermediate neutral conformation in which the hydrogen of the carboxylate group is aligned with the amine group. Since all the amino acids considered in this work are solvated in bulk water, they all exhibit the zwitterionic form. Therefore the results presented here for the zwitterionic form of glycine apply to all four amino acids examined.

4.1.5. DFTB Simulations of Amino Acid Adsorption

Molecular dynamics simulations for the four amino acids are performed using the DFTB+ code starting from geometries analogous to the one used in the DFT simulations. Analysis of the obtained data shows that, if the amino group of the backbone resides close to the first water layer, a transfer of H atoms from the backbone amino groups to hydroxyl groups of the first surface hydration layer is observed. This transfer is followed by the desorption of the newly formed water molecule making room for the carboxylic group of the backbone and resulting in stable direct bonds to the surface. However, this behavior was never observed in any of the performed DFT simulations, unless the surface was forcedly undercoordinated *a priori* (see figure 4.3). In fact, in test MD simulations performed with DFT starting from snapshots of the DFTB trajectories just after the H transfer, the H atom moves back to the backbone amino group. Therefore even though a temporal transfer of hydrogen is observed using DFT (*e.g.* in the case of cysteine type I), a permanent separation of the hydrogen from the backbone amino group is never observed. DFTB thus seems to wrongly promote the H transfer reaction despite the use of the modified *miomod:nh* parameter set for N-H interactions. Therefore, to hinder the H transfer, artificial distance constraints are set on all three N-H bonds of the backbone amino group.

Adsorption Geometries: Comparison between DFT and DFTB

Applying this constraint, the results of the DFTB MD runs (15 ps), as far as the obtained adsorption geometries are concerned, are very similar to the ones obtained with full DFT. Namely, the surface adsorption is mediated by the first surface hydration layer via a more or less developed network of H bonds, depending on the chosen starting configurations. The different adsorption modes obtained for glutamine are displayed in the rightmost column in Fig. 4.6.

A more detailed analysis of the adsorption modes is obtained by comparing the time evolutions of the positions of the functional groups obtained in the DFTB and DFT simulations, as reported

in the first two columns Fig. 4.6 for the case of glutamine. Comparison of the results reveals characteristic features of the adsorption modes common to both DFT and DFTB emerging from this analysis. The adsorption via the backbone (Fig.4.6 a) is mediated by H-bonds to one of the O atoms and the N atom. Both atoms remain stable at about 3 Å above the surface. However, towards the end of the longer DFTB trajectory, at about 12 ps, the H-bond to the oxygen is unlinked. Starting from the initial configuration (II), adsorption takes place through the backbone N atom and the sidechain O atom, at heights between 3 and 4 Å above the surface (Fig. 4.6 b). In configuration III the sidechain group also forms indirect H bonds to the surface. Nonetheless, these bonds are in general longer and less stable in the DFTB simulation, at the end of which the amino acid actually desorbs from the surface (Fig. 4.6 c). A good agreement between DFT and DFTB results is also found for the two configurations with the incomplete first water layer. Starting with one water molecule removed from the hydration layer leads to identical adsorption modes in the DFT and DFTB calculations (Fig. 4.6 d). Although the decrease of the distance of one backbone O atom at about 6 ps suggests a bidentate binding mode in DFTB, this cannot be confirmed by the analysis of the trajectory. Rather this drop in distance is due to a H-bond formation to a surface hydroxyl group. Finally, starting with two water molecules removed from the hydration layer both DFT and DFTB predicts the formation of direct Zn-N bonds and of at least one Zn-O bond to the backbone carboxylate group. Only in the DFTB simulation, the second O atom points away from the surface, while the sidechain bends towards the surface and forms an additional H bond to the water layer (Fig. 4.6 e) .

Glutamate with its two carboxylic groups constitutes theoretically a good binding partner for the hydrated $(10\bar{1}0)$ surface. Analysis of the time evolution of the distance of the functional groups above the surface (see figure 4.7) shows that for configuration I both DFT and DFTB predict a mono dentate (only one oxygen involved) bond formation between the backbone carboxylic group and a surface zinc. For configuration II the adsorption mode obtained by DFTB calculations differs from the final DFT result, however this is due to the longer simulations performed with DFTB, as the glutamate changes its surface orientation after 10 ps of simulation time. Although the adsorption configuration type III for glutamate looks identical comparing DFT and DFTB results, there is a significant distinction between the two due to the behavior of the first water layer. While in the DFT trajectory, the water molecule close to the adsorption site of the side chain carboxylic group is just slightly delocated, it desorbed in the case of DFTB. The path of desorption can thereby be described as follows. In the initial configuration one oxygen of the side chain is positioned closely to a hydroxylated surface zinc atom. Subsequent to a transfer of one hydrogen from a neighboring water molecule, this newly formed water desorbs from the surface. This desorption occurs within the first few picoseconds of the DFTB simulation. Since the surface zinc atom constitutes a completely free binding site in DFTB, the binding characteristics of the side chain to the surface in DFTB and DFT differ.

In the case of serine the DFT results for the backbone adsorption resembled previous DFT

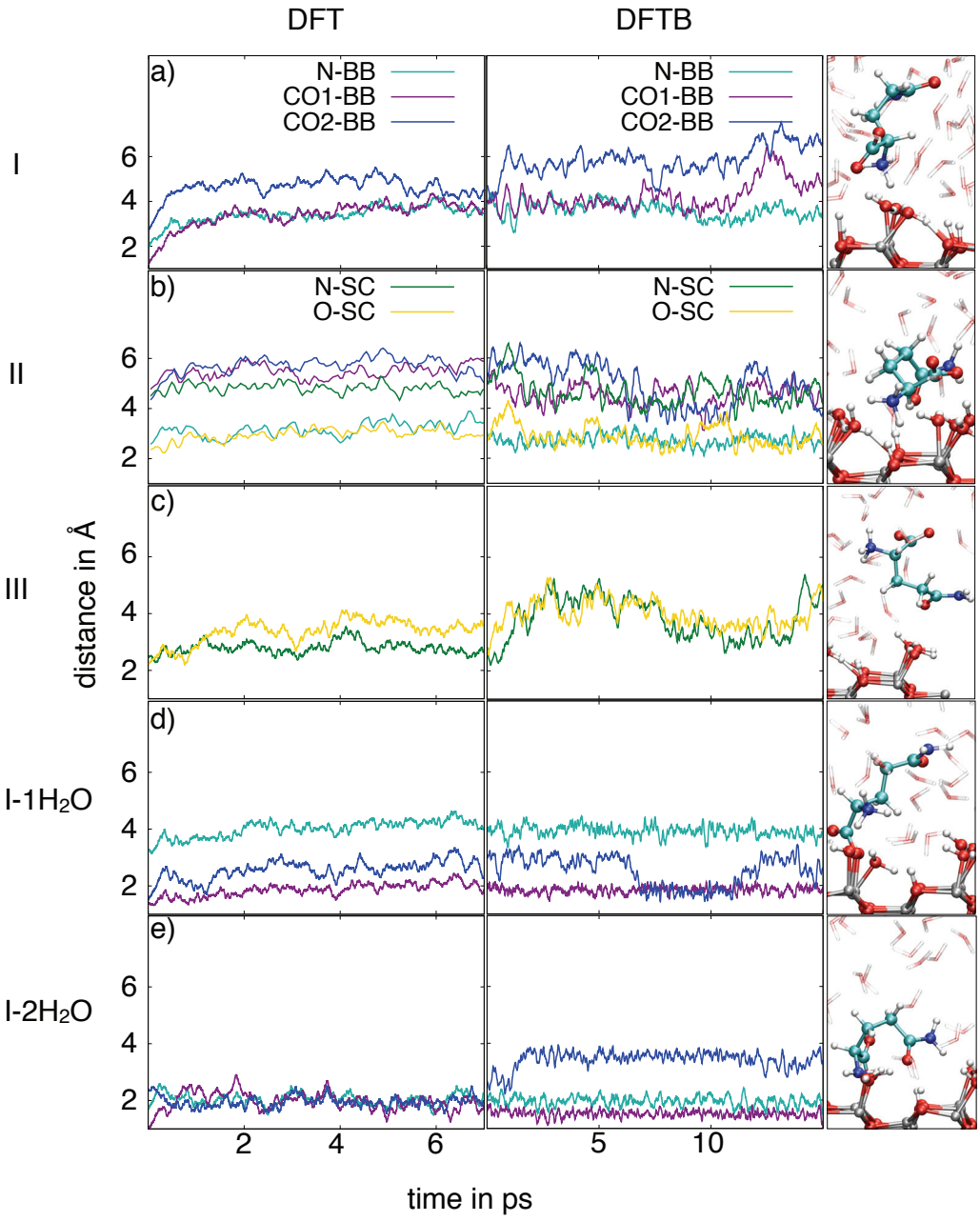

Figure 4.6.: Comparison of the height of the functional groups above the surface in Å during the performed MD runs for glutamine for the initial configurations: type I (a), type II (b), type III (c), type I one water removed (d) and type II two water removed (e). The rightmost column depicts the final snapshots of the corresponding DFTB trajectories.

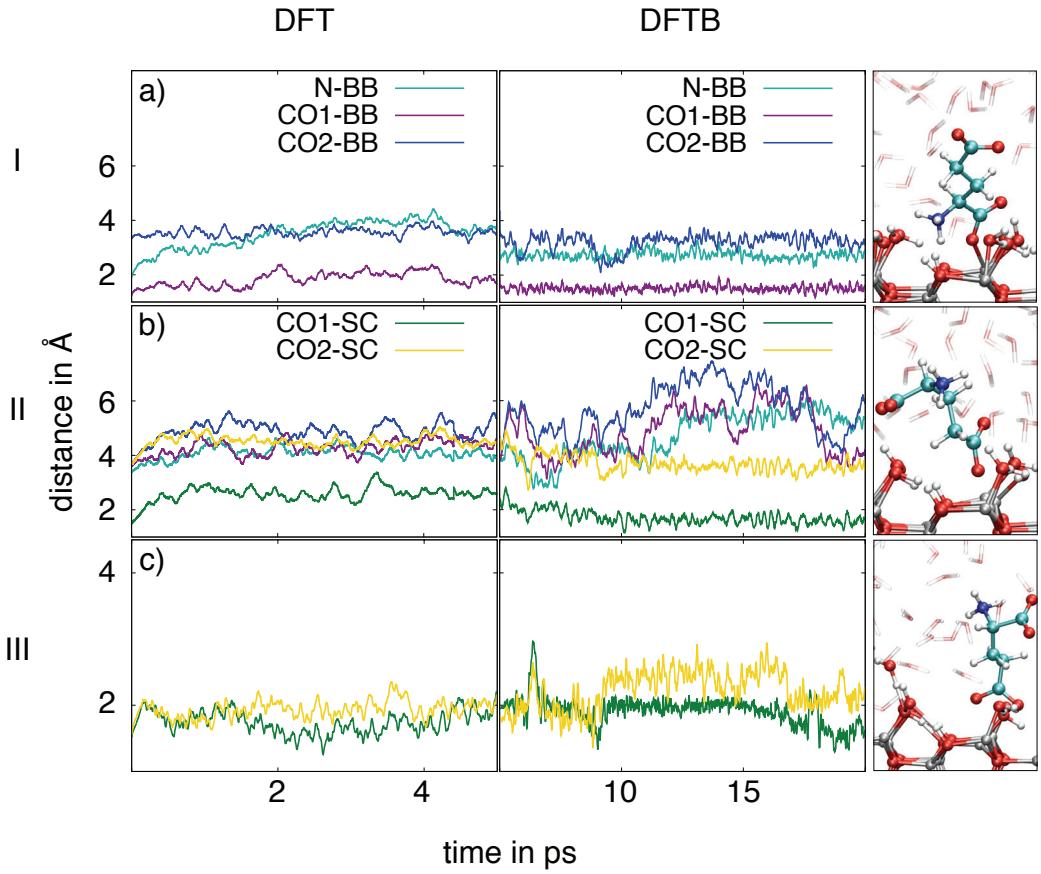

Figure 4.7.: Comparison of the height of the functional groups above the surface in Å during the performed MD runs for glutamate for the initial configurations: type I (a), type II (b), type III I'. The zero point is chosen according to the initial positions of the zinc atoms of the uppermost surface dimers. The rightmost column depicts the final snapshots of the corresponding DFTB trajectories.

results as depicted in figure 4.8. For configuration II and III the H-bonds formed between the side chain and the surface are less stable in DFTB compared to DFT calculations. In the case of configuration II this results in a desorption of serine from the surface. However this occurs after about 5 ps of simulation time and therefore does not conflict with the DFT results.

Like for DFT, DFTB results of cysteine show that in the case when its side chain is close to the first water layer (configuration II&III) the hydrogen of the thiol group is transferred to the surface/first water layer(see figure 4.9). In the longer DFTB simulations, however, cysteine may also desorb from the surface after the H transfer has taken place (configuration III). For configuration I and II in DFTB the adsorption of cysteine is dominated by direct bonds between the backbone carboxylic group and a surface zinc atom.

Altogether, despite the small differences highlighted above for the case of the four amino

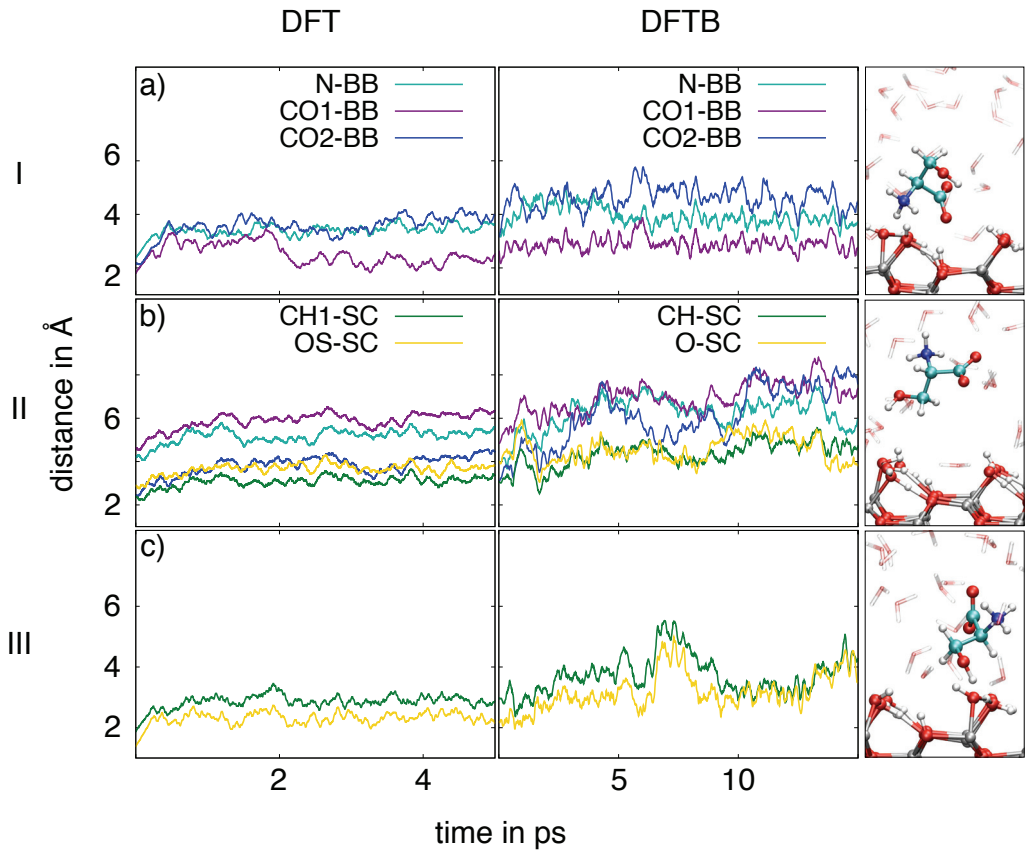

Figure 4.8.: Comparison of the height of the functional groups above the surface in Å during the performed MD runs for serine for the initial configurations: type I (a), type II (b), type III I'. The zero point is chosen according to the initial positions of the zinc atoms of the uppermost surface dimers. The rightmost column depicts the final snapshots of the corresponding DFTB trajectories.

acids, the overall trends in the adsorption of the individual atoms belonging to the various functional group of all investigated amino acids show a very good agreement between the DFT and the DFTB simulations . By comparing the DFTB with the DFT trajectories, a slightly more pronounced tendency of DFTB to form direct ionic or H-bonds with the surface is observed (compare *e.g.* cystein configuration I&II and glutamate configuration III). Moreover, differently from the DFT case, this direct adsorption is sometimes accompanied by the desorption of water molecules, less strongly bound to the surface in the DFTB case. Notably the adsorption geometries from DFT and DFTB stress that the composition and configuration of the first strongly adsorbed water layer plays an important role in the formation of contact points between amino acid constituents and the surface. For TiO_2 a pH-dependent affinity of the basic amino acids residues of peptides was already demonstrated [SS03]. For the four amino acids considered in this work surface protons as well as surface hydroxyls are found to participate in the adsorption

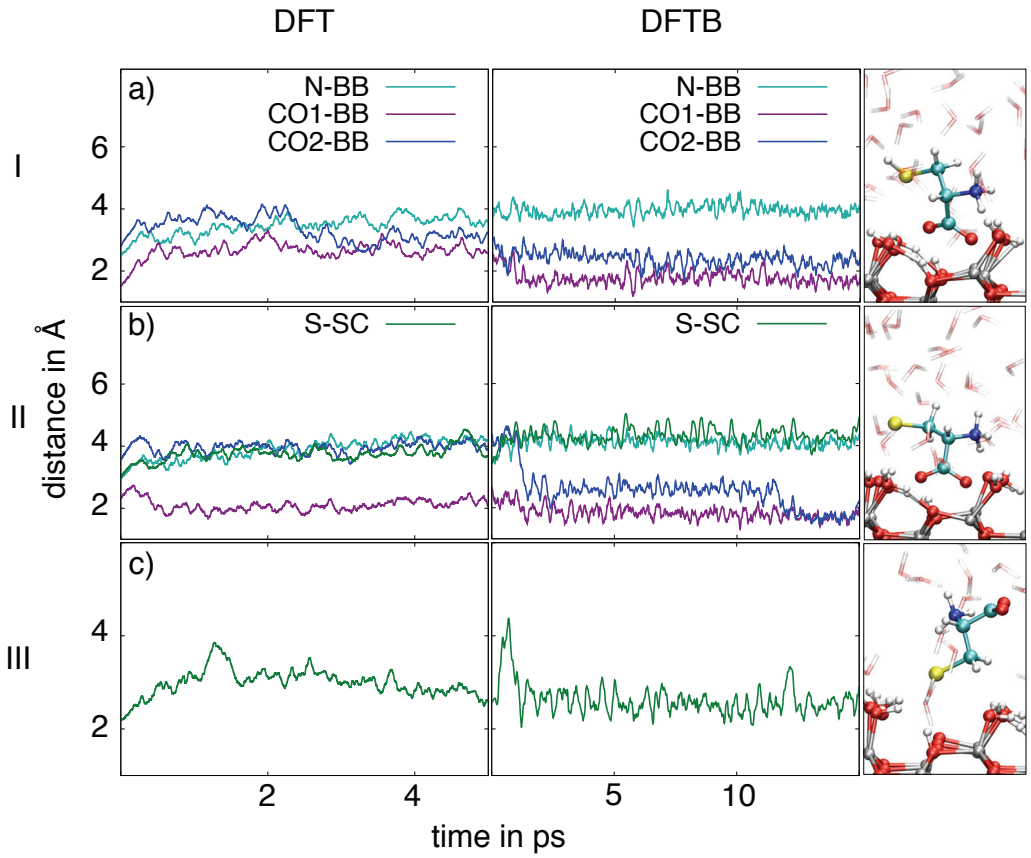

Figure 4.9.: Comparison of the height of the functional groups above the surface in Å during the performed MD runs for cysteine for the initial configurations: type I (a), type II (b), type III I'. The zero point is chosen according to the initial positions of the zinc atoms of the uppermost surface dimers. The rightmost column depicts the final snapshots of the corresponding DFTB trajectories.

process depending on the approaching amino acids. Moreover a systematic approach taking into account various kinds of amino acids (polar/charged side chain) on the ZnO $(10\bar{1}0)$ surface displaying different states of surface protonation and accordingly hydroxylation would be necessary to account for the effect of surface charge on the adsorption behavior (see chapter 5.3).

Water Densities

Similarly good agreement is found by comparing the profiles of water density obtained in the DFT and DFTB MD runs, as reported in Fig. 4.10 for the case of glutamine. The density profiles show a distinct first peak at about 1.9 Å accounting for the first surface hydration layer, and a smaller peak at about 2.4 Å . This second hydration layer stems from water molecules H-bonded to the first water layer, and is also found in simulations of pure water in contact

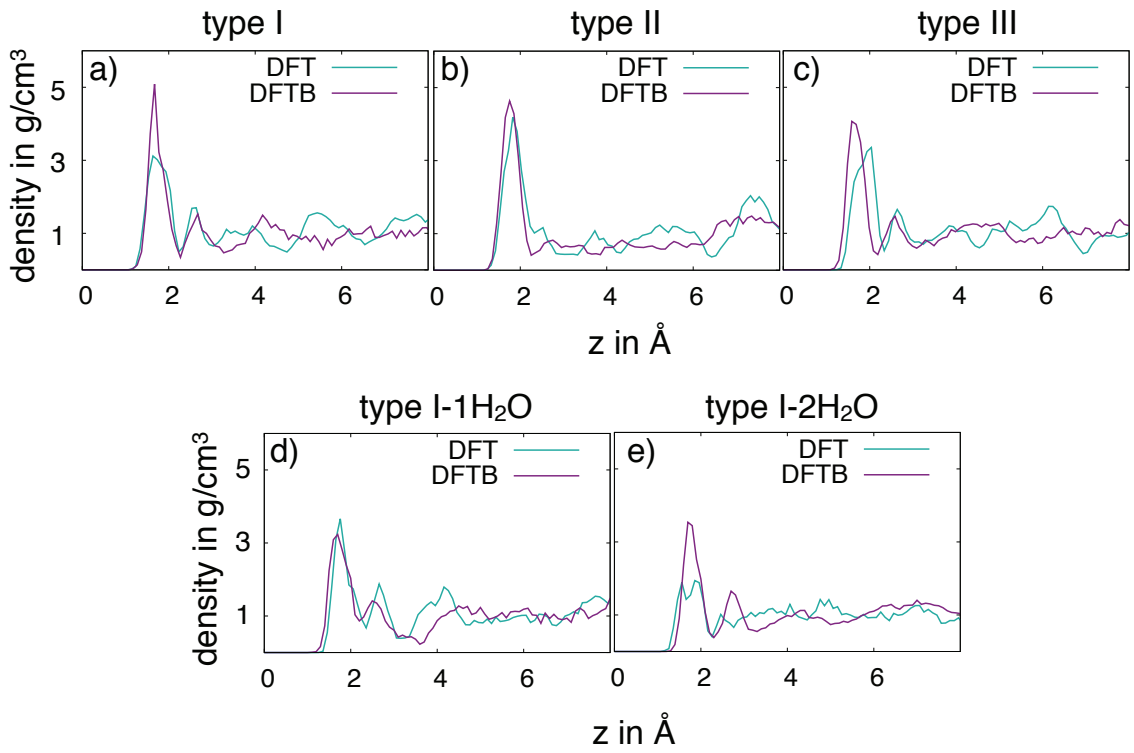

Figure 4.10.: Density of water perpendicular to the ZnO surface plane for glutamine for the initial configurations: type I (a), type II (b), type III (c), type I one water removed (d) type I two water removed (e). The zero point of the distance is chosen according to the initial positions of the zinc atoms of the uppermost surface dimers.

with the (10-10) surface, but is absent in the case of ZnO(1-210)/water interfaces [HKFCC12]. Note that in the simulation of glutamine starting in the configuration (II) the peak is also absent, because the amino acids lies flat above the first hydration layer, effectively replacing all water molecules of the second layer in the relatively small unit cell employed. For larger distances, the water approaches the liquid density of 1 g/cm^3 for all five model systems, suggesting that the employed cell sizes are large enough to mimic bulk water.

4.1.6. DFTB Adsorption Energies

The longer simulations times achieved using DFTB make an analysis of the adsorption energies associated with the different binding modes of the amino acids possible. To this aim, for each amino acid a 30 ps long reference simulation with the molecule dissolved in the water bulk between the two surface slab is performed. The distribution of all obtained potential energy values over the last 20 ps of this simulation is then fitted with a Gaussian function, as depicted in figure 4.11 a) The position of the Gaussian maximum is taken as the reference zero value to compute the adsorption energies of the different binding modes. The time evolution of

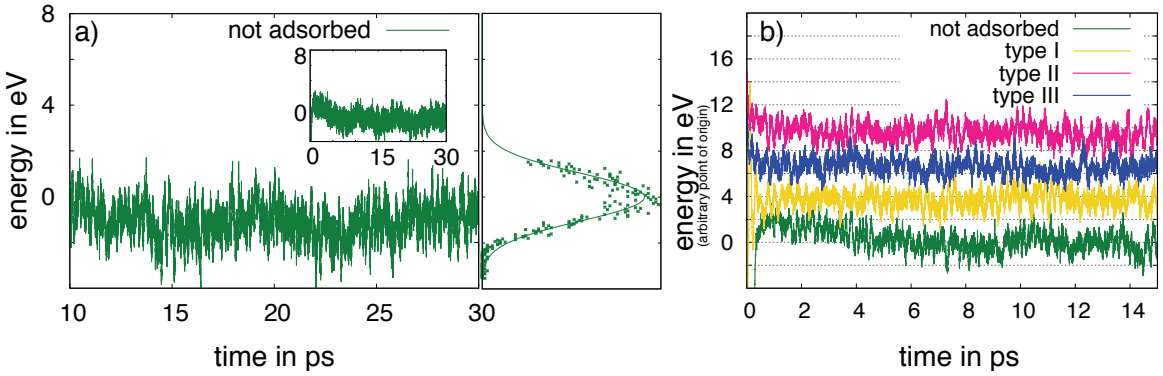

Figure 4.11.: Time evolution (a) of the energy for glutamine dissolved in the water bulk between the two surface slabs for simulation times between 10 and 30 ps. The inset depicts the complete time evolution for the MD run. In the rightmost part of a) the fit of the Gaussian function (line) is shown based on the distribution of energy (points). In b) the time evolution of the energy for glutamine simulated with DFTB for the initial configurations: type I (a), type II (b) and type III. The zero-energy value is chosen arbitrarily for the non-adsorbed case and shifted by multiples of 3 eV for the other cases, for clarity.

the potential energies calculated with DFTB for the glutamine binding modes are displayed in Fig. 4.11 b). It can be seen that reasonable convergence of the potential energy is reached after about 7 ps. Average potential energies for each binding mode are computed by Gaussian fits of the distribution of energy values within the last 5 ps of simulations lasting 15 ps. The distributions for all four amino acids together with their Gaussian fits are depicted in Fig. 4.12 for all cases where a stable adsorption configuration is found. The computed binding energies (the differences between the Gaussian maxima in the adsorbed and desorbed cases) are reported in Table 4.1. As a general trend, it is intriguing to observe that the binding energy for type I and type II adsorption modes are the same for all amino acids, except for serine, which desorbed from the surface in the simulation corresponding to mode II. For these two adsorption modes, similar adsorption energies result from similar hydrogen bonding patterns between the molecule and the first hydration layer of the surface. Glutamine interacts in either mode through two hydrogen bonds involving one amino and one carboxylate group, respectively (see Fig. 6 a and b), leading to a binding energy of -0,7 eV. Similarly, both in mode I and in mode II glutamate binds to the surface via a direct Zn-O bond and a further hydrogen bond, while cysteine form H-bonds via the two functional groups of its backbone (see figures 4.7 and 4.9).

However, neither the differences between the adsorption energy values of different amino acids nor other binding energy values (e.g. corresponding to adsorption mode III) can be always explained just by looking at the type and number of surface-molecule bonds. For instance, the sidechain binding mode of serine is characterized by a single hydrogen bond to the first surface

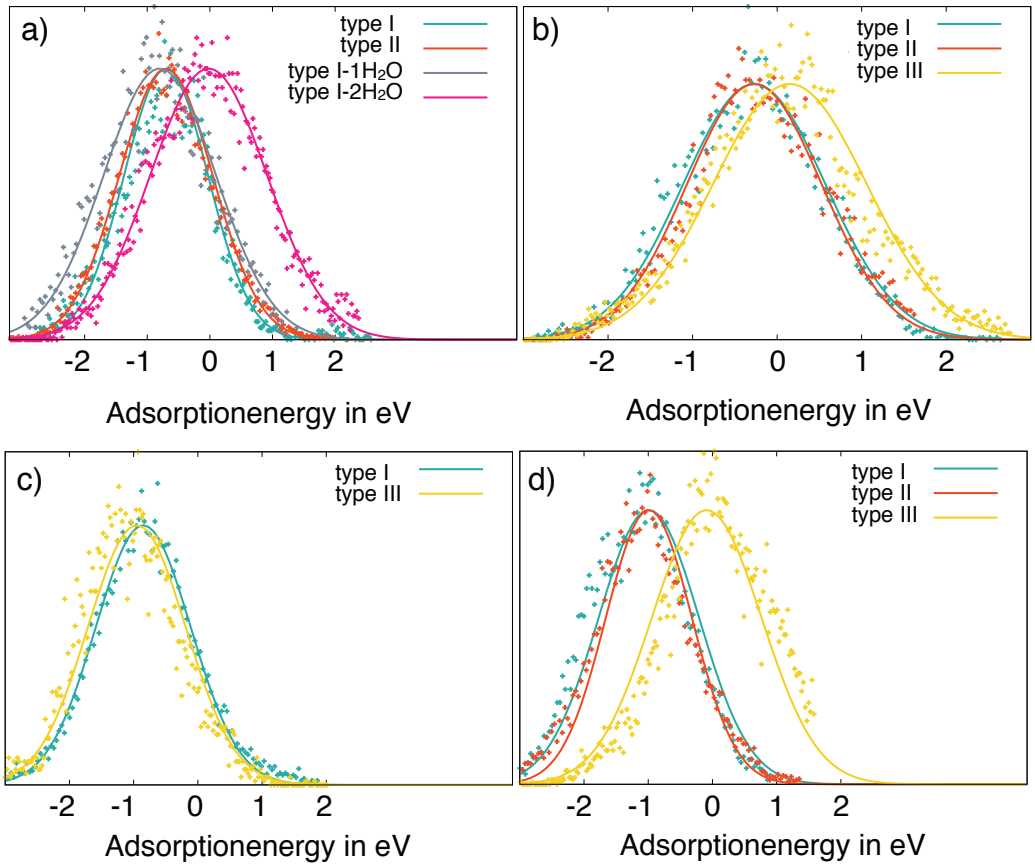

Figure 4.12.: Distribution of converged energies from DFTB calculation for the adsorption of glutamine (a), glutamate (b), serine (c) and cysteine (d). The Gaussian maximum of the corresponding desorbed case is taken as the zero point energy.

hydration layer, yet the binding energy value is even higher (-0.95) than in mode I (-0.85), where two surface-molecule H-bonds are formed. Moreover, for the case of glutamate the side-chain adsorption is accompanied by a detachment of a water molecule from the surface induced by the insertion of the carboxylic group into the first hydration layer, leading to an overall unfavorable binding energy (+0.15 eV). In contrast, a similar process taking place for the case of glutamine (mode BB 1 H_2O) leads to strongly favorable adsorption (-0.8 eV). Finally, for the case of cysteine, it is difficult to understand why the binding energy of the sidechain adsorption mode III is so low (-0.09 eV) even if a seemingly stable bond occurs after proton transfer from the thiol group to the surface (see figure 4.9). One can therefore conclude that along with the number and type of surface-molecule hydrogen bonds, it is also the local perturbation of the hydrogen bonding network in surface proximity that governs the energy of adsorption in a often non-intuitive and unpredictable way. A good example in this respect is the BB 2 H_2O adsorption mode of glutamine, in which strong direct surface-molecule bonds are induced by forcing the

Table 4.1.: Maxima of the distribution of converged energies in eV from DFTB calculations for glutamine, glutamate, serine and cysteine

	type I	type II	type III	BB 1 H_2O	BB 2 H_2O
Gln	-0.70	-0.70	-	-0.8	-0.02
Glu	-0.27	-0.27	0.15		
Ser	-0.85	-	-0.95		
Cys	-0.99	-0.99	-0.09		

substitution of two surface-bound water molecule with the functional group of the molecule (see figure 4.6). The resulting adsorption geometry, despite the strong surface-molecule bonds, is favored by only 0.02 eV compared to the desorbed state, as a consequence of the almost equally strong perturbation within the first water layer.

4.1.7. Comparison between DFTB and DFT adsorption energy

In contrast to the analysis of the adsorption geometry, comparing the adsorption energy calculated with DFT or DFTB is not straightforward due to the very slow convergence of the total energy with the simulation time, as already pointed out above. In order to allow at least a paraphrased comparison a comparative analysis of single-point energy values using selected adsorption geometries stemming from the DFTB molecular dynamics simulations and subsequent relaxation of the whole system is performed[2]. Namely, for the case of glutamine (neutral and polar side chain) and glutamate (negatively charged side chain) the energy of individual snapshots corresponding to the same desorbed reference state and various adsorbed states is computed using both with DFT and with DFTB. The resulting energy differences (desorbed minus adsorbed) are reported in Table 4.2.

For the case of glutamine, the two methods lead to trends that are not too dissimilar, although not always consistent. Notable is the strong underestimation of 1.27 eV of the binding energy of mode I at the DFTB level. However, for the case of glutamate, the computed energy clearly disagree. Similar results are obtained using snapshots geometries originating from DFT simulations (not reported in the table to avoid redundancy). A source of discrepancy may be due to the known tendency of DFTB to overestimate the hydrogen bond strength in liquid water [MAV10][GCE11]. Therefore it is very well possible that only inconsistencies in the bulk water configuration lead to the diverse results. Hence, in order to reduce the influence of the water description in the evaluation of the energies DFTB and DFT snapshots excluding all bulk water molecules except for the first surface hydration layer (systems BB-mono in Table 4.2) are also

[2]Identical calculations were performed using final structures obtained from DFT runs

Table 4.2.: Energy differences calculated with DFT and DFTB for selected relaxed non-adsorbed and adsorbed structures of glutamine and glutamate.

Ad.-Config.	Glutamine		Glutamate	
	ΔE_{DFT}	ΔE_{DFTB}	ΔE_{DFT}	ΔE_{DFTB}
type I	1.52	0.25	-0.92	0.64
type II	1.11	0.80	-1.54	0.24
type III	0.98	0.76	0.20	0.24
BB $1H_2O$	0.10	0.19	-	-
BB 2 H_2O	0.05	0.32	-	-
BB-mono-DFTB	1.04	1.48	-0.20	-1.73
BB-mono-DFT	1.72	2.11	-4.08	-5.65

taken into account. In these cases, DFTB energy differences points to consistent overbinding compared to DFT results. Independently of the origin of the investigated snapshots (DFTB or DFT MD simulations), the difference between DFT and DFTB results is approximately 0.4 eV for glutamine and 1.5 eV for glutamate.

The poor performance of DFTB in reproducing the DFT values for the case of glutamate might originate from the difficulty of the self-consistent-charge formalism to deal with molecules with a net charge. Despite these inconsistencies in terms of single-point energy values, the comparison between the adsorption geometries at the DFTB and DFT value is all in all very good. It remains an open question whether the discrepancies in terms of energy would be reduced when considering DFT energy averages from long enough MD simulations (which would represent a very large computational effort, as remarked above).

4.1.8. Adsorption Behavior of Glutamate at a Surface Kink on ZnO $(10\bar{1}0)$

The results so far on the adsorption of single amino acids on the ZnO $(10\bar{1}0)$ surface have shown that the interactions are dominated by hydrogen bonds between the amino acids and the first strongly adsorbed water layer. Still results by Xia et al. [XKL$^+$08] and Gerischer et al. [GS92] suggest that reactions occur at the ZnO/liquid/bio interface which lead to an enhanced solubility of ZnO. In chapter 3.4, the presumable starting points of the dissolution process, kink defects

at the surface, have already been shortly introduced. The results obtained for the adsorption of bulk water at these kink sites is now used to go one step further, by analyzing the adsorption behavior of glutamate at one of the discussed kink sites (only the oxygen kink site is considered in this work). Glutamate was chosen for these simulations, since it features a negatively charged side chain composed of a carboxylic group. Calculations using the perfect surface have already proven that this side chain shows a distinct affinity towards zinc surface atoms. The geometry of the carboxylic group is additionally a presumable good ligand to form a chelating complex with surface zinc atoms of the kink site.

Computational Methods and Model Systems

Since the results regarding adsorption geometries showed a good agreement between DFTB and DFT results, DFTB was chosen to simulate these rather large systems comprising over 500 atoms[3]. The DFTB calculations are performed with the DFTB$^+$ code [AHF07], using the tight-binding parameter set *znorg* introduced in ref. [MDA$^+$09]. The nitrogen-hydrogen interaction was replaced by the modified set *miomod:nh* by Gaus et al[GCE11] and the N-H bonds were constrained. To improve the performance of DFTB a γ-correction factor as introduced by Elstner and coworkers [Els07] is used in calculations to improve the polarization of hydrogen bonded complexes. The geometry optimizations at the DFTB level are performed using the conjugate gradient method on a $(1\times1\times1)$ Monkhorst-Pack grid for the k-point sampling, using a force error tolerance of 10^{-6} eV/Å. In the MD simulations only the Γ point is included and a Nosé-Hoover thermostat with an integration time step of 1 fs is applied, generating a NVT ensemble at 350K.

The hydrated slab comprising two surface kinks was taken from the calculations reported in chapter 3.4. Therefore the bulk water present in the system was deleted, apart from the water molecules close (within 2.5 Å) or bound to the surface. The glutamate configuration was obtained from the protein data bank and relaxed in bulk water for 5 ps prior to the adsorption simulation.

Adsorption Geometries

The glutamate is positioned in two different initial configuration differing in the orientation of the backbone and sidechain above the oxygen surface kink (compare type I and type III in figure 4.1). For each initial configuration the geometries are relaxed prior to the 8 ps MD run. A final snapshot of the trajectory for the initial configuration type III is shown in figures 4.13 a) and b). Already during the relaxation calculation the water molecule bound to the surface zinc closest to the oxygen kink desorbs making room for one oxygen of the carboxylate group of the side chain. This desorption process agrees with results obtained for the interaction between

[3]The parametrization of the reactive forcefield does not include the interaction with bio-molecules.

glutamate and the perfect surface using DFTB, since a displacement of adsorbed water molecules was also observed in the proximity of the glutamate side chain. The formed Zn-O bond has a

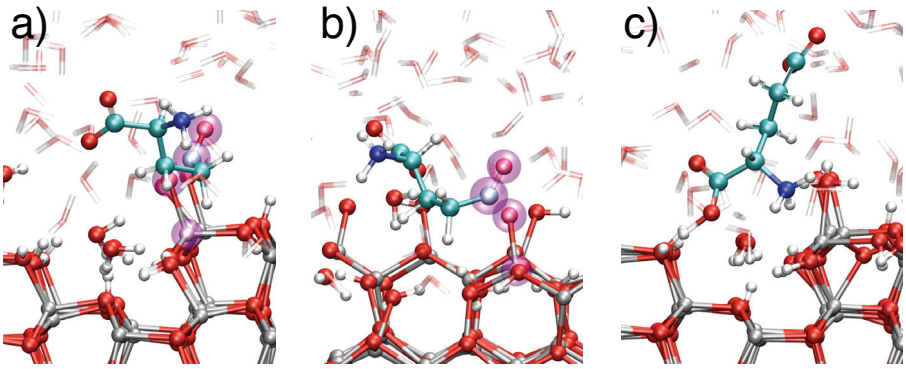

Figure 4.13.: Snapshots taken after 8 ps of simulation time for the initial configuration type III (a) and (b) and the initial configuration type I (c). The pink spheres in figures (a) and (b) mark the position of the side chain atoms and the zinc atom at the kink.

length of approximately 2.1 Å. The observed adsorption mode between carboxylate group and zinc is mononuclear mono dentate, and does not even change temporally during the calculated simulation time. That means a mononuclear bidentate adsorption, found for the adsorption at the clean surface, is not found to develop. The formation of a complex between the carboxylate group and the surface zinc is therefore seen in this analyzed trajectory.

The backbone adsorption at the kink site is dominated by a hydrogen bond to a neighboring row of dissociated water molecules (see figure 4.13 c). Although the glutamate backbone is positioned close to the kink site at the beginning of the relaxation run, no interaction between kink site atoms and the backbone is being observed. Consequently the water configurations close to the kink remain unchanged. Nevertheless the hydrogen bond formed between one oxygen of the carboxylate group and a hydrogen of an adsorbed water after 6 ps stabilizes the glutamate in a bridging position close to the oxygen kink.

4.2. Adsorption of a Specific Binder Motif RQIRK on ZnO (10$\bar{1}$0)

The results of the DFTB adsorption geometries obtained in the previous chapter are a motivation to use DFTB in systems not addressable by *ab-initio* DFT. Thereby the simulation of proteins that constitute a specific binder for ZnO (see chapter 1.1) embody an appropriate model-system being a very prevailing field of interest [STB$^+$03]. Since the variety of studies focusing on specific binding proteins of ZnO all arrive at different results (compare e.g. [HYY$^+$08, KSK01, LDPP11, UMT$^+$05]), that means different binding motifs, one one of these studies is picked as

a motivation and reference for the simulation performed in this part of the thesis[4]. Hence in this section the DFTB formalism is used to investigate the adsorption geometry of a pentapeptide with the sequence Arg-Gln-Ile-Arg-Lys[5] (RQIRK)[6] on the ZnO($10\bar{1}0$) surface, since this system contains the Arg-X-X-Arg-Lys (RXXRK) motif that has been found in many specific ZnO-binding peptides by Thai and co-workers [TDS+04].

Method, Slab Model and Calculation Protocols

The calculations were conducted using the DFTB+ code [AHF07]. A set-up identical to the one for the calculations of the glutamate adsorption on a surface kink was applied. Again the H-N bonds were constrained. For the molecular dynamics simulations a (1x1x1) Monkhorst-Pack grid, a time step of 1 fs and a Nosé-Hoover thermostat were used.

The peptide was assembled using the Amber package [AMB]. After relaxation of the peptide structure in a (25x25x25) $Å^3$ cell filled with only water molecules, the system is placed near the ZnO surface using a cell size of (26.30x21.21x22) $Å^3$ and the empty space between the surface slab and its periodic image is filled with water molecules. This results in a system comprised of 1206 atoms, whose dynamical evolution is followed during 6 ps of MD simulation at 350 K. Performing MD studies of such a large system at the full quantum mechanical level is very costly, and even for the DFTB+ code the system size allows only a relatively short relaxation of the system.

Evaluation of Contact Points

The final snapshot of the simulation is depicted in figure 4.14(a). As in the case of single amino acids, the interaction between the peptide and the surface is dominated by hydrogen bonds to the first water layer. The surface contact points are marked with pink spheres in Fig. 4.14(a). In addition, direct interactions between the terminal carboxylate group and surface zinc atoms are also established within the first two picoseconds of simulation (marked by yellow spheres). The positions of the heavy atoms (N, O) of each side chain above the ZnO surface are displayed in Fig. 4.14(b). The direct interaction to the C-terminus is clearly visible, leading to an average height of about 2 Å above the surface for the C atom of the carboxylate group. A second group of atoms, namely the N-terminus group (N) as well as one of the arginine (Arg2) and the lysine (Lys) sidechain groups settle at a height of about 4 Å above the surface, corresponding to indirect surface interactions mediated by the first hydration layer. The remaining sidechains (Arg1, Gln and Ile) remain further away from the surface at heights ranging from 7 to 10 Å. Thai et al. [TDS+04] suggested that efficient ZnO interactions occur when an angle

[4] Unfortunately a coordinated study comprising experimental and theoretical investigation of this hybrid interface is still missing in current literature.
[5] This nomenclature refers to the three letter code of amino acids.
[6] This nomenclature refers to the one letter code of amino acids.

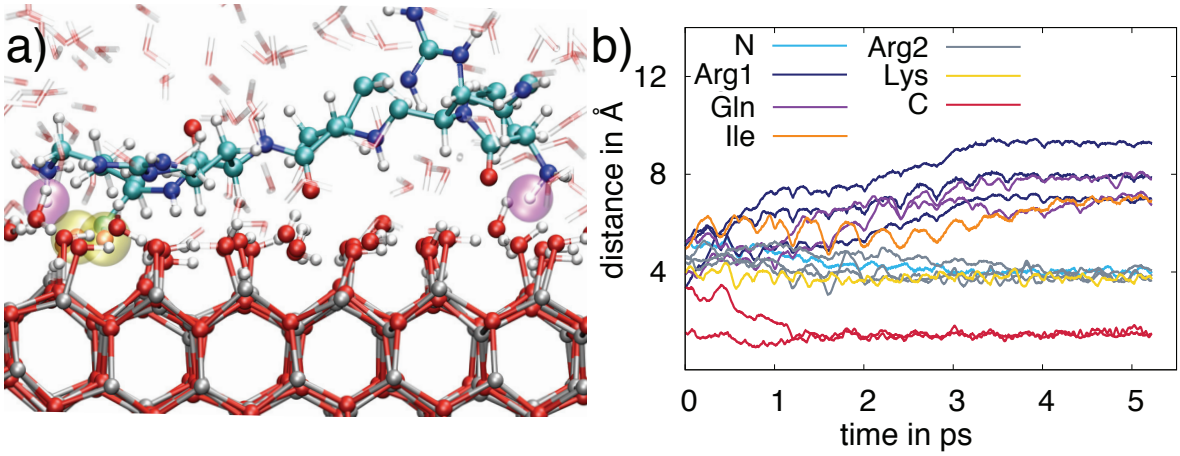

Figure 4.14.: Final snapshot of the trajectory of the adsorption of the pentapeptide RQIRK simulated with DFTB a).The pink spheres mark atoms that form hydrogen bonds to the first water layer while the yellow spheres indicate a direct contact to surface atoms. The corresponding heights of selected functional groups above the surface as a function of the simulation time are shown in b).

of approximately 135° is formed between the first arginine and the lysine, because in this case an optimal orientation of the lysine residue towards the surface is obtained. This angle is in the same order of magnitude as the angle of 117° evaluated from DFTB simulations. Therefore in view of the development of DFTB in the direction of a wider variety of molecular dynamics tools (*e.g.* constraints) as well as to parallelization, DFTB is a very promising methods to investigate complex system on a full quantum level.

4.3. Adsorption of Acetic Acid on ZnO Nanowires

As highlighted before in the introduction of this thesis, one of the big advantages of the material ZnO is the possibility to assemble it in various kind of nano-structures. The properties of these nano devices can further be customized by the introduction of chemical species as ligands onto the surfaces to create novel hybrid functional devices. One field of interest thereby is on the functionalization of ZnO nano wires (NW), because of their application in sensing devices or in dye-sensitized solar cells (DSSCs). A functionalization of the nano wire surface with well-selected group could trigger the electrical properties either increasing the sensing sensitivity or improve the charge injection. One example is the adsorption of molecular dyes on nano-ZnO in DSSCs. Even though electron mobility is much higher in ZnO compared to TiO_2, the efficiency of DSSCs involving ZnO is much lower compared to ones using TiO_2 [QEHB07]. Studies suggested that this effect could be caused by problems with the adsorption process [BBMH01].

To devise experiments in order to understand the functionalization of nano structures on an

atomic level is very difficult due to the small sizes involved. In this context theoretical calculations are very useful to understand the basic binding characteristics involved. Calzolari and co-workers [CRC11] focused in a DFT study on the adsorption of catechol on ZnO $(10\bar{1}0)$ and the effect of the adsorption on the electrical properties. They found that the adsorption and therefore the band alignment between ligand and substrate is highly dependent on the character and composition of the wurtzite ZnO surface.

One possible anchoring group to bind molecules to ZnO surfaces is the carboxylic group as already suggested by the results of the preceding chapters and earlier studies [TGW+06]. A DFT study focusing on the adsorption of a ML acetic acid (AcOH) molecules to the ZnO $(10\bar{1}0)$ surface revealed two stable binding configurations displaying either a dissociated bidentate chelating or dissociated bidentate bridging binding mode between oxygen and surface zinc [MRF09]. In calculations done by Adriel Dominguez [DHK+14] the dissociated bidentate chelating mode was found to be the stable adsorption mode for a ZnO nanowire under dry conditions. Since the environment might also have an impact on the adsorption geometries this chapter of the thesis will depict an extended approach by explicitly including bulk water into a AcOH/nanowire system[7].

4.3.1. Method and Model Systems

Molecular Dynamic (MD) simulations were performed using Car-Parinello MD as implemented in the Code CPMD [CPM]. For all MD simulations the Brillouin zone integration was performed using the Γ-point only. All systems were heated up to 300 K using a Nose-Hoover thermostat applying the heating figure introduced in Ref. [KBL08]. The nano wire model was provided by A. Dominguez. The nanowire was built up of 48 atom with a cell dimension of $(30\times30\times5.41)$ Å^3. The initial adsorption configuration of the adsorbed molecule was the optimized structure for the adsorption in gas phase (private communication A. Dominguez)[8]. This model is suitable as a first approximation to investigate the stability of modified nano wires in a wet environment. The region between the periodically repeated nano wires was filled with water molecules up to a density of about 1g/cm^3 which corresponds to 124 water molecules per supercell. The coverage is defined according to $\theta = \frac{N_{AcOH}}{N_{\mathrm{Zn}}}$, where N_{AcOH} and N_{Zn} denote the numbers of adsorbed AcOH molecules and of possible Zn binding sites on the surface area of the simulation cell. Molecular coverages of AcOH of $\theta = 0$, 0.5 and 1 were considered [9]

4.3.2. Adsorption Configurations for Full Coverage

In order to analyze the influence of the aqueous media on the ligand adsorption, an eight ps MD run was performed. To verify if the considered supercell is large enough to sample a bulk water

[7] This part of the thesis was motivated by work by Adriel Dominguez-Garcia and Andreia de la Rosa. The results and the discussion presented here were produced in close cooperation and published in [DHK+14].
[8] Declared earlier as dissociated bidentate chelating mode.
[9] Full coverage corresponds to 12 AcOH molecules adsorbed on the NW surface.

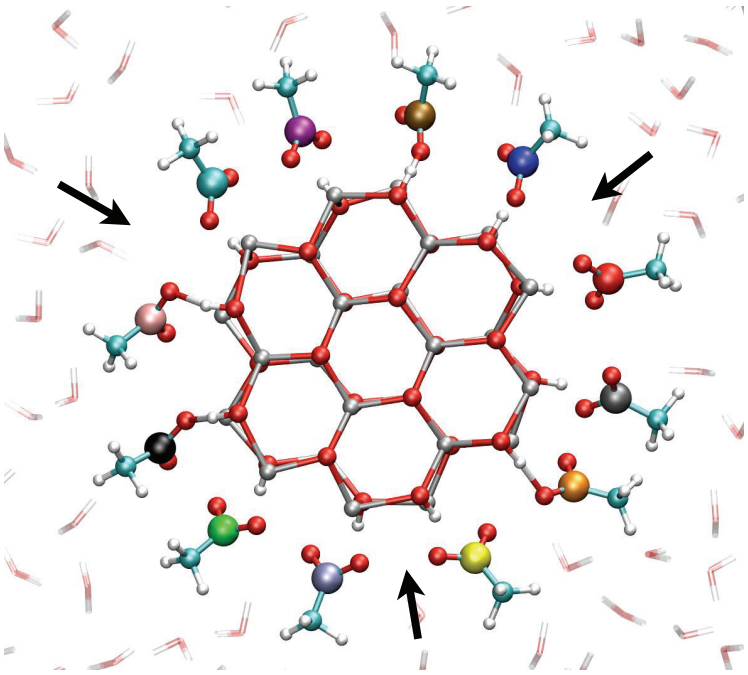

Figure 4.15.: Final snapshot of the molecular dynamics run for the fully-covered ZnO nanowire in aqueous medium. To distinguish between the twelve identical adsorbents, the carbon atoms of the carboxylic groups are shown in different colors. Zinc, oxygen and hydrogen atoms are displayed by silver, red and white spheres, respectively, whereas the carbon atoms of the methyl groups have been represented by cyan spheres. For ease of viewing the bulk water is displayed transparent. The black arrows indicate the sites where bulk water is able to settle in.

regime, in a first step the radial water density surrounding the nanowire during the MD run is calculated. Evaluation of the results show that the water density matched the standard water density of 1 g/cm^3 in the region between the wire and its periodic image. Accordingly the size of the supercell is chosen large enough.

A snapshot at 8 ps of the corresponding trajectory is depicted in Figure 4.15. The adsorption of the AcOH molecules is mediated through the formation of two bonds. Since a dissociated AcOH molecule is considered as the initial configuration, a strong hydrogen bond is formed between one oxygen of the carboxylic group and the transferred hydrogen at the surface. The remaining oxygen of the carboxylic group forms a bond to a surface zinc. In order to describe the dynamics involved, the length of these two stabilizing bonds, H-O and Zn-O, are evaluated over time. Figure 4.16 shows the bond length between one hydrogen and one of the carboxylic oxygens along the simulation time for all twelve AcOH molecules. The employed color code corresponds to the one used in the snapshot of the trajectory (Figure 4.15) and the hydrogen bonds are

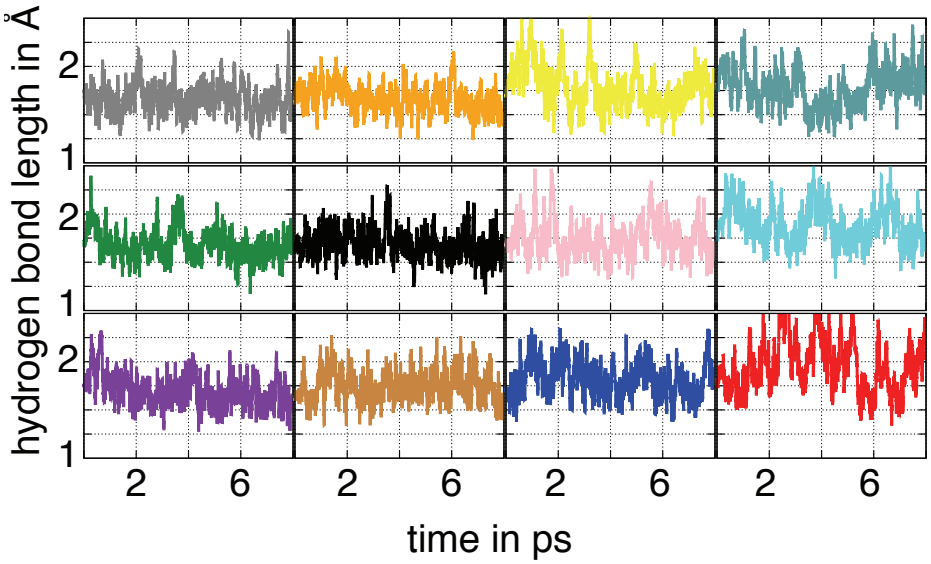

Figure 4.16.: Hydrogen bond lengths between one oxygen atom of the carboxyl group and the dissociated hydrogen for the fully-covered ZnO nanowire during the simulation time. The color code corresponds to the one used in Figure 4.15.

plotted clockwise starting from the -COOH group with the gray-dyed carbon atom. The curves shown in Figure 4.16 can be split into two different groups depending on their hydrogen bond stability. The first group comprises the plots in the first two columns, which yield very stable hydrogen bonds with an average length ranging from approximately 1.65Å to 1.75Å. In these cases AcOH binds to two adsorption sites (surface Zn and adsorbed hydrogen) thereby bridging two Zn-O surface dimer. The hydrogen bonds for the second group of adsorbates (third and fourth column in Figure 4.16) exhibit a stronger overall fluctuation of the bond length. In the case of the red-dyed ligand, the fluctuations are quite distinct, with interim O-H distances well above 2.5Å. These more distinct fluctuations can be explained by looking at the positions of the ligands on the nano wire surface. All six AcOH molecules belonging to the second group adsorb right next to a more ligand-free region indicated by black arrows in Figure 4.15. In fact, our results indicate that these ligand-free regions allow bulk water to approach the surface and interact with the carboxylic groups in the second group of adsorbates via formation of hydrogen bonds. From the analysis of the hydrogen bond lengths, it is therefore straightforward to identify a first influence of the bulk water on the adsorption of AcOH on the nano wires.

The analysis of the Zn-O bond length, depicted in figure 4.17, yields that the -COOH group adsorbs in a mono dentate mode. The reemerging feature among the twelve plots is the formation of a bond between Zn and one oxygen of the carboxyl group with an average bond length of about 2 Å. The distance between the second oxygen and Zn shows strong fluctuations ranging from 2.2 to 3.2 Å. Thereby the role of the two oxygens is interchangeable during the

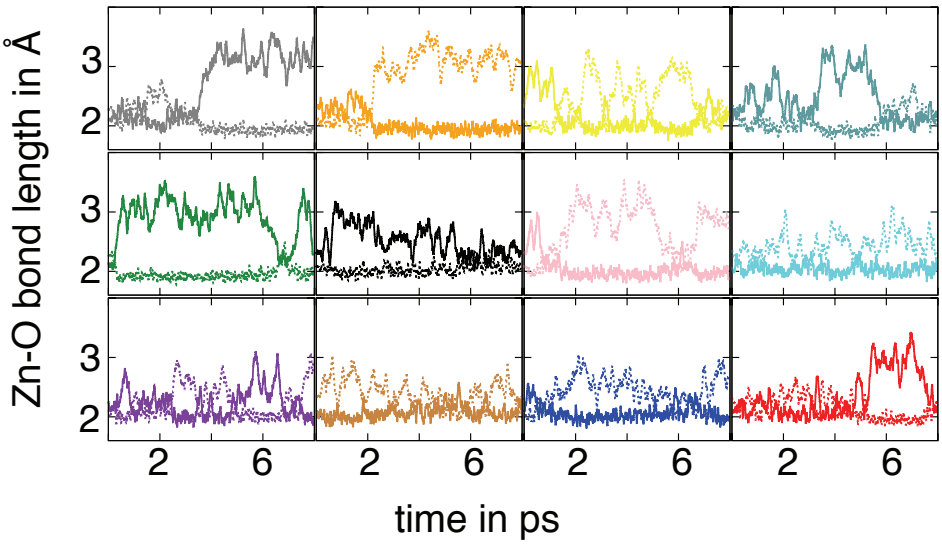

Figure 4.17.: Bond lengths between one oxygen atom of the carboxyl group and the surface zinc atoms for the fully-covered ZnO nanowire during the simulation time. The color code corresponds to the one used in Figure 4.15.

MD run (see *e.g.* yellow curves in figure 4.17). Thus, the results suggests that the AcOH-Zn interaction is dominated by a bond to one of the oxygens of the carboxyl group with a bond length resembling the Zn-O bonds in bulk ZnO. Further analysis of the trajectory shows that this tendency to a monodentate adsorption in the hydrated system is not mainly because of the interaction with bulk water but rather the thermal bond fluctuations apparent in the MD are sufficient to loosen the second zinc oxygen bond. The overall adsorption mode of the ligands indicates, therefore, that the presence of bulk water appears to play only a minor role in the adsorption mode for a fully AcOH-covered ZnO nanowire, as the initial configuration obtained from a gas phase calculation does not change significantly.

4.3.3. Influence of Coverage and Adsorption Energies

To investigate if this result depends on the ligand coverage, a second model is considered where the nanowire is capped with a one-half monolayer of AcOH ($\theta = 0.5$) in a bulk water environment by means of a six ps MD run. There are, doubtlessly, numerous ways to model the semi-covered ZnO nanowire, but as just the direct interaction between neighboring ligands is of interest here, a configuration is chosen that exhibits the largest but also equally spaced intermolecular distances, which means, that (compared to full coverage) every second ligand is removed from the surface. The evaluation of the corresponding trajectory regarding the two types of stabilizing bonds, discussed earlier, is shown in Figure 4.18. The time evolution for the hydrogen bond lengths exhibit strong fluctuations, especially distinct for the molecules marked with the gray and yellow-

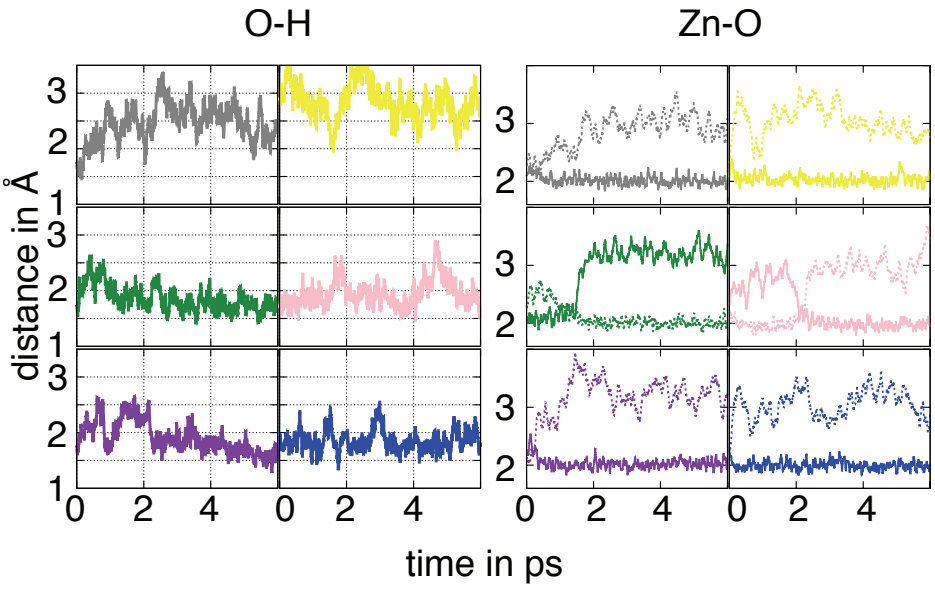

Figure 4.18.: Hydrogen bond lengths (left) and zinc-oxygen bond lengths (right) for the half-covered ZnO nanowire during the simulation time. The color code corresponds to the one used in Figure 4.15. Only the adsorbed molecules are shown.

dyed carbon, where the O-H distance are found to be well over 2.5 Å (Fig 4.18 first and second column). Analysis of the corresponding trajectory shows that the bulk water is able to settle in between every neighboring AcOH molecules due to the newly available adsorption sites on the surface. These water molecules are able to form hydrogen bonds with the oxygen atoms of the carboxyl group. This interaction competes with the formation of hydrogen bonds between the molecule and the surface H atom. This finding is also reflected in the analysis of the Zn-O bond length over time. Only for the pink-dyed and green-dyed molecules the oxygen atoms of the carboxyl group alternately bind to the Zn site. For all other molecules the surface Zn atoms remain attached to the same molecular oxygen during the simulation (two rightmost columns in figure 4.18). Thus the results show that the adsorption of the ligands primarily occurs in a monodentate mode for a half-ML coverage.

The MD trajectories were additionally employed to compare the relative stabilities of the fully- and half-covered nanowires, in the same manner as presented for the adsorption of single amino acids in the previous chapter. As a matter of comparability, a system is considered in which all molecules are desorbed from the nanowire facets at the beginning of the simulation. This case corresponds to a coverage $\theta = 0$. The obtained potential energy versus time curves are depicted in Figure 4.19. The average energy within the last 1.5 ps of the system with all molecules desorbed is set as the zero point energy. Like in the case of the single amino acids the energy curves exhibit also quite pronounced oscillations and the energy cannot be interpreted as converged due to the short simulation times applicable. However the curves for the desorbed

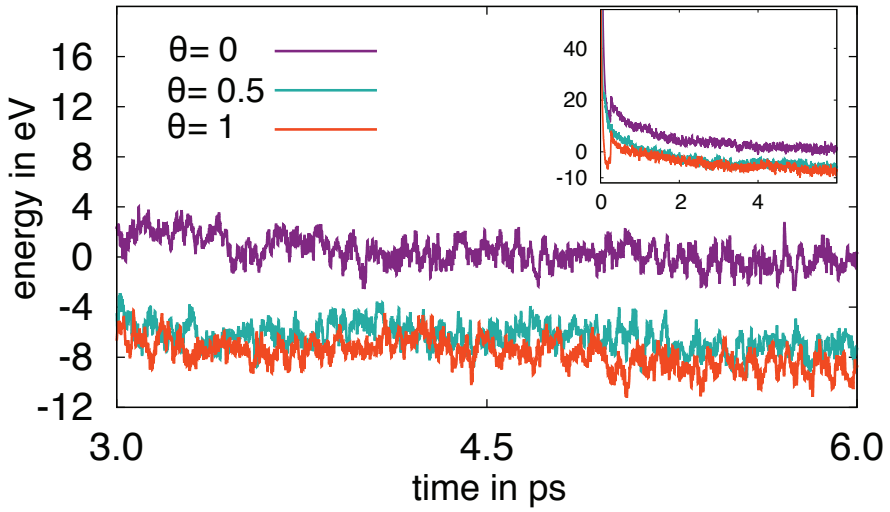

Figure 4.19.: Energy distribution over the last picosecond of the simulation time obtained for the ZnO nanowire with the three considered coverages: full coverage (θ=1), half-coverage (θ=0.5) and total ligand desorption (θ=0). The energy of the ligand-free nanowire was set to the zero of energy. The inset shows the course of the energy over the entire simulation time.

state can be clearly distinguished from the partly and fully covered nano wire owing to the high number of adsorbed molecules. The energy plots corresponding to θ = 1 and 0.5 show a similar trend and exhibit a strong overlap over nearly all time regimes. For θ = 0 the energy converges to a somewhat higher value during the MD run. In order to obtain a measure for the involved adsorption energies we evaluated the energies obtained during the MD simulations in an approach similar to the one employed in previous chapter. Again a Gaussian curve (compare Fig. 4.11) was fitted to the energy distribution obtained in the 1.5 picoseconds of the simulation. Taking the system with θ = 0 as the reference structure, the corresponding Gaussian maxima were used to estimate the associated adsorption energies. By doing so, the difference in energy of the configuration with θ = 1 compared to the fully-desorbed case is 8.84 eV, which corresponds to approximately -0.74 eV per molecule. For θ = 0.5 we found an adsorption energy of -0.57 eV per adsorbate (including six AcOH molecules and six adsorbed water molecules). Therefore the results indicate that the fully-covered ZnO nanowire is more stable compared to a half-covered wire. This suggest that a complete functionalization of a ZnO wire in solution is possible under ligand-rich conditions. This is in agreement with recent experiments, which have demonstrated the successful functionalization of ZnO nanotips by immersing them in solutions of AcOH diluted to 2 mM per liter [TGW+06]. However, one should keep in mind that an energy barrier needs to be overcome in order to replace molecules from the first water layer by AcOH. Therefore this work on hydrated nano wires system of ZnO only constitutes the first step on the way to a deeper understanding of the effect different functionalizations and also different adsorption

modes on the properties of the nano device.

4.4. Conclusions

A fundamental understanding of the physical and chemical interactions between amino acids and the ZnO/water interface is not only needed to understand the influence of ZnO nanoparticles on our environment [XKL+08], but also to understand the mechanisms of adsorption of specific ZnO peptide binders. It has been suggested that the specific recognition of a material by peptides is governed by the local structure of water at the solid/liquid interface [SC12]. Theoretical studies that also take into account the possibility of simple chemical reactions such as proton transfer or formation of covalent surface-molecule bonds are very rare due to the large computational cost associated with DFT-based simulations of these hybrid system [CCC+10]. Approximative methods such as DFTB are therefore needed in order to be able to investigate larger biological systems beyond the reach of DFT but with acceptable chemical predictivity.

The presented results show that DFTB reliably reproduces the average adsorption geometries obtained by DFT. In particular, these highlight the important role played by the first hydration layer in mediating indirect surface-molecule interactions. The hydration layer on ZnO(10-10) is composed of a mixture of dissociated and undissociated water molecules, as already found in previous investigations [MMD+04, MRM06] and is even more markedly structured than the hydration layer on the other important non-polar ZnO(1-210) surface [HKFCC12]. At the level of single amino acids, adsorption via both backbone functional groups is very often observed and is associated with binding energies between 0.3 and 1.0 eV. This is seemingly due to the good geometrical matching between the position of the surface-adsorbed water and OH groups and the functional groups. Among the studied amino acids side chains, carboxylate groups are observed to often penetrate into the first hydration layer and form direct surface-molecule bonds. Particularly interesting is the case of cysteine, whose thiol group is observed to be prone to oxidation by the ZnO surface, with donation of an H atom to the surface terminal groups. Importantly, this reaction has been observed both in DFT and in DFTB simulations.

Comparatively less clear than the adsorption geometries are the results concerning the adsorption energies. The values obtained as averages in MD simulations are not always easy to rationalize from the type and number of surface-molecule hydrogen bonds, and most probably are heavily influenced by the perturbation of the hydrogen bond network in surface proximity. The same reason makes a comparison of adsorption energy values at the level of DFT and DFTB unreliable. Indeed, DFTB is known to overestimate the H-bond strength in liquid water, which leads to strong discrepancies with respect to DFT adsorption energy values, despite the remarkably good agreement in the adsorption geometries and water density profiles (see Figs. 4.6 4.7 4.8 4.9 and 4.10). The worst results are obtained for molecules with a net charge, such as glutamate. The overbinding tendency of DFTB is consistent with results of Hellstroem

et. al. [HJB+13], who reported that an overbinding of 0.3-0.4 eV for a single water molecule bound to ZnO (10-10) is found employing the parametrization set znopt. The description of hydrogen bonding and in general of charged systems within the DFTB formalism has been shown to be considerable improved by the extended DFTB-based approach, DFTB3, by Gaus and co-workers [GCE11]. However the problem of a description of the nitrogen hybridization is not corrected in this approach, impeding a transition between different hybridization states during the simulation. Despite these shortcomings, as a general result, the obtained adsorption energies are considerably smaller than those characterizing the adsorption of amino acids on other oxides, such as TiO_2 [KBL08].

Despite its limitations regarding the quantification of adsorption energies, DFTB appears to be a good method when it comes to predicting the adsorption behavior of more complex systems comprising surface defects or describing the interaction of small polypeptides. DFTB in these cases proved as a good compromise to yield an unbiased description of the chemical reactivity of surface/adsorbate interface. Two first and simple examples of more elaborated systems have been introduced in this part of the work. The results of the oxygen kink showed a district reactivity toward bond formation with the glutamate side chain. However the formation of a chelating complex has not been observed. Furthermore a possible adsorption geometry of the putative good ZnO-binding motif Arg-Gln-Ile-Arg-Lys has been simulated. Certainly the results shown so far do not give a last statement about possible adsorption scenarios that might trigger the bond breaking at kink site nor do they to sample the conformational space of the peptide-surface interactions with acceptable statistical relevance [SC12]. Short simulations of this kind, however, are useful to check whether the system is prone to chemical reactivity and constitute one step that combined with e.g. longer and more complex force fields simulations will help to draw a more complete picture of the ZnO/water/bio interface.

In the final section of this chapter the effect of a water environment on the adsorption geometries of the AcOH interface was investigated. The results show that bulk water settles close to the adsorbents of the nanowire which leads in some cases to a change of the bidentate binuclear adsorption mode to a monodenate mononuclear adsorption mode, thereby destabilizing one Zn-O bond. This finding was even more pronounced for the case of an only partly functionalized nanowire. Nonetheless if such a change in the adsorption has a measurable influence on the relevant electronic properties needed to utilize ZnO nano wires as e.g. sensor devices remains an open questions. The evaluation of the energies showed a higher binding energy per adsorbent(0.17 eV) for a full coverage of the NW compared to the half-covered model. But this value should be interpreted with caution, since the fluctuations of the potential energy curves observed within a couple of ps are in the same order of magnitude as the obtained binding energies per molecule and the full quantum approach does not allow simulation lengths that would ensure a converged energy. Nonetheless the evaluation of the energies do suggest that a functionalization with AcOH is favorable under humid conditions.

Chapter 5.

5 A force field for the hybrid ZnO/water/organic interface: On our way to more complex systems

The previous chapters focused on small model systems, which describe different aspects of the complex nano-ZnO/bio interface. The employed full quantum methods like CPMD or even more approximate methods like DFTB or ReaxFF are computationally too demanding to efficiently simulate larger and more elaborated systems but they are a good reference to set the correct chemical state of interfacial systems in simulations with non-reactive biomolecular force fields. Hence on the way to a more realistic system it is necessary to increase system sizes and simulation lengths at the cost of a particularly detailed description. Therefore the last chapter of this work presents the parametrization of a classical forcefield, especially tailored to the requirements needed for the description of complex nano-ZnO/bio interfaces. Starting from a systematic discussion of the DFT reference method, the parametrization process of the force field and the utilized model systems are described in detail. Lastly as a first application, the new forcefield is used to describe the adsorption behavior of a small peptide on the $(10\bar{1}0)$ surface in different hydration states.

5.1. Validation of the DFT Reference Method

A reliable parametrization is based on a well chosen reference set up. The results of the previous chapters showed that DFT is able to produce reliable results when used for ZnO. However as addressed before, DFT has its difficulties when it comes to describing electronic properties, like the correct band gap, for ZnO. In chapter 2.2.1 a theoretical ansatz to correct for this underestimation of the band gap was introduced. In order to provide dependable DFT reference calculations this approach is applied in this paramterization. Therefore in a first step the parameter U defined in the LDA+U approach has to be assigned to its correct value. Results from

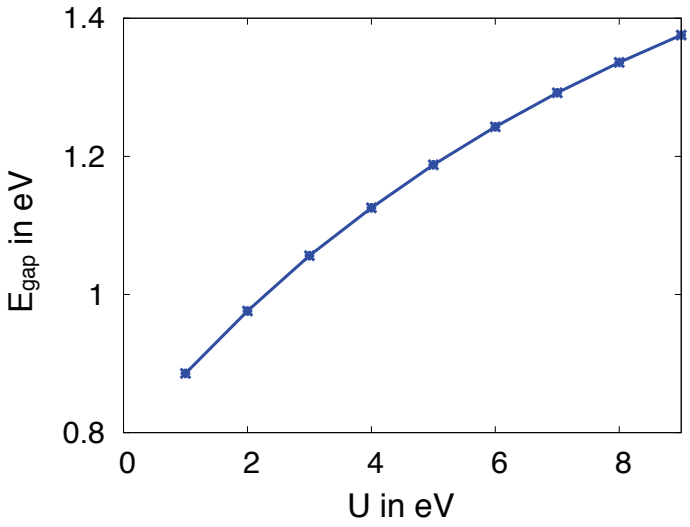

Figure 5.1.: Influence of the parameter U on the band gap of wurzite ZnO

previous studies show inconclusive results. Huang [HWW12] and co-workers found an optimum effective U parameter of 5.0 eV for a wurtzite supercell comprising 96 atoms. However a different study by Palacios et al. applied an effective U parameters of 8.5 eV in their calculations. Owing to these diverse results the effect of the choice of the parameter U is tested.

Computational Set Up

All following DFT calculations are done using the code PWSCF as implemented in the package Quantum Espresso[GBB$^+$09]. Ultrasoft pseudopotentials are used to decrease the required basis size [PP]. The energy cutoff is set to 30 Ryd and the Brillouin Zone is sampled using a Monkhorst-Pack grid of (8×8×8). The plus-U correction is used as a correction to the Zinc d-orbitals. Wurtzite ZnO is modeled using the 4 atoms of the primitive cell with the cell parameters determined in chapter 3.1.2.

Results

The influence of the effective U parameter on the ZnO band gap energy is depicted in figure 5.1. With an increasing value of U the band gap of ZnO also broadens, yielding energies between 0.84 and 1.39 eV. The effectiveness of the LDA+U correction can be followed by looking at the density of states (DOS) for the primitive cell for different values of U. In figure 5.2 the DOS is projected onto the s and d orbitals of zinc and on the s and p orbitals of oxygen. The dotted pink line marks the experimentally measured positions of the zinc d states [PSM71]. The zero point energy corresponds to the Fermi energy. Comparison of the different projections shows that the conduction band states are unaffected by the change in the parameter U. The same is

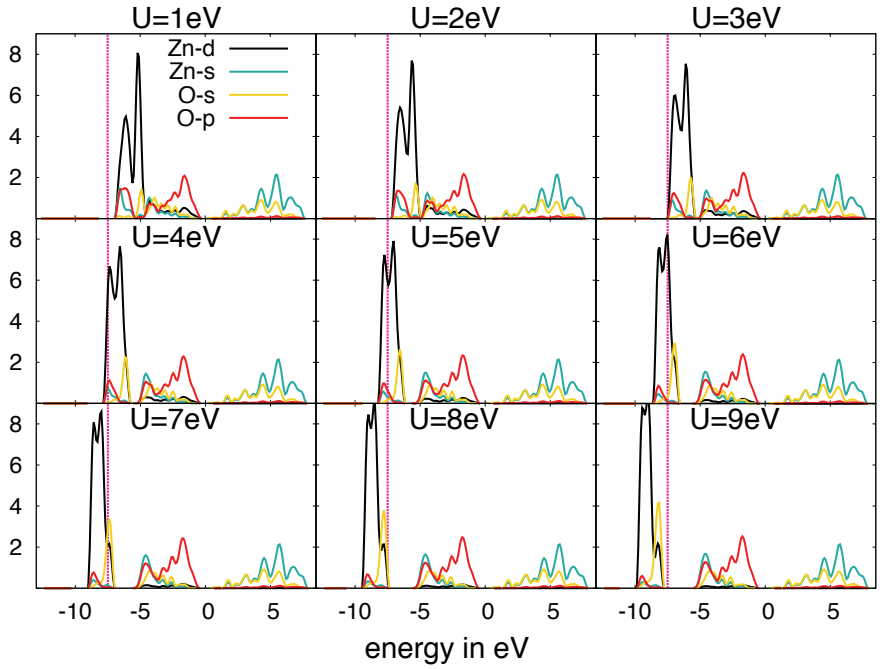

Figure 5.2.: Projected density of states (PDos) for a primitive cell of wurtzite ZnO for U values ranging from 1 to 9 eV . The dotted pink line marks the position of the Zn d states obtained from experimental results [PSM71]. The Fermi energy was chosen as the zero point of the x-axis.

true for the upper valence band states. However with increasing U the zinc d states are shifted down in energy from approximately -6 eV for U=1eV to approximately -10eV for U=9eV. During this process the valence band is split into two parts, separated by a small gap at about 6 eV. The highest overlap with the experimental position of the d-states is found for a value of U = 5eV. This corresponds to the results of a previously published study [HWW12]. In all following DFT calculation comprising the LDA+U correction, the effective U parameter is therefore set to 5 eV.

Besides the band gap problem the influence of the van der Waals (vdW) dispersion energy continues to grow as the considered systems sizes increase. Although this energy component is small compared to covalent or hydrogen bonds it plays an important role e.g. in intramolecular binding energies. The DFT theory does not exclude the description of dispersion effect a priori. In fact if an exact solution of the Kohn-Sham Equations was known, dynamic correlation effects, like dispersion, effect would be included in this solution. Nevertheless prevalent exchange-correlation functionals like the GGA approach used in this work neglect these effects. One way to correct for that is the introduction of empirically determined correction functions. The total energy of

the system is then given by:

$$E_{DFT+vdW} = E_{DFT} + E_{Disp}. \tag{5.1}$$

The dispersion function applied in the code PWSCF is given by following approach [Gri06]:

$$E_{Disp} = -s_6 \sum_{i=1}^{N_{at}-1} \sum_{j=i+1}^{N_{at}} \frac{C_6^{ij}}{R_{ij}^6} f_{dmp}(R_{ij}). \tag{5.2}$$

For a system of N_{at} atoms s_6 denotes a global scaling factor which depends on the type of density functional used. The parameter C_6^{ij} is the dispersion coefficient for the atom pair ij which is separated by the interatomic distance R_{ij}. The damping function f_{dml} is introduced to avoid singularities for small interatomic distances which would otherwise result in infinite attraction. Despite the need for an extra fitting procedure for this empirical correction term the results show a distinct improvement compared to a standard GGA approach regarding noncovalently bound complexes or thermochemical transitions. The effectiveness of a vdW correction factor for the systems relevant in this work are clarified in figure 5.3. For this test calculation a water molecule is positioned in different distances above the surface. The total energy of the systems are calculated using single point calculations. The position of the minima (approx. 2.1 Å) is found to be similar for all three approaches. However the energy depth is more that doubled using vdW correction compared to standard DFT-GGA. The influence of the U correction term is also visible but not as distinct.

Taking into account all obtained results, the reference calculations for the classical forcefield will be performed using a DFT+U approach (U = 5eV) in addition to an empirical vdW correction function according to Grimme [Gri06].

5.2. Parametrization of the Forcefield

The main requirement of the forcefield, that is going to be parameterized, is a good description of the interactions occurring at the biomolecule/surface interface. Furthermore the form of the energy potential and the involved fitting parameters are kept as simple and general as possible to facilitate transferability. The parametrization of the interaction between surface and adsorbate is based on the approximation that only the non-bonded parameters, that means only the Coulomb and the Lennard-Jones interactions, are considered explicitly,

$$E_{ij} = E_{Coul} + E_{LJ}. \tag{5.3}$$

This assumption is in this case reasonable as we consider hydrated ZnO surfaces. Investigations of the two surfaces in chapter 3 have shown that no further dissociation is promoted under

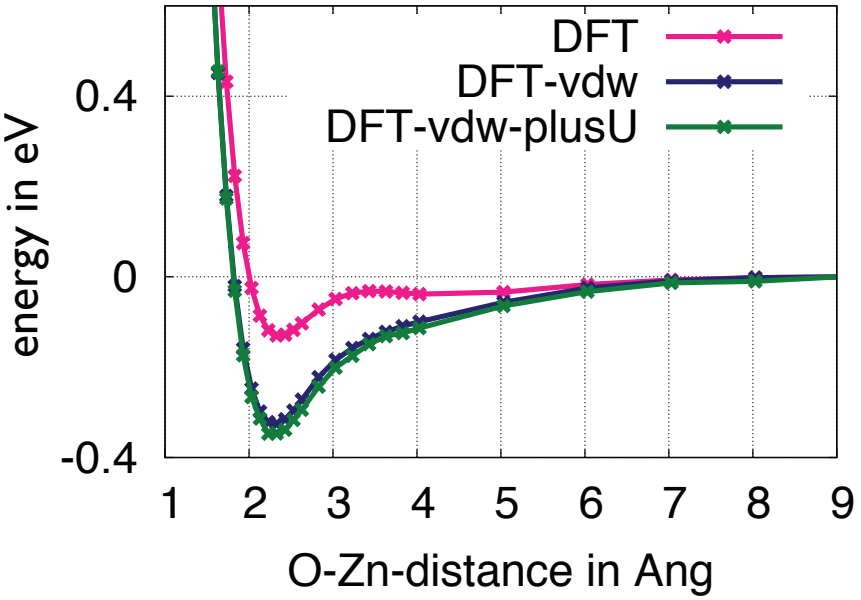

Figure 5.3.: Distance against energy graph for a water molecule on ZnO $(10\bar{1}0)$ using standard DFT, DFT with an added empirical vdW correction function and the DFT+U approach with added vdw correction.

the influence of bulk water. Furthermore analysis of the adsorption mechanism of single amino acids on ZnO $(10\bar{1}0)$ in chapter 4.1 has shown that only for specific cases (e.g. cysteine) a dissociative adsorption is observed. Excluding these special cases, allows a description of the interactions through electrostatic and Lennard-Jones forces only. Thereby the Coulomb energy is calculated as:

$$E_{Coul} = \frac{1}{2}\sum_{i\neq j}\frac{q_i q_j}{\varepsilon r_{ij}} \qquad \text{for } r_{ij} < r_{cut} \tag{5.4}$$

Here q_i corresponds to the charge of the i-th atom, ε is the dielectric constant and r_{ij} is the distance between atoms i and j.
The Lennard-Jones energy is given by:

$$E_{LJ} = 4\sum_{i\neq j}\varepsilon_{ij}\left[\left(\frac{\sigma_{ij}}{r_{ij}}\right)^{12} - \left(\frac{\sigma_{ij}}{r_{ij}}\right)^{6}\right] \qquad \text{for } r_{ij} < r_{cut} \tag{5.5}$$

In this presentation of the Lennard-Jones potential ε_{ij} characterizes the depth of the corresponding potential well, while σ_{ij} denotes the position where the interatomic interaction is zero. The pair coefficients ε_{ij} and σ_{ij} can be derived from the atomic parameters set in the fitting process

through the so called Lorentz-Berthelot combination rules:

$$\varepsilon_{ij} = \sqrt{\varepsilon_i \cdot \varepsilon_j} \tag{5.6}$$

$$\sigma_{ij} = \frac{1}{2} \cdot (\sigma_i + \sigma j) \tag{5.7}$$

The parameterization presented in this work is very closely modeled on the parameters published in the OPLS-AA forcefield [JMTR96]. That means that apart from the non-bonded parameters of the zinc and oxygen atoms of the ZnO slab all parameters are determined according to their values in the OPLS-AA forcefield (see chapter 2.2.3). As shown in [SC11] for the case of water on the TiO_2 surface, the zinc and oxygen parameters are determined from a fit of the energy landscape of the corresponding molecule desorbing from the ZnO surface. For this purpose a meaningful test set [1] of molecules is necessary.

Computational Set-Up and Technical Details

The DFT calculation are performed using the code PWSCF [GBB$^+$09] applying the DFT+U and a vdW correction as motivated in the previous chapter. For all atom species ultrasoft pseudopotentials[PP] are used. The plane wave cutoff energy was set to 30 Ryd (300 Ryd) for the electronic wavefunctions (charge density). The convergence threshold for the single point calculations is set to 1.0×10^{-6}H. The calculations are performed in the Γ-point approximation.

The forcefield calculations are performed using the code LAMMPS [Pli95, LAM14] in which the force field for the ZnO surface is implemented. The Coulomb interaction between each atom pair is defined by the atomic partial charges. The Lennard-Jones interaction is imposed through the definition of pair coefficients for each considered atom pair. Thereby only atom pairs consisting of one atom of the surface and one atom of the approaching molecule are taken into account for the parametrization process. The intramolecular Lennard-Jones interactions were defined using the parameters of the OPLS forcefield [JMTR96]. The cut off for the Lennard-Jones and Coulomb interaction is set to 12 Å and 14 Å respectively.

The slab size of the $(10\bar{1}0)$ surface is $(13.15\times10.60\times27.78)$ Å^3 comprising a 15 Å vacuum region. Accordingly a supercell with dimensions of $(11.38\times10.60\times27.04)$ Å^3 is chosen for the $(1\bar{2}10)$ surface. Both surfaces are saturated with a water ML according to results discussed in chapter 3.

Specification of the Point Charges

There are many ways to calculate charges in an atomic system, e.g. Bader charges, Löwdin charges or Hirshfeld charges [MS94]. They all differ in the way how they interpret the charge of

[1] Meaningful in a sense that it covers the most important interactions expected at the ZnO/water/bio interface.

an atom. A common approach to assign reasonable point charges to atoms in classical forcefield is the calculation of electrostatic potential (ESP) charges[2]. These charges are set to fit the electrostatic potential outside of the molecule.

Consequently in a first approach the ESP charges[3]for zinc and oxygen, are calculated using PWSCF and the REPEAT program. In this context a hydrated slab model was used. A detailed differentiation between various types of surface and 'bulk' zinc and oxygen species led to good results for the evaluation of the energy landscape of a single water molecule, however it lacked transferability since it failed to reproduce DFT data for the cases of the acetic acid and the nitrogen containing compounds. Averaging over the obtained ESP charges and just assigning one value per atom type (zinc, oxygen) led to average point charges of (+1.2) and (-1.2) for zinc and oxygen respectively. However also this approach failed to reproduce the needed depths of the corresponding potential wells. Prompted by a publication by Kawska and co-workers [KDHZ08] the point charges of zinc and oxygen atoms of the ZnO slab model are set to the formal charges corresponding to their oxidation state of (+2.0) and (-2.0) respectively. Although these charges are not derived by direct calculations, they are needed to reproduce the obtained DFT results.

Parametrization Set

The parameterization set is built up of three different molecule/ZnO surface interactions. The first scenario focuses on the interaction with a single water molecule. For this case the ZnO $(10\bar{1}0)$ and the $(1\bar{2}10)$ surface are considered. For the following calculations the surfaces are saturated with a water ML according to the adsorption configurations reported in chapter 3. Starting from a minimized configuration for each surface, the position of one water molecule, which is molecularly adsorbed to the surface, is shifted in order to alter the distance to the surface zinc and oxygen atoms. Per surface three different orientations of the water molecule are taken into account. In the first one (*ideal*) the relaxed position of the water from calculations of the water ML is used (see insets figure 5.4). Configuration two and three differ in the orientation of the hydrogen atoms regarding the surface. In the *top*-case a position in which both hydrogen atoms point away from the surface (see insets figure A.1 a) & c) in A1) is considered, while they point towards the surface (see insets figure A.1 b) & d) in A1) for the *bottom*-case.

Since this parametrization aims at describing the interaction with larger biomolecules the second trial molecule is acetic acid. It is selected because it isolates the interaction between a carboxylic group with the surface. In total six different orientations of the acetic acid above the $(10\bar{1}0)$ surface are considered (see insets figure 5.5 and A.2) The test-set for the parametrization is completed through the analysis of the interaction of three different compounds containing nitrogen in different hybridization states with the $(10\bar{1}0)$ surface. These are the NH_3 molecule,

[2]A plain and short discussion of the ability and pitfalls of ESP charges can be found in the Amber Manual [AMB]

[3]In detail REPEAT charges are calculated using a code introduced in [CMW09]. These are ESP charges calculated using a modified error functional that allows to evaluate ESP charges even for periodic crystalline systems

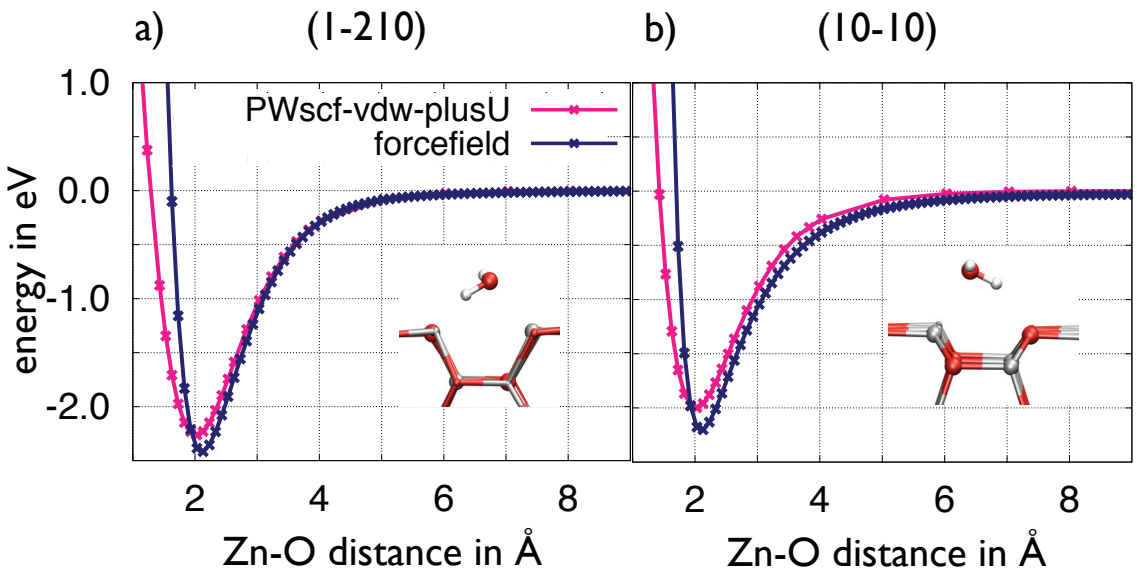

Figure 5.4.: Energy curves evaluated from single point calculations of one water molecule in different distances from the corresponding surface. In figure a) the results for the $(1\bar{2}10)$ surface are displayed while figure b) shows the results for the $(10\bar{1}0)$ surface.Both insets present the orientation of water above the surface(Ideal).

the side chain of glutamine (capped with a methyl group) and a imidazole molecule. The acetic acid as well as the nitrogen-containing molecules replace one molecularly adsorbed water of the first water ML on the $(10\bar{1}0)$ surface. This leaves one surface zinc and one surface oxygen as possible adsorption sites for the considered molecules.

Interactions with a Water Molecule

One exemplary energy landscape for the desorption of a single water molecule in an ideal initial configuration for each ZnO surface is shown in figure 5.4. DFT predicts a potential minimum of -2.26 eV for the $(1\bar{2}10)$ and a minimum of -1.99 eV for the $(10\bar{1}0)$ surface. The values obtained from the classical calculation with the optimized Lennard-Jones parameters listed in table A.1 are only slightly higher with -2.41 and -2.2 eV respectively. The curves of both energy landscapes show a good agreement. The energy curves displaying the desorption of the water molecule in the two remaining orientations (Top and Bottom) for the two ZnO surfaces can be found in figure A.1 in the appendix. The maximal deviation of the potential minimum also does not exceed 0.2 eV for these cases while the overall appearance of the DFT landscapes is reproduced in all four classical calculations.

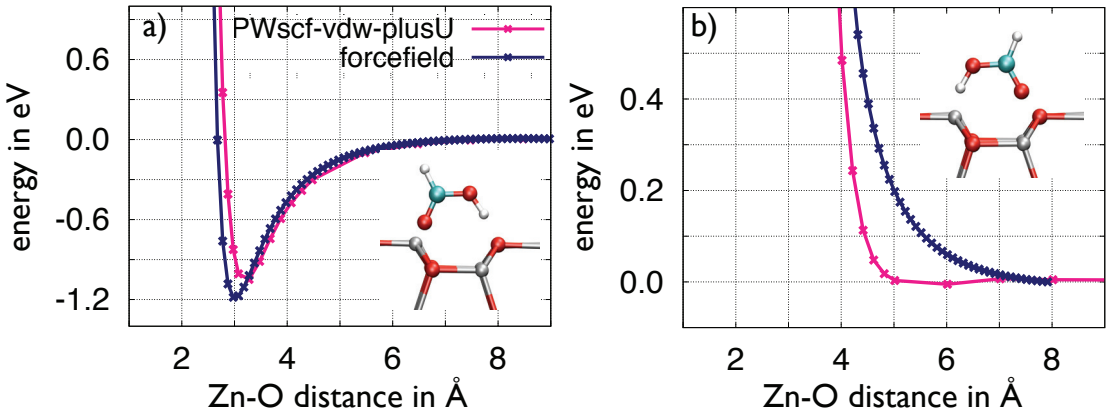

Figure 5.5.: Energy curves evaluated from single point calculations of acetic acid in different distances from the $(10\bar{1}0)$ surface for two different initial orientations. Both insets represent the initial orientation of the acetic acid above the surface.

Interaction with Acetic Acid

Six different orientations of the acetic acid above the ZnO $(10\bar{1}0)$ surface are evaluated. The LJ parameters employed for the description of the atoms of the acetic acid are listed in table A.2, the zinc and oxygen parameters were assigned consistent with the ones taken for the single water molecule adsorption(see first two lines of table A.1). An example of an energy landscape for an attractive interaction and a repulsive interaction are displayed in figure 5.5 a) and b) respectively. The remaining four energy comparisons can be found in figure A.2 in the appendix. In figure 5.5 a) the classical forcefield predicts a potential minimum about 0.12 eV lower in energy, while the position is shifted by 0.27 Å to smaller distances. However this overestimation of the potential minimum and the equilibrium distance is not observed in all energy curves displaying an attractive potential (see figure A.2 a), b) and c)). For two of these cases (a&b) the forcefield underestimates the potential minimum by 0.25 eV and 0.11 eV respectively. At the same time the classical calculations slightly underestimate the equilibrium distance for case a) and over estimate it for case b). The choice of the optimal LJ parameter is therefore based on the best agreement between DFT and classical energy landscapes averaged over all orientations of COOH. For the two repulsive cases depicted (see figures 5.5 b) and A.2 c) the forcefield reproduces the repulsive behavior but overestimates the repulsion for longer distances. This finding could not be improved by assigning different values to the LJ parameters of zinc and oxygen.

Interaction with Nitrogen-Containing Molecules

For the last set of molecules in the parametrization test set, identical energy calculations of a desorption process are performed above the $(10\bar{1}0)$ surface for each molecule . The energy curves

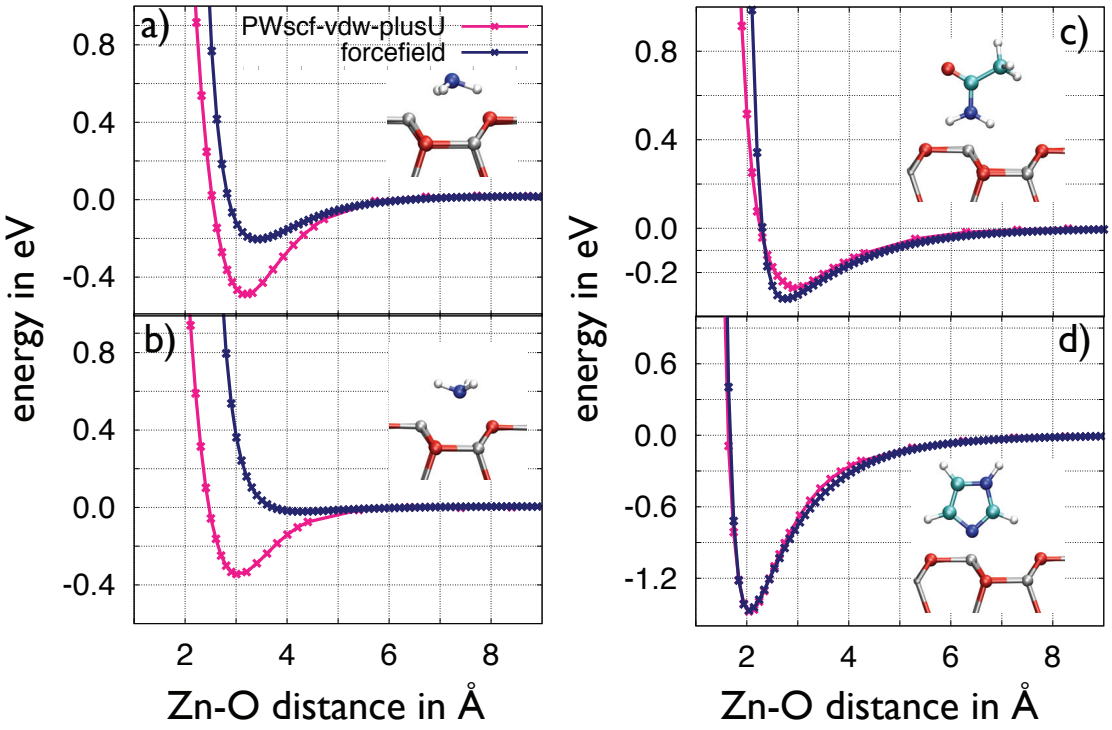

Figure 5.6.: Energy curves evaluated from single point calculations of NH_3 (a,b), the glutamine side chain l' and imidazole (d) in different distances from the $(10\bar{1}0)$ surface.. All four insets represent the initial orientation of the molecule above the surface.

calculated with the charges and LJ parameters specified in the OPLS-AA forcefield together with the fitted optimal parameter identified in the water and acetic acid calculation did not lead to an acceptable overlap between DFT and classical results. Even a very distinct modification of the zinc and oxygen LJ parameters and partial charges did not yield a satisfactory agreement for all three molecules considered. Furthermore this alteration of the LJ parameters led to a deterioration of the good results obtained for the first two test sets using water and acetic acid. In a first solution-oriented approach, a different potential form of the Lennard-Jones potential is considered. Based on an earlier work [SC11], instead of the 12/6 form (see equation 5.5) a so called 9/6 approach,

$$E_{LJ} = 4 \sum_{i \neq j} \varepsilon_{ij} \left[\left(\frac{\sigma_{ij}}{r_{ij}} \right)^9 - \left(\frac{\sigma_{ij}}{r_{ij}} \right)^6 \right] \qquad \text{for } r_{ij} < r_{cut}, \tag{5.8}$$

is used as an alternative, to model the interactions between nitrogen and the surface atoms. Nevertheless this approach also failed to produce reasonable agreements with DFT results for the nitrogen-containing molecules. Therefore in a second brute-force attempt the Lennard-

Jones pair-coefficients for the 12/6 potential form of the Lennard-Jones potential characterizing the nitrogen-surface interactions are set directly. That means they are implemented, thereby disregarding the combination rules, introduced in equation 5.6. Additionally to improve the overlap with the obtained DFT energy curves, the choice of the direct pair-coefficient depends on the bonding characteristics of the nitrogen in the molecule. More precisely the forcefield differentiates if nitrogen is bound to hydrogen or not. The optimized LJ parameters for these two particular cases, as well as the remaining (OPLS-AA) parameters are listed in table A.3.
The comparison of the potential energy surfaces obtained with DFT and the forcefield are depicted in figure 5.6. The results for the ammonia molecule only show a conditional agreement with DFT results. For the desorption of the orientation depicted in figure 5.6 a) the forcefield underestimates the potential minimum by 0.2 eV, and yields a good agreement in the equilibrium distance. However for a turn in the orientation by 180 degree (figure 5.6 b)), the forcefield predicts a repulsive interaction while the DFT results clearly show an attractive behavior. Despite these shortcoming in the description of the ammonia desorption the utilized parameters produce an excellent agreement of the potential energy curves in the case of the glutamine side chain and the imidazole (see figures 5.6 c) and d)). Since the latter two cases are structurally speaking closer to the systems the forcefield is intended to describe, no further optimization of the parameters describing interaction involving nitrogen is pursued in the framework of this thesis.

5.3. Analysis of a Specific Binding Motif on ZnO (10$\bar{1}$0)

The importance of specific binding peptides and their various applications have already been discussed in chapter 1.1. First results on the binding characteristics of a specific sequence motif using DFTB (see chapter 4.2) have shown possible contact points, however the system sizes and simulation times achievable turned out to be a limiting factor for further analysis. Therefore this system constitutes a good starting point for the application of the newly parameterized forcefield.

Hence, this part of the work will focus on an extended analysis of the binding analysis of the specific binding motif Arg-Gln-Ile-Arg-Lys identified by Thai et al. [TDS$^+$04] on the ZnO(10$\bar{1}$0) surface. Apart from the primary topology of the ZnO surface, the composition and configuration of the first strongly adsorbed water layer is known to play an important role in the formation of contact points between peptide constituents and the surface [MW11, SC12] (see also adsorption of single amino acids in chapter 4.1). Furthermore for another oxide surface, namely TiO_2, a pH-dependent affinity of the basic amino acids residues of the peptide was observed [SS03]. On that account three different surface models are considered in this analysis. In the first case a stoichiometric hydration of the surface assumed. Starting point for this purpose are the DFT calculations of Meyer and co-workers [MRM06] and the continued analysis in chapter

3.2. That means the surface is saturated with a monolayer of water molecules in which every second molecule is dissociatively adsorbed to the surface. Furthermore two systems in which the equilibrium of hydroxyl and protons is shifted to one side respectively are built by randomly deleting 50 % of the corresponding groups. In doing so two differently charged surfaces are simulated in contact with the peptide sequence. The obtained results can then be used as a first guess on the influence of different pH-values on the adsorption behavior[4].

Computational Details and Surface Model Development

All simulations are performed using the forcefield parameters described in chapter 5.2 within the LAMMPS code [Pli95, LAM14]. The Coulomb interaction between each atom pair is defined by the atomic partial charges. The Lennard-Jones interaction is imposed through the definition of pair coefficients for each considered atom pair. Thereby for atom pairs consisting of one atom of the surface and one atom of the adsorbent the self-parameterized forcefield is applied. Intramolecular and interactions between bulk water and the peptide are simulated using OPLS parameters [JMTR96]. The cutoff for the Lennard-Jones and Coulomb interaction is set to 12 Å and 14 Å respectively. Consequently for all bulk water molecules a TIP3P model [JCM$^+$83] is assumed. Since the TIP3P model is based on a rigid water molecule, during the simulation the shake algorithm is applied to omit the vibrations of the water molecules. The temperature is controlled via a Nosé-Hoover thermostat.

The size of all three supercells is set to (52.52×42.10×110)Å^3. The surface models with either a hydroxyl or proton excess are created by deletion of molecules/atoms randomly over the entire surface area. Thereby the dissociated water (stoichiometric case) and the hydroxyl groups and protons (hydroxyl or proton excess) are defined as part of the surface. That means, they are kept fixed during the simulation. After the peptide is placed in an identical orientation over the surface, all three systems are filled with bulk water and the z-parameter of the simulation cell is relaxed at 300K in a NPT run until the water density approximately matches the standard density of liquid water (1g/cm^3). Subsequently a NVT run of 10 ns at 300K is performed for each system, followed by an NVE production run of 10 ns. The total charge of the model system is balanced by the implementation of counter ions (Cl^- and Na^+) into the simulation cell.

Stoichiometric Hydration

The evaluation of the obtained trajectories is carried out similar to the analysis of the DFTB trajectory in chapter 4.2. In order to get a clearer picture about formed contact points the distances of the different side chains of the pentapeptide are analyzed over the NVE simulation

[4] In the case considered here, just two extreme cases of a distinct overrepresentation of either surface hydroxyl groups or surface protons are considered which are not aimed to resemble a certain pH-value. A more accurate calculation of the distribution of charged groups on the surface is possible [KL06], however the necessary experimental data was not available when these model systems were developed.

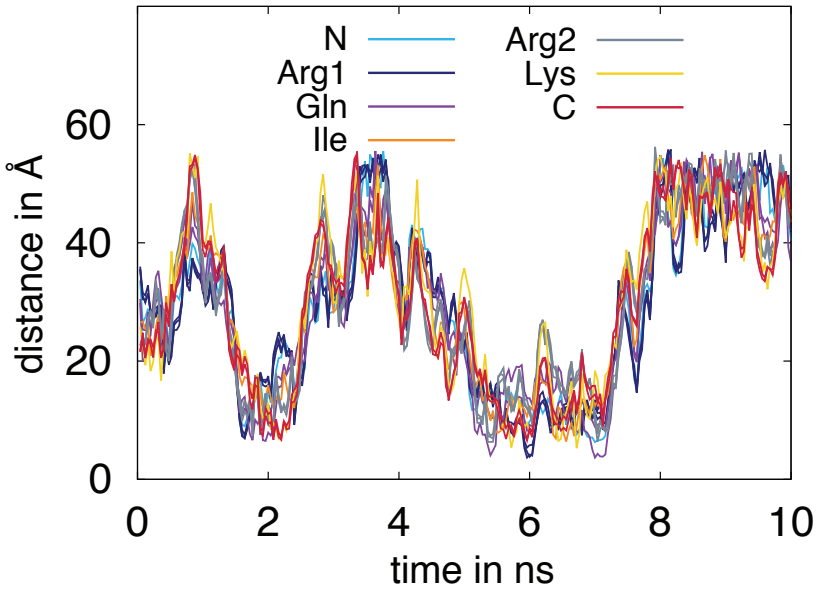

Figure 5.7.: Distance of side chains of the pentapeptide from the ZnO surface layer for a stoichiometric first water layer.

time. The distribution of distances for the stoichiometric hydration layer is depicted in figure 5.7. At the beginning of the NVE run the pentapeptide already displays distances of well beyond 20 Å from the ZnO surface layer, indicating that no stable adsorption configuration was obtained during the 10 ns NVT run. Although the pentapeptide approaches the surface after about 2 ns and 5-7 ns of the 10 ns NVE run, this does not lead to a stabilization of the pentapeptide within bonding distance of the surface. Compared to the results obtained in the DFTB simulation, the forcefield results also show an interaction between peptide and surface, however since longer simulation times are applicable in this case the results also suggest that no stable adsorption (> 10 ns) configuration is adopted.

The layering of the bulk water can be analyzed by looking at the corresponding density perpendicular to the surface plane (see figure 5.8). Thereby the average over the positions of the zinc atoms of the first surface layer is taken as the point of origin. The plot displays a first peak at a distance of 1.08 Å from the surface. A second peak, which is strongly overlapping with the first one, is found at 1.28 Å . Both peaks appear at distances about 1 Å closer to the zinc surface atoms compared to previous water density profiles for the ZnO (10$\bar{1}$0) (see chapter 4.1 figure 4.10). What this actually means for the obtained configuration is displayed in the inset of figure 5.8 depicting a snapshot of the corresponding trajectory. The water molecules of the first water layer stabilize very close to the surface during the simulation (marked by pink spheres in the figure). Thereby two different configurations are adopted. On the free binding sites in between

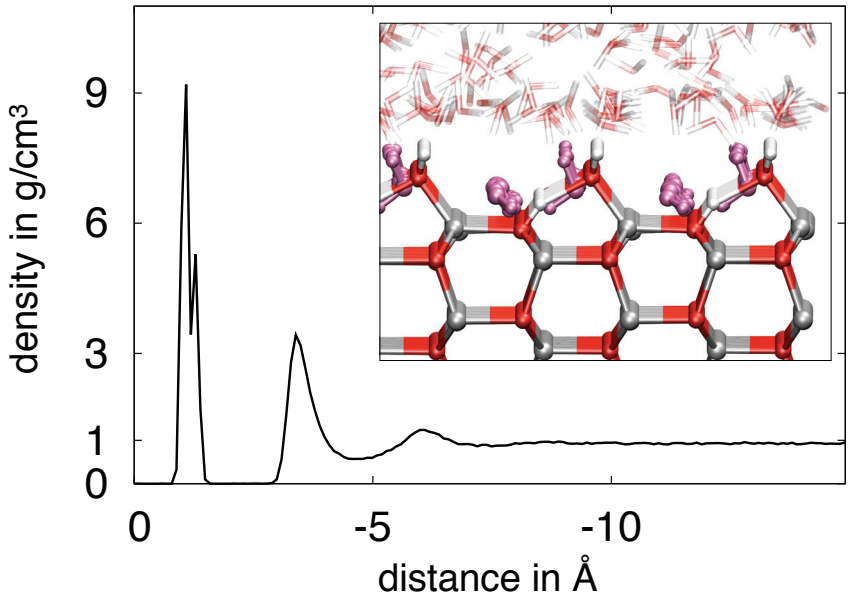

Figure 5.8.: Distribution of the water density during the 10 ns NVE production run.. The inset depicts a snapshot of the corresponding trajectory highlighting the different water layers formed (pink spheres first layer, transparent second and higher layers)

adsorbed surface hydroxyl groups the adsorbed water is tilted towards the Zn-O surface dimers. That means that they do not exactly restore the tetrahedral coordination found in earlier studies and also present in bulk ZnO. Furthermore bulk water settles in between rows of adsorbed water. This deviation from earlier *ab-initio* results is most probably due to the increased partial charges of the surface atoms. Consequently this leads to an increased electrostatic interaction between water and surface binding sites. However even though the position of the water is bent towards the surface the related Zn-OW bonds resemble the bulk length of 2 Å . The second water layer has its maximum in density at a position of about 3.4 Å . Therefore a depletion region of water is clearly seen between the first two water layers, which is slightly more pronounced compared to the findings of the DFT calculations. A less pronounced third maxima in the water density distribution shows at a distance of 6.2 Å above the surface plane. For larger distances a bulk water regime displaying the normal density under ambient conditions of 1 g/cm^3 is observed from the evaluation. The three chlorine counter ions present do not show a uniform behavior in the simulation. While one ions settles in between the first and second water layer, the remaining two drift randomly in the bulk water regime. This is to be expected since in the case of a stoichiometric hydration of the ZnO surface no excess charge is present on the surface.

Partially Protonated First Water Layer: Model for an Acidic Environment

For the protonated water layer surface hydroxyl groups are randomly deleted from the entire surface until a total surface charge of +26.0 e is reached[5]. The adopted distances of the five residues throughout the 10 ns NVE run are depicted in figure 5.9. As expected for a positively charged surface the terminal carboxyl (C) group of the pentapeptide stabilizes closest to the surface for the duration of the simulation. In particular the positions of the two oxygens of this terminal group only show little fluctuations, which is probably an indication for a stable adsorption configuration. The positions of the other five residues and the terminal amino group

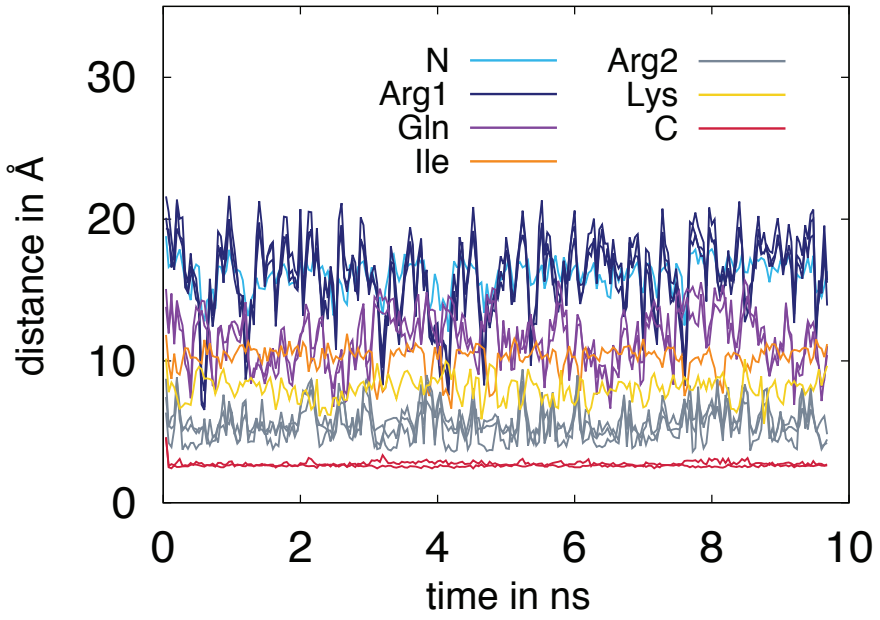

Figure 5.9.: Distance of amino acids residues of the pentapeptide from the ZnO surface layer for a partly protonated first water layer.

perpendicular to the surface plane are affected by large fluctuations in the order of up to 10 Å . Furthermore they do not show distances smaller than 4 Å with respect to the ZnO surface plane. A direct interaction with the surface or the first water layer can therefore be ruled out. A deeper understanding about the nature of interaction between the C-group and the surface can be obtained from the analysis of the water layering and the position of the chlorine counter ions above the surface. The corresponding distributions of density are displayed in figure 5.10. Like for the previous case the maximum corresponding to the first water layer is split into two peaks. With maxima at 1.09 Å and 1.29 Å these peaks resemble previous results for the stoichiometric

[5]The number of removed hydroxyl groups was thereby determined by the resulting total charge. This total charge was set to be an integer to facilitate the compensation with counter ions

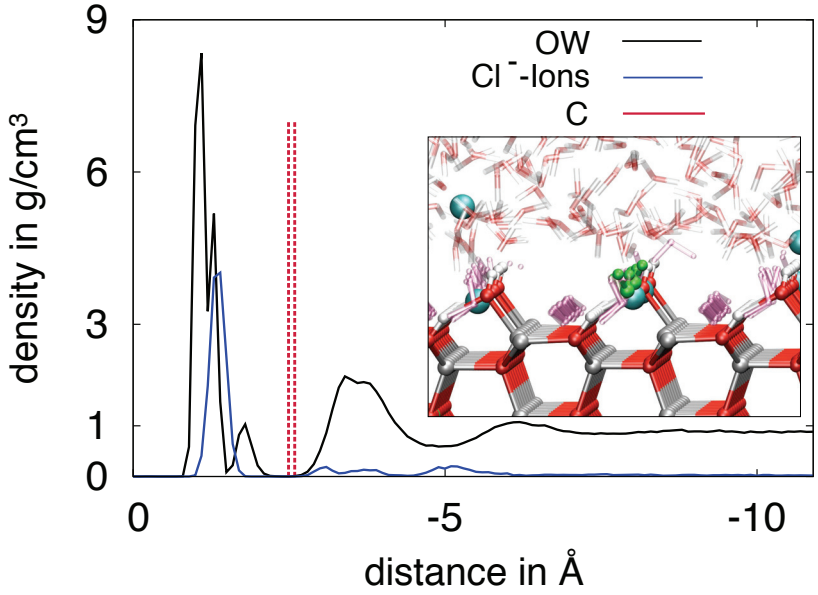

Figure 5.10.: Distribution of the density of bulk water and chlorine ions during the 10 ns NVE production run. Additionally the averaged positions of the two oxygens of the terminal carboxylic group are marked by red lines. The inset depicts a snapshot of the corresponding trajectory. Water molecules effecting the first two peaks of the first maximum of the water density are marked by pink transparent bonds, while those corresponding to the third peak are depicted by green spheres. Water molecules belonging to second and higher layers are marked by transparent dynamical bonds.

water layer. However for the partially protonated first water layer a third, less distinct, peak is visible at a distance of 1.79 Å with respect to the surface plane. The source of this third maximum can be explained by looking at a snapshot of the corresponding trajectory (see inset figure 5.10). The two peaks of the first maximum correspond to bulk water that adsorbs in between the fixed dissociated water molecules and on the zinc oxygen dimers in between rows of adsorbed water (transparent pink spheres). For the partly protonated first water layer bulk water can additionally settle into the gaps formed by the missing surface hydroxyl groups (marked by green spheres in figure 5.10). For this configuration the two hydrogen atoms of the water point away from the surface. These water molecules adopt a slightly higher position perpendicular to the surface, which gives rise to the third peak of the first water layer. The formation of a second water layer can then again be identified by the occurrence of a maxima at a distance of 3.4 Å above the surface, followed by a broader maxima corresponding to a third water layer at 6.2 Å. The positions of the second and third water layers thereby match the findings for the stoichiometric first water layer. This is somewhat surprising, since 26 more chlorine ions are needed in the protonated case to balance the surface charge. As shown in the density distribution

in figure 5.10 and also in the snapshot of the trajectory (marked by cyan colored spheres), a major part of the chlorine ions stabilize in the first water layer. Therefore they screen the surface charge by taking the position of a missing hydroxyl group. This finding is different from results published on TiO_2 surfaces [KL06]. Koeppen and co-workers found that the chlorine ions settle in between the first and second water layer, resulting in a shift of the second water layer away from the surface. However this effect is not visible in the simulations performed here.

The terminal C group of the pentapetide is found to settle in the depletion region in between the first and second water layer. A closer look at the corresponding trajectory yields that the carboxyl group stabilizes above a free zinc binding site, that means it replaces one removed hydroxyl group. This configuration is stabilized by the formation of two different types of bonds. On the one hand a hydrogen bond to a surface proton with an average bond length of 2.1 Å is established. Secondly the two oxygens of the carboxylic group form a bond to the surface zinc atom. The related bonding lengths are between 2.5 and 3.1 Å and therefore exceed the average ZnO bulk bond lengths by about 1 ÅṪhese bonds are therefore considerable longer compared to distances found for the side chain of glutamate using DFT and DFTB (see chapter 4.1). Nevertheless once again is the presence of a charged carboxyl group in proximity to the hydrated ZnO surface connected to a direct interaction with surface atoms.

Partially Hydroxylated First Water Layer: Model for a Basic Environment

The partly hydroxylated surface is built by randomly removing protons from the dissociated water molecules above the entire surface area until a total charge of -26.0 was reached. The development of the heights of the 5 different amino acid residues and 2 terminal groups during the NVE run is depicted in figure 5.11. For the first 4.5 ns of the simulation the pentapeptide adopts a stable configuration above the surface. Thereby the lysine, one arginine and the glutamine residue constitute the possible contact points. Since the surface exhibits a negative surface charge the development of contact point between positively charges residues (arginine, lysine) is an expected outcome. They stabilize at distances between 3.5 and 4.0 Å above the ZnO surface plane. During this first phase of the NVE run the second arginine residue points away from the surface. A more detailed analysis of the character of the contact points can be obtained by looking at the corresponding trajectory. A snapshot of the three contact points after 2.5 ns of the NVE run is shown in figure 5.12 a). The atoms of the evaluated residues (Gln, Lys, Arg2) that settle closely to the first water layer are highlighted by yellow spheres. In the case of the glutamine residue the interaction is mediated through the sidechain oxygen. It forms a strong hydrogen bond with a hydroxyl group of the first water layer with an average bond length of 1.3 Å. The nitrogen-containing residue arginine also develops hydrogen bonds to the first water layer. They display bond lengths of 1.9 to 2.1 Å. The third possible contact point, namely the amino group of the lysine residue only shows a weak interaction with the first water layer. Although its position is very stable over the first 4.5 ns of the simulation time,

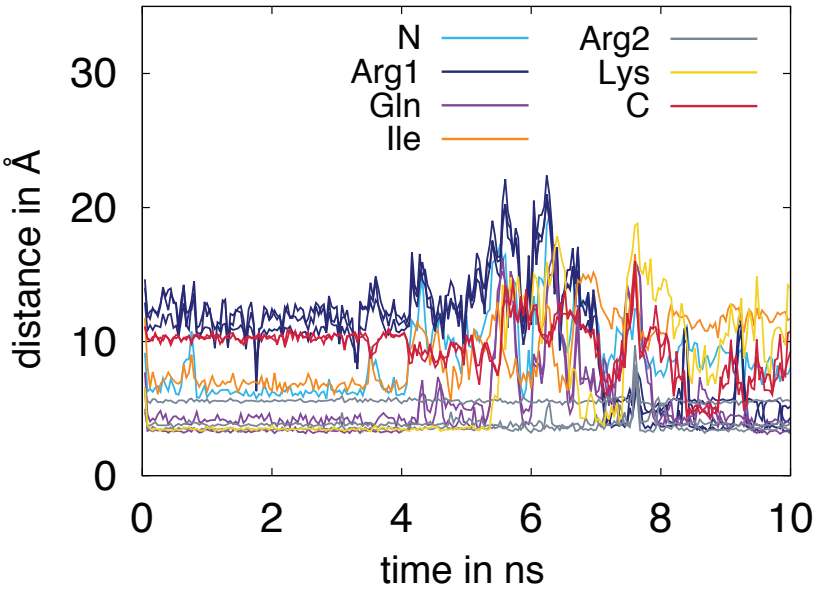

Figure 5.11.: Distance of amino acids residues of the pentapeptide from the ZnO surface layer for a partly hydroxylated first water layer.

the average distances between the hydrogen atoms of the amino group and adsorbed hydroxyl molecules are between 2.3 and 3.5 Å and therefore quite long as to be interpreted as stable hydrogen bonds. Rather the position of the lysine seems to be additionally stabilized through the adopted secondary structure of the pentapeptide and through interaction with molecules from the second water layer.

After 5.4 ns of simulation time the glutamine as well as the lysine residue leave the near-surface region and only the arginine persist as a contact point to the surface. Subsequent to a short transitional phase, in which the peptide totally desorbs from the surface (approx 7.8 ns), again three possible contact point establish to the first water layer. Apart from the arginine and the glutamine residues the second arginine residue settles in proximity to the surface. Again a look at the corresponding part of the trajectory provides clarity about the interactions at these contact points (figure 5.12 b)). The configuration of the glutamine side chain is identical to the one obtained before the reconfiguration process. The interaction is again dominated by a hydrogen bond between the oxygen and a hydroxyl group of the first water layer. The same is true for the Arg2 residue. The new contact point formed by the second arginine residue (Arg1) adopts a configuration identical to the one for the Arg2. Hydrogen bonds of average lengths between 1.9 and 2.2 Å establish between the arginine side chain and surface hydroxyl groups. However longer simulations times will be necessary to analyze if this adopted conformation is stable enough to exist for several nanoseconds of simulation time.

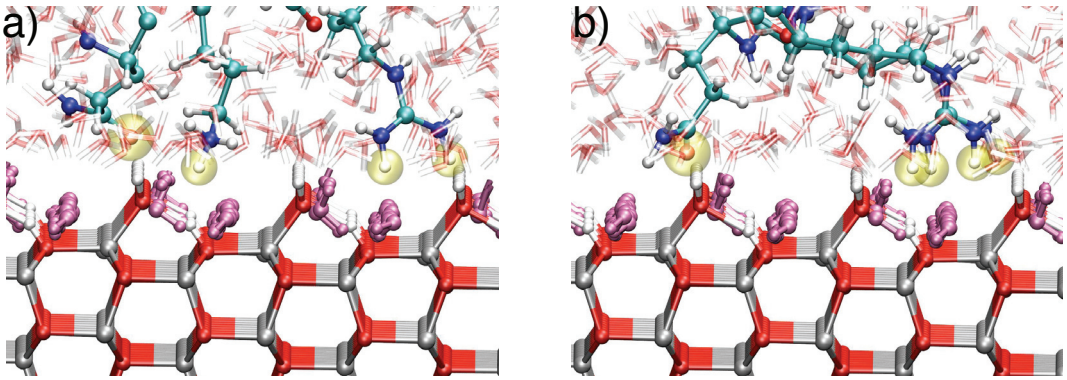

Figure 5.12.: Snapshot of the contact point (yellow spheres) after 2.5 ns (a) and 10 ns (b) of the simulation.

The formation of water layers above the partly hydroxylated surface is depicted in figure 5.13. The water density distribution displays three distinct maxima before the density drops to the standard density of water. The maxima corresponding to the first water layer consist, like for the stoichiometric case, of two overlapping peaks. However compared to the latter the peak positions are shifted to larger distances, yielding positions of 1.2 Å and 1.4 Å respectively. Analysis of single snapshots of the trajectory reveals that the reason for this shift is a small tilt in the orientation of the water molecules, resulting in slightly longer Zn-OW bonds (approx. 0.15 Å) and with that an alteration in the density profile. The tilt is most probably due to the deficit of surface protons which in turn strengthens the bonds formed between these free binding sites and the approaching water. The second water layer is described by a maximum in density at a position of 3.5 Å . While the third layer is found at a distance of 6.2 Å resembling the results for the stoichiometric hydration. The distribution of the 26 sodium counter ions utilized in this simulation is also depicted in figure 5.13. During the simulation the sodium ions are equally distributed between the two surfaces of the slab considered. They stabilize in between the first an second water layer. This is different from the findings for the case of the chlorine ions and the partially protonated water layer, since there the ions stabilized within the first layer. The larger distance to the surface of the sodium ions is probably due to the strongly coordinated configuration of the first water layer. In that case the free binding sites, owing to the shortage of surface protons, would be too small for the sodium ions. Furthermore the stabilization of the sodium ions in between the first and second water layer might explain the by 0.1 Å shifted second maximum compared to the stoichiometric case which is in agreement with studies on TiO_2 [KBL08]. The position of the three chlorine ions shows a broader distribution over the simulation box. While two ions settle in between the second and third water layer, displayed in maxima at the positions of 3.9 and 5.2 Å , the remaining ion is solvated in the bulk water regime. The distribution of the counter ions in the simulation cell corresponds to the formation

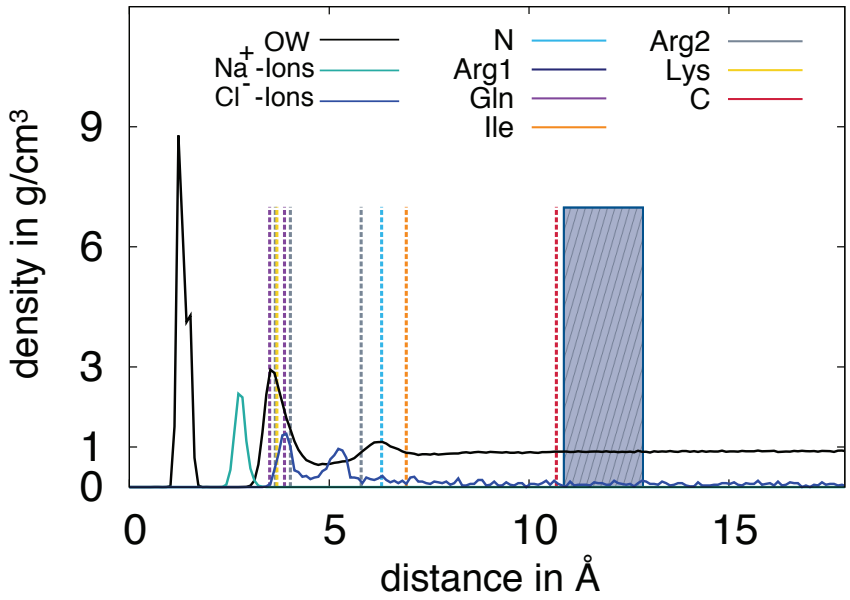

Figure 5.13.: Distribution of the density of bulk water, sodium ions and chlorine ions during the 10 ns NVE production run.. Additionally the averaged positions for the first 4 ns of NVE simulations time of the amino acid residues are marked by colored lines(hatched area for Arg1).

of an electrical double layer [HV05]. Thereby the partially hydroxylated water layer constitutes the first layer and is responsible for the surface charge. The sodium ions then give rise to the diffuse layer, which screens the surface charge but is only loosely bound to the first layer via electrostatical forces.

The nature of the bonding of the contact points between the amino acid residues and the surface can also be explained by looking at the height of the single residues compared to the formed water layer. Therefore in figure 5.13 the average positions of the different residues over the first 4 ns of simulations are plotted in relation to the water density. All three residues (Arg2, Lys, Gln) that display direct contact points lie within the second water layer. This finding strengthens the argument that no direct interaction between the pentapeptide and the surface is observed. Furthermore this finding is in agreement with the adsorption configurations for single amino acids obtained with DFT and DFTB (see chapter 4.1). Since the results of both model systems emphasize the importance of the role of the first water layer in interactions with approaching adsorbents. Hence in both cases, the single amino acids and the residue of the pentapeptide, the interaction is mediated by the first water layer which therefore strongly dominates the possible adsorption conformations.

Secondary Structure of the Pentapeptide

In order to evaluate the structure of the pentatpeptide for all three different surface hydration states, the corresponding Ramachandran plots are analyzed. In this kind of evaluation the backbone dihedral angles, between N-C_α-C-N (Ψ) and C-N-C_α-C (Φ) connecting the amino acids constituents of the peptide are plotted against each other for all configurations present in the trajectory. The Ramachandran plot of the pentapeptide on the stoichiometric surface and on the partially pronated surface are displayed in figure 5.14. For both cases the configurations

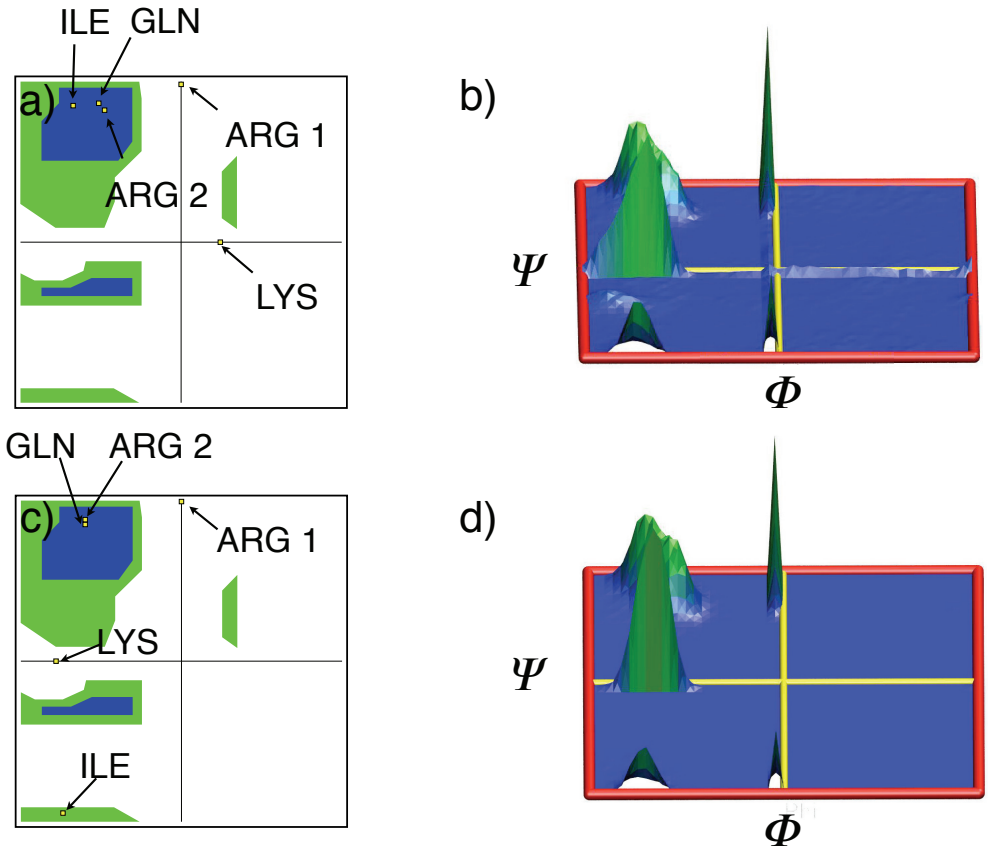

Figure 5.14.: Ramachandran plot of the pentapeptide during the 10 ns NVE run for the case of a stochiometric hydration (a) & (b) and a partially protonated hydration (c) & (d) of the ZnO (10$\bar{1}$0) surface.

adopted by the three center amino acid residues (Ile,Gln,Arg2) of the peptide belong to beta-sheet conformations. The two remaining residues, due to their position in the peptide, do not display a culmination within one of the three significant regions. Since the residues of the pentatpetide in these two cases do not display a stable adsorption to either the surface or the first water layer one can conclude that the adopted beta sheet configuration correspond to the one found for the pentapeptide solvated in bulk water.

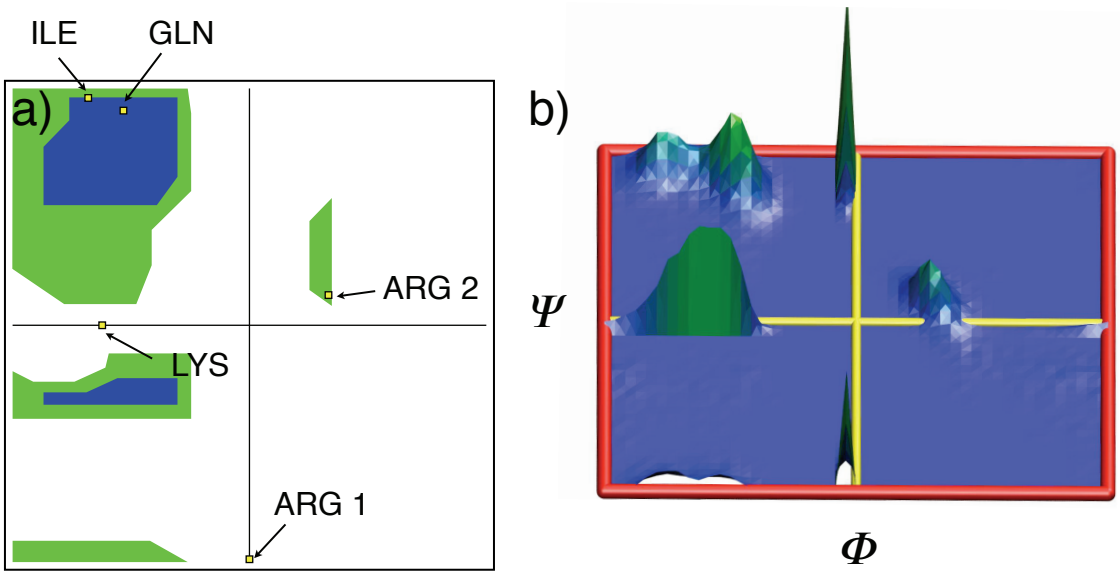

Figure 5.15.: Ramachandran plot of the pentpeptide during the 10 ns NVE run for the case of a partly hydroxylated ZnO $(10\bar{1}0)$ surface.

The secondary structure of the pentapeptide shows a different characteristic for the case of the partially hydroxylated surface, as shown in the corresponding Ramachandran plot (see figure 5.15) Apart from a beta sheet configuration for the three inner amino acid residues, one arginine residue (Arg2) temporarily displays a left-handed helix conformation. The reason for this discrepancy can be explained with the help of a time dependent plot of the corresponding dihedral angles Ψ and Φ (figure 5.16). From the time evolution of both angles it is evident that the configuration adopted by the pentapeptide in the first 6 ns of the simulation corresponds to a left-handed helix conformation. Comparison with the evaluation of the height of the residues with respect to time yields that this conformation is formed when glutamine, lysine and one arginine form contact points to the surface. Subsequent to the short temporary desorption of the pentapeptide the dihedral angles of the Arg2 residues are found to switch into a beta-sheet conformation, corresponding to the adsorption configuration stabilized by contact points between the two arginine residues and the glutamine to the first water layer. Therefore the change of the adsorption mode is closely catenated with a change in the secondary structure of the pentapeptide. Since the non-desorbed pentapetide displayed a beta-sheet configuration (stoichiometric case) one can interpret that the first adsorption mode (time frame 0 to approx. 4.5 ns) is accompanied by a resulting strain in the secondary structure of the pentapeptide, visible through the occurrence of the a left-handed helix conformation. This strain is loosened through the rearrangement of the contact point, leaving the pentapetide in the more relaxed secondary structure of a beta sheet.

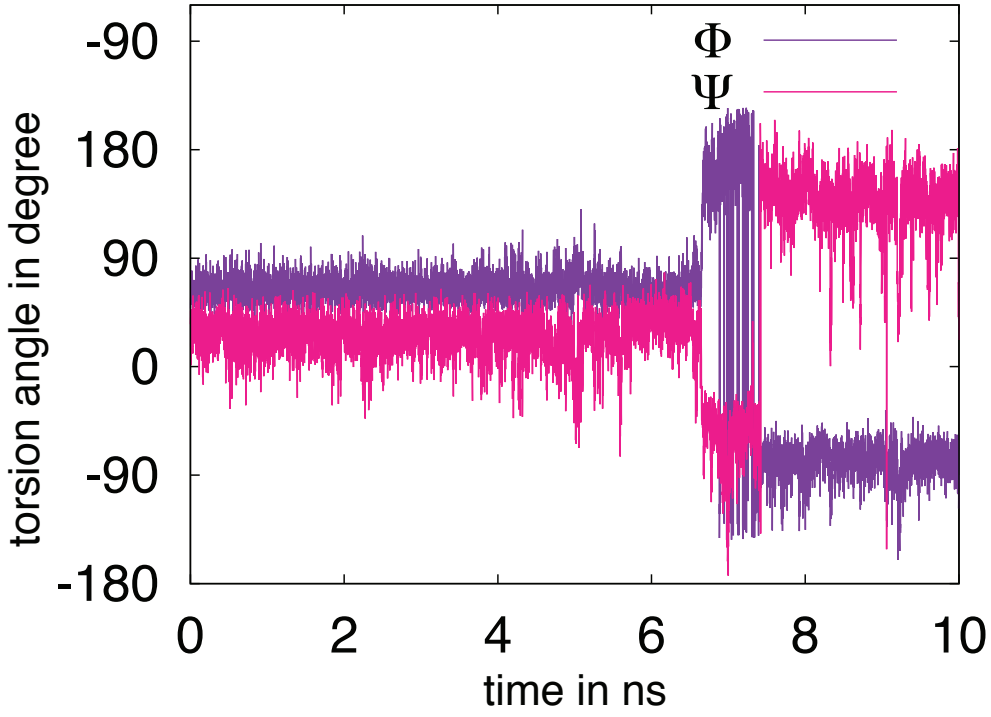

Figure 5.16.: Time evolution of the torsion angles Φ and Ψ of the residue Arg2.

5.4. Conclusions

The presented results show that the parameterized forcefield is able to resemble DFT results for a pre-chosen parameterization set comprising the interaction between a hydrated ZnO surface and with water molecules as well as with small bio molecules. Nevertheless the introduction of special cases were necessary to also achieve satisfactory results for the interaction with nitrogen-containing compounds.

In the final section of this chapter the newly parameterized forcefield was used to analyze the influence of the hydration state of the ZnO $(10\bar{1}0)$ on the formation of contact points between the surface and the previously in chapter 4 introduced pentapeptide. The obtained results showed a distinct dependency of the adsorption mode on the charges present on the surface. For the stoichiometric hydration no permanent adsorption was visible. In the case of the protonated surface the terminal C group formed a contact point, which was found to even interact directly with a surface zinc atom. This pronounced affinity between the carboxylate group and surface zinc atoms resembles previous findings for other oxide surfaces. Using classical forcefield calculations, Monti and co-workers showed [MCZY07] that for the interaction between two different dipeptides (AE and AK) and the (100) rutile surface of TiO_2 carbonyl oxygens apart from nitrogen atoms are the most probable contact points. This was also found by experimental techniques, which proved a complex formation of the backbone carboxyl groups of various amino

acids with the surface of TiO_2 powder samples [Sch01].

Since the considered pentapeptide is positively charged, the most pronounced interactions [6] were observed for the partially hydroxylated surface. The adsorption was thereby found to be dominated by the charged residues of the peptide. Interestingly the most probable contact points comprised the basic arginine residue. A leading role of this residue concerning the binding process to ZnO surfaces was also concluded from the experimental findings by Thai et al. [TDS+04]. In addition a study using a cell display procedure to identify good binding sequences also found arginine to be one of four overrepresented residues in the evaluated binding sequences[KSSK00].

For all three cases, the water was found to form a very structured first water layer, compared to previous DFT results (see chapter 4.1 [RDG+11, MRM06]. Since the configuration of the local structure was proven to be of elemental importance for possible adsorption scenarios this deficiency is a weak point in the parameterization of the classical forcefield. Furthermore the water model used in these OPLS-AA based calculations, namely TIP3P is known to exhibit several shortcomings in the description of liquid water [KB11]. In order to analyze the influence of the applied water model on the obtained results a study comparing different water model like SPC/E or the TIP4P water model should be taken into account in future calculations. Nevertheless the overall adsorption mode evaluated in this section using TIP3P water was found to resemble previous DFT/DFTB results for the adsorption of single amino acids, since it was dominated by H-bond formation between the first water layer and the biomolecule. Especially this finding therefore justifies the approach, often applied in the theoretical treatment of larger biomolecules with inorganic surfaces (and also chapter 4.1), that uses highly sophisticated methods like DFT calculations in a reduced systems comprising just one residue and the hybrid interface in order to describe the adsorption of a larger peptide onto the latter. Yet one has to stress that the size of the pentapetide discussed in this chapter is still small and much more complex peptide configurations are accessible by classical forcefield calculations.

Our results also emphasize that not only the direct interactions at the contact points have an influence on the overall adsorption mode, also the secondary structure of the biomolecule can play an important role in the formation of contact points to the surface. This is especially true if numerous contact points are formed with the surface [MCZY07] as evident by the comparison of the secondary structure obtained in the cases of a protonated first layer layer where only one contact point was formed set aside with the one of a hydroxylated water layer correlated with three contact points. This finding therefore exhibits one major challenge in the description of peptide interactions with inorganic surface: A description of such a complex interface at a molecular level is ideally an interplay between the difference methods. Therefore if we proceed to combine the knowledge acquired by DFT simulation, that are aimed at describing smaller parts of the systems in more detail, with more complex model of the ZnO/water/bio interface we are one step closer to creating a whole picture out of the single puzzle pieces.

[6] In this context pronounced refers to the number of formed contact points

6 Chapter 6. Concluding Remarks and Outlook

This thesis was set out to theoretically investigate the complex ZnO/water/bio interface. In this work I have presented results using a step-by-step approach, comprising different model systems, which aimed to depict various aspects of this complex surface, starting from the primitive cell of bulk ZnO, going to a slab model including a surface charge in contact with a pentapeptide. One of the main focus points in all the different model systems was thereby the interaction between the inorganic surface and water and how a water environment changes the adsorption characteristics of approaching molecules. This is an aspect that has until today only been considered by a few theoretical studies focusing on ZnO. Nevertheless the results presented in this work prove that its influence is of tremendous importance for many systems.

One distinctive feature of this thesis is the application of four different methods within the framework of the presented work. Although all four of them rely on the widely used method of molecular dynamics simulations, they differ in the way they describe and approximate the electron-electron interactions. This particular interaction was described using a fully quantum mechanic based method, namely density functional theory (which was also used for all reference calculations), over to two approximate methods, DFTB and ReaxFF, through to a fully classical description by means of a forcefield parameterized for this purpose. Depending on the underlying requirement of the system regarding the methods, the results for the various systems were produced using a selection out of these four methods. In this context particular attention was paid to a careful validation of the applied methods in order to ensure a reliable interpretation of the results reported in this work. Undoubtedly this will also be of great help for future studies focusing on this hybrid interface.

Before a biomolecule is able to interact with a ZnO surface under ambient conditions it will get into contact with the adsorbed water molecules and the solution present at this interface. Through a sequence of both geometry relaxations and molecular dynamics simulations using DFT, I have demonstrated that the water molecules of the first strongly adsorbed water monolayer are partially dissociated on the ZnO $(1\bar{2}10)$ surface. The results also showed that the

degree of dissociation of the first water monolayer, especially under the influence of additional bulk water, is highly dependent on the applied method, namely DFT, DFTB or ReaxFF.

Going one step further by considering the adsorption of four single amino acids on the hydrated ZnO $(10\bar{1}0)$ surface, DFT results showed that in most cases the interaction between molecule and surface is mediated by the first layer of adsorbed water molecules. This finding emphasized the need for a correct description of the local water structure when considering adsorption processes and stresses the urge for a solution of the discrepancies of the obtained water structures described for the case of the ZnO $(1\bar{2}10)$ surface. A validation of the DFTB set up on the subject of adsorption characteristics of amino acids on the ZnO $(10\bar{1}0)$ surface showed a good agreement with DFT results regarding adsorption geometries, nonetheless the results exhibited a misinterpretation of the underlying energetics. Looking at the affinities of the different sidechains considered as part of this work (either as part of the acetic acid, single amino acids or residues and terminal groups of the pentapeptide), for the perfect $(10\bar{1}0)$ surface, for the ZnO-nanowire as well as for a kinked $(10\bar{1}0)$ surface, the carboxylic group present e.g. in the side chain of glutamate is found to display a strong affinity towards surface zinc atoms. This aspect was found in simulations performed with DFT, DFTB and the classical forcefield, however results regarding the adsorption of a specific binder motif also suggested that a possible interaction was highly dependent on the present surface charge, i.e. on the existent pH-value.

The adsorption of a pentapeptide comprising a specific binding motif of ZnO was used as a first application of the newly introduced forcefield, since DFTB calculations on that system proved to be helpful but insufficient concerning applicable simulation times. The results showed that the adsorption mode was highly dependent on the surface hydration state. In addition further analysis demonstrated that the secondary structure of the considered pentapeptide is also a factor of tremendous importance when simulating the adsorption of such large biomolecules. Therefore in this last chapter I was able to build a bridge between results obtainable from quantum-mechanical molecular dynamics and molecular mechanics simulations. I concluded that the results emphasize the need for a coordinated interplay between ab-initio and classical methods in order to reliably describe interfaces of this complexity.

The model system considered and the results presented in the framework of this work were seen as single puzzle pieces, which when combined will deliver a description of processes occurring at the ZnO/water/bio interface. Doubtlessly the findings obtained, have brought us an important step further along the way however they have also given rise to new challenges and research fields beyond the scope of this thesis. One of the challenges is the correct description of the first water layer on the ZnO $(1\bar{2}10)$ surface, which will be essential for further analysis of adsorption mechanisms at this hybrid interface. Since the theoretical results revealed discrepancies on that matter, only a corresponding experimental study can help to judge about the degree of dissociation. Currently, motivated by the presented theoretical results, an experimental study using infrared spectroscopy under ultra-high vacuum conditions is focusing at this

topic. Unfortunately first evaluations of the obtained spectra did not show a clear result, so that further measurements are necessary to differentiate between the number of molecular and dissolved water molecules present on the surface[1].

Furthermore the variety of model systems should also be extended in future studies in order to build more complex models of the ZnO/water/bio interface. Especially a detailed analysis of the role of surface roughness or defects in adsorption processes is until today still missing in theoretical studies on ZnO interfaces. Although preliminary results on defect surfaces have been reported as part of this work, larger and more diverse models based on experimental findings (e.g. from atomic force spectroscopy) are necessary in order to describe realistic surface conditions.

The presented results in the adsorption of a pentapepetide constitute an excellent starting point for a systematic analysis of "good" and "bad" binding peptide sequences. Therefore a comparison between good and bad binding motifs using molecular dynamics has to be conducted in close cooperation with experimental measurement. Moreover the results on the adsorption of small peptides could be used to extend the model system in order to understand the adsorption of whole proteins.

One issue, which constitutes also the initial motivation of this thesis that combines all different puzzle pieces and future challenges is the question about the solubility and in detail the dissolution of ZnO. Therefore in future molecular dynamic studies based on this work, more sophisticated methods that are able to explore complex energy landscapes and describe rare events are needed. A promising method in this field is an approach called metadynamics. First calculations using DFTB with metadynamics to validate this combined approach using the well studied torsion angles of chondroitin sulfate as a model system, showed a good agreement with literature results. Yet the description of a dissolution process comprising all its possible degrees of freedom is still a huge challenge in todays computational materials science. However I believe that this work constitutes a reliable basis and will be of great help for this and various other kinds of future challenges focusing on the hybrid inorganic/bio surface.

[1] These experiments are expected to start in March 2014.

Appendix A.

A Appendix I

A.1. Extensions to the Forcefield Parametrization

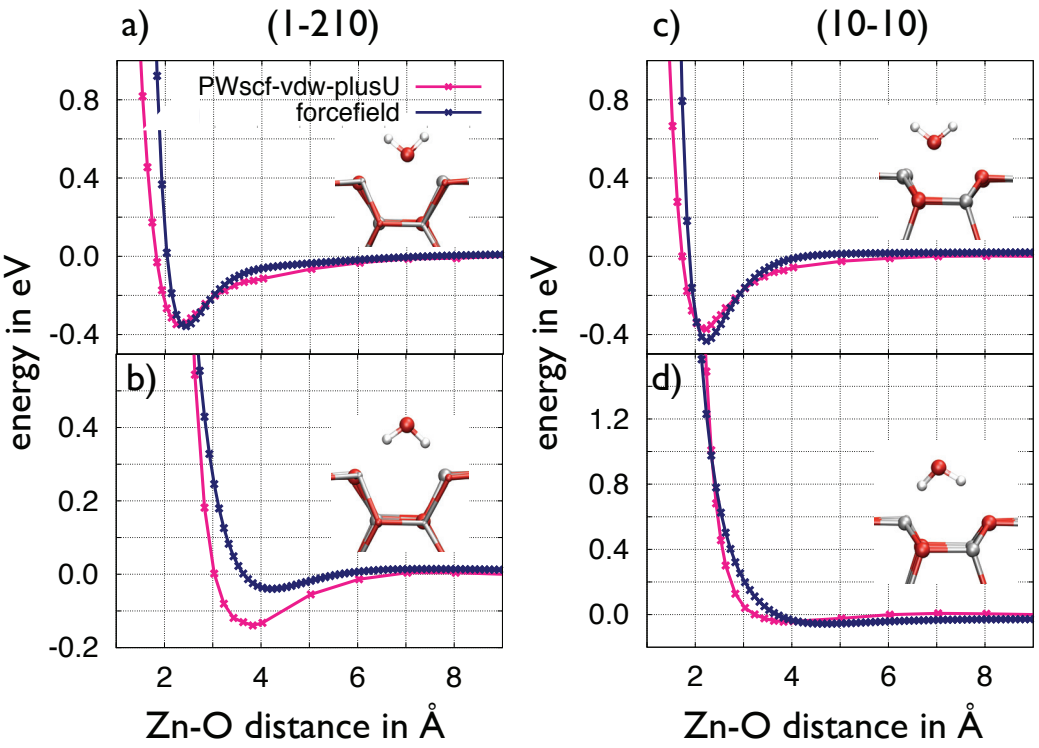

Figure A.1.: Energy curves evaluated from single point calculations of one water molecule in different distances from the corresponding surface. Figures a) and B) display the results for the $(1\bar{2}10)$ surface while figures c) and d) show the results for the $(10\bar{1}0)$ surface.All four insets present the orientation of water above the surface(a) & c) Top and b) and d) Bottom).

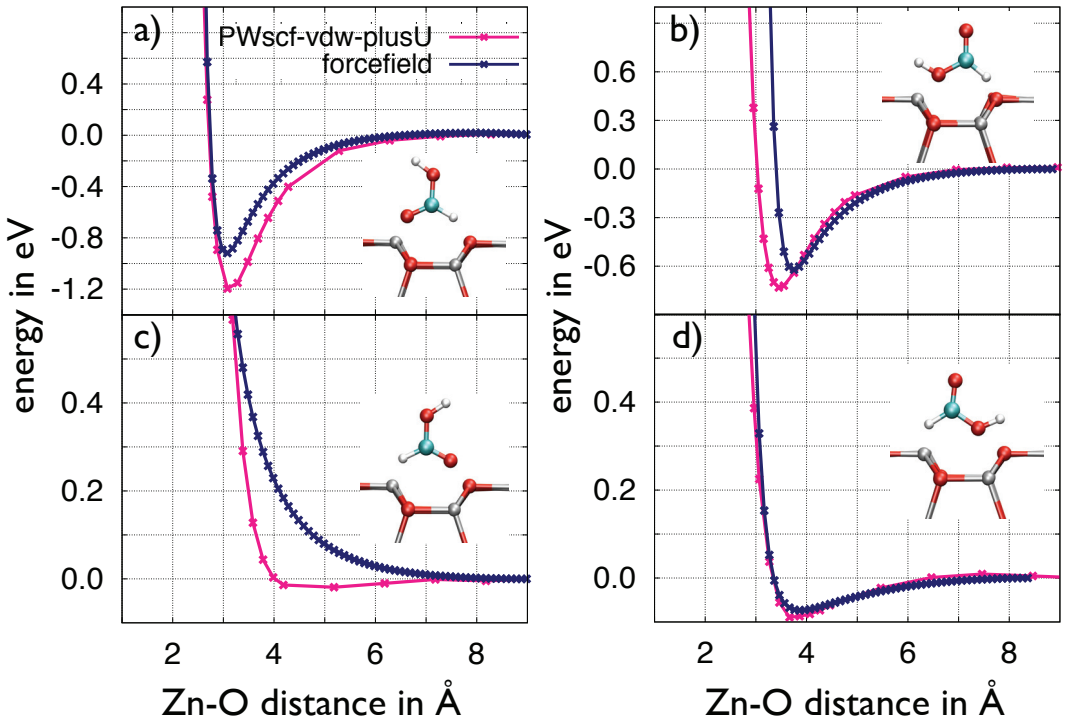

Figure A.2.: Energy curves evaluated from single point calculations of acetic acid in different distances from the $(10\bar{1}0)$ surface for four different initial orientations.

Table A.1.: Partial Charges and Lennard-Jones Parameters of surface atoms and the water molecule used in the calculation of the classical energy profiles.

atomtype i	**q_i/e**	**σ_i/ Å**	**ϵ_i/ kcal mol^{-1}**	**reference**
Zn	2.0	2.02	0.72	
O(Zn**O**)	-2.0	2.25	0.30	
O(ZnO-**O**H)	-0.834*	2.25	0.30	* [JCM$^+$83]
H(ZnO-O**H**)	-0.417*	0.00	0.00	* [JCM$^+$83]
O(H_2**O**)	-0.834	3.1507	0.152	[JCM$^+$83]
H(**H_2**O)	-0.417	0.00	0.00	[JCM$^+$83]

Table A.2.: Partial Charges and Lennard-Jones Parameters of atoms of the acetic acids molecule used in the calculation of the classical energy profiles.

atomtype i	q_i/e	σ_i/ Å	ε_i/ kcal mol^{-1}	reference
C(**C**H_2O_2)	0.51	3.75	0.105	[JMTR96]
H1(C**H**$_2O_2$)	0.45	0.00	0.00	[JMTR96]
H2(C**H**$_2O_2$)	0.06	2.42	0.015	[JMTR96]
O1(CH_2**O**$_2$)	-0.50	3.00	0.170	[JMTR96]
O2(CH_2**O**$_2$)	-0.46	2.96	0.210	[JMTR96]

Table A.3.: Partial Charges and Lennard-Jones Parameters of atoms of the nitrogen-containing molecules used in the calculation of the classical energy profiles.

atomtype i	q_i/e	$\sigma_i(\sigma_{ij})$/ Å	$\varepsilon_i(\varepsilon_{ij})$/ kcal mol^{-1}	reference
Zn-N(**N**H_3)	-0.84*	2.80	0.30	*[JMTR96]
O-N(**N**H_3)	-0.84*	3.20	0.40	*[JMTR96]
H(N**H**$_3$)	0.28	0.00	0.00	[JMTR96]
C(**C**ONH_2)	0.50	3.75	0.105	[JMTR96]
O(C**O**NH_2)	-0.50	2.96	0.21	[JMTR96]
Zn-N(CO**N**H_2)	-0.76*	2.8	0.30	* [JMTR96]
O-N(CO**N**H_2)	-0.76*	3.20	0.40	*[JMTR96]
H(CON**H**$_2$)	0.38	0.00	0.00	[JMTR96]
C1(**C**$_3H_4$N2)	0.275	3.55	0.070	[JMTR96]
C2(**C**$_3H_4$N2)	0.185	3.55	0.070	[JMTR96]
C3(**C**$_3H_4$N2)	-0.286	3.55	0.070	[JMTR96]
H1(C_3**H**$_4$N2)	0.306	0.00	0.00	[JMTR96]
H2(C_3**H**$_4$N2)	0.078	2.42	0.030	[JMTR96]
H3(C_3**H**$_4$N2)	0.075	2.42	0.030	[JMTR96]
H4(C_3**H**$_4$N2)	0.187	2.42	0.030	[JMTR96]
N1(C_3H_4**N**2)	-0.257	3.25	0.170	[JMTR96]
Zn-N2(C_3H_4**N**2)	-0.563*	2.31	0.20	* [JMTR96]
O-N2(C_3H_4**N**2)	-0.563*	3.24	0.70	*[JMTR96]

Bibliography

[AB69] Abrahams, S. C. ; Bernstein, J. L.: Remeasurement of the structure of hexagonal ZnO. In: *Acta Crystallographica Section B* 25 (1969), Jul, Nr. 7, S. 1233–1236

[AHF07] Aradi, B. ; Hourahine, B. ; Frauenheim, Th.: DFTB+, a Sparse Matrix-Based Implementation of the DFTB Method. In: *The Journal of Physical Chemistry A* 111 (2007), Nr. 26, S. 5678–5684

[AMB] *D.A. Case, T.A. Darden, T.E. Cheatham, III, C.L. Simmerling, J. Wang, R.E. Duke, R. Luo, R.C. Walker, W. Zhang, K.M. Merz, B. Roberts, S. Hayik, A. Roitberg, G. Seabra, J. Swails, A.W. Goetz, I. Kolossváry, K.F. Wong, F. Paesani, J. Vanicek, R.M. Wolf, J. Liu, X. Wu, S.R. Brozell, T. Steinbrecher, H. Gohlke, Q. Cai, X. Ye, J. Wang, M.-J. Hsieh, G. Cui, D.R. Roe, D.H. Mathews, M.G. Seetin, R. Salomon-Ferrer, C. Sagui, V. Babin, T. Luchko, S. Gusarov, A. Kovalenko, and P.A. Kollman (2012), AMBER 12, University of California, San Francisco.*

[AZA91] Anisimov, Vladimir I. ; Zaanen, Jan ; Andersen, Ole K.: Band theory and Mott insulators: Hubbard *U* instead of Stoner *I*. In: *Phys. Rev. B* 44 (1991), Jul, S. 943–954

[BBB+09] Bonomi, Massimiliano ; Branduardi, Davide ; Bussi, Giovanni ; Camilloni, Carlo ; Provasi, Davide ; Raiteri, Paolo ; Donadio, Davide ; Marinelli, Fabrizio ; Pietrucci, Fabio ; Broglia, Ricardo A. ; Parrinello, Michele: PLUMED: A portable plugin for free-energy calculations with molecular dynamics. In: *Computer Physics Communications* 180 (2009), Nr. 10, S. 1961 – 1972

[BBMH01] Bauer, Christophe ; Boschloo, Gerrit ; Mukhtar, Emad ; Hagfeldt, Anders: Electron Injection and Recombination in $Ru(dcbpy)_2(NCS)_2$ Sensitized Nanostructured ZnO. In: *The Journal of Physical Chemistry B* 105 (2001), Nr. 24, S. 5585–5588

[BBO+83] Brooks, Bernard R. ; Bruccoleri, Robert E. ; Olafson, Barry D. ; States, David J. ; Swaminathan, S. ; Karplus, Martin: CHARMM: A program for macromolecular energy, minimization, and dynamics calculations. In: *Journal of Computational Chemistry* 4 (1983), Nr. 2, S. 187–217

[BFS+04] Bondar, Ana-Nicoleta ; Fischer, Stefan ; Smith, Jeremy C. ; Elstner, Marcus ; Suhai, Sándor: Key Role of Electrostatic Interactions in Bacteriorhodopsin Proton Transfer. In: *Journal of the American Chemical Society* 126 (2004), Nr. 44, S. 14668–14677

[Blo29] Bloch, Felix: Über die Quantenmechanik der Elektronen in Kristallgittern. In: *Zeitschrift für Physik* 52 (1929), Nr. 7-8, S. 555–600. – ISSN 0044–3328

[BXAM09] Bai, Hanying ; Xu, Fen ; Anjia, Luona ; Matsui, Hiroshi: Low temperature synthesis of ZnO nanowires by using a genetically-modified collagen-like triple helix as a catalytic template. In: *Soft Matter* 5 (2009), S. 966–969

[BZ04] Barnard, A. S. ; Zapol, P.: Effects of particle morphology and surface hydrogenation on the phase stability of TiO_2. In: *Phys. Rev. B* 70 (2004), Dec, S. 235403

[BZT+10] Bai, Wei ; Zhang, Zhiyong ; Tian, Wenjing ; He, Xiao ; Ma, Yuhui ; Zhao, Yuliang ; Chai, Zhifang: Toxicity of zinc oxide nanoparticles to zebrafish embryo: a physicochemical study of toxicity mechanism. In: *Journal of Nanoparticle Research* 12 (2010), Nr. 5, S. 1645–1654

[CC09] Calzolari, Arrigo ; Catellani, Alessandra: Water Adsorption on Nonpolar ZnO(10-10) Surface: A Microscopic Understanding. In: *The Journal of Physical Chemistry C* 113 (2009), Nr. 7, S. 2896–2902

[CCC+10] Calzolari, Arrigo ; Cicero, Giancarlo ; Cavazzoni, Carlo ; Di Felice, Rosa ; Catellani, Alessandra ; Corni, Stefano: Hydroxyl-Rich β-Sheet Adhesion to the Gold Surface in Water by First-Principle Simulations. In: *Journal of the American Chemical Society* 132 (2010), Nr. 13, S. 4790–4795

[CEE12] Cakir, Alisah C. ; Erten-Ela, Sule: Comparison between synthesis techniques to obtain ZnO nanorods and its effect on dye sensitized solar cells. In: *Advanced Powder Technology* 23 (2012), Nr. 5, S. 655 – 660

[CG05] Cococcioni, Matteo ; Gironcoli, Stefano de: Linear response approach to the calculation of the effective interaction parameters in the LDA + U method. In: *Phys. Rev. B* 71 (2005), Jan, S. 035105

[CMP06] Cooke, David J. ; Marmier, Arnaud ; Parker, Stephen C.: Surface Structure of $(10\bar{1}0)$ and $(11\bar{2}0)$ Surfaces of ZnO with Density Functional Theory and Atomistic Simulation. In: *The Journal of Physical Chemistry B* 110 (2006), Nr. 15, S. 7985–7991

[CMW09] Campañá, Carlos ; Mussard, Bastien ; Woo, Tom K.: Electrostatic Potential Derived Atomic Charges for Periodic Systems Using a Modified Error Functional. In: *Journal of Chemical Theory and Computation* 5 (2009), Nr. 10, S. 2866–2878

[CP85] Car, R. ; Parrinello, M.: Unified Approach for Molecular Dynamics and Density-Functional Theory. In: *Phys. Rev. Lett.* 55 (1985), Nov, S. 2471–2474

[CPM] *CPMD, Copyright IBM Corp 1990-2004, Copyright MPI fuer Festkoerperforschung Stuttgart 1997- 2001*

[CRC11] Calzolari, Arrigo ; Ruini, Alice ; Catellani, Alessandra: Anchor Group versus Conjugation: Toward the Gap-State Engineering of Functionalized ZnO(101?0) Surface for Optoelectronic Applications. In: *Journal of the American Chemical Society* 133 (2011), Nr. 15, S. 5893–5899

[CVTG09] Cole, Martin A. ; Voelcker, Nicolas H. ; Thissen, Helmut ; Griesser, Hans J.: Stimuli-responsive interfaces and systems for the control of protein-surface and cell-surface interactions. In: *Biomaterials* 30 (2009), Nr. 9, S. 1827–1850

[Czy07] Czycholl, G.: *Theoretische Festkörperphysik: Von den klassischen Modellen zu modernen Forschungsthemen*. Springer, 2007 (Springer-Lehrbuch)

[DCT+05] Dai, Haixia ; Choe, Woo-Seok ; Thai, Corrine K. ; Sarikaya, Mehmet ; Traxler, Beth A. ; Baneyx, François ; Schwartz, Daniel T.: Nonequilibrium Synthesis and Assembly of Hybrid Inorganic-Protein Nanostructures Using an Engineered DNA Binding Protein. In: *Journal of the American Chemical Society* 127 (2005), Nr. 44, S. 15637–15643

[DCZ97] Dong, L.F. ; Cui, Z.L. ; Zhang, Z.K.: Gas sensing properties of nano-ZnO prepared by arc plasma method. In: *Nanostructured Materials* 8 (1997), Nr. 7, S. 815 – 823

[DDLG01] Duin, Adri C. T. ; Dasgupta, Siddharth ; Lorant, Francois ; Goddard, William A.: ReaxFF: A Reactive Force Field for Hydrocarbons. In: *The Journal of Physical Chemistry A* 105 (2001), Nr. 41, S. 9396–9409

[DHK+14] Dominguez, Adriel ; Holthaus, Svea grosse ; KOppen, Susan ; Frauenheim, Thomas ; Rosa, Andreia L.: The role of water co-adsorption on the modification of ZnO nanowires with acetic acid. In: *Phys. Chem. Chem. Phys.* (2014), S. –

[Die03] Diebold, Ulrike: The surface science of titanium dioxide. In: *Surface Science Reports* 48 (2003), Nr. 5-8, S. 53–229

[DKD04] Diebold, Ulrike ; Koplitz, Lynn V. ; Dulub, Olga: Atomic-scale properties of low-index ZnO surfaces. In: *Applied Surface Science* 237 (2004), Nr. 1-4, S. 336 – 342

[DLC+77] Duke, C. B. ; Lubinsky, A. R. ; Chang, S. C. ; Lee, B. W. ; Mark, P.: Low-energy-electron-diffraction analysis of the atomic geometry of ZnO $(10\bar{1}0)$. In: *Phys. Rev. B* 15 (1977), May, S. 4865–4873

[DMD+11] Domínguez, A. ; Moreira, N. H. ; Dolgonos, G. ; Frauenheim, T. ; Rosa, A. L.: Glycine Adsorption on $(10\bar{1}0)$ ZnO Surfaces. In: *The Journal of Physical Chemistry C* 115 (2011), Nr. 14, S. 6491–6495

[Els98] Elstner, Marcus: *Weiterentwicklung quantenmechanischer Rechenverfahren für organische Moleküle und Polymere*. Paderborn, Germany, University of Paderborn, Faculty Physics, Diss., 4 1998

[Els07] Elstner, M.: SCC-DFTB: What Is the Proper Degree of Self-Consistency? In: *The Journal of Physical Chemistry A* 111 (2007), Nr. 26, S. 5614–5621

[EPJ+98] Elstner, M. ; Porezag, D. ; Jungnickel, G. ; Elsner, J. ; Haugk, M. ; Frauenheim, Th. ; Suhai, S. ; Seifert, G.: Self-consistent-charge density-functional tight-binding method for simulations of complex materials properties. In: *Phys. Rev. B* 58 (1998), Sep, Nr. 11, S. 7260–7268

[ES83] Evarestov, R. A. ; Smirnov, V. P.: Special points of the brillouin zone and their use in the solid state theory. In: *physica status solidi (b)* 119 (1983), Nr. 1, S. 9–40

[Fie07] Field, M.J.: *A Practical Introduction to the Simulation of Molecular Systems*. Cambridge University Press, 2007

[FRA+07] Franklin, Natasha M. ; Rogers, Nicola J. ; Apte, Simon C. ; Batley, Graeme E. ; Gadd, Gerald E. ; Casey, Philip S.: Comparative Toxicity of Nanoparticulate ZnO, Bulk ZnO, and ZnCl2 to a Freshwater Microalga (Pseudokirchneriella subcapitata): The Importance of Particle Solubility. In: *Environmental Science and Technology* 41 (2007), Nr. 24, S. 8484–8490

[FS01] Frenkel, Daan ; Smit, B.: *Understanding Molecular Simulation, Second Edition: From Algorithms to Applications (Computational Science)*. 2. Academic Press, 2001. – ISBN 0122673514

[FSE+00] Frauenheim, Th. ; Seifert, G. ; Elstner, M. ; Hajnal, Z. ; Jungnickel, G. ; Porezag, D. ; Suhai, S. ; Scholz, R.: A Self-Consistent Charge Density-Functional Based Tight-Binding Method for Predictive Materials Simulations in Physics, Chemistry and Biology. In: *physica status solidi (b)* 217 (2000), Nr. 1, S. 41–62

[Gau11] Gaus, Michael: *Extension and Parametrization of an Approximate Density Functional Method for Organic and Biomolecules*. Karlsruhe, Germany, Karlsruher Institut for Technology (KIT), Faculty of Chemistry, Diss., 7 2011

[GBB+09] Giannozzi, Paolo ; Baroni, Stefano ; Bonini, Nicola ; Calandra, Matteo ; Car, Roberto ; Cavazzoni, Carlo ; Ceresoli, Davide ; Chiarotti, Guido L. ; Cococcioni, Matteo ; Dabo, Ismaila ; Corso, Andrea D. ; Gironcoli, Stefano de ; Fabris, Stefano ; Fratesi, Guido ; Gebauer, Ralph ; Gerstmann, Uwe ; Gougoussis, Christos ; Kokalj, Anton ; Lazzeri, Michele ; Martin-Samos, Layla ; Marzari, Nicola ; Mauri, Francesco ; Mazzarello, Riccardo ; Paolini, Stefano ; Pasquarello, Alfredo ; Paulatto, Lorenzo ; Sbraccia, Carlo ; Scandolo, Sandro ; Sclauzero, Gabriele ; Seitsonen, Ari P. ; Smogunov, Alexander ; Umari, Paolo ; Wentzcovitch, Renata M.: QUANTUM ESPRESSO: a modular and open-source software project for quantum simulations of materials. In: *Journal of Physics: Condensed Matter* 21 (2009), Nr. 39, S. 395502

[GCE11] Gaus, Michael ; Cui, Qiang ; Elstner, Marcus: DFTB3: Extension of the Self-Consistent-Charge Density-Functional Tight-Binding Method (SCC-DFTB). In: *Journal of Chemical Theory and Computation* 7 (2011), Nr. 4, S. 931–948

[Gri06] Grimme, Stefan: Semiempirical GGA-type density functional constructed with a long-range dispersion correction. In: *Journal of Computational Chemistry* 27 (2006), Nr. 15, S. 1787–1799

[GS92] Gerischer, H. ; Sorg, N.: Chemical dissolution of zinc oxide crystals in aqueous electrolytes-An analysis of the kinetics. In: *Electrochimica Acta* 37 (1992), Nr. 5, S. 827 – 835

[GTS+09] Gao, Y.K. ; Traeger, F. ; Shekhah, O. ; Idriss, H. ; Wöll, C.: Probing the interaction of the amino acid alanine with the surface of ZnO. In: *Journal of Colloid and Interface Science* 338 (2009), Nr. 1, S. 16 – 21

[Hag76] Hagemark, K.I.: Defect structure of Zn-doped ZnO. In: *Journal of Solid State Chemistry* 16 (1976), Nr. 3Ð4, S. 293 – 299

[Har54] Harrison, Sol E.: Conductivity and Hall Effect of ZnO at Low Temperatures. In: *Phys. Rev.* 93 (1954), Jan, S. 52–62

[HCK+13] Huang, Jian ; Chu, Sheng ; Kong, Jieying ; Zhang, Long ; Schwarz, Casey M. ; Wang, Guoping ; Chernyak, Leonid ; Chen, Zhanghai ; Liu, Jianlin: ZnO pÐn Homojunction Random Laser Diode Based on Nitrogen-Doped p-type Nanowires. In: *Advanced Optical Materials* 1 (2013), Nr. 2, S. 179–185

[HCWH09] Hu, Xiaoke ; Cook, Sean ; Wang, Peng ; Hwang, Huey min: In vitro evaluation of cytotoxicity of engineered metal oxide nanoparticles. In: *Science of The Total Environment* 407 (2009), Nr. 8, S. 3070 – 3072

[Hed65] Hedin, Lars: New Method for Calculating the One-Particle Green's Function with Application to the Electron-Gas Problem. In: *Phys. Rev.* 139 (1965), Aug, S. A796–A823

[HIB+08] Heinlaan, Margit ; Ivask, Angela ; Blinova, Irina ; Dubourguier, Henri-Charles ; Kahru, Anne: Toxicity of nanosized and bulk ZnO, CuO and TiO2 to bacteria Vibrio fischeri and crustaceans Daphnia magna and Thamnocephalus platyurus. In: *Chemosphere* 71 (2008), Nr. 7, S. 1308 – 1316

[HJB+13] Hellström, Matti ; Jorner, Kjell ; Bryngelsson, Maria ; Huber, Stefan E. ; Kullgren, Jolla ; Frauenheim, Thomas ; Broqvist, Peter: An SCC-DFTB Repulsive Potential for Various ZnO Polymorphs and the ZnO-Water System. In: *The Journal of Physical Chemistry C* 117 (2013), Nr. 33, S. 17004–17015

[HK64] Hohenberg, P. ; Kohn, W.: Inhomogeneous Electron Gas. In: *Phys. Rev.* 136 (1964), Nov, S. B864–B871

[HKFCC12] Holthaus, Svea große ; Köppen, Susan ; Frauenheim, Thomas ; Colombi Ciacchi, Lucio: Atomistic Simulations of the ZnO($1\bar{2}10$)/Water Interface: A Comparison between First-Principles, Tight-Binding, and Empirical Methods. In: *Journal of Chemical Theory and Computation* 8 (2012), Nr. 11, S. 4517–4526

[Hoo85] Hoover, William G.: Canonical dynamics: Equilibrium phase-space distributions. In: *Phys. Rev. A* 31 (1985), Mar, S. 1695–1697

[HSC79] Hamann, D. R. ; Schlüter, M. ; Chiang, C.: Norm-Conserving Pseudopotentials. In: *Phys. Rev. Lett.* 43 (1979), Nov, S. 1494–1497

[HSG+08] Horinek, D. ; Serr, A. ; Geisler, M. ; Pirzer, T. ; Slotta, U. ; Lud, S. Q. ; Garrido, J. A. ; Scheibel, T. ; Hugel, T. ; Netz, R. R.: Peptide adsorption on a hydrophobic surface results from an interplay of solvation, surface, and intrapeptide forces. In: *Proceedings of the National Academy of Sciences* 105 (2008), Nr. 8, S. 2842–2847

[HV05] Hamann, C.H. ; Vielstich, W.: *Elektrochemie*. John Wiley & Sons Australia, Limited, 2005. – ISBN 9783527310685

[HWF+01] Huang, M. H. ; Wu, Y. ; Feick, H. ; Tran, N. ; Weber, E. ; Yang, P.: Catalytic Growth of Zinc Oxide Nanowires by Vapor Transport. In: *Advanced Materials* 13 (2001), Nr. 2, S. 113–116

[HWW12] Huang, Gui-Yang ; Wang, Chong-Yu ; Wang, Jian-Tao: Detailed check of the LDA+U and GGA+U corrected method for defect calculations in wurtzite ZnO. In: *Computer Physics Communications* 183 (2012), Nr. 8, S. 1749 – 1752

[HYY+08] Huang, Zhongbing ; Yan, Danhong ; Yang, Mei ; Liao, Xiaoming ; Kang, Yunqing ; Yin, Guangfu ; Yao, Yadong ; Hao, Baoqing: Preparation and characterization of the biomineralized zinc oxide particles in spider silk peptides. In: *Journal of Colloid and Interface Science* 325 (2008), Nr. 2, S. 356 – 362

[ICM09] Irrera, S. ; Costa, D. ; Marcus, P.: DFT periodic study of adsorption of glycine on the (0001) surface of zinc terminated ZnO. In: *Journal of Molecular Structure: {THEOCHEM}* 903 (2009), Nr. 1–3, S. 49 – 58

[IHS14] *Information Handling Services*. `http://www.ihs.com/index.aspx`. Version: 2014

[JBT+95] Janssens, Geert O. A. ; Baekelandt, Bart G. ; Toufar, Helge ; Mortier, Wilfried J. ; Schoonheydt, Robert A.: Comparison of Cluster and Infinite Crystal Calculations on Zeolites with the Electronegativity Equalization Method (EEM). In: *The Journal of Physical Chemistry* 99 (1995), Nr. 10, S. 3251–3258

[JCM+83] Jorgensen, William L. ; Chandrasekhar, Jayaraman ; Madura, Jeffry D. ; Impey, Roger W. ; Klein, Michael L.: Comparison of simple potential functions for simulating liquid water. In: *The Journal of Chemical Physics* 79 (1983), Nr. 2, S. 926–935

[JM83] Jorgensen, William L. ; Madura, Jeffry D.: Quantum and statistical mechanical studies of liquids. 25. Solvation and conformation of methanol in water. In: *Journal of the American Chemical Society* 105 (1983), Nr. 6, S. 1407–1413

[JMTR96] Jorgensen, William L. ; Maxwell, David S. ; Tirado-Rives, Julian: Development and Testing of the OPLS All-Atom Force Field on Conformational Energetics and Properties of Organic Liquids. In: *Journal of the American Chemical Society* 118 (1996), Nr. 45, S. 11225–11236

[KB09] Kannemann, Felix O. ; Becke, Axel D.: Van der Waals Interactions in Density-Functional Theory: Rare-Gas Diatomics. In: *Journal of Chemical Theory and Computation* 5 (2009), Nr. 4, S. 719–727

[KB11] Kiss, Peter T. ; Baranyai, Andras: Sources of the deficiencies in the popular SPC/E and TIP3P models of water. In: *The Journal of Chemical Physics* 134 (2011), Nr. 5

[KBL08] Köppen, Susan ; Bronkalla, Oliver ; Langel, Walter: Adsorption Configurations and Energies of Amino Acids on Anatase and Rutile Surfaces. In: *The Journal of Physical Chemistry C* 112 (2008), Nr. 35, S. 13600–13606

[KDHZ08] Kawska, Agnieszka ; Duchstein, Patrick ; Hochrein, Oliver ; Zahn, Dirk: Atomistic Mechanisms of ZnO Aggregation from Ethanolic Solution: Ion Association, Proton Transfer, and Self-Organization. In: *Nano Letters* 8 (2008), Nr. 8, S. 2336–2340

[KH01] Koch, Wolfram ; Holthausen, Max C.: *A Chemist's Guide to Density Functional Theory, 2nd Edition*. 2. Wiley-VCH, 2001

[KL06] Köppen, S. ; Langel, W.: Simulation of the interface of (100) rutile with aqueous ionic solution. In: *Surface Science* 600 (2006), Nr. 10, S. 2040–2050

[KL10] Köppen, Susan ; Langel, Walter: Simulation of Adhesion Forces and Energies of Peptides on Titanium Dioxide Surfaces. In: *Langmuir* 26 (2010), Nr. 19, S. 15248–15256

[Kli07] Klingshirn, C.: ZnO: Material, Physics and Applications. In: *ChemPhysChem* 8 (2007), Nr. 6, S. 782–803

[KLK+11] Ko, Seung H. ; Lee, Daeho ; Kang, Hyun W. ; Nam, Koo H. ; Yeo, Joon Y. ; Hong, Suk J. ; Grigoropoulos, Costas P. ; Sung, Hyung J.: Nanoforest of Hydrothermally Grown Hierarchical ZnO Nanowires for a High Efficiency Dye-Sensitized Solar Cell. In: *Nano Letters* 11 (2011), Nr. 2, S. 666–671

[KSK01] Kjærgaard, Kristian ; Schembri, Mark A. ; Klemm, Per: Novel Zn2+-Chelating Peptides Selected from a Fimbria-Displayed Random Peptide Library. In: *Applied and Environmental Microbiology* 67 (2001), Nr. 12, S. 5467–5473

[KSSK00] Kjærgaard, Kristian ; Sørensen, Jack K. ; Schembri, Mark A. ; Klemm, Per: Sequestration of Zinc Oxide by Fimbrial Designer Chelators. In: *Applied and Environmental Microbiology* 66 (2000), Nr. 1, S. 10–14

[LAM14] *LAMMPS Molecular Dynamics Simulator*. `http://lammps.sandia.gov`. Version: Februar 2014

[LCR+11] Litton, C.W. ; Collins, T.C. ; Reynolds, D.C. ; Capper, P. ; Kasap, S. ; Willoughby, A.: *Zinc Oxide Materials for Electronic and Optoelectronic Device Applications*. Wiley, 2011 (Wiley series in materials for electronic and optoelectronic applications)

[LDC+76] Lubinsky, A. R. ; Duke, C. B. ; Chang, S. C. ; Lee, B. W. ; Mark, P.: Atomic geometry of the low£index surfaces of ZnO: LEED analysis. In: *Journal of Vacuum Science and Technology* 13 (1976), Nr. 1, S. 189–192

[LDPP11] Liang, Mei-Keat ; Deschaume, Olivier ; Patwardhan, Siddharth V. ; Perry, Carole C.: direct evidence of zno morphology modification via the selective adsorption of zno-binding peptides. In: *j. mater. chem.* 21 (2011), S. 80–89

[LFR+05] Look, D. C. ; Farlow, G. C. ; Reunchan, Pakpoom ; Limpijumnong, Sukit ; Zhang, S. B. ; Nordlund, K.: Evidence for Native-Defect Donors in *n*-Type ZnO. In: *Phys. Rev. Lett.* 95 (2005), Nov, S. 225502

[LG08] Laio, Alessandro ; Gervasio, Francesco L.: Metadynamics: a method to simulate rare events and reconstruct the free energy in biophysics, chemistry and material science. In: *Reports on Progress in Physics* 71 (2008), Nr. 12, S. 126601

[LHS99] Look, D. C. ; Hemsky, J. W. ; Sizelove, J. R.: Residual Native Shallow Donor in ZnO. In: *Phys. Rev. Lett.* 82 (1999), Mar, S. 2552–2555

[Lid09] Lide, David R.: *Handbook of Chemistry and Physics*. CRC, 2009

[LN89] Liu, D. C. ; Nocedal, J.: On the limited memory BFGS method for large scale optimization. In: *Math. Program.* 45 (1989), Dezember, Nr. 3, S. 503–528

[LZTM10] Liu, Li-Min ; Zhang, Changjun ; Thornton, Geoff ; Michaelides, Angelos: Structure and dynamics of liquid water on rutile TiO2(110). In: *Phys. Rev. B* 82 (2010), S. 161415

[MAV10] Maupin, C. M. ; Aradi, Bálint ; Voth, Gregory A.: The Self-Consistent Charge Density Functional Tight Binding Method Applied to Liquid Water and the Hydrated Excess Proton: Benchmark Simulations. In: *The Journal of Physical Chemistry B* 114 (2010), Nr. 20, S. 6922–6931

[MCZY07] Monti, Susanna ; Carravetta, Vincenzo ; Zhang, Wenhua ; Yang, Jinlong: Effects Due to Interadsorbate Interactions on the Dipeptide/TiO2 Surface Binding Mechanism Investigated by Molecular Dynamics Simulations. In: *The Journal of Physical Chemistry C* 111 (2007), Nr. 21, S. 7765–7771

[MDA+09] Moreira, Ney H. ; Dolgonos, Grygoriy ; Aradi, Bálint ; Rosa, Andreia L. ; Frauenheim, Thomas: Toward an Accurate Density-Functional Tight-Binding Description of Zinc-Containing Compounds. In: *Journal of Chemical Theory and Computation* 5 (2009), Nr. 3, S. 605–614

[MH09] Marx, D. ; Hutter, J.: *Ab Initio Molecular Dynamics: Basic Theory and Advanced Methods*. Cambridge University Press, 2009 (Ab Initio Molecular Dynamics: Basic Theory and Advanced Methods). – ISBN 9780521898638

[ML10] Marx, A. ; Langel, W.: Measurement of adsorption isotherms in the gas phase on native titanium dioxide surfaces by quartz crystal microbalance technique. In: *Journal of Vacuum Science & Technology A* 28 (2010), Nr. 2, S. 232–237

[MM03] Meyer, B. ; Marx, D.: Density-functional study of the structure and stability of ZnO surfaces. In: *Phys. Rev. B* 67 (2003), Jan, Nr. 3, S. 035403

[MMD+04] Meyer, Bernd ; Marx, Dominik ; Dulub, Olga ; Diebold, Ulrike ; Kunat, Martin ; Langenberg, Deler ; Wöll, Christof: Partial Dissociation of Water Leads to Stable Superstructures on the Surface of Zinc Oxide. In: *Angewandte Chemie International Edition* 43 (2004), Nr. 48, S. 6641–6645

[MRF09] Moreira, Ney H. ; Rosa, Andreia L. ; Frauenheim, Thomas: Covalent functionalization of ZnO surfaces: A density functional tight binding study. In: *Applied Physics Letters* 94 (2009), Nr. 19

[MRM06] Meyer, Bernd ; Rabaa, Hassan ; Marx, Dominik: Water adsorption on ZnO($10\bar{1}0$): from single molecules to partially dissociated monolayers. In: *Phys. Chem. Chem. Phys.* 8 (2006), S. 1513–1520

[MS94] Meister, J. ; Schwarz, W. H. E.: Principal Components of Ionicity. In: *The Journal of Physical Chemistry* 98 (1994), Nr. 33, S. 8245–8252

[MTTK96] Martyna, Glenn J. ; Tuckerman, Mark E. ; Tobias, Douglas J. ; Klein, Michael L.: Explicit reversible integrators for extended systems dynamics. In: *Molecular Physics* 87 (1996), Nr. 5, S. 1117–1157

[MW11] Monti, Susanna ; Walsh, Tiffany R.: Molecular Dynamics Simulations of the Adsorption and Dynamical Behavior of Single DNA Components on TiO2. In: *The Journal of Physical Chemistry C* 115 (2011), 2012/07/30, Nr. 49, S. 24238–24246

[NMV+09] Nel, Andre E. ; Madler, Lutz ; Velegol, Darrell ; Xia, Tian ; Hoek, Eric M. V. ; Somasundaran, Ponisseril ; Klaessig, Fred ; Castranova, Vince ; Thompson, Mike: Understanding biophysicochemical interactions at the nano-bio interface. In: *Nat Mater* 8 (2009), 07, Nr. 7, S. 543–557

[NOU+03] Nomura, Kenji ; Ohta, Hiromichi ; Ueda, Kazushige ; Kamiya, Toshio ; Hirano, Masahiro ; Hosono, Hideo: Thin-Film Transistor Fabricated in Single-Crystalline Transparent Oxide Semiconductor. In: *Science* 300 (2003), Nr. 5623, S. 1269–1272

[OR93] Ohtaki, Hitoshi. ; Radnai, Tamas.: Structure and dynamics of hydrated ions. In: *Chemical Reviews* 93 (1993), Nr. 3, S. 1157–1204

[PB11] Pathria, R. K. ; Beale, P.D.: *Statistical Mechanics*. Third. Oxford, UK : Butterworth Heineman, 2011

[PBE96] Perdew, John P. ; Burke, Kieron ; Ernzerhof, Matthias: Generalized Gradient Approximation Made Simple. In: *Phys. Rev. Lett.* 77 (1996), Oct, S. 3865–3868

[PDW01] Pan, Zheng W. ; Dai, Zu R. ; Wang, Zhong L.: Nanobelts of Semiconducting Oxides. In: *Science* 291 (2001), Nr. 5510, S. 1947–1949

[PFK+95] Porezag, D. ; Frauenheim, Th. ; Köhler, Th. ; Seifert, G. ; Kaschner, R.: Construction of tight-binding-like potentials on the basis of density-functional theory: Application to carbon. In: *Phys. Rev. B* 51 (1995), May, S. 12947–12957

[PKJY02] Park, W. I. ; Kim, D. H. ; Jung, S.-W. ; Yi, Gyu-Chul: Metalorganic vapor-phase epitaxial growth of vertically well-aligned ZnO nanorods. In: *Applied Physics Letters* 80 (2002), Nr. 22, S. 4232–4234

[Pla91] Plato, Jan: Boltzmann's ergodic hypothesis. In: *Archive for History of Exact Sciences* 42 (1991), Nr. 1, S. 71–89. – ISSN 0003–9519

[Pli95] Plimpton, Steve: Fast Parallel Algorithms for Short-Range Molecular Dynamics. In: *Journal of Computational Physics* 117 (1995), Nr. 1, S. 1 – 19

[PLP+11] Park, Eunkyung ; Lee, Jungwoo ; Park, Taehee ; Lee, Jongtaek ; Lee, Donghwan ; Yi, Whikun: Aqueous synthesis of n-/p-type ZnO nanorods on porous silicon for the application of p-n junction device. In: *Nanotechnology (IEEE-NANO), 2011 11th IEEE Conference on*, 2011, S. 1226–1229

[PM77] Pack, James D. ; Monkhorst, Hendrik J.: "Special points for Brillouin-zone integrations"—a reply. In: *Phys. Rev. B* 16 (1977), Aug, S. 1748–1749

[PP] *We used the pseudopotentials 030-Zn0gpbe–bm.uspp, 008-O-gpbe–bm.uspp and 001-H-gpbe–bm.uspp from http://www.physics.rutgers.edu/ dhv/uspp/*

[PQCW06] Peng, Wenqin ; Qu, Shengchun ; Cong, Guangwei ; Wang, Zhanguo: Synthesis and Structures of Morphology-Controlled ZnO Nano- and Microcrystals. In: *Crystal Growth and Design* 6 (2006), Nr. 6, S. 1518–1522

[PSM71] Powell, R. A. ; Spicer, W. E. ; McMenamin, J. C.: Location of the Zn 3 d States in ZnO. In: *Phys. Rev. Lett.* 27 (1971), Jul, S. 97–100

[PW92] Perdew, John P. ; Wang, Yue: Accurate and simple analytic representation of the electron-gas correlation energy. In: *Phys. Rev. B* 45 (1992), Jun, S. 13244–13249

[PZ81a] Perdew, J. P. ; Zunger, Alex: Self-interaction correction to density-functional approximations for many-electron systems. In: *Phys. Rev. B* 23 (1981), May, S. 5048–5079

[PZ81b] Perdew, J. P. ; Zunger, Alex: Self-interaction correction to density-functional approximations for many-electron systems. In: *Phys. Rev. B* 23 (1981), May, S. 5048–5079

[PZW02] Park, C. H. ; Zhang, S. B. ; Wei, Su-Huai: Origin of *p* -type doping difficulty in ZnO: The impurity perspective. In: *Phys. Rev. B* 66 (2002), Aug, S. 073202

[QEHB07] Quintana, María ; Edvinsson, Tomas ; Hagfeldt, Anders ; Boschloo, Gerrit: Comparison of Dye-Sensitized ZnO and TiO2 Solar Cells:? Studies of Charge Transport and Carrier Lifetime. In: *The Journal of Physical Chemistry C* 111 (2007), Nr. 2, S. 1035–1041

[RDBH08] Raymand, David ; Duin, Adri C. ; Baudin, Micael ; Hermansson, Kersti: A reactive force field (ReaxFF) for zinc oxide. In: *Surface Science* 602 (2008), Nr. 5, S. 1020 – 1031

[RDG+11] Raymand, David ; Duin, Adri C. ; Goddard, William A. ; Hermansson, Kersti ; Spångberg, Daniel: Hydroxylation Structure and Proton Transfer Reactivity at the Zinc Oxide/Water Interface. In: *The Journal of Physical Chemistry C* 115 (2011), Nr. 17, S. 8573–8579

[RDS+10] Raymand, David ; Duin, Adri C. ; Spångberg, Daniel ; Goddard, William A. ; Hermansson, Kersti: Water adsorption on stepped ZnO surfaces from MD simulation. In: *Surface Science* 604 (2010), Nr. 9-10, S. 741 – 752

[SABW82] Swope, William C. ; Andersen, Hans C. ; Berens, Peter H. ; Wilson, Kent R.: A computer simulation method for the calculation of equilibrium constants for the formation of physical clusters of molecules: Application to small water clusters. In: *The Journal of Chemical Physics* 76 (1982), Nr. 1, S. 637–649

[SC98] Srikant, V. ; Clarke, D. R.: On the optical band gap of zinc oxide. In: *Journal of Applied Physics* 83 (1998), Nr. 10, S. 5447–5451

[SC11] Schneider, Julian ; Ciacchi, Lucio C.: A Classical Potential to Model the Adsorption of Biological Molecules on Oxidized Titanium Surfaces. In: *Journal of Chemical Theory and Computation* 7 (2011), Nr. 2, S. 473–484

[SC12] Schneider, Julian ; Colombi Ciacchi, Lucio: Specific Material Recognition by Small Peptides Mediated by the Interfacial Solvent Structure. In: *Journal of the American Chemical Society* 134 (2012), Nr. 4, S. 2407–2413

[Sch01] Schmidt, M.: X-ray photoelectron spectroscopy studies on adsorption of amino acids from aqueous solutions onto oxidised titanium surfaces. In: *Archives of Orthopaedic and Trauma Surgery* 121 (2001), Nr. 7, S. 403–410

[SDCF94] Stephens, P. J. ; Devlin, F. J. ; Chabalowski, C. F. ; Frisch, M. J.: Ab Initio Calculation of Vibrational Absorption and Circular Dichroism Spectra Using Density Functional Force Fields. In: *The Journal of Physical Chemistry* 98 (1994), Nr. 45, S. 11623–11627

[Sei07] Seifert, G.: Tight-Binding Density Functional Theory::An Approximate Kohn-Sham DFT Scheme. In: *The Journal of Physical Chemistry A* 111 (2007), Nr. 26, S. 5609–5613

[SFFB06] Schleife, A. ; Fuchs, F. ; Furthmüller, J. ; Bechstedt, F.: First-principles study of ground- and excited-state properties of MgO, ZnO, and CdO polymorphs. In: *Phys. Rev. B* 73 (2006), Jun, S. 245212

[SFR07] Sousa, Sérgio F. ; Fernandes, Pedro A. ; Ramos, Maria J.: General Performance of Density Functionals. In: *The Journal of Physical Chemistry A* 111 (2007), Nr. 42, S. 10439–10452

[SJ12] Seifert, Gotthard ; Joswig, Jan-Ole: Density-functional tight binding: An approximate density-functional theory method. In: *Wiley Interdisciplinary Reviews: Computational Molecular Science* 2 (2012), Nr. 3, S. 456–465

[SLW09] Skelton, Adam A. ; Liang, Taining ; Walsh, Tiffany R.: Interplay of Sequence, Conformation, and Binding at the Peptide-Titania Interface as Mediated by Water. In: *ACS Appl. Mater. Interfaces* 1 (2009), S. 1482–1491

[SS03] Sano, Ken-Ichi ; Shiba, Kiyotaka: A Hexapeptide Motif that Electrostatically Binds to the Surface of Titanium. In: *Journal of the American Chemical Society* 125 (2003), Nr. 47, S. 14234–14235

[SSB+92] Scarano, D. ; Spoto, G. ; Bordiga, S. ; Zecchina, A. ; Lamberti, C.: Lateral interactions in CO adlayers on prismatic ZnO faces: a FTIR and HRTEM study. In: *Surface Science* 276 (1992), Nr. 1-3, S. 281 – 298

[STB+03] Sarikaya, M. ; Tamerler, C. ; Bordiga, A. K. Y. ; Schulten, K. ; F.Baneyx: Molecular biomimetics: nanotechnology through biology. In: *Nat Mater* 2 (2003), S. 577 – 585

[TDS+04] Thai, Corrine K. ; Dai, Haixia ; Sastry, M. S. R. ; Sarikaya, Mehmet ; Schwartz, Daniel T. ; Baneyx, François: Identification and characterization of Cu2O- and

ZnO-binding polypeptides by Escherichia coli cell surface display: toward an understanding of metal oxide binding. In: *Biotechnology and Bioengineering* 87 (2004), Nr. 2, S. 129–137

[TGW+06] Taratula, Olena ; Galoppini, Elena ; Wang, Dong ; Chu, Dorothy ; Zhang, Zheng ; Chen, Hanhong ; Saraf, Gaurav ; Lu, Yicheng: Binding Studies of Molecular Linkers to ZnO and MgZnO Nanotip Films. In: *The Journal of Physical Chemistry B* 110 (2006), Nr. 13, S. 6506–6515

[TMP02] Tani, Takao ; Mädler, Lutz ; Pratsinis, Sotiris E.: Homogeneous ZnO Nanoparticles by Flame Spray Pyrolysis. In: *Journal of Nanoparticle Research* 4 (2002), S. 337–343

[TSRL00] Tunon, Inaki ; Silla, Estanislao ; Ruiz-López, Manuel F.: On the tautomerization process of glycine in aqueous solution. In: *Chemical Physics Letters* 321 (2000), Nr. 5-6, S. 433 – 437

[UH75] Utsch, B. ; Hausmann, A.: Halleffekt und Leitfähigkeitsmessungen an Zinkoxid-Einkristallen mit Sauerstofflücken als Donatoren. In: *Zeitschrift für Physik B Condensed Matter* 21 (1975), Nr. 1, S. 27–31

[UMT+05] Umetsu, M. ; Mizuta, M. ; Tsumoto, K. ; Ohara, S. ; Takami, S. ; Watanabe, H. ; Kumagai, I. ; Adschiri, T.: Bioassisted Room-Temperature Immobilization and Mineralization of Zinc Oxide£The Structural Ordering of ZnO Nanoparticles into a Flower-Type Morphology. In: *Advanced Materials* 17 (2005), Nr. 21, S. 2571–2575

[Van90] Vanderbilt, David: Soft self-consistent pseudopotentials in a generalized eigenvalue formalism. In: *Phys. Rev. B* 41 (1990), Apr, S. 7892–7895

[Vay03] Vayssieres, L.: Growth of Arrayed Nanorods and Nanowires of ZnO from Aqueous Solutions. In: *Advanced Materials* 15 (2003), Nr. 5, S. 464–466

[Ver67] Verlet, Loup: Computer "Experiments" on Classical Fluids. I. Thermodynamical Properties of Lennard-Jones Molecules. In: *Phys. Rev.* 159 (1967), Jul, S. 98–103

[VWN80] Vosko, S. H. ; Wilk, L. ; Nusair, M.: Accurate spin-dependent electron liquid correlation energies for local spin density calculations: a critical analysis. In: *Canadian Journal of Physics* 58 (1980), Nr. 8, S. 1200–1211

[WAK+07] Wahab, Rizc ; Ansari, S.G. ; Kim, Y.S. ; Seo, H.K. ; Kim, G.S. ; Khang, Gilson ; Shin, Hyung-Shik: Low temperature solution synthesis and characterization of ZnO nano-flowers. In: *Materials Research Bulletin* 42 (2007), Nr. 9, S. 1640 – 1648

[Wan04] Wang, Zhong L.: Zinc oxide nanostructures: growth, properties and applications. In: *Journal of Physics: Condensed Matter* 16 (2004), Nr. 25, S. R829

[WLC+04] Wan, Q. ; Li, Q. H. ; Chen, Y. J. ; Wang, T. H. ; He, X. L. ; Li, J. P. ; Lin, C. L.: Fabrication and ethanol sensing characteristics of ZnO nanowire gas sensors. In: *Applied Physics Letters* 84 (2004), Nr. 18, S. 3654–3656

[WOO14] *Etacude*. `http://chemicals.etacude.com/z/zinc_oxide.php`. Version: 2014

[WWC+04] Wang, Junmei ; Wolf, Romain M. ; Caldwell, James W. ; Kollman, Peter A. ; Case, David A.: Development and testing of a general amber force field. In: *Journal of Computational Chemistry* 25 (2004), Nr. 9, S. 1157–1174

[XKL+08] Xia, Tian ; Kovochich, Michael ; Liong, Monty ; Mädler, Lutz ; Gilbert, Benjamin ; Shi, Haibin ; Yeh, Joanne I. ; Zink, Jeffrey I. ; Nel, Andre E.: Comparison of the Mechanism of Toxicity of Zinc Oxide and Cerium Oxide Nanoparticles Based on Dissolution and Oxidative Stress Properties. In: *ACS Nano* 2 (2008), Nr. 10, S. 2121–2134

[YPK+06] Yadav, A ; Prasad, Virendra ; Kathe, AA ; Raj, Sheela ; Yadav, Deepti ; Sundaramoorthy, C ; Vigneshwaran, N: Functional finishing in cotton fabrics using zinc oxide nanoparticles. In: *Bulletin of Materials Science* 29 (2006), Nr. 6, S. 641–645

[YYY+07] Yang ; Yu, Haibo ; York, Darrin ; Cui, Qiang ; Elstner, Marcus: Extension of the Self-Consistent-Charge Density-Functional Tight-Binding Method: Third-Order Expansion of the Density Functional Theory Total Energy and Introduction of a Modified Effective Coulomb Interaction. In: *The Journal of Physical Chemistry A* 111 (2007), Nr. 42, S. 10861–10873

[YZJ+08] Yuan, G. D. ; Zhang, W. J. ; Jie, J. S. ; Fan, X. ; Zapien, J. A. ; Leung, Y. H. ; Luo, L. B. ; Wang, P. F. ; Lee, C. S. ; Lee, S. T.: p-Type ZnO Nanowire Arrays. In: *Nano Letters* 8 (2008), Nr. 8, S. 2591–2597

[ZKA+97] Zhu, Z. ; Kurtz, E. ; Arai, K. ; Chen, Y. F. ; Bagnall, D. M. ; Tomashini, P. ; Lu, F. ; Sekiguchi, T. ; Yao, T. ; Yasuda, T. ; Segawa, Y.: Self-Organized Growth of II-VI Wide Bandgap Quantum Dot Structures. In: *physica status solidi (b)* 202 (1997), Nr. 2, S. 827–833

[ZLP+13] Zheng, Zhaoke ; Lim, Zhi S. ; Peng, Yuan ; You, Lu ; Chen, Lang ; Wang, Junling: General Route to ZnO Nanorod Arrays on Conducting Substrates via Galvanic-cell-based approach. In: *Sci. Rep.* 3 (2013), 08

[ZXW06] Zhou, J. ; Xu, N.S. ; Wang, Z.L.: Dissolving Behavior and Stability of ZnO Wires in Biofluids: A Study on Biodegradability and Biocompatibility of ZnO Nanostructures. In: *Advanced Materials* 18 (2006), Nr. 18, S. 2432–2435

Danksagung

An dieser Stelle möchte ich mich bei allen Menschen bedanken, die mir die Erstellung meiner Dissertation möglich gemacht haben.

Da meine Arbeit in enger Kooperation zwischen den Arbeitsgruppen von Herrn Prof. Thomas Frauenheim und Herrn Prof. Lucio Colombi Ciacci erstellt wurde, möchte ich mich bei beiden sehr herzlich für diese Möglichkeit und Ihre Betreuung bedanken. Dank des mir von beiden entgegen gebrachten Vertrauens konnte ich stets sehr selbständig arbeiten und somit wertvolle Erfahrungen sammeln.
Bei meiner Betreuerin Dr. Susi Köppen bedanke ich mich für den Mut Ihre erste Doktorandin sein zu dürfen. Ihre fortwährende Unterstützung und Motivation in Phasen, in denen ich nicht mehr weiter wusste, hatten einen großen Anteil an der Fertigstellung dieser Arbeit.
Frau Prof. Franziska Traeger danke ich für die tolle Kooperation zum Thema der Wasseradsorption auf ZnO. Ihre Einführung in die Vorgehensweise experimenteller Aufbauten waren für eine Theoretikerin wie mich sehr interessant und wertvoll.
Für Ihre Mühe beim Korrekturlesen dieser Arbeit danke ich Tatjana Dabrowski und Julian Bartels. Mein größter Dank gilt jedoch Dr. Volker Weiß. Das unglaublich schnelle und dabei noch sehr gründliche Korrekturlesen von Volker war für mich in der Endphase dieser Arbeit wirklich von unschätzbarem Wert.
Bei Dr. Christof Köhler möchte ich mich für die sehr gute Betreuung des Computer- und Clustersystems bedanken, wodurch die Erstellung der Ergebnisse dieser Arbeit sehr erleichtert wurde.
Bei meinen Büronachbarn Tino, Adriel und Michael bedanke ich mich für die ungezwungene Atmossphäre, die wissenschaftlichen wie auch privaten Gespräche und die Späße, die Rückschläge in den eigenen Ergebnissen oft sehr viel erträglicher machten. Mein Dank gilt zudem allen Mitarbeitern des BCCMS für die stete Hilfsbereitschaft und freundliche Arbeitsatmossphäre.

Meinen Freundinnen Lotta, Meike, Susi und Pia danke ich für die aufmunternden Worte und die Ablenkungen zur richtigen Zeit. Es tut immer sehr gut mit euch auf ganz andere Gedanken fernab der Physik zu kommen.
Meiner gesamten Familie danke ich für die permanente und liebevolle Unterstützung während meiner Promotionszeit. Obwohl das Fachgebiet der Physik für viele ein absolutes Schreckgespenst ist, habt Ihr immer viel Interesse und Verständnis aufgebracht. Natürlich danke ich auch

Mücke, der mir jeden Tag gezeigt hat, wann es Zeit ist auch mal eine Pause zu machen.

Zuletzt möchte ich dem wichtigsten Menschen in meinem Leben, meinem Mann Marzellus, danken. Jemanden wie dich bedingungslos an meiner Seite zu wissen, war während der ganzen Zeit der größte Rückhalt für mich.

Eidesstattliche Erklärung

Hiermit erkläre ich an Eides Statt, daß die vorliegende Promotionsarbeit - abgesehen von der Beratung durch meine wissenschaftlichen Betreuer - nach Inhalt und Form meine eigene Arbeit ist. Sie wurde weder ganz noch in Teilen an anderer Stelle im Rahmen eines Prüfungsverfahrens vorgelegt.

Bremen den 05.05.14

.....
(Svea große Holthaus)